

DISSERTATION

MOIST SYNOPTIC TRANSPORT OF CO₂ ALONG MIDLATITUDE STORM
TRACKS, TRANSPORT UNCERTAINTY, AND IMPLICATIONS FOR FLUX
ESTIMATION

Submitted by

Nicholas C. Parazoo

Department of Atmospheric Science

In partial fulfillment of the requirements

For the Degree of Doctor of Philosophy

Colorado State University

Fort Collins, Colorado

Summer 2011

Doctoral Committee:

Advisor: A. Scott Denning

David Randall

Eric Maloney

Randy Kawa

Keith Paustian

ABSTRACT

MOIST SYNOPTIC TRANSPORT OF CO₂ ALONG MIDLATITUDE STORM TRACKS, TRANSPORT UNCERTAINTY, AND IMPLICATIONS FOR FLUX ESTIMATION

Mass transport along moist isentropic surfaces on baroclinic waves represents an important component of the atmospheric heat engine that operates between the equator and poles. This is also an important vehicle for tracer transport, and is correlated with ecosystem metabolism because large-scale baroclinicity and photosynthesis are both driven seasonally by variations in solar radiation. In this research, I pursue a dynamical framework for explaining atmospheric transport of CO₂ by synoptic weather systems at middle and high latitudes. A global model of atmospheric tracer transport, driven by meteorological analysis in combination with a detailed description of surface fluxes, is used to create time varying CO₂ distributions in the atmosphere. Simulated mass fluxes of CO₂ are then decomposed into a zonal monthly mean component and deviations from the monthly mean in space and time. Mass fluxes of CO₂ are described on moist isentropic surfaces to represent frontal transport along storm tracks.

Forward simulations suggest that synoptic weather systems transport large amounts of CO₂ north and south in northern mid-latitudes, up to 1 PgC month⁻¹ during winter when baroclinic wave activity peaks. During boreal winter when northern plants respire, warm moist air, high in CO₂, is swept upward and poleward along the east side of baroclinic waves and injected into the polar vortex, while cold dry air, low in CO₂, that had been transported into the polar vortex earlier in the

year is advected equatorward. These synoptic eddies act to strongly reduce seasonality of CO₂ in the biologically active mid-latitudes by 50% of that implied by local net ecosystem exchange while correspondingly amplifying seasonality in the Arctic. Transport along stormtracks is correlated with rising, moist, cloudy air, which systematically hides this CO₂ transport from satellite observing systems. Meridional fluxes of CO₂ are of comparable magnitude as surface exchange of CO₂ in mid-latitudes, and thus require careful consideration in (inverse) modeling of the carbon cycle.

Because synoptic transport of CO₂ by frontal systems and moist processes is generally unobserved and poorly represented in global models, it may be a source of error for inverse flux estimates. Uncertainty in CO₂ transport by synoptic eddies is investigated using a global model driven by four reanalysis products from the Goddard EOS Data Assimilation System for 2005. Eddy transport is found to be highly variable between model analysis, with significant seasonal differences of up to 0.2 PgC, which represents up to 50% of fossil fuel emissions. The variations are caused primarily by differences in grid spacing and vertical mixing by moist convection and PBL turbulence. To test for aliasing of transport bias into inverse flux estimates, synthetic satellite data is generated using a model at 50 km global resolution and inverted using a global model run with coarse grid transport. An ensemble filtering method called the Maximum Likelihood Ensemble Filter (MLEF) is used to optimize fluxes. Flux estimates are found to be highly sensitive to transport biases at pixel and continental scale, with errors of up to 0.5 PgC year⁻¹ in Europe and North America.

ACKNOWLEDGEMENTS

I am very grateful for the guidance and support of my advisor, Professor A. Scott Denning. This dissertation could not have been written without his expertise and encouragement. Scott has been a thrill to work with over the years, and has inspired me to become a great scientist with the right motivation and perspective. While Scott is always a friend and colleague first, he is a professional in the workplace and always encourages honorable and ethical research practices. His natural leadership makes him easy to approach and fun to work with. In addition to being a great mentor, he has given me numerous opportunities to travel around the world to learn more about carbon science and present my findings to others in the scientific community.

To my committee members David A. Randall, Randy S. Kawa, Eric Maloney, and Keith Paustian for sitting through the various meetings and closed door sessions, taking time to read through my Dissertation, and in general providing constructive feedback on my research. In addition, I would like to thank David Randall for help in deriving equations and constructing a rigorous methodology for interpreting CO₂ transport by the atmospheric circulation, enthusiasm in the classroom, open door policy, simple explanations, and fostering the logical deduction part of my brain. I want to thank Randy Kawa for funding a significant portion of my research, carefully reading through all of my publications and Dissertation, flying to Colorado when duty called, and providing ample computer time needed to finish my research in time for Summer graduation. I also want to thank Keith Paustian and Eric Maloney for showing interest in my work despite his background.

I am also thankful to the entire Denning research group, including: Ian Baker for help with SiB and perhaps more importantly his open door policy, friendly demeanor and advice concerning

any and all matters, my long time of ce mate Anna Harper for excellent discussions regarding all research and non-research related topics, Ravindra Lokupitiya for help running PCTM and MLEF, Erica McGrath-Spangler for introducing the concept of planning ahead, Erandi Lokupitiya for help implementing SiB-CROP into PCTM and her constant smiles, Andrew Schuh for help interpreting my inversion study, Kevin Schaefer for help with SiB, and nally to Kathy Corbin, Marek Uliasz, Parker Kraus, Isaac Medina, and Biljana Orescanin for great feedback during group meetings.

A special thanks to all of my collaborators over the years. It is a long list and I can't name them all, but I'd like to name a selected few who at times went out of there way to move my research forward. In particular is Joe Berry, who like Scott remains motivated and full of insight yet always puts the student rst in accomplishing research goals. Another person who stands out is David Baker, whom always seemed to help at the drop of the hat and like Scott goes out of his way at meetings to introduce me around. I also want to thank the Carbon Cycle and Greenhouse Gases group at NOAA GMD in Boulder for the support over the years.

Finally, I want to thank all friends and family. My family has always been 100% behind me at all times, and a special shout-out goes to my mom Cyndy and my dad John for making the arduous journey from Oregon to Colorado for my Masters and Doctorate graduation ceremonies to cheer me on. Another special thanks to my aunt, Laurie, for helping to fly friends and family back and forth between Oregon and Colorado so that it was not 7 years spent alone.

This research is funded by National Aeronautics & Space Administration contracts NNX06AC75G, NNX08AM56G and NNG08AT77G.

CONTENTS

1	Background and Objectives	1
1.1	Background	1
1.1.1	Atmospheric Observations	4
1.1.2	Transport Models	9
1.1.3	Optimization Technique	15
1.2	Motivation	19
1.3	Objectives of this Study	20
2	Experimental Methods	23
2.1	Model Description	23
2.1.1	PCTM	23
2.2	Surface Boundary Conditions	25
2.2.1	Terrestrial Fluxes	25
2.2.2	Fossil Fuel Fluxes	27
2.2.3	Oceanic Fluxes	28
2.3	Transport Driver Data	28
2.3.1	GEOS4-1.25x1	29
2.3.2	GEOS4-2.5x2	30
2.3.3	GEOS5-0.67x0.5	30
2.3.4	GEOS5-1.25x1	31

2.4	Transport Simulations for Parts 1 and 2	31
2.5	Methodology for Transport Analysis	33
2.5.1	Tendency Equation for Atmospheric CO_2	33
2.5.2	Eddy Decomposition	36
2.5.3	Vertical Coordinate	38
2.6	Methodology for Inversion used in Part 3	42
2.6.1	Assimilation Scheme	43
2.6.2	Synthetic Satellite Data	45
2.6.3	MLEF	50
2.6.4	Covariance Smoothing and Localization	53
2.6.5	Defining Priors	53
2.6.6	Terminology	54
2.6.7	Flux and Uncertainty Calculation	54
3	Moist Synoptic Transport of CO_2 Along the Midlatitude Storm Track	57
3.1	Introduction	57
3.2	The Zonal Mean Circulation - Streamfunctions	59
3.2.1	Streamfunction on Terrain Following Surfaces (η)	60
3.2.2	Streamfunction on θ	62
3.2.3	Streamfunction on θ_e	64
3.3	Energy Transport	66
3.4	Seasonal Covariance of Baroclinicity and Ecosystem Metabolism	69
3.5	Meridional Transport of CO_2 by Mean and Eddy Circulations	70
3.5.1	CO_2 Transport by the MMC	71
3.5.2	CO_2 Transport by Synoptic Eddies	75
3.5.3	Vertically Integrated Transport	83

3.5.4	Dependence on Vertical Coordinate	85
3.6	Seasonal Variations	90
3.7	Conceptual Diagram	90
3.8	Discussion and Conclusions from Part 1	93
4	Sensitivity of Moist Synoptic Transport of CO₂ to Changing Meteorological Data	96
4.1	Introduction	97
4.2	Comparison to Observations	100
4.3	Model Differences in CO ₂ Transport by Eddy and Mean Circulations	103
4.4	Reasons for Model Differences in Eddy CO ₂ Transport	110
4.5	Discussion and Conclusions from Part 2	118
5	Implications of Transport Bias for Inverse Flux Estimation	123
5.1	Introduction	123
5.2	Control Experiments - Perfect Transport	127
5.2.1	Experiment 1: Perfect Transport, Unbiased Truth, and no Cloud Screening	127
5.2.2	Experiment 2: Perfect Transport, Unbiased Truth, and Cloud Screening . . .	135
5.2.3	Aggregation of Experiments 1 and 2 up to TransCom Regions	139
5.3	Bias Recovery and Perfect Transport	145
5.3.1	Experiment 3: Perfect Transport, Constant and Unperturbed Biases, and Cloud Screening	147
5.3.2	Experiment 4: Perfect Transport, Seasonal and Noisy Biases, and Cloud Screening	149
5.4	Biased Transport	149
5.4.1	Experiment 5: Biased Transport, Unbiased Truth, and Cloud Screening . . .	151
5.4.2	Experiment 6: Biased Transport, Biased Truth, and Cloud Screening	152
5.5	Discussion and Conclusions from Part 3	153

6 Conclusions and Future Work	171
--------------------------------------	------------

Bibliography	175
---------------------	------------

FIGURES

1.1	Components of the global CO ₂ budget [taken from Le Quere et al., 2009].	2
1.2	World map showing the NOAA ESRL/GMD CCGG Cooperative Air Sampling Network	5
1.3	Earth's net radiation budget [courtesy of Pearson Prentice Hall, Inc].	11
1.4	Illustration of frontal transports associated with a baroclinic wave.	11
1.5	Model representation of a cold front and associated divergence / convergence couplet (courtesy The COMET Program, http://www.meted.ucar.edu/).	14
2.1	Number of points sampled by pixels in GEOS4-2.5x2 along the GOSAT orbit in one year for all days (a) and clear days (b).	46
2.2	Fraction of points retained after cloud screening for winter (top left), spring (top right), summer (bottom left), and fall (bottom right).	48
2.3	Percent of points retained after cloud screening for 1 year (prepared for comparison with Figure 1 of Eguchi and Yokota [2008]).	49
3.1	The global mean circulation computed on Eta surfaces from GEOS4-1.25x1 for 2005. Contour interval is $2.5 \times 10^{10} \text{ kg s}^{-1}$. Solid red contours are positive values of Ψ and correspond counterclockwise circulations, with northward flow at low levels and southward flow at high levels. Dashed blue contours are negative values of Ψ and correspond to clockwise circulations, with southward flow at low levels and northward flow at high levels.	61

3.2	Same as Figure 3.1, except computed on potential temperature surfaces.	63
3.3	Same as Figure 3.2, except computed on equivalent potential temperature surfaces.	65
3.4	Annual mean transport of moist static energy by various components of the mid-latitude circulation. Energy has units of PW month ⁻¹	68
3.5	Seasonal covariance of moist static energy transport (<i>h</i> , black line) and zonally-monthly averaged terrestrial net ecosystem exchange (NEE, green line) for boreal winter (A, Dec-Jan-Feb) and boreal summer (B, Jun-Jul-Aug). NEE is plotted as a zonal mean in units of $\mu\text{mol m}^{-2} \text{s}^{-1}$ on the right y-axis.	70
3.6	Diagnosis of vertical distribution of atmospheric CO ₂ transport by the MMC on θ_e in the annual mean (A) and during boreal winter (B) and summer (C). Red (blue) contours indicate poleward (equatorward) transport. Units are PgC K ⁻¹ month ⁻¹ .	72
3.7	Zonal and monthly mean distribution of CO ₂ (shaded) and mass flux (contours) in the annual mean (A) and during boreal winter (B) and summer (C). Shaded values are represented by the colorbar in (C), where the hemispheric mean has been subtracted (hence “CO ₂ anomaly”). Contour intervals of mass fluxes are 0.05 Pg s ⁻¹ K ⁻¹ . Red solid (blue dashed) contours correspond to poleward (equatorward) flow.	73
3.8	Diagnosis of vertical distribution of atmospheric CO ₂ transport by synoptic eddies (stationary and transient waves combined) on θ_e in the annual mean (A) and during boreal winter (B) and summer (C). Red (blue) contours indicate poleward (equatorward) transport. Units are PgC K ⁻¹ month ⁻¹	76
3.9	Case study from 13 Jan 2005 showing an example of eddy CO ₂ transport associated with a typical mid-latitude cyclone. The surface composite map in (A) is reproduced with permission of Unisys Corporation (c) 2011. Model output of anomalous CO ₂ (ppm, shaded) and mass flux ($1 \times 10^{-4} \text{ kg m}^{-1} \text{ K}^{-1}$, contour) along $\theta_e = 300 \text{ K}$ is plotted in (B). Taken from Parazoo et al., [2011]	78

3.10	Annual mean correlation coefficient of mass flux and CO ₂ deviations for (A) transient eddies and (B) stationary eddies (bottom plot), plotted as a function of θ_e . Colorbar is the correlation coefficient.	80
3.11	The annual mean spatial distribution of column integrated transport by (A) transient and stationary eddies, (B) transient eddies and (C) stationary eddies. The colorbar for each plot is shown at the bottom in units of PgC month ⁻¹	82
3.12	Column integrated transport in the annual mean (A) and during boreal winter (B) and summer (C). Total transport (black line) is parsed into transport by total eddy (red, transient + stationary), transient eddy (magenta), stationary eddy (cyan) and mean (blue) components.	83
3.13	Column integrated transport in the annual mean as a function of vertical coordinate. Transport is calculated on moist isentropic surfaces (θ_e , solid line), dry isentropic surfaces (θ , dashed line), and terrain following surfaces (η , dotted line). Total transport (black) is partitioned to transport by eddy (red) and mean (blue) components.	85
3.14	Zonal and month mean distribution of CO ₂ (shaded) and meridional mass flux (contours) in the annual mean on θ_e (A) and η (B). The colorbar for CO ₂ (in ppm) is shown on the bottom. CO ₂ is plotted on the same scale.	88
3.15	Diagram of isentropic surfaces and air streams along polar front (courtesy http://www-das.uwyo.edu/geerts/cwx/notes/chap01/tropo.html).	89

3.16	Column integrated seasonal CO ₂ budget tendencies (ppm month ⁻¹) on θ_e binned into (A) high latitudes and (B) mid-latitudes. Transport by transient and stationary eddies is plotted in blue, mean meridional transport in red, the total CO ₂ tendency in black, and the total surface flux of carbon from land, ocean, and fossil fuels in green. The fossil fuel tendency is plotted as a dashed green line. The sum of individual tendencies (red, blue and green lines) is equal to the total tendency (black line). Error bars represent the root mean squared error for the two years of averaging used. Taken from Parazoo et al., [2011]	91
3.17	Illustration of important CO ₂ transport mechanisms associated with a baroclinic wave. Adapted from Parazoo et al. [2011]	92
4.1	Lag Correlations between model and observations at mid-latitude sites in North America and Europe. The four line styles refers to the model used in the correlation, where GEOS5-0.67x0.5 is solid, GEOS5-1.25x1 as dashed, GEOS4-1.25x1 is dotted, and GEOS4-2.5x2 is dash-dotted. These same line styles are used in the remaining figures in the Chapter.	101
4.2	Modeled and observed CO ₂ mixing ratio from January 1-30, 2005 at a site in northern Wisconsin (LEF) (A) 30 m above the surface (lowest model level, 50 m) and (B) 396 m above the surface (3rd model level in GEOS4 and 5th model level in GEOS5, ~ 500 m). Observations are plotted in black. Line styles for models are the same as in Figure 4.1	102
4.3	Total column integrated CO ₂ transport (black) partitioned into transport by the mean circulation (blue) and synoptic eddies (baroclinic + stationary waves, red) in the annual mean (A) and during boreal winter (Jan-Feb, B) and summer (Jun-Jul-Aug, C).	104

4.4	Column integrated seasonal CO ₂ budget tendencies (ppm month ⁻¹) for eddies binned into high latitudes (70-90°N, A) and mid-latitudes (30-70°N, B). Tendencies due to total surface flux (green solid) and fossil fuel emissions (green dashed) are shown in (B).	106
4.5	CO ₂ transport by stationary waves (cyan) and baroclinic waves (magenta) along θ_e in the annual mean (A) and during boreal winter (B) and boreal summer (C).	108
4.6	Spatial structure of annual mean column integrated CO ₂ transport by synoptic eddies along θ_e for GEOS4-2.5x2 (A), GEOS4-1.25x1 (B), GEOS5-1.25x1 (C) and GEOS5-0.67x0.5 (D). The colorbar is shown in units of PgC month ⁻¹	110
4.7	Column CO ₂ snapshots on 10 January 2005 for GEOS5-0.67x0.5 (a) and GEOS4-2.5x2 (b)	112
4.8	Zonal-annual mean values for vertical diffusion (A) and cumulus mass flux (B) binned into mid-latitudes (30-70°N) and plotted as a function of the terrain following coordinate eta (η) for each reanalysis product. These values are taken directly from the driver files used to force vertical mixing in PCTM. GEOS4 lines are identical and lie directly over one another.	113
4.9	Zonal-annual mean CO ₂ mixing ratio (ppm) binned into mid-latitudes (30-70°N) and plotted as a function of η	114
4.10	Eddy CO ₂ transport by GEOS5-1.25x1 (A) and GEO4-1.25x1 (B). Difference in eddy transport between models are shown in (C).	116
4.11	Mass transport of low-level cold dry air (blue line), low-level warm moist air (red line), and upper-level warm dry air (black line) as defined in Eqs. (5a)-(5c) of Pauluis et al. [2009].	117
5.1	Annual mean errors in terrestrial NEE in units of $\mu moles m^{-2} s^{-1}$ at pixel scale (2.5°x2°) for Experiment 1.	128

5.2	Similar to Figure 5.1 except plotted as a function of season for Experiment 1: (a) boreal winter, or December-January-February (DJF), (b) boreal spring, or March-April-May (MAM), (c) boreal summer, or June-July-August (JJA), and (d) boreal fall, or September-October-November (SOM). The colorbar has the same scale as in Figure 5.1.	129
5.3	Seasonal distribution of prior estimate of terrestrial NEE, plotted on the same scale as Figure 5.1. These priors are used for all experiments in this chapter.	130
5.4	Seasonal flux errors for Experiment 1 plotted as a fraction of the prior.	131
5.5	Annual mean uncertainties in Experiment 1 for (a) prior and (b) analyzed flux (units of $\mu\text{moles m}^{-2} \text{s}^{-1}$). Uncertainty reduction for terrestrial NEE is shown in the bottom plot (c).	132
5.6	Same as Figure 5.1 but for air-sea exchange for Experiment 1. Note difference in scale between land and ocean.	133
5.7	Same as Figure 5.6 but for prior air-sea exchange.	134
5.8	Similar to Figure 5.6 for Experiment 1, except plotted as a function of season (a) DJF, (b) MAM, (c) JJA, and (d) SON. The colorbar has the same scale as in Figure 5.6.	135
5.9	Same as Figure 5.8 except for air-sea exchange priors.	136
5.10	Seasonal errors in air-sea exchange in Experiment 1 plotted as a fraction of the prior.	137
5.11	Annual mean uncertainties in Experiment 1 for (a) prior and (b) analyzed air-seas exchange. Uncertainty reduction is shown in the bottom plot (c).	138
5.12	Same as Figure 5.1 except for Experiment 2.	139
5.13	Flux errors plotted as a function of season for Experiment 2: (a) boreal winter, or December-January-February (DJF), (b) boreal spring, or March-April-May (MAM), (c) boreal summer, or June-July-August (JJA), and (d) boreal fall, or September-October-November (SOM). The colorbar has the same scale as in Figure 5.12. . . .	140

5.14	Annual mean uncertainties in Experiment 2 for (a) prior and (b) analyzed flux. Uncertainty reduction for terrestrial NEE is shown in the bottom plot (c).	141
5.15	TransCom basis functions.	142
5.16	Bar plot of total annual fluxes from prior (dark blue), and recovered fluxes from Experiment 1 (green) and 2 (red) with corresponding posterior uncertainty estimates (error bars), aggregated up to TransCom Regions (see Figure 5.15), in GtC year ⁻¹ . The top 11 regions correspond to land, the next 11 regions correspond to ocean, and the bottom two regions correspond to total land and ocean.	143
5.17	Seasonal flux errors for TransCom land regions 1-11 for Experiment 1 (green) and Experiment 2 (red), plotted in GtC month ⁻¹ .	144
5.18	Multiplicative correction factors β_{GPP} (a), β_{RESP} (b), and β_{OCEAN} (c).	157
5.19	True (a) and recovered (b) annual mean terrestrial NEE in $\mu moles m^2 s^{-1}$ for Experiment 3.	158
5.20	Difference between true and recovered annual mean flux, in $\mu moles m^2 s^{-1}$, for Experiment 3.	159
5.21	Bar plot of annual prior flux (dark blue), true flux (green), and recovered flux (red), aggregated up to TransCom regions like Figure 5.16, and plotted in GtC year ⁻¹ for Experiment 3. Posterior uncertainty is plotted in red.	160
5.22	Seasonal cycle of prior (black), true (red), and recovered (blue) TransCom fluxes for Experiment 3 (biased truth) for land regions 1-11, plotted in GtC month ⁻¹ . Posterior (red) uncertainties are plotted as error bars.	161
5.23	True (a) and recovered (b) annual mean terrestrial NEE in $\mu moles m^2 s^{-1}$ for Experiment 4.	162
5.24	Bar plot of annual prior flux (dark blue), true flux (green), and recovered fluxes (red) for Experiment 4.	163

5.25	Annual mean flux errors over land for Experiment 5 (unbiased truth), plotted in $\mu\text{moles m}^{-2} \text{s}^{-1}$ at pixel scale ($2.5^\circ \times 2^\circ$).	164
5.26	Seasonal flux errors over land for Experiment 5 (same units and scale as Figure 5.25).	165
5.27	Bar plot of annual prior (dark blue), flux errors from Experiment 1 (light blue, perfect transport and no cloud screening), Experiment 2 (yellow, perfect transport and cloud screening), and Experiment 5 (red, biased transport and cloud screening), aggregated up to TransCom land regions and plotted in GtC year^{-1}	166
5.28	Seasonal cycle of true (black) and recovered (red) TransCom fluxes for Experiment 5 (unbiased truth) for land regions 1-11, plotted in GtC month^{-1} . Prior (blue) and posterior (red) uncertainties are plotted as error bars.	167
5.29	Bar plot of annual prior (dark blue), flux errors from Experiment 4 (green, perfect transport and monthly varying sinks), and Experiment 6 (red, biased transport and monthly varying sinks), aggregated up to TransCom land regions and plotted in GtC year^{-1}	168
5.30	Seasonal cycle of true (black) and recovered (red) TransCom fluxes for Experiment 6 (biased truth) for land regions 1-11, plotted in GtC month^{-1} . Prior (blue) and posterior (red) uncertainties are plotted as error bars.	169
5.31	Seasonal flux errors for TransCom land regions 1-11 for Experiment 5 (blue) and Experiment 6 (green), plotted in GtC month^{-1}	170

Chapter 1

BACKGROUND AND OBJECTIVES

1.1 Background

CO₂ emissions from fossil fuel combustion, including small contributions from cement production and gas flaring, were about 8.7±0.5 PgC yr⁻¹ in 2008, with emissions increasing at a rate of 3.4% per year between 2000 and 2008 [Le Quere et al., 2009, see Figure 1.1]. Fossil fuel emissions are expected to double over the next 50 years under business as usual conditions [Pacala and Socolow, 2004], and likely more as new economies emerge [Le Quere et al., 2009], causing atmospheric CO₂ concentrations to nearly triple from pre-industrial levels by the end of the century. The trend is even worse considering land use change (LUC) emissions due to anthropogenic activities such as deforestation, logging, and intensive cultivation of cropland soils (see Figure 1.1b). Although there is much interannual variability in LUC fluxes, especially in tropical regions, the 2008 LUC emissions were about 1.2 PgC yr⁻¹, bringing total anthropogenic CO₂ emissions to 9.9±0.9 PgC yr⁻¹ in 2008.

Rising CO₂ is expected to alter radiative forcing, warm climate, and cause significant global climatic changes in the near future, including natural and socioeconomic impacts. Projections of future CO₂ levels and the associated climate forcing depend strongly on our scientific understanding of both the anthropogenic and natural components of the carbon cycle and our ability to accurately predict future sources and sinks of carbon [Cox et al., 2000; Friedlingstein et al., 2006; IPCC, 2007]. The existing network of surface in situ CO₂ measurement stations [GLOBALVIEW-CO₂, 2009] suggest that on average 43% of total CO₂ emissions each year between 1959 and 2008 remained

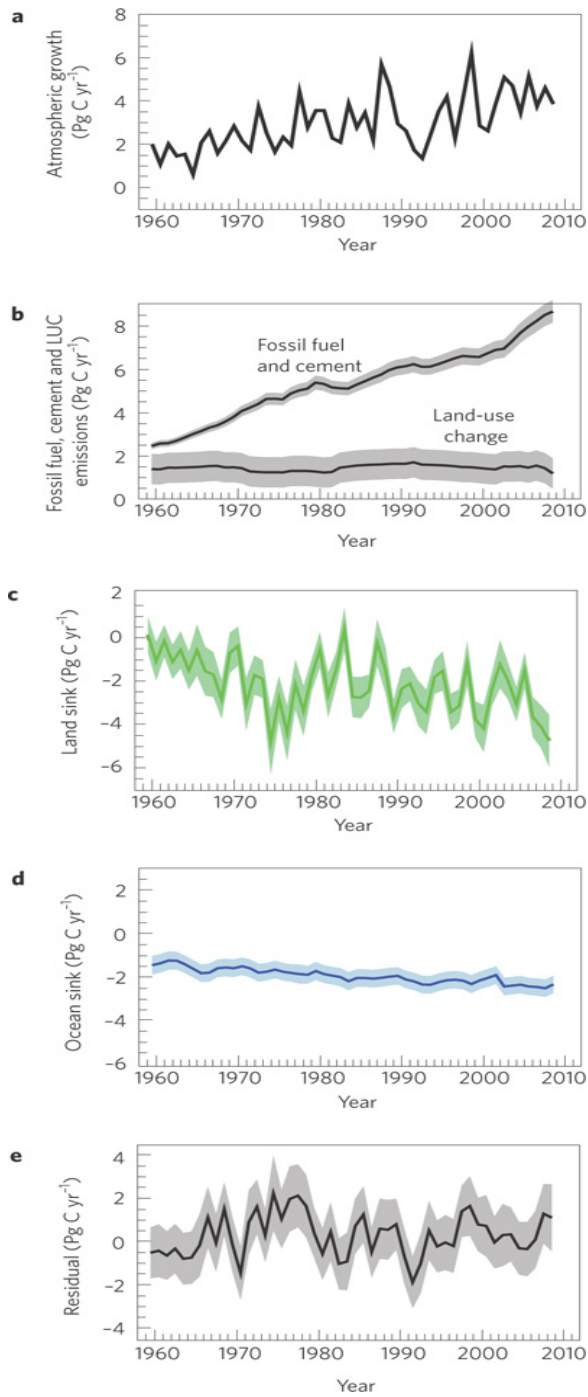


Figure 1.1: Components of the global CO₂ budget [taken from Le Quere et al., 2009].

in the atmosphere (see Figure 1.1a, Le Quere et al. [2009]). The remaining fraction, roughly 4-5 PgC yr^{-1} , was absorbed naturally by land and ocean sinks (see Figure 1.1 c and d, respectively).

Atmospheric and ocean observations constrain the global land sink to 2.6 ± 0.7 and the ocean sink to 2.2 ± 0.4 PgC yr^{-1} for 1990-2000 [McNeil et al., 2003; Manning and Keeling, 2006; Canadell et al., 2007; Denman et al., 2007; Gruber et al., 2009]. This natural sink, however, is not guaranteed to grow or even sustain its current capacity [Fung et al., 2005; Le Quere et al., 2009]. Natural emissions might actually increase, for example, as a result of already observable rapid warming in parts of the Arctic [Hinzman et al., 2005] due to mobilization of carbon currently stored in permafrost [Zimov et al., 2006; Khvorostyanov et al., 2008].

One of the first studies to determine that a combination of terrestrial and oceanic processes are responsible for net removal of CO_2 from that atmosphere was Tans et al. [1990], who compared relatively well known fossil fuel emissions and the corresponding north-south gradient in atmospheric CO_2 as determined by a three-dimensional atmospheric general circulation model to the north-south gradient observed from a global network of flask measurements. Combined with pCO_2 measurements to constrain the ocean sink, this technique implied a Northern Hemisphere (NH) terrestrial sink, but was unable to reveal information about regional processes that determine the sink. It is understanding regional processes, and how they determine the time and spatially varying source/sink distribution on synoptic, seasonal, interannual (e.g., Figure 1.1c) and climatic time scales, that has motivated more recent (\sim mid 1990's to present) research.

Variations of atmospheric CO_2 contain information about sources and sinks. Atmospheric inverse models combine tracer transport simulations with atmospheric measurements of CO_2 mixing ratio to optimize estimates of the strength and spatiotemporal distribution of sources and sinks [Gurney et al., 2002; Rödenbeck et al., 2003; Baker et al., 2006]. Results are limited by (1) data availability and precision; (2) model fidelity; and (3) optimization technique. While this research is strongly motivated by addressing a key weakness in this second component of inversion systems, the following sections describe in more detail each component, including underlying weaknesses. After stating key weaknesses, objectives of this study will be discussed in Section 1.2.

1.1.1 Atmospheric Observations

Atmospheric observations of CO₂ mixing ratio include in situ and remotely sensed measurements. The in situ network consists of surface observations by flask (weekly) and continuous (hourly) instruments, which measure at a fixed location continuously in time, as well as airborne measurements taken from aircraft, which can sample most parts of the atmosphere but tend to have fair weather bias. Remotely sensed measurements are typically column integrated and taken from aircraft or satellite. Data accuracy and density are important constraints for inversions, as illustrated by the inversion intercomparison experiment, TransCom. For example, in an annual mean inversion of flask data for 22 source regions, TransCom found uncertainties in surface flux estimates related to data sparsity ranging from 0.2-1.1 GtC yr⁻¹ [Gurney et al., 2002], which represents as much as 25% of global sink estimates.

The TransCom 3 experiment, described in Gurney et al. [2002, 2003, 2004], was based on flask measurements, which are taken under “clean-air” or “baseline” conditions in order to sample air representative of large-scale air masses. While flask sites are ideally chosen for making precise measurements of background concentrations, they are not designed to measure continental or any kind of fine scale variations due to nearby terrestrial sources and sinks. Continuous measurements are therefore a nice complement to the flask network, as can be seen in Figure 1.2,. Continuous measurement sites have existed for a number of years and the network continues to grow, especially in northern middle latitudes, and are extremely desirable for carbon cycle studies in that they are (1) collected on site and can sample more frequently (i.e., hourly) in time; (2) well-calibrated and high precision (~0.1 ppm); (3) typically located over continents close to terrestrial source and sinks; and (4) influenced by strong synoptic signals that contain upstream surface flux information. Because of continuous on-site monitoring, they are especially useful for sampling CO₂ mixing ratios contained in air masses advecting across continents at synoptic scales (~1000km), with total upstream footprint (i.e., degree of influence by surface fluxes upstream of measurements) proportional to measurement height above the surface [Bakwin et al., 1998]. Tall tower measurements

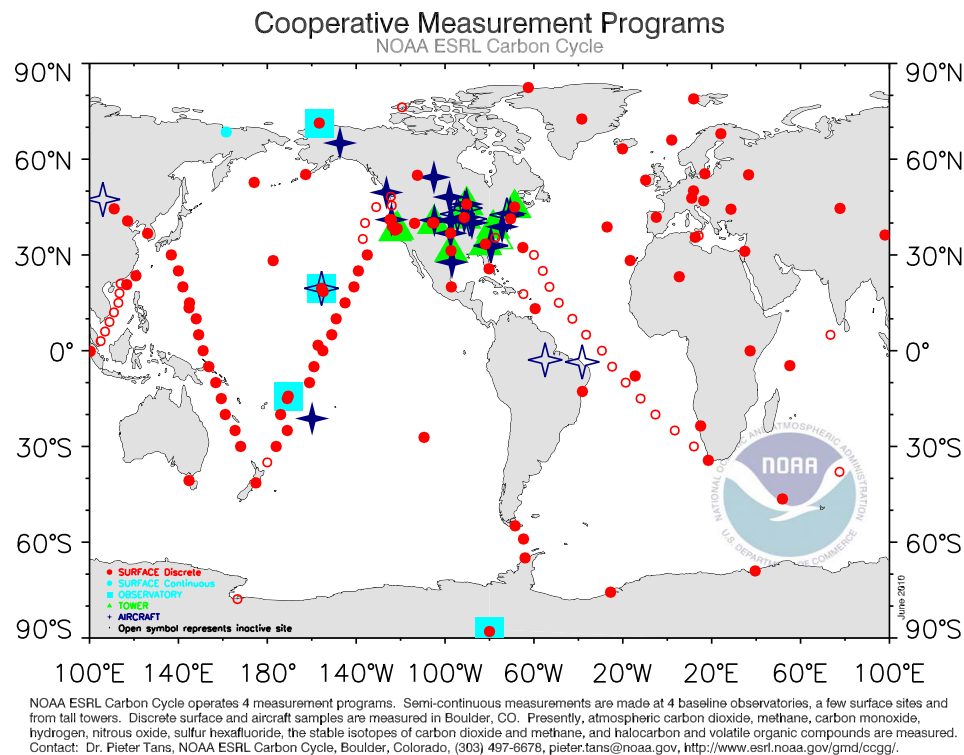


Figure 1.2: World map showing the NOAA ESRL/GMD CCGG Cooperative Air Sampling Network from National Oceanic and Atmospheric Administration (NOAA) Earth System Research Laboratory (ESRL) Global Monitoring Division (GMD), for example, can measure continuously at up to 400 m above the surface and can “feel” the influence of surface fluxes for hundreds of kilometers, while surface measurements are typically much closer to the ground (i.e., < 30 m above ground level) and more strongly influenced by local processes.

There is an interesting relationship between atmospheric measurements and surface fluxes. It is desirable for measurements to contain as much information about upstream sources and sinks as possible. Other than process based land surface models, mixing ratio measurements are our primary source of information regarding ecosystem scale fluxes of CO₂. Measurements have a higher probability of influence from larger scales the higher a measurement is above the surface.

This is where the tradeoff begins because more distance requires longer transport by atmospheric winds. In general, the more information we want to know about surface fluxes (i.e., the higher up and more frequent a measurement is) the better we (i.e., modelers) have to be at representing atmospheric transport between upstream flux and downstream concentration.

Nevertheless, use of high frequency data in CO₂ inversions has been shown to reduce overall flux uncertainties [Law et al., 2002], even more so when combined with monthly mean flask observations [e.g., Rödenbeck et al., 2003]. While continuous measurements improve our process-based understanding of local and upstream terrestrial sources and sinks [Gloor et al., 2001; Worthy et al., 2003; Geels et al., 2004; Hurwitz et al., 2004], they contain signals that result from complex atmospheric processes. At first this may seem a bad thing, because this presents an interesting challenge for models of the atmosphere to correctly represent these processes (more detail in Section 1.1.2); that being said, much has been learned about the carbon cycle and numerical models of the carbon cycle as a result of these measurements. It is also worth mentioning here that aircraft measurements are very useful for profiling vertical distributions and have helped further constrain carbon budgets at regional scales when combined with tower measurements [Lauvaux et al., 2008].

A major shortcoming of the in-situ network, as seen in Figure 1.2, is that large geographic data gaps exist, especially over the oceans, in the Southern Hemisphere (SH) and in the tropics. The surface network, despite continuous monitoring at high precision, is insufficient to precisely infer surface fluxes at regional scales. Satellites measure column averaged CO₂ mixing ratio with good spatial coverage, thus complementing data poor regions of surface measurements, but have strict precision requirements for top-down inversion because source and sink information is contained in column averaged variations, which are small (and diluted) in contrast to Planetary Boundary Layer (PBL) variations where surface networks reside. In an effort to evaluate the potential usefulness of remotely sensed mixing ratios, synthesis inversion models indicate that regional surface flux uncertainties could be reduced if in-situ data are combined with column-integrated measurements with precision of <1%, or ~3 ppm [Rayner and O'Brien, 2001; Houweling et al., 2004]. Miller et

al. [2007] estimate that precisions of 1-2 ppm are necessary to monitor carbon fluxes at regional scales.

The first space-based measurements of CO₂ were performed by NOAA's Television Infrared Observation Satellite Operational Vertical Sounder (TOVS, Smith et al. [1979]), which is able to retrieve seasonality and growth rate with some reliability [Chedin et al., 2002, 2003] but was not originally designed to monitor CO₂. Later studies found that TOVS was not ideally suited for surface flux inversion [Chevallier et al., 2005]. Like TOVS, the SCanning Imaging Absorption SpectroMeter for Atmospheric CHartographY (SCIAMACHY, Bovensmann et al., [1999]) was not designed specifically for CO₂ retrieval. Unlike TOVS, SCIAMACHY uses short wave near infrared spectrometers to measure CO₂. SCIAMACHY is thus more sensitive to surface variations and ultimately found to better constrain surface fluxes given certain levels of precision [Houweling et al., 2004]. Observations from the Atmospheric Infrared Sounder (AIRS, Aumann and Pagano [1994]), which uses a thermal infrared spectrometer, are higher precision and more numerous, but are mostly sensitive to the upper troposphere, making flux retrieval difficult.

High-precision with sensitivity down to the surface is possible when taking advantage of reflected sunlight and clear-sky conditions [O'Brien, 1990; Houweling et al., 2004]. Recently, two satellites have been designed specifically to measure the column-averaged dry air mole fraction of CO₂ (X_{CO_2}) at high (1) precision, (2) surface sensitivity, (3) global coverage and (4) regional scale resolution, all of which are necessary to characterize CO₂ sources and sinks on regional scales and thus provide the most realistic opportunity to supplement data poor regions: Japan's Greenhouse Gases Observing Satellite (GOSAT, Kuze et al., [2010]) and the National Aeronautics and Space Administration (NASA) Orbiting Carbon Observatory [OCO, Rayner et al., 2002; Crisp et al., 2004; Houweling et al., 2004; Baker et al., 2006; Miller et al., 2007; Chevallier et al., 2007]. GOSAT was launched successfully in January 2009. OCO failed to launch in February 2009; however, the OCO design had certain strong points that have led to a scheduled relaunch (OCO-2) as soon as 2013. In particular, OCO-2 would measure more frequently than GOSAT (180 vs. 13.4 cross-scans

per minute) with a smaller field of view ($\sim 2 \text{ km}^2$ vs. $\sim 100 \text{ km}^2$) and thus ought to find more cloud free scenes [Crisp et al., 2004].

The instruments discussed previously use passive measurements based on shortwave or thermal infrared sensing, with shortwave (SCIAMACHY, GOSAT, and OCO) providing more information than thermal (AIRS) and OCO providing more information than GOSAT [Hungerschofer et al., 2010]. Another instrument being explored that may overcome certain issues with OCO and GOSAT and provide even better surface flux constraint is a new satellite-based laser-sounder. Such an instrument would use Light Detection and Ranging (or LIDAR) technology to measure CO_2 absorption at nadir in laser pulses sent from the satellite to the surface and back. In this way CO_2 is measured actively (satellite carries own light source in laser), allowing continuous measurements during day and night, over land and ocean, throughout all latitudes and seasons, with less sensitivity to aerosol and thin clouds yet strong sensitivity to the lower troposphere. NASA's Active Sensing of CO_2 Emissions over Nights, Days, and Seasons (ASCENDS, Abshire et al. [2008]) and the European Space Agency (ESA) Advanced Space Carbon and Climate Observation of Planet Earth (A-SCOPE, Ingmann, [2009]) are two promising missions under consideration.

Nevertheless, cloud contamination does represent a problem for remote measurements from space, and using column satellite measurements to represent a transport model grid column introduces temporal, spatial, and local-clear sky sampling errors into inversions. Since satellite measurement requires clear-sky conditions, systematic differences in atmospheric CO_2 concentration between clear and cloudy conditions introduces sampling biases of up to -0.2 to -0.4 ppm into tracer transport inversions that use satellite CO_2 products to represent temporal averages [Corbin and Denning, 2006]. Spatially coherent biases as small as a few tenths of ppm alters flux estimates by a few tenths of a gigaton of carbon [Chevallier et al., 2007; Miller et al., 2007]. Spatial representation errors of mixed layer average CO_2 can reach 1-2 ppm for a typical 200-400 km horizontal resolution grid cell, due to unaccounted for horizontal spatial heterogeneity [Gerbig et al., 2003], while column CO_2 spatial representation errors can reach ~ 0.6 - 0.7 ppm over the land and ~ 0.2 - 0.3 ppm

over the ocean [Lin et al., 2004], with much seasonal and geographical sensitivity [Miller et al., 2007]. Spatial and local clear-sky errors tend to increase when a single satellite track is used to represent a coarse (450 x 450 km) versus fine (100 x 100 km) grid column, with local clear-sky errors biased and large (> 2 ppm) in North America [Corbin et al., 2008].

Spatial and clear-sky sampling errors are attributed partly to differences in net ecosystem exchange (NEE) on clear and cloudy days as well as surface heterogeneity, but mostly to differential advection by synoptic systems on clear and cloudy days, leading to the largest clear-sky biases in mid-latitude regions [Corbin et al., 2008]. This is not surprising considering CO₂ observations show large day-to-day CO₂ variations associated with passing weather disturbances and horizontal and vertical mixing along fronts [Parazoo et al., 2008]. Since frontal systems create large gradients of CO₂ that are associated with clouds and thus more prone to data elimination by cloud screening algorithms in satellites, inversions that use satellite measurements to represent coarse regions may incur large and biased spatial and local clear-sky errors. Considering that inversions are influenced by biases as small as a tenth of a ppm in the total column [Chevallier et al., 2007; Miller et al., 2007] and sampling errors grow as large as 2 ppm with a negative bias in coarse grid columns of NH mid-latitudes [Corbin et al., 2008], it is recommended that transport models be run at the finest possible horizontal grid spacing to avoid introducing large errors and bias. Improved grid spacing, however, is likely just one of several factors to account for when considering errors due to transport bias.

1.1.2 Transport Models

Although improvements to the global measurement network reduce uncertainty in inverse flux estimates, accounting for other unknowns such as fossil fuel emissions, wildfires, deforestation, land use change, and interannual climate variability in the carbon budget contribute additional uncertainty. Variable inversion setup, including surface flux prior estimates, transport model choice and optimization technique (discussed in Section 1.1.3), has made it difficult to reconcile differences

in inverse estimates [Peylin et al., 2002]. The model intercomparison experiment widely known as TransCom3 was designed specifically to isolate the effect of differences in transport using common surface flux “prior” estimates and atmospheric observations. TransCom3 revealed a terrestrial carbon sink distributed evenly among NH continents. The magnitude of the sink, however, was sensitive to transport differences among 16 different models, and led to the conclusion that simulated transport is one of the greatest sources of uncertainty in inversions [Gurney et al., 2002, 2003, 2004; Baker et al., 2006]. Since transport models are the primary link between atmospheric measurements and surface fluxes, uncertainty in simulated transport reduces the ability to fully utilize surface and satellite data [Houweling et al., 2010].

As discussed in the previous section, the global CO₂ observing system has grown to include continuous records at continental locations close to terrestrial sources. These records allow quantitative flux estimation at finer spatial scales than previously possible [e.g., Law et al., 2003; Peylin et al., 2005; Zupanski et al., 2007; Lauvaux et al., 2008; Schuh et al., 2009], but feature much greater variance at synoptic scales. Interpretations of these variations require accurate simulation of structure, timing, and vertical motions associated with synoptic waves and frontal weather systems [Geels et al., 2004; Hurwitz et al., 2004; Wang et al., 2007; Parazoo et al., 2008].

Strong variance at synoptic scales results from an imbalance of net heating in the tropics and cooling at high latitudes (see Figure 1.3) which, combined with Earth’s rapid rotation and angular momentum constraints, produces synoptic eddies of cyclone scale along midlatitude storm tracks that transport energy poleward. A recent analysis by Pauluis et al. [2008] found that mass transport along moist isentropic surfaces on baroclinic waves represents an important component of the atmospheric heat engine that operates between the equator and poles and is therefore an important vehicle for tracer transport. Because of strong vertical wind shear and horizontal temperature gradients, tracer transport by “slantwise convection” in baroclinic waves involves strong vertical and meridional components and is intimately tied to condensation and precipitation processes. Poleward transport by rising warm moist air follows a warm conveyor belt (WCB) above warm fronts, and

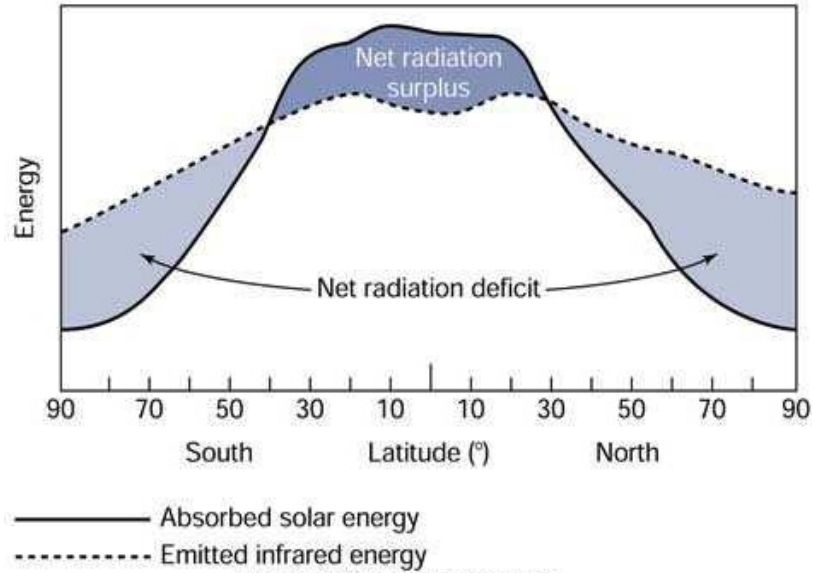


Figure 1.3: Earth's net radiation budget [courtesy of Pearson Prentice Hall, Inc].

is compensated by equatorward transport by sinking cold dry air following a dry air intrusion (DI) behind cold fronts (see Figure 1.4; e.g., Cooper et al., [2001] and Stohl, [2001]). To complicate mat-

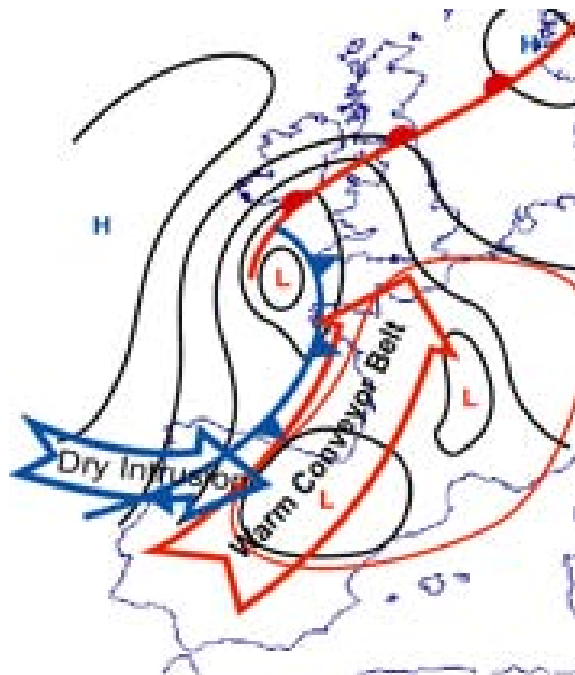


Figure 1.4: Illustration of frontal transports associated with a baroclinic wave.

ters, transport by these synoptic waves is correlated with ecosystem metabolism because large scale baroclinicity and photosynthesis are both driven seasonally by variations in solar radiation. Baroclinic wave activity is enhanced in winter when respiration and decomposition dominate ecosystem metabolism, and is suppressed in summer when photosynthesis dominates.

Pollution transport by synoptic weather systems, in particular along WCBs, has received much attention in the scientific literature. Carlson [1981] presented empirical evidence indicating aerosol transport into the Arctic along moist isentropic surfaces. More recently, models and aircraft measurements from intensive field campaigns (e.g., North American Regional Experiment) have helped create conceptual models that explain how WCBs transport gases such as O_3 and CO upward, poleward, and eastward away from continents and across ocean basins [e.g., Bethan et al., 1998; Cooper et al., 2001]. Strong pollution transport by WCBs is not surprising considering WCBs originate near the surface in polluted boundary layers and are responsible for most of a midlatitude cyclones meridional energy transport [Eckhardt et al., 2004].

CO_2 transport by baroclinic waves was described in detail by Fung et al. [1983] and was included in the study by Tans et al. [1990] that established the concept of a terrestrial carbon sink but has not received much attention since (however, see Miyazaki et al. [2008] and Keppel–Aleks et al. [2011]). It is important to refine our understanding of synoptic transport of CO_2 to understand the role that synoptic weather systems, and the embedded moist processes, play in the atmospheric carbon cycle. Furthermore, in order to interpret observed synoptic CO_2 variations in models and therefore correctly communicate between observation and surface flux in inversion experiments, we must be aware of key limitations and sensitivities of models in simulating various features associated with synoptic waves. So what are these limitations?

Tracer transport by baroclinic waves is associated with large- and small-scale features. Representation of large-scale features (~ 1000 km's) in numerical models, such as the position and timing of a baroclinic wave, is strongly dependent on grid spacing, with finer grid spacing improving the chances of representing features within a wave. Model inter-comparison studies show that

simulations at higher spatial resolution produce better match with observed synoptic variations at northern mid-latitudes sites [Geels et al., 2007; Patra et al., 2008; Ahmadov et al., 2009].

Unfortunately, certain features of synoptic waves occur at scales smaller than most global inverse models (1° globally or coarser, ~ 100 km) can resolve. The general rule of thumb is that only features represented by at least 6 model grid points are considered resolved by an atmospheric model. As an example, let's see what kind of features associated with a typical cold front embedded in an extratropical cyclone a model run with 50 km grid spacing (which is considered the grid spacing for most global models) can resolve (see Figure 1.5). Key features to point out in Figure 1.5 include the cold front (blue line), a divergence / convergence couplet across the front (purple and red lines), and moist processes, including vertical mixing by moist convection, within clouds (depicted by white shading). At 50 km grid spacing, features such as the convergence and divergence zones and locations of pre-frontal clouds are fairly well resolved. Assuming features in Figure 1.5 are depicted at the right physical scale, a model with 50 km grid spacing (and adequate vertical grid spacing) will likely be able to resolve horizontal and vertical circulations across the front (divergence and convergence zone), the location of the front, and the location of pre-frontal clouds assuming the thermodynamics within the model indicates the possibility of moist convection. However, even resolving frontal circulations at 50 km grid spacing may be optimistic considering a study that finds frontal ascent of tracer is often confined to a 60 km wide region [Donnel et al., 2001]. Frontal circulations of this scale are therefore unresolved down to grid spacing of 10 km or less.

WCBs are heavily influenced by moist processes due to the influx of warm moist air out of the subtropics. Fine scale vertical mixing by moist convection within the cloudy regions depicted in Figure 1.5, however, typically occur at scales of < 10 km and thus cannot be solved explicitly at 50 km grid spacing. These processes must instead be solved through parameterization - semiempirical statistical theory governing how subgrid-scale processes manifest themselves on the resolved grid - which is highly variable between models, not as easily constrained in reanalysis products as

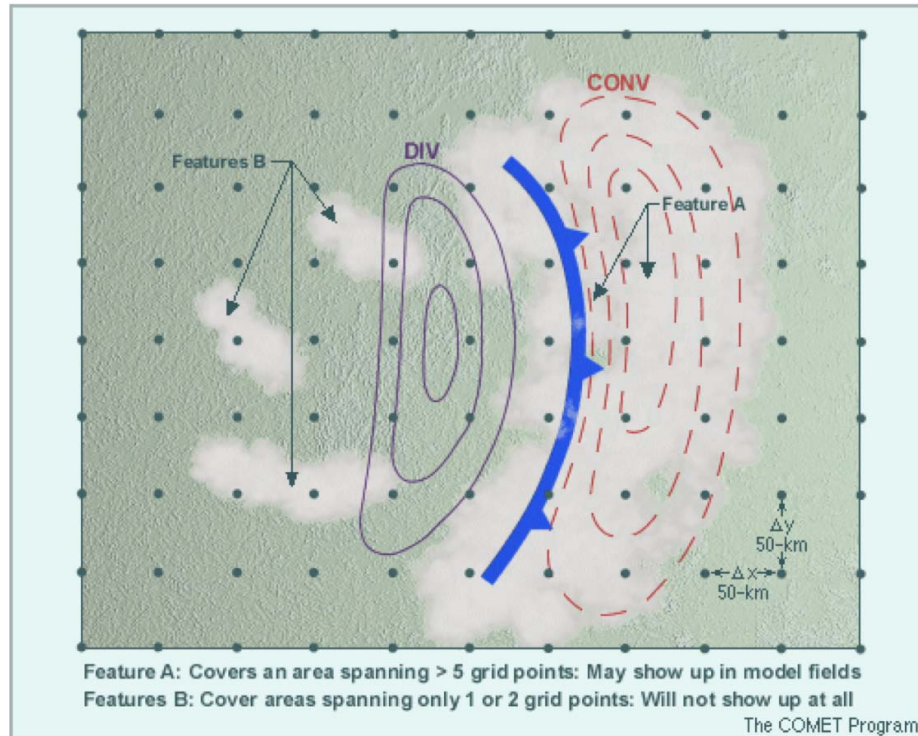


Figure 1.5: Model representation of a cold front and associated divergence / convergence couplet (courtesy The COMET Program, <http://www.meted.ucar.edu/>).

resolvable flows, and therefore highly uncertain. This presents a potentially serious problem considering strong latent heat release associated with condensation and moist processes is found to enhance ascent along WCBs [Sinclair et al., 2008]. Furthermore, small inaccuracies in convective representation that specify total latent heat release can lead to large inaccuracies in numerical simulation of dynamical systems where latent heat release is important [Emanuel, 1988]. Mixing by PBL turbulence, essential for boundary layer ventilation of tracer to levels that can be penetrated by conveyor belts [Donnell et al., 2001; Sinclair et al., 2008], is also unresolved at scales greater than 10 km and, because this process must also be parameterized, presents another source of uncertainty for modeling transport by synoptic waves.

In the era of remotely-sensed observations of trace gas from satellites, an additional complication arises because the strongest horizontal gradients in CO_2 occur along frontal boundaries that are typically hidden from orbital sensors by clouds [Corbin et al., 2006], and much of the sea-

sonality at northern latitudes is determined by moist conveyors which will hide CO₂ transport from satellites [Parazoo et al., 2011]. Corbin et al. [2008] analyzed simulated column-mean CO₂ using a clear-sky sampling regime along hypothetical satellite orbits and found that systematic sampling errors of up to 1.5 ppm in the seasonal mean were caused by cloud masking of frontal CO₂ gradients. Covariance of synoptic transport with surface CO₂ flux is likely to cause errors in top-down flux estimates if not represented correctly in transport models. Since a portion of the synoptic signal is unobserved, it is important to understand model sensitivity of synoptic transport processes, in particular to parameterization of fine scale vertical mixing and grid spacing.

1.1.3 Optimization Technique

Spatial and temporal gradients of observed CO₂ mixing ratio are directly related to surface carbon fluxes. In-situ and satellite observations can exploit surface flux information contained in synoptic signals if they are modeled well. Unfortunately, there is no standard way of quantifying transport uncertainty, so even if processes aren't modeled well, inversions often assume perfect transport. Nevertheless, methods are needed to optimally combine models and observations to provide estimates of carbon fluxes and their uncertainties. The scale at which surface fluxes may be optimally inferred therefore depends on the grid spacing of the transport model and prior information, the number and frequency of observations, and the optimization technique, the latter of which has tended to progress along with (or adapt to) the former components. Observing System Simulation Experiments (OSSEs), designed to quantitatively assess the value of atmospheric observing systems to numerical forecasting, have been applied by the CO₂ inversion community in a similar manner to assess assimilation techniques and the potential of atmospheric CO₂ observations to provide constraint for surface flux estimation.

Early inversions solved for CO₂ fluxes at monthly and annual time scales over continental scale regions using monthly mean in-situ data from networks such as GLOBALVIEW-CO₂ [e.g., Rayner and Law, 1999; Bousquet et al., 2000; Peylin et al., 2002; Gurney et al., 2002; Law et al.,

2003]. “Bayesian synthesis” or “batch mode” approaches were used to solve for a single vector of unknowns (spatio-temporal distribution of surface CO₂ flux) that maximized consistency between atmospheric observations and a priori (or “background”) surface fluxes estimated from “bottom-up” approaches. In Bayesian synthesis, a cost function (defined in Section 2.6.3) consisting of two components is optimized. The first term of the cost function involves the observations and controls the difference between the observed and predicted CO₂ mixing ratios. The second term constrains the solutions by an a priori flux distribution, which is necessary to stabilize the solution when the inversion problem is under-constrained. A linear system of equations, representing the relationship between unknown (CO₂ flux) and known (atmospheric CO₂ observations) quantities, is solved using singular value decomposition to invert large matrices such that fluxes for all source regions are estimated at all times simultaneously using all observations. The TransCom3 experiment is an example of a large-region inversion in which the globe is divided into 22 regions, consisting of 11 land and 11 ocean regions [Gurney et al., 2002]. Such large regions were necessary at the time because of the sparseness of the in situ network. This technique is mathematically overdetermined because the number of unknowns is much less than the available observations.

Large-region inversions work well for solving for a set of relatively few unknowns because they are computationally efficient, but likely lead to aggregation errors [Kaminski et al, 2001; Engelen et al., 2002] because atmospheric CO₂ is sensitive to the distribution of sources and sinks within large basis regions. New approaches were needed to supplement large-region estimates to solve for more unknowns with the same number of observations to improve the detail of fluxes. Grid scale inversions are an example of such an approach. Large-region inversions like TransCom3 are essentially grid point inversions, except that grid points are perfectly correlated in space in a region and the number of regions is order of magnitudes smaller than the number of grid points. In “pixel-scale” grid scale inversions, if grid boxes are assumed to be uncorrelated, the problem becomes mathematically underdetermined because the number of unknowns exceeds the available observations, but can be solved using the priors. Since it is not desirable for inversions to be too heavily weighted by

priors, grid-scale inversions must compromise by correlating grid cells.

Grid scale inversions have become a very popular technique for estimating CO₂ fluxes [Kaminski et al., 1999; Houweling et al., 1999; Rödenbeck et al., 2003; Peylin et al., 2005]. Rödenbeck et al. [2003] performed a grid scale inversion at 10° longitude by 8° latitude by accounting for unique spatial covariance of flux uncertainties over land and ocean. Geostatistical techniques use Bayesian methods that replace prior flux estimates with prespecified covariance structure from vegetation cover, leaf area index, greenness fraction, etc., that varies with the mean behavior of the fluxes [Michalak et al., 2004]. This technique acts as a good independent estimate to bottom-up estimates. Peylin et al [2005] used continuous measurements to estimate daily CO₂ fluxes at the model grid scale over Europe.

Bayesian techniques worked well with the relatively sparse observation network. Each new year brings with it more surface measurements at hourly resolution and huge arrays of satellites measurements at sub-hourly resolution, which together increases the observation vector beyond the capacity of bayesian techniques. Given that enhanced observation density will improve optimization at finer scales, alternative assimilation techniques to batch inversions are needed. Bruhwiler et al. [2005] introduced a fixed-lag Kalman smoother, used extensively in Numerical Weather Prediction, which steps through observations sequentially in time to optimize a subset of observations and update forecast error covariance. This method assumes that information contained in measurements smooths out over time due to atmospheric mixing of spatial gradients such that fewer observations (6-9 months worth) need be used compared to large Bayesian systems (1 year or longer). Although the Kalman smoother is not ideally suited for continuous observations, it was innovative for inverse studies of CO₂.

Peters et al. [2005] expanded on the fixed lag Kalman smoother by introducing an ensemble based approach in which the covariance matrix was approximated by ensemble members. An advantage of ensemble approaches is that they can incorporate uncertainty in estimates of flux distributions that arise from errors in the observations and transport model. These approaches attempt

to estimate the probability distribution functions (PDFs) of the analysis and forecasts using a relatively small ensemble of random realizations from the distributions. Ensemble Kalman filters such as that proposed by Peters et al. [2005] use ensemble estimates of error covariance such that surface flux estimates are those that best fit the assimilated observations. The so called “fixed-lag ensemble Kalman smoother” replaces bottom-up flux estimates with background fluxes that result from the assimilation process and therefore contain information from previous analysis cycles. While this technique can ingest large amounts of observations without the need to precalculate observation operators, it is still too computationally expensive for large observation vectors that occur in the satellite era.

Baker et al. [2006] and Chevallier et al. [2005] introduced variational data assimilation schemes as an alternative to pure matrix-based schemes in order to cope with the large amount of satellite data. Four-dimensional variational data assimilation uses an adjoint version of the transport model to estimate the atmospheric state that best fits assimilated observations. Because the “atmospheric memory” can be quite long, variational approaches are desirable in that it is possible to optimize fluxes using a year or more’s worth of observations that contain information at multiple mixing time scales. Calculation of the model adjoint can be complicated, especially if frequent changes are introduced to models and maintenance of the adjoint is necessary. Ensemble methods have the advantage that there is no need to compute model adjoints. Additionally, variational methods must prescribe a forecast error covariance while in Kalman filter like methods, including ensemble approximations, the forecast error covariance evolves in time between data assimilation cycles according to model dynamics. Another ensemble-based data assimilation approach involves the Maximum Likelihood Ensemble Filter, or MLEF [Zupanski, 2005; Zupanski and Zupanski, 2006; Zupanski et al., 2006; Zupanski et al., 2007; Lokupitiya et al., 2008], which is designed to be able to handle large observational datasets without the need for a model adjoint. Like the fixed-lag ensemble Kalman smoother, MLEF is able to approximate the Kalman filter and evolve the forecast error covariance and state in time, but work efficiently with large datasets in a massively parallel

environment. An important weakness of MLEF, like other ensemble techniques, is the requirement that a large number of unknowns are estimated using relatively small sample sizes.

1.2 Motivation

A major science objective of most carbon cycle studies is quantification of carbon sources and sinks at the finest possible resolution with the highest possible accuracy. CO₂ inversion studies attempt to map and quantify source and sink distributions using atmospheric transport models to communicate observed signals to the surface through increasingly sophisticated optimization techniques. The literature review has examined each of the three major components of this top-down approach, and revealed several well known weaknesses, most importantly: (1) fair weather bias in observations, (2) uncertainties in both grid scale and subgrid scale synoptic winds, and (3) even the best optimization techniques must sacrifice accuracy at the expense of accommodating large satellite datasets. While observations with global coverage and high precision and accurate optimization techniques are key components of the inversion, the transport model is the primary tool by which the inversion determines at what geographic location a given parcel of air containing some mixing ratio of CO₂. Given that the distribution of CO₂ mixing ratios is ultimately determined by winds between the surface flux and the observation, it is crucial to get the winds at both grid and sub-grid scale correct. Inability of atmospheric models to properly represent important dynamical processes associated with weather systems is a leading cause of incorrect winds; given the role of winds in the inversion, these incorrect winds may influence estimates of source and sink maps. This study is motivated by (1) getting the winds correct and (2) quantifying the effect of incorrect winds on inverse estimates of CO₂ flux from satellite data.

To account for all winds in the atmosphere would be well beyond the scope of any single study. This research therefore focuses on a certain set of winds that have received relatively little attention in the carbon science literature: winds in extratropical cyclones. Extratropical cyclones are a crucial component of the moist circulation and are responsible for the bulk of weather in mid-

latitudes, yet involve processes such as fine scale vertical mixing by cumulus convection and PBL turbulence, which must be parameterized in today's global CTMs, and features such as frontal circulations, whose winds may or may not be resolved depending on grid spacing, that are sensitive to model choice. They are also responsible for a great deal of variance in CO₂ at continental observing stations in northern middle latitudes. Such highly variable CO₂ distributions are actually signals that contain important upstream surface flux information at synoptic and seasonal scales, so it is important to represent them well. Unfortunately, these weather systems and resulting CO₂ variations are difficult to represent numerically, and as it turns out are difficult to observe.

1.3 Objectives of this Study

Seasonal covariance between synoptic processes and terrestrial ecosystem metabolism, and resulting meridional CO₂ transport within the mid-latitude storm track, has received very little attention in the literature. This research seeks a comprehensive description of CO₂ transport by synoptic processes and an understanding of possible implications of synoptic transport (and underlying uncertainties) for surface flux estimates and carbon science. This study consists of three parts:

- (1) Part 1 establishes a dynamical framework for explaining synoptic transport processes for CO₂. In particular, Part 1 explores how the moist component of the mid-latitude atmospheric circulation acts as a vehicle for transport of CO₂ between middle and polar latitudes. This part of the study is motivated by recent findings [Pauluis et al., 2008] that mass transport along moist isentropic surfaces on baroclinic waves represents an important component of the atmospheric heat engine that operates between the equator and poles, and that moist transport accounts for as much as half the air in polar regions. Additionally, moist synoptic transport along the mid-latitude storm track is correlated with ecosystem metabolism because large-scale baroclinicity and photosynthesis are both driven seasonally by variations in solar radiation. This seasonal covariance between meridional heat transport and surface fluxes of CO₂ therefore has important implications for the seasonal

cycle of CO₂ in northern latitudes. Results from Part 1 are discussed in Chapter 3.

- (2) Part 2 seeks to quantify uncertainty associated with modeled transport by synoptic waves. As discussed in Section 1.1.2, there are many inherent uncertainties associated with synoptic transport, including moist processes within warm conveyors, frontal circulations, and near-scale vertical transport by moist convection and PBL turbulence. These uncertainties are linked in models to grid spacing and parameterization of sub-grid scale vertical mixing. The uncertainties are investigated using a self-consistent modeling framework driven by reanalysis products that are similar numerically, but have important differences in grid spacing and vertical mixing schemes. Many carbon cycle studies conclude that it is important to improve the representation of important transport processes within tracer transport models. Part 2 of this study seeks to identify and explain key differences in modeled synoptic transport. Results from Part 2 are discussed in Chapter 4.
- (3) Part 3 seeks to quantify errors in estimates of surface fluxes of CO₂ that result from transport biases. Synoptic transport of CO₂ occurs on scales that may be poorly represented in global models, so may be a source of inversion errors. Part 3 uses an OSSE framework to test (1) the ability of an ensemble technique for flux estimation to retrieve realistic looking sinks hidden within satellite data and (2) how sink estimates are degraded in the presence of imperfect transport. Results from Part 3 are discussed in Chapter 5.

Each results chapter also includes an introduction, motivation, and conclusions section. Conclusions from all parts of this research are tied together in Chapter 6. Transport simulations are performed with the Parameterized Chemistry and Transport Model (PCTM). Chapter 2 includes description of PCTM (Chapter 2.1), along with prescribed ocean and terrestrial surface fluxes (Chapter 2.2), various meteorological driver data sets (Chapter 2.3), and forward simulation experiments (Chapter 2.4). Parts 1 and 2 of this study require special analysis techniques to characterize moist synoptic transport at global scales, which are described in Chapter 2.5. The inversion methodology

used for Part 3 is described in Chapter 2.6.

Chapter 2

EXPERIMENTAL METHODS

2.1 Model Description

2.1.1 PCTM

Forward simulations are needed to produce time and spatially varying distributions of atmospheric CO₂ as determined by surface fluxes and analyzed weather. The chemistry transport model used for forward simulations, PCTM, has been adapted from a full-chemistry and transport model [e.g., Douglass and Kawa, 1999], technical aspects of which are discussed in Nielson [2000]. Three-dimensional tracer advection in PCTM is based on the transport code of Lin and Rood [1996], which uses a flux form semi-Lagrangian formulation (FFSL). Several modifications were made to PCTM for mass conservation [Kawa et al., 2004]. Transport in PCTM can be driven by simulated or analyzed weather fields at the native resolution of the stored weather product (specifics for this study in Section 2.4).

All transport is calculated on the hybrid sigma-pressure ($\sigma - p$) terrain following vertical coordinate, which can be defined according to Simmons and Burridge [1981] by $\eta = \frac{p}{p_s} + \left(\frac{p}{p_s} - 1\right) \left(\frac{p}{p_s} - \frac{p}{p_o}\right)$, where p is pressure, p_s is surface pressure, and p_o is the reference pressure equal to 1000.0 mb. This equation forces η to be monotonic with height, where $\eta = 1$ when $p = p_s$ and $\eta \rightarrow 0$ as $p \rightarrow 0$, and is designed such that η is terrain following near the surface and tends uniformly to pressure at upper levels. Simmons and Strüing [1983] approximate η by specifying the pressure of each model level as a function of surface pressure and vertically dependent coefficients

a and b . The η coordinate can be generalized such that pressure is given by

$$p(i, j, k, t) = a(k) + b(k) p_s(i, j, t) \quad (2.1)$$

where for a given time t , p is the pressure at the coordinates i, j, k and $a(k)$ and $b(k)$ are components of the hybrid coordinate at the layer edge k . $p_s(i, j, k)$ is the surface pressure at the horizontal grid point (i, j) and time t . $a(k)$ and $b(k)$ at the layer edges are stored as global metadata values in each η product file. This study uses transport fields saved on η from four versions of the NASA Goddard Earth Observation System (GEOS, discussed below). Surface boundary conditions (i.e., sources and sinks of CO_2) include terrestrial, oceanic, and anthropogenic fluxes, also discussed below.

PCTM solves the constituent continuity equation

$$\frac{\partial \chi}{\partial t} = -\tilde{\mathbf{V}} \cdot \nabla \chi + L(\chi) + P(\chi) \quad (2.2)$$

where χ is the constituent mixing ratio, t is time, $\tilde{\mathbf{V}}$ is the total velocity vector, and $P(\chi)$ and $L(\chi)$ are the production and loss rates, respectively using a technique known as process splitting [Nielson, 2000]. The Lin and Rood scheme offers several major advantages of FFSL necessary to maintain the statistics of advected tracers. One includes independence of stability on time step [Lin and Rood, 1996]. In addition, the scheme meets the physical constraints of tracer advection and accounts for the problem of consistency between the tracer continuity equation and the underlying equation of continuity of air due to process splitting techniques [Lin and Rood, 1996]. CO_2 is treated as a passive tracer in these simulations such chemical production rates $L(\chi)$ and $P(\chi)$ are zero. The accuracy of the code for large-scale transport is well documented [Kawa et al., 2004].

PCTM simulations that use analyzed meteorology face the problem of local non-conservation of mass that arises during the assimilation process, which leads to inconsistencies between surface pressure tendencies and mass flux convergence. This, in turn, introduces errors in the advected tracer field. Kawa et al. [2004] add a pressure corrector [Rotman et al., 2001] to the model, which acts to remove zonally distributed pressure errors without inducing a vertical wind change, and find that inconsistencies are removed.

Subgrid-scale vertical mixing processes such as cumulus convection and PBL turbulence are also important for atmospheric tracer transport. Convective mixing is implemented in PCTM using a mass conserving, semi-implicit convective transport module [Kawa et al., 2004], formulated to be consistent with convective mass fluxes provided by the Zhang and McFarlane [1995] deep convection scheme used in the finite volume GCM (FVGCM). Mixing by PBL turbulence is implemented using diffusion between adjacent layers.

2.2 Surface Boundary Conditions

This section briefly discusses surface flux data, which act as sources and sinks of CO₂ to the atmosphere. Surface fluxes used in this study include terrestrial biological fluxes, anthropogenic sources, and oceanic fluxes. Fluxes due to land use change and fire emissions are not included.

2.2.1 Terrestrial Fluxes

The Simple Biosphere model (SiB) was developed by Sellers et al. [1986] to calculate surface energy budgets in climate models and after substantial modification [Sellers et al., 1996 a,b] became SiB2. Vegetation parameters are derived directly from processed satellite data. The parameterization of stomatal and canopy conductance used in the calculation of the surface terrestrial energy budget involves the direct calculation of carbon assimilation by photosynthesis [Farquhar et al., 1980], making possible the calculation of CO₂ exchange between the land and atmosphere [Denning et al., 1996, 2003]. Photosynthetic carbon assimilation is linked to stomatal conductance and thence to the surface energy budget and atmospheric climate by the Ball-Berry equation [Collatz et al., 1991, 1992]. SiB models include a prognostic canopy airspace of temperature, moisture, and CO₂. Time invariant biophysical parameters include canopy height, leaf angle distribution, leaf transmittance, photosynthetic parameters, and soil properties. Time and spatially varying biophysical parameters are calculated from satellite observations (see below) and include leaf area index (LAI) and fraction of absorbed photosynthetic active radiation (fPAR).

Additional modifications have occurred since SiB2. For example, the ability to accumulate up to five layers of snow, each with unique thermodynamic properties, has been added, improving the treatment of soil insulation and thermal properties in the winter. A more realistic root profile is used, with 10 soil layers and an initial soil column depth of 3.5 meters, along with better treatment of soil water stress and frozen soil. Respiration includes an autotrophic component, accounting for maintenance and growth. The revised model is referred to as SiB3 [Baker et al., 2008].

Soil respiration is modeled as a function of temperature and moisture of each layer of soil, and is scaled with annual gross primary production (GPP) to achieve carbon balance over an annual cycle [Denning et al., 1996a]. Running SiB3 in this steady state mode, such that ecosystem respiration balance GPP over one year at every grid point, is necessary because processes governing long term sources and sinks of CO₂ such as forest regrowth and soil carbon pools are not simulated in SiB3. Processes that govern biospheric exchange over diurnal, synoptic, and seasonal time scales, which are controlled primarily by climate and weather, are modeled very well by SiB3. For example, SiB3 has been evaluated against eddy covariance measurements at a number of sites [Baker et al., 2003; Hanan et al., 2005; Vidale and Stockli, 2005].

Net ecosystem exchange (NEE, representing the net terrestrial biogenic flux of CO₂ and calculated as Respiration - GPP) estimates from SiB3 are provided at hourly resolution. In this experiment, initial conditions for soil moisture and temperature are specified using an 18-year global spinup of SiB3 (January 1, 1982 to December 31, 1999) driven by the National Center for Environmental Prediction Department of Energy reanalysis (NCEP2) 1° x 1° (longitude x latitude) global dataset [Kanamitsu et al., 2002]. A different reanalysis product is used to drive SiB3 for the PCTM simulation period (discussed below).

Land Surface Parameters

Vegetation greenness is prescribed using LAI and fPAR estimates from the MODerate Resolution Imaging Spectroradiometer (MODIS) on board the NASA EOS satellite TERRA. LAI and

fPAR products (MOD15A2) are produced as 8-day composites at 1-km resolution; this study uses a version regridded to $0.25^\circ \times 0.25^\circ$ and corrected for cloud and aerosol contamination produced jointly by Boston University and the University of Montana (Myneni et al. [2003]; data courtesy <http://cybele.bu.edu>). The use of satellite derived LAI and fPAR parameters is used for calculation of surface photosynthesis, evapotranspiration, and annual net primary production, and provides adequate resolution in time and space for studies of terrestrial carbon processes at synoptic and seasonal scales.

The soil map for SiB3 is provided by the International Geosphere-Biosphere Programme (IGBP) at a resolution of 10 km and then modified to correspond to SiB3 classes. The biome map is a satellite data product of the University of Maryland with a resolution of 1 km, converted to the resolution of SiB3 (see Section 2.4). Biome types are also converted to SiB3 classes. SiB3 combines information about MODIS, biome, and soil type to determine surface characteristics, which are used in CO₂ flux calculations.

2.2.2 *Fossil Fuel Fluxes*

Fossil fuel fluxes are prescribed from anthropogenic CO₂ emission ($\text{kg C m}^{-2} \text{ s}^{-1}$) estimates based on calculations done by Andres et al. [1996] at 1° by 1° resolution for the entire globe using fossil fuel consumption, cement manufacture, and population density data from 1998. Fossil fuel fluxes represent a source of CO₂ from the land to the atmosphere. Although fossil fuel fluxes are spatially variable, they are constant in time, and therefore do not accurately portray diurnally, weekly, and seasonally variability [Gurney et al., 2005] or the correct atmospheric growth rates. It should be noted that such incorrect specification of temporal and spatial variability, along with rapid fossil fuel growth rates in emerging economies, is likely to lead to underestimates of variability and therefore transport of CO₂ anomalies by synoptic eddies.

2.2.3 *Oceanic Fluxes*

The ocean source is from the Community Climate System Model (CCSM-3) coupled ocean Biogeochemical Elemental Cycling model (BEC). This is a process based physical-biogeochemical-ecological model driven by reanalysis, capable of producing interannual variability in air-sea CO₂ flux. The BEC model consists of upper ocean ecological [Moore et al., 2004] and full-depth biogeochemical [Doney et al., 2006] modules imbedded in a global 3-D Parallel Ocean Program (POP) ocean general circulation model [Smith and Gent, 2004; Collins et al., 2006]. The model is forced with atmospheric reanalysis from the CORE Inter-Annual Forcing (CIAF) version 2 dataset [Large and Yeager, 2004] and time-varying dust deposition [Mahowald et al., 2003] and saved at daily resolution. These models are described and analyzed in more detail in Doney et al [2009]. Note that the weather product used to drive ocean fluxes is not the same as the weather product used in SiB3 or PCTM, and therefore ocean fluxes variations, in particular at synoptic scales, albeit much weaker than terrestrial fluxes, are not consistent with weather in PCTM.

2.3 **Transport Driver Data**

Transport in PCTM is driven in offline mode; that is, transport fields are produced from a parent GCM, which are then saved for later transport in a chemistry transport model (CTM) such as PCTM. Parent GCMs used in this study are developed, tested, and run at NASA Goddard Global Modeling and Assimilation Office (GMAO). Weather fields in these GCMs are analyzed (or re-analyzed) through assimilation of data from conventional (radiosondes, wind profiles, radar, etc.) and satellite streams. Transport is driven by resolved processes, including horizontal winds and vertical divergence, which are used for advective processes, and unresolved processes solved through parameterization, including cumulus convection and PBL turbulence, which are used for vertical mixing. CO₂ transport in PCTM is then determined offline (i.e., CO₂ is not transported within the parent GCM nor does any assimilation of CO₂ take place in the offline simulations) using analyzed and re-analyzed meteorological fields from the GEOS Data Assimilation System

(DAS).

Goddard datasets are produced from two primary parent atmospheric general circulation models (AGCMs), GEOS version 4 (GEOS4) and GEOS version 5 (GEOS5). Each parent AGCM has a unique set of vertical mixing schemes to generate moist convective mass fluxes and vertical mixing. GEOS4 runs with a native spatial resolution of 1.25° by 1° with 55 vertical layers while GEOS5 runs with a native resolution of 0.67° by 0.5° and 72 vertical layers. These two products are discussed in more detail below. Also discussed below are two other products used in this study, one regrided to coarser resolution from the analyzed GEOS4 winds and another where GEOS5 is run at its native resolution and saved at a coarser spatial resolution. This gives a total of four weather products that can be used to test sensitivity of forward simulation of atmospheric CO_2 to transport. The key differences between these models are specified below.

2.3.1 *GEOS4-1.25x1*

The first product is based on version 4 of GEOS-DAS (GEOS4-DAS). Kawa et al. [2004], Douglass et al. [2003], and Bloom et al. [2005] discuss this data in detail. Like PCTM, GEOS4-DAS uses finite volume dynamics based on the Lin-Rood dynamical core [Lin and Rood, 1996]. Observations used in the finite volume data assimilation system (FVDAS) include both meteorological products and satellite data. Physical parameterizations are determined using the National Center for Atmospheric Research Community Climate Model, Version 3 (CCM3) package [Kiehl et al., 1998], which include deep convection [Zhang and McFarlane, 1995], shallow convection [Hack, 1994], and PBL turbulence [Holtslag and Boville, 1993]. GEOS4-DAS transport fields are saved at 6-hourly resolution and 1.25° by 1° (representing the native resolution of GEOS4-DAS) grid spacing with 55 hybrid vertical levels up to 1 mb. This re-analysis driver data will be referred to as GEOS4-1.25x1.

Of the 55 vertical levels, only 14 are located within the troposphere. Since the mixing time scale between the troposphere and stratosphere is approximately 10 years, and this study is focused

on processes in the troposphere at time scales much less than 10 years, the 55 vertical levels in GEOS4-1.25x1 are condensed to 25 levels while retaining all levels in the troposphere. 1.25° by 1° transport in PCTM is run with a 7.5 minute time step.

2.3.2 *GEOS4-2.5x2*

GEOS4-1.25x1 is regridded horizontally to 2.5° by 2° to study transport at coarser horizontal resolution. Vertical mixing by moist convection and turbulent diffusion is identical to GEOS4-1.25x1. Wind vectors are also conserved, but regridding to coarser resolution has smoothed spatial gradients. All 25 vertical levels are retained, and transport fields are still saved at 6-hourly resolution. Time-stepping through PCTM is doubled to 15 minutes to be consistent with CFL and doubling of horizontal grid spacing. This regridded re-analysis driver data will be referred to as GEOS4-2.5x2.

2.3.3 *GEOS5-0.67x0.5*

The third product is based on version 5 of GEOS-DAS [GEOS5-DAS, Rienecker et al., 2010]. GEOS5-DAS maintains the finite-volume dynamics used from GEOS4-DAS [Lin, 2004] and is integrated with physics packages under the Earth System Modeling framework (e.g., Collins et al., 2005), including the Relaxed Arakawa-Schubert (RAS) scheme for convection [Moorthi and Suarez, 1992] and separate PBL turbulent mixing schemes for stable [Louis et al., 1982] and unstable [Lock et al., 2000] conditions. Aside from different native spatial resolution, these new vertical mixing schemes in GEOS5 are another key difference between GEOS4 and GEOS5, the effect on CO₂ transport of which, unfortunately, is not separable from grid spacing since these products are produced offline from PCTM. DAS integrates GEOS5-DAS with three-dimensional variational analysis (3DVar) referred to as Gridpoint Statistical Interpolation (GSI) analysis, with a focus on wind fields for studies of tropospheric transport.

This GEOS5-DAS product is technically based on version 5.1.0 of GEOS5-DAS, which was

used for tuning and development issues for the Modern Era Retrospective-analysis for Research Applications (MERRA, e.g., Bosilovich et al. [2006]). The native grid of GEOS5-DAS (and the grid at which the analysis is performed) is 0.67° by 0.5° horizontal resolution with 72 layers to 0.01 hPa, 31 of which are in the troposphere and the rest above the tropopause. The 72 vertical layers are condensed to 42 levels while retaining the 31 tropospheric levels. Transport fields are saved at 6-hourly resolution. In order to maintain CFL criteria, 0.67° by 0.5° transport is run with a 3.75 minute time step in PCTM. Instantaneous transport fields are output (in contrast to the re-analysis version of GEOS5-DAS discussed below). Since the analysis is based on GEOS5-DAS, this driver data will be referred to as GEOS5-0.67x0.5.

2.3.4 *GEOS5-1.25x1*

The fourth (and final) product is similar to GEOS5-0.67x0.5 except is a newer version (5.2.0) of GEOS5-DAS used for MERRA which addresses a deficiency in the diurnal cycle in the high latitudes. Except for changes to address high latitude diurnal cycles, GEOS5-DAS version 5.2.0 is nearly the same as GEOS5-0.67x0.5. Transport fields are re-analyzed (saved during a corrector segment of the Incremental Analysis Update rather than the analysis segment) and saved every 3 hours at a reduced horizontal resolution of 1.25° by 1° to facilitate comparison with GEOS4-1.25x1. This re-analyzed driver data will be referred to as GEOS5-1.25x1.

2.4 **Transport Simulations for Parts 1 and 2**

Transport simulations are run from January 1, 2000 through December 31, 2004 to properly spin up atmospheric gradients of CO_2 . Transport in the spin up run is driven by GEOS4-1.25x1. All terrestrial, oceanic, and anthropogenic surface fluxes of carbon are used in the spin up. Flux and energy calculations in SiB are also driven by GEOS4-1.25x1 meteorology from 2000-2004 such that transport and surface fluxes of CO_2 are synchronized. GEOS4-1.25x1 precipitation is scaled by monthly precipitation from the Global Precipitation Climatology Project (GPCP, see Huffman

et al. [2001]) to force total monthly precipitation in GEOS4-1.25x1 to match that of GPCP. The time at which precipitation occurs remains unchanged so that covariance of anomalies in cloudiness, moisture, and vertical transport is conserved. Note that, even though convective transport and precipitation are produced in the same way in the parent GCM, convective transport is not scaled to precipitation, and hence local surface fluxes of CO₂ and vertical mixing by moist convection are not consistent in the forward simulations. Anthropogenic and oceanic surface flux maps are regridded to 1.25° by 1° using the conservative remapping scheme of the SCRIP software package [Jones, 1999]. CO₂, which is given as a mole fraction in units of parts per million (ppm).

Three-dimensional CO₂ fields from PCTM are saved at 0z on January 1, 2005 and regridded to the appropriate horizontal and vertical resolution depending on the driver data. PCTM is run from January 1, 2005 through December 31, 2005 to comprise the analysis period. Part 1 of this study includes one forward simulation in which PCTM is driven by GEOS4-1.25x1. Part 2 of this study consists of four forward simulations, one for each of the meteorological driver data sets. All driver data is run through the same version of PCTM. All transport simulations are prescribed with the same set of surface fluxes. SiB3 is run at 1.25° by 1° driven by two-dimensional surface meteorology from GEOS4-1.25x1. Ocean, fossil fuel, and terrestrial fluxes are regridded to the resolution of the meteorological driver data. For Part 2, this experimental design is important because all simulations use a common transport model and set of surface fluxes such that the only difference between experiments is the meteorological fields. Any differences in CO₂ transport in Part 2 can therefore be attributed to differences in meteorological driver data.

With regard to Part 2, it is important to note that, while the dynamical core is consistent between GEOS models and with the dynamical core of PCTM, there are many other factors that may cause transport differences. Inconsistencies between horizontal and vertical grid spacing, data assimilation technique, mass balance errors associated with data assimilation, number and type of observations used in data assimilation, physical parameterization schemes for vertical mixing are probably the most dominant factors. That being said, GEOS4-2.5x2 and GEOS4-1.25x1 are

different only in horizontal grid spacing. The same can be said for GEOS5-1.25x1 and GEOS5-0.67x0.5 except for some minor differences in the PBL scheme in the Arctic and the number and type of data assimilated may also be important (more discussion in Chapter 4). The biggest model differences in synoptic transport of CO₂ will most likely arise between GEOS4-DAS and GEOS5-DAS as a result of some combination of all of the factors listed above.

2.5 Methodology for Transport Analysis

PCTM solves the constituent continuity equation on η , but tracer transport can be diagnosed from the model output on any vertical coordinate (height, pressure, isentropes, etc). It is important to note that regriding between vertical coordinates will not change CO₂ distributions throughout the atmosphere, nor total meridional transport around a latitude circle. It will, however, change our interpretation of important physical processes in the atmosphere that are important for CO₂ variations and meridional transport. Because the underlying mechanisms governing CO₂ transport are open to interpretation, analysis of meridional transport in Part 1 will be performed on three vertical coordinate systems (discussed below) representing Eulerian and Lagrangian frames of reference. This section begins by expressing tracer transport as a function of a generalized vertical coordinate. The eddy decomposition technique, including for completeness a complete derivation, for analyzing large scale tracer transport by symmetric and asymmetric components of the circulation is then described. Transport equations are then extended to three vertical coordinates.

2.5.1 Tendency Equation for Atmospheric CO₂

The equation expressing conservation of an arbitrary intensive scalar, ψ , on an arbitrary vertical coordinate, ζ , can be written as

$$\begin{aligned} \frac{\partial}{\partial t} m_{\zeta} \psi_{\zeta} + \frac{1}{a \cos \varphi} \frac{\partial}{\partial \lambda} m_{\zeta} u_{\zeta} \psi_{\zeta} + \frac{1}{a \cos \varphi} \frac{\partial}{\partial \varphi} m_{\zeta} v_{\zeta} \psi_{\zeta} \cos \varphi \\ + \frac{\partial}{\partial \zeta} m_{\zeta} \dot{\zeta} \psi_{\zeta} = \frac{\partial}{\partial \zeta} S_{\psi}, \end{aligned} \quad (2.3)$$

where $m_\zeta = -\frac{1}{g} \frac{\partial p}{\partial \zeta}$ is the pseudo-density (equivalent to the amount of mass (as measured by the pressure difference) between two ζ surfaces), p is pressure, g is gravity, a is the radius of Earth, φ is longitude, λ is latitude, u is the zonal wind, v is the meridional wind, and S_ψ is the vertical flux of ψ . $\dot{\zeta} \equiv \frac{D\zeta}{Dt}$ is defined as the rate of change of ζ following an air parcel. The horizontal advection terms, $\frac{1}{a \cos \varphi} \frac{\partial}{\partial \lambda} m_\zeta u_\zeta \psi_\zeta + \frac{1}{a \cos \varphi} \frac{\partial}{\partial \varphi} m_\zeta v_\zeta \psi_\zeta \cos \varphi$, can be rewritten as $\nabla_\zeta \cdot m_\zeta \mathbf{V}_\zeta \psi_\zeta$, where \mathbf{V}_ζ is the horizontal wind vector pointing along a surface of ζ . Equation 2.3 then reduces to

$$\frac{\partial}{\partial t} m_\zeta \psi_\zeta + \nabla_\zeta \cdot m_\zeta \mathbf{V}_\zeta \psi_\zeta + \frac{\partial}{\partial \zeta} m_\zeta \dot{\zeta} \psi_\zeta = \frac{\partial}{\partial \zeta} S_\psi. \quad (2.4)$$

To solve for conservation of ψ through an atmospheric column, Equation 2.4 is integrated vertically from the surface to the top of the atmosphere. This gives

$$\begin{aligned} \frac{\partial}{\partial t} \int_{\zeta_S}^{\zeta_T} m_\zeta \psi_\zeta d\zeta + \nabla_\zeta \cdot \int_{\zeta_S}^{\zeta_T} m_\zeta \mathbf{V}_\zeta \psi_\zeta d\zeta \\ + (m\psi)_{\zeta_S} \left(\frac{\partial \zeta_S}{\partial t} + \mathbf{V}_{\zeta_S} \cdot \nabla \zeta_S - \dot{\zeta}_S \right) \\ - (m\psi)_{\zeta_T} \left(\frac{\partial \zeta_T}{\partial t} + \mathbf{V}_{\zeta_T} \cdot \nabla \zeta_T - \dot{\zeta}_T \right) \\ = S_{\psi_S} - S_{\psi_T}, \end{aligned} \quad (2.5)$$

where T refers to the top of the model atmosphere, S refers to the bottom of the atmosphere (or surface), ζ_T is the value of ζ at the top of the model atmosphere, and ζ_S is the value of ζ at the bottom of the model atmosphere. The lower boundary condition, i.e., that no mass crosses the Earth's surface, is expressed by requiring that a particle that is on the Earth's surface remains there:

$$\frac{\partial \zeta_S}{\partial t} + \mathbf{V}_S \cdot \nabla \zeta_S - \dot{\zeta}_S = 0. \quad (2.6)$$

Similarly, $\frac{\partial \zeta_T}{\partial t} + \mathbf{V}_T \cdot \nabla \zeta_T - \dot{\zeta}_T$ represents the mass flux across the top of the atmosphere, which we assume to be zero, i.e.,

$$\frac{\partial \zeta_T}{\partial t} + \mathbf{V}_T \cdot \nabla \zeta_T - \dot{\zeta}_T = 0. \quad (2.7)$$

Assuming also that there are no sources or sinks of ψ at the top of the atmosphere, and substituting

Equations 2.6 and 2.7 into Equation 2.5, Equation 2.5 reduces to:

$$\frac{\partial}{\partial t} \int_{\zeta_S}^{\zeta_T} m_\zeta \psi_\zeta d\zeta + \nabla_\zeta \cdot \int_{\zeta_S}^{\zeta_T} m_\zeta \mathbf{V}_\zeta \psi_\zeta d\zeta = S_{\psi_S} \quad (2.8)$$

or, expanding the second term on the right hand side (RHS) of Equation 2.8,

$$\begin{aligned} \frac{\partial}{\partial t} \int_{\zeta_S}^{\zeta_T} m_\zeta \psi_\zeta d\zeta + \frac{1}{a \cos \varphi} \frac{\partial}{\partial \lambda} \int_{\zeta_S}^{\zeta_T} m_\zeta u_\zeta \psi_\zeta d\zeta \\ + \frac{1}{a \cos \varphi} \frac{\partial}{\partial \varphi} \int_{\zeta_S}^{\zeta_T} m_\zeta v_\zeta \psi_\zeta \cos \varphi d\zeta = S_{\psi_S}. \end{aligned} \quad (2.9)$$

Vertical integration through the atmospheric column and application of surface and upper boundary conditions has provided an equation for the column integrated time rate of change of constituent (ψ) per unit mass (first term on the left hand side (LHS) of Equation 2.9) as a function of column integrated zonal transport (or flux convergence, second term on LHS), meridional transport (third term on LHS), and sources and sinks of ψ at the Earth's surface (RHS of Equation 2.9). The zonal term is eliminated from Equation 2.9 by averaging around a latitude circle using the zonal mean operator $[\overline{(\)}]$. Averaging in time using the time mean operator $\overline{(\)}$ reduces Equation 2.9 to

$$\frac{\partial}{\partial t} \left[\overline{\int_{\zeta_S}^{\zeta_T} m_\zeta \psi_\zeta d\zeta} \right] + \frac{1}{a \cos \varphi} \frac{\partial}{\partial \varphi} \left[\overline{\int_{\zeta_S}^{\zeta_T} m_\zeta v_\zeta \psi_\zeta \cos \varphi d\zeta} \right] = \overline{[S_{\psi_S}]}. \quad (2.10)$$

Finally, assuming ζ_T and ζ_S do not vary in time or space, the mean operators, $\overline{(\)}$ and $[\overline{(\)}]$, may be moved inside the vertical integrals. Equation 2.10 is then rewritten as

$$\frac{\partial}{\partial t} \int_{\zeta_S}^{\zeta_T} \overline{[m_\zeta \psi_\zeta]} d\zeta + \frac{1}{a \cos \varphi} \frac{\partial}{\partial \varphi} \int_{\zeta_S}^{\zeta_T} \overline{[m_\zeta v_\zeta \psi_\zeta]} \cos \varphi d\zeta = \overline{[S_{\psi_S}]}. \quad (2.11)$$

Equation 2.11 reduces to the continuity equation for total mass (air) by setting ψ to unity and the source term on the RHS to zero; for total mass, the net meridional transport averages to zero over sufficiently long time periods. This represents total mass balance for a “ring” of air along a latitude circle.

By setting ψ to CO₂ mixing ratio (C), the zonal and time averaged vertically integrated tendency equation for atmospheric CO₂ is expressed as

$$\frac{\partial}{\partial t} \int_{\zeta_T}^{\zeta_S} \overline{[m_\zeta C_\zeta]} d\zeta + \frac{1}{a \cos \varphi} \frac{\partial}{\partial \varphi} \int_{\zeta_T}^{\zeta_S} \overline{[m_\zeta v_\zeta C_\zeta]} \cos \varphi d\zeta = \overline{[(F_c)_S]}, \quad (2.12)$$

where $(F_c)_S$ is the surface flux of CO₂, which has units of $kgC m^{-2} s^{-1}$.

2.5.2 Eddy Decomposition

The integrand of the second term on the LHS of Equation 2.12, $\overline{m_\zeta v_\zeta C_\zeta}$, represents net meridional transport of CO₂ by the atmosphere in the time and zonal mean at an arbitrary atmospheric layer. However, CO₂ and mass fluxes of CO₂ are highly variable in time and space; as a result, CO₂ transport itself is also highly variable in time and space. According to Peixoto and Oort [1992], the statistics of CO₂ transport by various components of the general circulation can be described over longer time and spatial averages using statistics defined in a mixed space-time domain following Starr and White [1954]. To assess influences of the mean circulation and baroclinic waves on meridional transport and polar seasonality, a technique called eddy decomposition is applied according to methods outlined by Peixoto and Oort [1992], in which quantities (lets call these x , representing mass flux $(mv)_\zeta$ and tracer mixing ratio C_ζ) are “perturbed” (i.e., separated into a mean component and a component representing the deviation from the mean) along an arbitrary ζ surface and rewritten as $x = \bar{x} + x'$, representing the time mean and its temporal deviation () or “transient component”, and $x = [x] + x^*$, representing the zonal mean and its zonal deviation ()^{*} or “eddy component”. The use here of eddy decomposition is similar in concept to Reynolds averaging, in which quantities associated with parcels of air are separated into a volume average and turbulent deviations from the average. Rather than analyze quantities local to an air parcel, here I analyze quantities associated with the large scale circulation.

With these definitions, we consider various statistics derived from the three-dimensional fields of $(mv)_\zeta$ and C_ζ . To begin eddy decomposition, we first set $a = (mv)_\zeta$ and $b = C_\zeta$. \overline{ab} is then decomposed into its time mean and transient components and rewritten as

$$\begin{aligned}
 \overline{ab} &= \overline{(\bar{a} + a')(\bar{b} + b')} \\
 &= \overline{\bar{a}\bar{b}} + \overline{\bar{a}b'} + \overline{a'\bar{b}} + \overline{a'b'} \\
 &= \overline{\bar{a}\bar{b}} + \overline{a'\bar{b}} + \overline{\bar{a}b'} + \overline{a'b'} \\
 &= \overline{\bar{a}\bar{b}} + \overline{a'b'}.
 \end{aligned} \tag{2.13}$$

The RHS of Equation 2.13 simplifies from four terms (third line) to two terms (fourth line) because the time average of a prime, namely \bar{a} and \bar{b} , is approximately zero over sufficiently long time intervals. Next, zonal averaging is applied to Equation 2.13 and both terms on the RHS are decomposed into its zonal mean and eddy components. The first term is rewritten as

$$\begin{aligned}
[\bar{a}\bar{b}] &= \left[\overline{([a] + a^*) ([b] + b^*)} \right] \\
&= [\bar{a}][\bar{b}] + [\bar{a}]b^* + a^*[\bar{b}] + a^*b^* \\
&= [\bar{a}][\bar{b}] + [\bar{a}][\bar{b}^*] + [a^*][\bar{b}] + [a^*b^*] \\
&= [\bar{a}][\bar{b}] + [a^*b^*], \tag{2.14}
\end{aligned}$$

where the RHS of Equation 2.14 simplifies from four terms (third line) to two terms (fourth line) because the zonal average of an eddy, namely $[a^*]$ and $[\bar{b}^*]$, is by definition zero around a latitude circle. Similarly, the second term in the RHS of Equation 2.13 is rewritten as

$$\begin{aligned}
[\bar{a}b] &= \left[\overline{([a] + a^*) ([b] + b^*)} \right] \\
&= \left[\overline{[a][b] + [a]b^* + a^*[\bar{b}] + a^*b^*} \right] \\
&= \overline{[a][b]} + \overline{[a][b^*]} + \overline{[a^*][\bar{b}]} + \overline{[a^*b^*]} \\
&= \overline{[a][b]} + \overline{[a^*b^*]} \tag{2.15}
\end{aligned}$$

where the RHS of Equation 2.14 simplifies from four terms (third line) to two terms (fourth line) because the zonal average of the eddy of a prime, namely $[a^*]$ and $[\bar{b}^*]$, is by definition zero around a latitude circle.

Combining Equations 2.14 and 2.15 and substitution of $(mv)_\zeta$ and C_ζ for a and b yields

$$\overline{[m_\zeta v_\zeta C_\zeta]} = \left[\overline{(mv)_\zeta} \right] \overline{[C_\zeta]} + \left[\overline{(mv)_\zeta^* C_\zeta^*} \right] + \left[\overline{(mv)_\zeta} \right] \overline{[C_\zeta]} + \left[\overline{(mv)_\zeta^* C_\zeta^*} \right]. \tag{2.16}$$

Eddy decomposition is an extension of Reynolds averaging and applies to the large-scale, geostrophically and hydrostatically balanced flow. Time averaging of one month is applied, and assumed to be a sufficiently long period for time averaged prime quantities to disappear on the third line of

Equation 2.13. The focus of this study is synoptic transport by baroclinic waves, which occurs on time scales of $\sim 3-7$ days and spatial scales of ~ 1000 kms. By defining the time mean using a time window larger than the synoptic time scale, the net effect of eddies over multiple synoptic cycles is captured. Through these zonal and temporal averaging techniques, the statistics of CO_2 transport is reduced to meridional and vertical statistics.

The first term on the RHS of Equation 2.16 refers to the mean meridional circulation (MMC), and accounts for transport of mean CO_2 by the mean meridional mass flux. The second term refers to stationary eddies, and represents transport by stationary waves due to correlated zonal deviations of mass flux and CO_2 . These are forced primarily by the geographic anchoring of planetary scale atmospheric waves by zonal inhomogeneities in boundary conditions such as continents, oceans, ice sheets and mountains. The third term accounts for temporal variations from zonal mean circulations, namely the transient symmetric circulation, and contributes to temporal fluctuations in circulations such as the Hadley Cell due to north-south seasonal migration. The fourth term accounts for temporal variations from the stationary planetary waves, that is transient eddies, representing transport by time varying dynamical processes such as baroclinic waves due to correlated temporal variations of mass flux and CO_2 . In mid-latitudes, baroclinic instability is a major driver of transient eddies. The transient symmetric circulation is small in middle latitudes relative to the other terms and will be absorbed into transient wave term for the remainder of this study. Transport by transient and stationary waves together represents the eddy component of the large-scale mid-latitude circulation.

2.5.3 *Vertical Coordinate*

Eddy decomposition allows for analysis of global transport of atmospheric constituents such as CO_2 by large scale mean and eddy circulations. These transport processes are analyzed in different vertical coordinate frameworks to simplify our understanding of eddy and mean transport of CO_2 . This study analyzes transport in both Eulerian and Lagrangian coordinate systems.

Eulerian coordinate systems represent a reference system that is fixed with respect to time

and space. Pressure coordinates (p) are a standard way of analyzing three-dimensional atmospheric fields. Pressure surfaces, however, intersect the ground at locations that change with time. Because of the spatio-temporal dependence of pressure levels, the column integral operation in Equation 2.10 cannot be moved outside of the averaging operators and eddy decomposition cannot be applied for single atmospheric layers. Terrain following coordinates such as η , on the other hand, work well for eddy decomposition because vertical layers are fixed in time and space.

Lagrangian vertical coordinate systems follow the motion of an air parcel as it moves vertically, and can be thought of as a reference system that is fixed with respect to the motion of a parcel of air. An example of a Lagrangian coordinate system is potential temperature, which is defined by $\theta = T \left(\frac{p_0}{p} \right)^{\frac{R}{C_p}}$, with p the pressure, R the ideal gas constant, C_p the specific heat, T the temperature, and $p_0 = 1000$ mbar an arbitrary reference pressure. Surfaces of constant θ are isentropic surfaces. θ is conserved following a particle for reversible dry adiabatic transformations. This means that the vertical motion in θ -coordinates is proportional to the heating rate, and that in the absence of diabatic heating (radiation, evaporation, sensible heating), there is “no vertical motion,” from the point of view of θ -coordinates. θ increases upwards in a statically stable atmosphere so that there is a monotonic relationship between θ and height above ground level, z .

Eddy decomposition on isentropic coordinates is relatively straightforward, but some definitions must first be made to accommodate some complications. Namely, it is common for isentropic surfaces to intersect the lower boundary in the presence of strong horizontal temperature gradients, as occur for example along frontal zones. To avoid surfaces running through the ground, isentropic surfaces are assumed in this study to follow the surface boundary. This effect is imposed by defining imaginary “massless layers,” such that the pressure difference (or thickness) between two θ surfaces is zero. Since no mass resides between the θ surfaces in the portion of the domain where they “touch the Earth’s surface,” no mass conservation laws are violated when computing mass transport of tracer. This does, however, present a problem for tracer transport along massless surfaces because tracers such as C are undefined.

The following definitions are therefore made for quantities involving C so that massless layers can be applied to zonal and temporal averaging techniques (i.e., Equation 2.16) when isentropic coordinates intersect the surface:

$$\overline{C_\zeta(i, j, k)} = \frac{1}{T_{mass}} \sum_{t=1}^{T_{mass}} C_\zeta(i, j, k, t) \quad \text{for } m_\zeta(i, j, k, t) > 0 \quad (2.17)$$

$$C_\zeta(i, j, k, t) = \overline{C_\zeta(i, j, k)} \quad \text{for } m_\zeta(i, j, k, t) = 0 \quad (2.18)$$

$$C_\zeta(i, j, k, t) = C_\zeta(i, j, k, t) - \frac{1}{T_{mass}} \sum_{t=1}^{T_{mass}} C(i, j, k, t), \quad (2.19)$$

where i, j, k, t are indices for longitude, latitude, height, time and T_{mass} is equal to the total number of layers in the time averaging window (1 month) that have non-zero mass ($m_\zeta > 0$). These definitions guarantee that $C = 0$ for massless layers.

As a proof of concept, these definitions are applied to Equation 2.13

$$\begin{aligned} \overline{(mv)C} &= \overline{(\overline{mv} + (mv)) (\overline{C} + C)} \\ &= \overline{(\overline{mv} + (mv)) \left(\frac{1}{T_{mass}} \sum_{t=1}^{T_{mass}} C + \left(C - \frac{1}{T_{mass}} \sum_{t=1}^{T_{mass}} C \right) \right)}. \end{aligned}$$

Rearranging terms gives

$$= \overline{(\overline{mv} + (mv)) \left(\frac{1}{T_{mass}} \sum_{t=1}^{T_{mass}} C - \frac{1}{T_{mass}} \sum_{t=1}^{T_{mass}} C + C \right)},$$

Finally, terms involving C cancel out, leaving

$$= \overline{(mv) (\overline{C})}.$$

This guarantees that the LHS and RHS of the first line in Equation 2.13 are equal for massless layers as long as definitions 2.17-2.19 are applied consistently throughout eddy decomposition.

Next I show how definitions 2.17-2.19 are applied to Equation 2.13 so that the first line of Equation 2.13 simplifies to the last line of Equation 2.13. Substitution of mv for a and C for b in

Equation 2.13 gives

$$\begin{aligned}
\overline{(mv)C} &= \overline{(\overline{mv} + (mv)) (\overline{C} + C)} \\
&= \overline{(\overline{mv})\overline{C}} + \overline{(\overline{mv})C} + \overline{(mv)\overline{C}} + \overline{(mv)C} \\
&= \overline{(\overline{mv})\overline{C}} + \overline{(\overline{mv})\overline{C}} + \overline{(\overline{mv})\overline{C}} + \overline{(\overline{mv})C}.
\end{aligned} \tag{2.20}$$

Averages of terms involving C are taken for layers with mass (\overline{C} and \overline{C}) using Equation 2.17 and 2.19, averages of terms involving mv are taken over all layers (\overline{mv} and $\overline{(mv)}$), and averages of terms involving both mv and C are taken over all layers ($\overline{(mv)C}$ and $\overline{(mv)C}$) using Equation 2.18. Using these definitions, the time average of primes in Equation 2.20 are zero and Equation 2.20 reduces to

$$\overline{(mv)C} = \overline{(\overline{mv})\overline{C}} + \overline{(\overline{mv})C}. \tag{2.21}$$

Note also that, with these definitions, averages of terms involving C can be taken for all layers with the same result. In the results that follow, \overline{C} is defined for layers with non-zero mass.

The LHS of Equation 2.21 is independent of our definition of C for massless layers because by definition m is zero and thus C is always multiplied by zero. The balance of terms on the RHS is however strongly influenced. For example, by setting C to zero for massless layers and using all layers in the calculation of $[\overline{C}]$ in the first term on the RHS, $[\overline{C}]$ attains a physically unrealistic value for a particular θ surface in the presence of massless layers due to including layers with $C = 0$ in the average, and is therefore biased towards small values. This small bias also reduces mean meridional transport of CO_2 , forcing the eddy term to compensate in order to keep balance. It is more desirable for mean meridional transport of CO_2 to involve transport of a physically meaningful value of tracer that represents an average value for layers with mass. As long as $C = C + \overline{C}$ and $C = C^* + [C]$ is consistent throughout eddy decomposition, the LHS of Equation 2.13 is always equal to the RHS when massless layers are encountered in the statistics. The definitions provided here, however, assure that partitioning of eddy and mean transport is done in a physically realistic manner. Furthermore, since these definitions result in non-zero mixing ratios for massless layers, no

additional definitions are necessary for zonal quantities, and Equations 2.14 and 2.15 can be solved using all layers.

When describing eddy and mean transport processes in an averaged sense, “dry isentropes” (referred to here as surfaces of constant θ) and “moist isentropes” (equivalent potential temperature, the potential temperature that moist air would have if all vapor condensed out, defined as $\theta_e \sim \theta + \frac{L_v}{c_p} q$, with L_v the latent heat of vaporization and q the water vapor concentration) are more indicative of parcel trajectories through mid-latitude stormtracks than Eulerian averages. Horizontal flow along isentropic surfaces contains (approximately) the adiabatic component of vertical motion (assuming radiative cooling and sensible heating are relatively unimportant for synoptic motions) that is often neglected in a Eulerian reference system. In addition, θ_e is approximately conserved (internal energy neither lost nor gained) in the presence of latent heating [Pauluis et al., 2008]. Mass transport on θ_e surfaces includes a large contribution from moist air rising within stormtracks, while other forms of averaging (Eulerian or dry isentropes) miss entirely this contribution (the corresponding transport ends up in the mean term). The vertical component of motion gained from latent heat release in condensing moist air is critical for describing tracer transport by moist ascent within baroclinic waves. One could also consider the effect latent heat release due to ice formation in deep convective regimes, like condensation another source of potential temperature, but that is ignored in this study). In Chapter 3, eddy and mean transport is examined by setting ζ to η , θ , and θ_e in Equation 2.16. In Chapter 4, transport is examined only with ζ set to θ_e .

2.6 Methodology for Inversion used in Part 3

End-to-end inversion experiments are carried out in Chapter 5 to determine whether systematic differences in model transport discussed in Chapter 4 is aliased into errors in surface flux estimation. The inversion system uses the ensemble-based MLEF optimization technique, which was discussed briefly toward the end of Chapter 1.1.3. The following section includes discussion of the inversion technique, followed by discussion of the strategy for sampling forward transport sim-

ulations for synthetic satellite data, then a detailed description of the major steps in the MLEF data assimilation cycle, and ending with details regarding covariance smoothing, prior flux estimates, basic terminology, and net flux and uncertainty calculations. MLEF discussion follows techniques and discussion provided by Lokupitiya et al. [2008].

2.6.1 Assimilation Scheme

The optimization problem solves for unknown persistent multiplicative biases in photosynthesis, respiration, and air-sea gas exchange. Net exchange of carbon within a single grid point is represented as

$$F(x, y, t) = (1 + \beta_{RESP}(x, y))RESP(x, y, t) - (1 + \beta_{GPP}(x, y))GPP(x, y, t) + (1 + \beta_{OCEAN}(x, y))OCEAN(x, y, t) + FF(x, y, t), \quad (2.22)$$

where x is latitude, y is longitude, and t is time. β 's represent persistent multiplicative biases in time-varying grid-scale component land and ocean fluxes. Land fluxes are represented by heterotrophic respiration, or $RESP(x, y, t)$, and gross primary production, or $GPP(x, y, t)$, which are derived from SiB3 at hourly resolution. Ocean fluxes are represented by a net daily flux, or $OCEAN(x, y, t)$, and are derived from Doney et al. [2009]. Fossil fuel flux, $FF(x, y, t)$, is derived from the Vulcan Project [Gurney et al., 2009] and is assumed to be perfect (i.e., biases aren't included in the fossil fuel term).

Unlike ocean flux, which is prescribed as a net flux, fluxes in SiB3 have components into and out of the land (GPP and $RESP$, respectively). The strategy over land is therefore not to solve for biases in net flux, but assume that biases exist in component fluxes. SiB3 is balanced annually such that the sum of GPP at some grid point (x, y) from $t = 1$ to $t = n$, where n is the total number of hours in a year, is equal to the sum of $RESP$ from $t = 1$ to $t = n$. The real world has slowly varying terrestrial sinks that add up to something like 2.0-3.0 $GtC\ yr^{-1}$ globally. To represent net annual sinks in this framework net uptake must exceed net respiration; i.e., GPP must be larger than $RESP$ in the annual mean. This is accomplished with β s. Let's assume, for

example, that SiB3 predicts respiration and GPP fluxes of 120 GtC yr^{-1} for the entire globe. There are an infinite number of combinations of β_{GPP} and β_{RESP} that could be used to obtain a 2.0 GtC yr^{-1} net terrestrial sink, as long as $\beta_{GPP} > \beta_{RESP}$. $\beta_{RESP} = -0.02$ and $\beta_{GPP} = 0.02$ are two possible values. Put into context, these values mean that modeled respiration is overestimated in SiB3 by about 2% and GPP is underestimated by about 2%. β_{GPP} can also be less than zero, suggesting SiB3 overestimates GPP, as long as β_{RESP} is more negative.

The idea is that high frequency time variations in respiration and photosynthesis are driven by relatively well-understood and easily modeled processes that are determined to first order by variations in solar radiation [Zupanski et al., 2007a]. Mechanisms governing the physiological response of plants to weather and quick turnover times in the soil carbon pool are fairly well represented in SiB3 by process based equations, reanalyzed weather fields, vegetation cover and soil texture maps, and satellite derived phenology. Processes not represented in SiB3 such as underestimation of available nitrogen, forest management, agricultural land-use may lead to persistent biases in photosynthesis, while poor prescription of soil carbon pools or coarse woody debris may bias respiration calculations. This technique allows for *RESP* and *GPP* to vary on hourly, synoptic, and seasonal timescales and for air-sea exchange on daily time scales, but assumes that biases in these fluxes persist for longer periods.

Lokupitiya et al. [2008] solved for 8 week biases using synthetic data based on the in-situ network. The 8 week window was chosen because it takes several weeks to months for the atmosphere to mix sufficiently such that in-situ stations can feel CO_2 pulses from distant source regions. Here biases are allowed to persist for 2 weeks because satellite data provides approximately global coverage in just a few days (GOSAT has global coverage in 3 days) such that processes that control slowly varying fluxes are sufficiently constrained.

2.6.2 *Synthetic Satellite Data*

To test for differences in simulated transport by midlatitude synoptic storms, one model is run forward in time to generate synthetic satellite data from a set of fluxes, called the “true flux”, and another is used to invert synthetic data to recover the true flux back. If the models are different in some persistent way, fluxes recovered from the inversion will differ systematically from the true flux used in creation of the synthetic data. Differences between recovered and true fluxes will serve as the diagnostic for flux estimation errors due to transport differences.

Synthetic satellite data refers to column averaged CO₂ mixing ratios obtained from a tracer transport model. This data is generated by sampling pressure weighted CO₂ output from GEOS5-0.67x0.5 along the GOSAT orbit using an orbit simulator provided by David Baker [personal communication, November 15, 2010]. GOSAT (discussed in Chapter 1.1.1) uses a sun-synchronous orbit with early afternoon sun-lit equator crossing time ($\sim 1:30$ pm local time) and orbital inclination near 98° . Since GOSAT measures CO₂ absorption using reflected solar radiation, the transport model is sampled only during daytime during the descending mode of the orbit. Subsequent orbits are separated by $\sim 25^\circ$ in longitude and ~ 99 minutes apart. GOSAT points near-nadir as well as at the sun glint spot, which greatly increases the signal over the ocean. GOSAT measures with 13.4 cross-scans per minute (5 total cross scans) with a field of view of ~ 100 km².

The number of points collected along a GOSAT orbit in one year (assuming cloudy pixels are not thrown away) according to the orbit simulator is shown in Figure 2.1A. A maximum of 281 measurements are sampled by GOSAT in one hour. This corresponds to 6744 points in a day and 94,416 points collected over a two week period. The number of samples over land is much larger than over ocean because of cross-scans. Also note this map represents the number of samples collected in a $2.5^\circ \times 2^\circ$ grid box. Multiple samples may occur over these large grid boxes during a single GOSAT pass but only one sample is used per grid box during a single satellite pass. The total number of measurements per year is dependent of the size of the grid box used for sampling. For example, the number of points per grid box is reduced significantly when $0.67^\circ \times 0.5^\circ$ grid spacing is

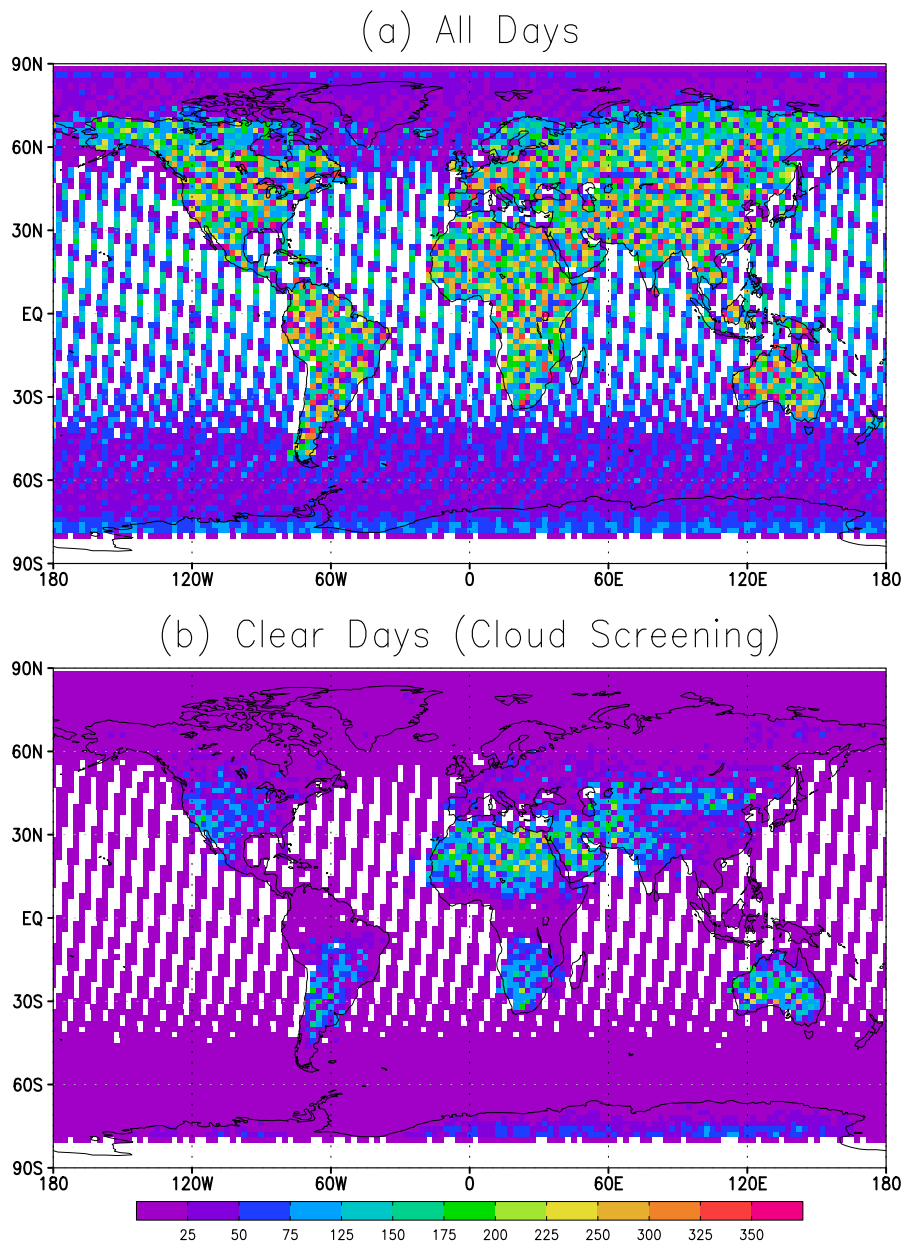


Figure 2.1: Number of points sampled by pixels in GEOS4-2.5x2 along the GOSAT orbit in one year for all days (a) and clear days (b).

used at the expense of more grid boxes. Nevertheless, these numbers represent a significant increase over the number of in-situ points.

A significant portion of satellite data must be thrown away due to cloud contamination. Cloud contamination is especially bad for GOSAT due to its large field of view relative to an OCO like

instrument. This means GOSAT will only detect CO₂ mixing ratios during fair weather days which could lead to temporal sampling biases as discussed in Chapter 1.1.1, especially if simulated transport differs greatly from reality (or other models) underneath cloudy pixels. Assuming satellites could see through gaps in clouds, and were therefore able to sample the atmosphere during inclement weather, it's possible temporal sampling errors would be much smaller (as might be the case for a laser sounder). As discussed in Chapter 5, synthetic data is generated, and then inverted, for all conditions (clear + cloudy sky) and clear conditions only to test for the effect of fair weather bias on flux optimization. Clear conditions are defined as grid cells whose cloud optical depth (τ) is less than 0.3. Cloud optical depth is prescribed from GEOS5-1.25x1 to be consistent with the transport model, and is defined as the grid scale value (total in-cloud optical depth from ice and liquid water times the three dimensional total cloud fraction in a grid box). Data reduction due to discarding pixels with $\tau > 0.3$ is shown in Figure 2.1B. Regions where clouds persist, such as tropical and boreal latitudes, become very poorly sampled as a result. The effect of data reduction is obvious when is plotted as a percentage (clear days divided by all days) in Figure 2.2.

Annual mean clear-sky ratio from MERRA is plotted in Figure 2.3 for comparison to clear-sky occurrence estimated from CALIOP (see Figure 1 of Eguchi and Yokota [2008]). In general, MERRA estimates of clear-sky ratio compare favorably with CALIOP estimates from Eguchi and Yokota [2008], in particular in northern middle and boreal latitudes and in tropical regions. MERRA tends to overestimate the percentage of clear sky days in southern Africa, Australia, the mid-continental portion of southern S. America near 30S, over the Southern Ocean, and finally the Arctic. Overall, MERRA seems to overestimate total clear sky days slightly relative to CALIOP, in part because MERRA estimates are aggregated up to 2 degree regions while CALIOP estimates are derived at 5 km resolution. The comparison is favorable enough to warrant the use of MERRA cloud optical depth as a proxy for cloud screening.

Observations, whether in-situ or remote, must be assigned some measure of uncertainty. This so-called observation error corresponds to the diagonal of the observation covariance matrix, \mathbf{R} (see

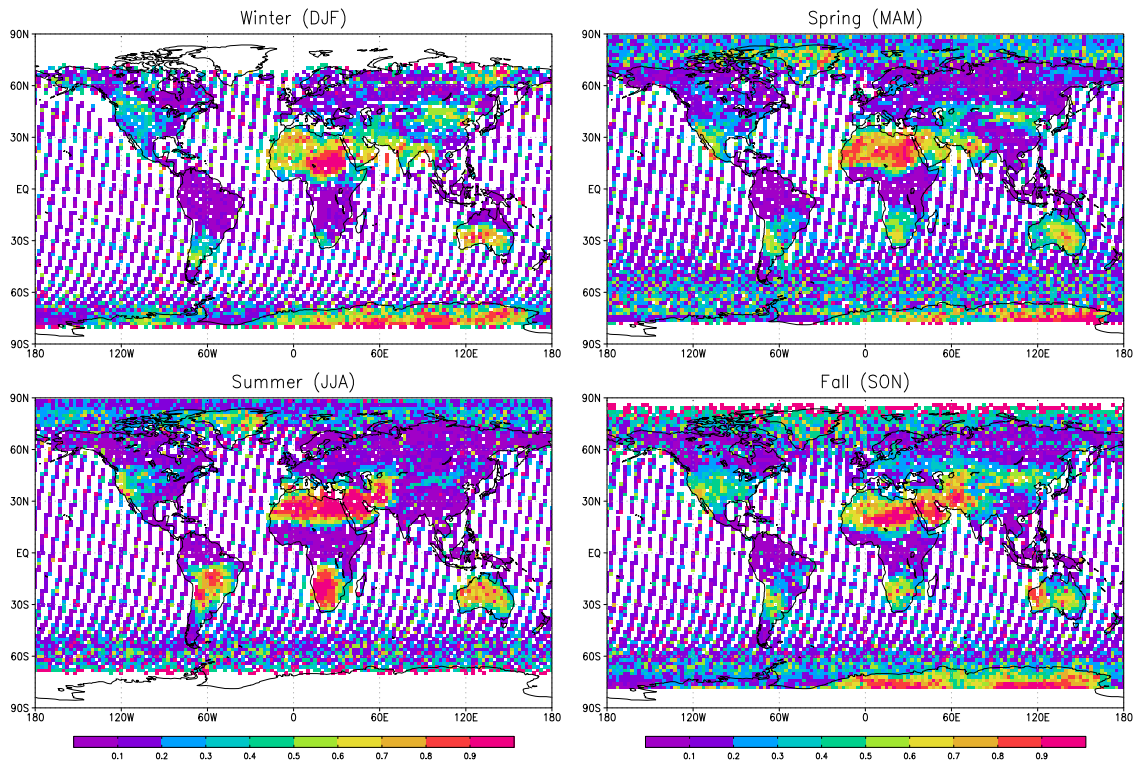


Figure 2.2: Fraction of points retained after cloud screening for winter (top left), spring (top right), summer (bottom left), and fall (bottom right).

next section). Observation error is determined by factors including (1) measuring instrument error, (2) transport error, and (3) the error due to scale mismatch between observations and the transport model, also referred to as representativeness error. Corbin et al. [2006], for example, investigated representativeness error for satellite data due to sampling only in clear conditions (clear-sky sampling error, discussed in more detail in Chapter 1) and found bias up to -0.4 ppm. Measurement errors, especially for high precision in-situ measurements, are typically very small (< 0.5 ppm). For satellites, measurement errors are typically much larger, more variable (depending on the satellite, active versus passive measurements, albedo effects over the surface, latitude, viewing angle, etc.), and generally larger than 1 ppm. Measurement errors may also be purely random or systematic and biased.

All OSSEs in Chapter 5 assume synthetic satellite data from GOSAT has a 3 ppm obser-

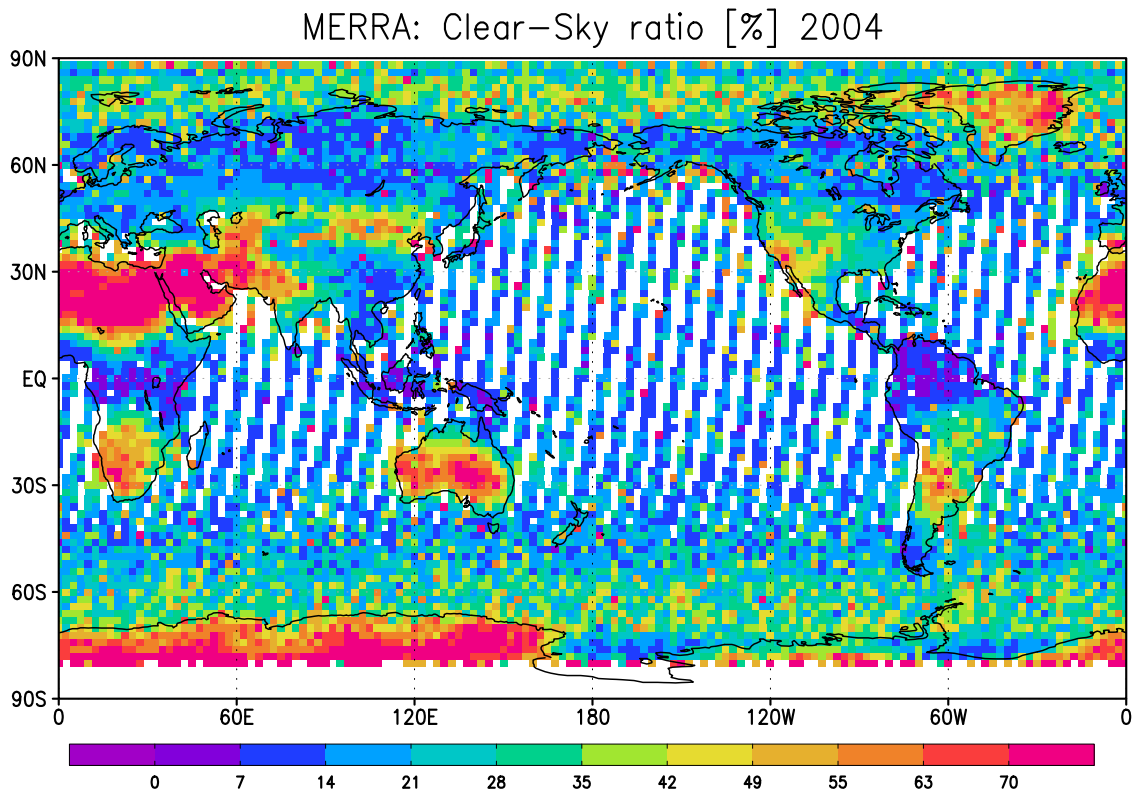


Figure 2.3: Percent of points retained after cloud screening for 1 year (prepared for comparison with Figure 1 of Eguchi and Yokota [2008]).

vation error ($\sigma = 3$ ppm) at grid scale due to random measurement error. This error is added to synthetic measurements as a measure of instrument precision by creating a vector of white gaussian noise, with mean of zero and $\sigma = 3$, that is equal to the size of the observation vector for one year. 3 ppm measurement noise is chosen as an upper bound from values computed by Chevallier et al. [2009], who account for measurement noise, smoothing error, interference error component, and overall random contribution of aerosols to retrieval noise, to represent the approximate uncertainty of GOSAT retrievals. This noise is added to synthetic measurements after sampling from the forward runs.

2.6.3 MLEF

There are two major steps involved in a data assimilation cycle: (1) the analysis step and (2) the forecast step. In the analysis step the optimal state is found by minimizing the cost function provided the observations inside the analysis window. In the forecast step, a prior for the next cycle is found by applying a forecast model, in this case PCTM, to the optimal state found in the analysis step.

MLEF attempts to find the maximum likelihood solution for the bias parameters β_{GPP} , β_{RESP} , and β_{OCEAN} using ensemble-based data assimilation by minimizing the following cost function

$$J(\beta) = \frac{1}{2}[\mathbf{y} - H(\beta)]^T \mathbf{R}^{-1}[\mathbf{y} - H(\beta)] + \frac{1}{2}[\beta - \beta_b] \mathbf{P}_f^{-1}[\beta - \beta_b], \quad (2.23)$$

where β is the vector of unknown bias correction terms (the state vector being solved), \mathbf{y} is a vector of observations, $H(\beta)$ is an observation operator, β_b is the prescribed prior estimate for bias correction terms, \mathbf{R} is the observation error covariance matrix, and \mathbf{P}_f is the forecast (prior) error covariance matrix. The vector of observations is represented by the synthetic satellite data. GEOS4-2.5x2 serves as the observation operator in Equation 2.23 to communicate surface fluxes to observation locations. The matrix \mathbf{P}_f defines the prior uncertainty of β , also known as the forecast error covariance.

Equation 2.23 is minimized via an iterative conjugate-gradient algorithm with Hessian preconditioning (described below), and is robust for non-linear processes (not considered in this study). Iterative minimization converges in a single iteration to the Kalman filter solution,

$$\beta = \beta_b + P_f H^T (H P_f^T H^T + R)^{-1} [y - H(\beta_b)], \quad (2.24)$$

when the observation operator is linear and the ensemble size is equal to the size of the control vector [Zupanski 2005, Appendix A]. Here the control variable is the vector of unknowns. However, in the following experiments, the ensemble size is much smaller than the size of the control variable, which may degrade the MLEF solution. As demonstrated by Zupanski et al. [2007a], however, the

MLEF solution smoothly converges to the KF solution as the ensemble size approaches the size of the control vector, which provides justification for using smaller ensemble sizes.

A major advantage of MLEF is that it produces an estimate of the analysis uncertainty, or analysis error covariance. Unlike variational techniques which require full rank of the solution, the prior and posterior uncertainties of Equation 2.24 are defined in ensemble subspace as square roots of the forecast error covariance $P_f^{\frac{1}{2}}$ and the analysis error covariance $P_a^{\frac{1}{2}}$:

$$P_a^{\frac{1}{2}} = P_f^{\frac{1}{2}}(I + A)^{-\frac{1}{2}} \quad (2.25)$$

where A is the information matrix in ensemble subspace [Zupanski et al., 2007b]. The analysis error covariance changes in time (decreasing, ideally) due to the impact of assimilated observations involved in A . The information matrix can also be used as a guide when determining an adequate ensemble size. According to Lokupitiya et al. [2008] the ensemble size can also be determined from the information measure referred to as Degrees of Freedom for Sigma, or DFS, with an ensemble size considered appropriate if further increase in ensemble size, given a certain number of observations, does not change DFS.

The major steps of MLEF, as described in Zupanski [2005], are summarized below.

Step 1: Ensemble Forecast

This step generates ensemble members using a parallel computing environment, using initial ensemble perturbations in the first assimilation cycle (“cold start”) or the analysis covariance matrix in subsequent assimilation cycles (“warm start”). Use of the analysis covariance matrix to generate ensemble members is an important way of propagating information between successive assimilation cycles. The purpose of this step is to generate a bunch of random guesses used in minimization of the cost function; the more ensembles used, the more certain the posterior probability distribution the solution generates. Ensemble members are also used in this step to calculate the forecast error covariance, which is used in a later step for calculation of the updated analysis error covariance.

Step 2: Innovation Vector

This is the first step in the analysis, in which the ensemble forecast is interpolated to observation locations. These calculations can be done on separate processors for each ensemble member.

Step 3: Hessian Preconditioning

The first step in minimizing the cost function is to compute second order partial derivatives of the cost function so that a maximum likelihood analysis solution is obtained in a single step. This is known as Hessian preconditioning and requires calculation of matrices from innovation vectors calculated in Step 2, which can also be done through parallel computing. Eigenvalue decomposition is used to speed up matrix inversion used in Hessian preconditioning. The motivation for this step is that minimizing the cost function directly from ensemble-spanned subspace can sometimes be difficult because multimodal distributions may be present and gradient search algorithms may not converge on the correct solution. Hessian preconditioning transforms the initial distribution to something that can be minimized in just a couple steps.

Step 4: Gradient Calculation

The next step is to calculate the gradient in ensemble-spanned subspace. Here the cost function is redefined through the change of variable introduced through Hessian preconditioning. The first derivative of the new cost function is defined and minimization is calculated using the preconditioned steepest descent.

Step 5: Analysis Error Covariance

MLEF calculates the analysis error covariance using the optimized analysis determined from Step 4 (the inverse Hessian calculated at the minimum). The analysis error covariance is then used as initial perturbations for the next assimilation cycle.

2.6.4 Covariance Smoothing and Localization

Strong covariance smoothing in the first assimilation cycle and covariance localization in all cycles are required in experiments where the observation vector is small compared to the number of unknowns [Lokupitiya et al., 2008]. This was certainly the case in Lokupitiya et al. [2008] because of the use of relatively sparse in-situ measurements. The observation vector is significantly larger in this experiment, but smoothing and localization are carried out nevertheless. This may be especially helpful when the number of observations is reduced by cloud screening. Covariance smoothing is applied during the “cold start” by adding spatial correlations with an e-folding length of 800 km over land and 1600 km over ocean. After the first assimilation cycle, covariance smoothing is not necessary. Spatial covariance improves with time because of propagation of the error covariance through the analysis system and the opportunity to learn about spatial structure from observations later in the year. Localization is important in ensemble data assimilation because it prevents sampling errors at large distances and thereby reduces the ensemble size required for the analysis.

2.6.5 Defining Priors

As a starting point, simulated carbon fluxes are assumed to be unbiased such that $\beta_{GPP} = \beta_{RESP} = \beta_{OCEAN} = 0$ at every grid point (in contrast to β 's centered around a value of 1 as in previous MLEF experiments). In all subsequent cycles, the estimated biases from the previous cycle are used as priors. If satellite data contains information that is different from the priors, β 's will evolve with time to match the data. Otherwise, there will be no need for β 's to change. Several OSSEs are run in Chapter 5 to determine if the inversion can distinguish between biased and unbiased satellite data. β 's may also change in time if the inversion “thinks” the satellite data contains information different from the priors (as might occur, for example, in the presence of biased transport).

Prior uncertainties for biases are selected that allow β 's to learn from the satellite data. Choosing too tight or too loose uncertainties may prevent reaching a reasonable solution. Since

the biases aren't known, constant prior standard deviations are assumed for the biases at each grid point of $\sigma_{GPP} = 0.2$, $\sigma_{RESP} = 0.2$, $\sigma_{OCEAN} = 0.1$. These uncertainties are somewhat generous considering they act on large component fluxes of GPP and $RESP$. In contrast, if operating on NEE, which is much smaller, more variable, and therefore more uncertain, the uncertainties would be considered too small over the land and possibly too large over the ocean.

2.6.6 Terminology

Five types of surface fluxes are discussed in Chapter 5: (1) prior fluxes or “priors”, (2) analyzed or optimized fluxes, (3) true fluxes or “truth”, (4) flux estimates, and (5) flux errors. Prior fluxes refer to modeled flux components including GPP , $RESP$, and $OCEAN$ that are used as a-priori fluxes for the inversion. These fluxes actually take the form $(1 - \beta_{GPP}) * GPP$, $(1 - \beta_{RESP}) * RESP$, $(1 - \beta_{OCEAN}) * OCEAN$, but are assumed to be unbiased at the start of the inversion with $\beta_{GPP} = \beta_{RESP} = \beta_{OCEAN} = 0$. Analyzed, or optimized, fluxes refer to a-posteriori fluxes that take the same form as the priors but with possibly non-zero β s in the case that the inversion finds a signal in the satellite data different from prior constraints. True fluxes are fluxes that are prescribed in forward simulations to generate synthetic satellite data. These can be “hypothetical” fluxes if used to mimic real world sinks by setting β correction terms to non-zero values, or can reduce to priors when β 's are set to zero. Flux estimates refer to the difference between analyzed and prior fluxes. Flux errors refer to the difference between analyzed and true fluxes.

2.6.7 Flux and Uncertainty Calculation

Fluxes and uncertainties are calculated according to Lokupitiya et al. [2008]. To estimate average terrestrial NEE over each assimilation window (14 days), the following calculation is used:

$$F_{CO_2} = (1 - \beta_{RESP})\overline{RESP} - (1 - \beta_{GPP})\overline{GPP}, \quad (2.26)$$

where $\overline{(\dots)}$ represents the 14 day average. The corresponding uncertainty estimate is given by

$$\begin{aligned}\sigma_{CO_2}^2 &= \overline{(RESP)}^2 \sigma_{\beta_{RESP}}^2 + \overline{(GPP)}^2 \sigma_{\beta_{GPP}}^2 \\ &\quad - 2 \times \overline{(RESP)} \times \overline{(GPP)} \times Cov(\beta_{RESP}, \beta_{GPP}),\end{aligned}\quad (2.27)$$

where $\sigma_{\beta_{RESP}}^2 = Var(\beta_{RESP})$ and $\sigma_{\beta_{GPP}}^2 = Var(\beta_{GPP})$, where $Var(\dots)$ represents the variance, which are represented by diagonal values within the covariance matrix. Similarly, the following calculation is used for air-sea exchange:

$$F_{CO_2} = (1 - \beta_{OCEAN}) \overline{OCEAN}, \quad (2.28)$$

with the corresponding uncertainty estimate given by

$$\sigma_{CO_2}^2 = \overline{(OCEAN)}^2 \sigma_{\beta_{OCEAN}}^2, \quad (2.29)$$

where $\sigma_{\beta_{OCEAN}}^2 = Var(\beta_{OCEAN})$.

Mean terrestrial NEE over a region of land comprised of multiple grid boxes can be estimated as

$$\bar{F}_{Region} = \frac{1}{n} \sum_i F_i = \frac{1}{n} \sum_i (1 - \beta_{RESP}) \overline{RESP}_i - \frac{1}{n} \sum_i (1 - \beta_{GPP}) \overline{GPP}_i. \quad (2.30)$$

The corresponding uncertainty in regional monthly NEE is given by

$$\begin{aligned}\sigma_{\bar{F}_{Region}}^2 &= \frac{1}{n^2} \sum_i \sum_j \overline{(RESP)}_i \times \overline{(RESP)}_j \times Cov(\beta_{RESP_i}, \beta_{RESP_j}) \\ &\quad + \frac{1}{n^2} \sum_i \sum_j \overline{(GPP)}_i \times \overline{(GPP)}_j \times Cov(\beta_{GPP_i}, \beta_{GPP_j}) \\ &\quad - \frac{2}{n^2} \sum_i \sum_j \overline{(RESP)}_i \times \overline{(GPP)}_j \times Cov(\beta_{RESP_i}, \beta_{GPP_j}),\end{aligned}\quad (2.31)$$

where i and j indicate the grid boxes within the region and n indicates the total number of grid boxes in the region. Similarly for air-sea exchange,

$$\bar{F}_{Region} = \frac{1}{n} \sum_i F_i = \frac{1}{n} \sum_i (1 - \beta_{OCEAN}) \overline{OCEAN}_i, \quad (2.32)$$

with the corresponding uncertainty in regional monthly air-sea exchange given by

$$\sigma_{F_{Region}}^2 = \frac{1}{n^2} \sum_i \sum_j \overline{(OCEAN)_i} \times \overline{(OCEAN)_j} \times Cov(\beta_{OCEAN_i}, \beta_{OCEAN_j}). \quad (2.33)$$

As noted in Lokupitiya et al. [2008], cross-correlations are added to smooth analyzed fluxes because the number of unknowns is large. It is also noted that the filter develops cross-correlations from the data during assimilation, an important advantage of MLEF, and that these cross-correlations need to be considered during interpretation of uncertainty estimates.

Chapter 3

MOIST SYNOPTIC TRANSPORT OF CO₂ ALONG THE MIDLATITUDE STORM TRACK

This first results section analyzes forward simulations of CO₂ from PCTM to understand and quantify how seasonal interaction of synoptic processes with ecosystem metabolism modulates seasonality in northern middle and polar latitudes. The concept of the large scale atmospheric circulation is first discussed from the perspective of streamfunctions on Eulerian and Isentropic coordinate systems in order to provide insight into how the mid-latitude circulation operates. Meridional CO₂ transport is then diagnosed in a moist isentropic framework and parsed to mean and eddy components to demonstrate the role of moist synoptic storms for meridional exchange of CO₂. The significance of these storms for carbon cycle studies is demonstrated first through a case study that shows the covariance of transport by these storms with cloudiness and then through budget calculations of atmospheric CO₂ tendencies for a column of air around a latitude circle to show how eddy transport compares to fossil fuel emissions and terrestrial net ecosystem exchange. Finally, a conceptual diagram is provided to illustrate key interactions between baroclinic waves and atmospheric CO₂.

3.1 Introduction

It has long been recognized that seasonal and diurnal covariance between terrestrial ecosystem metabolism and fine-scale vertical transport in the atmosphere is a strong determinant of vertical structure in CO₂ mixing ratio (the CO₂ rectifier, Denning et al. [1995], among others). Like the CO₂

rectifier, synoptic transport by baroclinic waves along the mid-latitude storm track involves strong vertical motion and is correlated with ecosystem metabolism because large-scale baroclinicity and photosynthesis are both driven seasonally by variations in solar radiation. Baroclinic wave activity is enhanced in winter when respiration and decomposition dominate ecosystem metabolism, and is suppressed in summer when photosynthesis dominates.

Unlike the CO₂ rectifier, tracer transport by slantwise convection in baroclinic waves involves a strong meridional component and is intimately tied to condensation and precipitation processes. A recent analysis by Pauluis et al. [2008] found that mass transport along θ_e surfaces in baroclinic waves represents an important component of the atmospheric heat engine that operates between the equator and poles. This is also an important vehicle for tracer transport. Poleward transport by rising warm moist air follows a warm conveyor belt (WCB) above warm fronts, and is compensated by equatorward transport by sinking cold dry air following a dry air intrusion (DI) behind cold fronts [Cooper et al., 2001; Stohl, 2001].

Pollution transport by WCBs has received much attention in the scientific literature. Carlson [1981] presented empirical evidence indicating aerosol transport into the Arctic along θ_e surfaces. More recently, models and aircraft measurements from intensive field campaigns (e.g., North American Regional Experiment) have helped create conceptual models that explain how WCBs transport gases such as O₃ and CO upward, poleward, and eastward away from continents and across ocean basins [e.g., Bethan et al., 1998; Cooper et al., 2001]. Strong pollution transport by WCBs is not surprising considering WCBs originate near the surface in polluted boundary layers and are responsible for most of a mid-latitude cyclones meridional energy transport [Eckhardt et al., 2004].

CO₂ transport by baroclinic waves was described in detail by Fung et al. [1983] and was included in the study by Tans et al. [1990] that established the concept of a terrestrial carbon sink but has not received much attention since [However, see Miyazaki et al., 2008; Keppel-Aleks et al., 2010]. In particular, Miyazaki et al. [2008] provide a detailed description of CO₂ transport by eddy and mean components of the atmospheric circulation on tropospheric CO₂ distributions.

However, the contribution of moist processes embedded within stormtracks (i.e., vertical mixing by moist convection along fronts and poleward transport along WCBs) to CO₂ distributions could not be provided, in part because of the use of a "dry" vertical coordinate. Part 1 of this study therefore describes the influence of synoptic weather systems and embedded moist processes on the seasonality of atmospheric CO₂ in middle latitudes, where plants are abundant, and high northern latitudes, where CO₂ is strongly seasonal despite limited vegetation. Simulated mass fluxes of CO₂ are decomposed into mean and eddy components and written on θ_e (described in Section 2) surfaces to include transport along frontal systems and moist conveyors in the eddy term.

Meridional transport of seasonally-varying CO₂ is analyzed in PCTM [Kawa et al., 2004; Parazoo et al., 2008], discussed in Section 2.1.1. PCTM produces realistic seasonal and synoptic variability, as well as interhemispheric mixing. "Eddy decomposition," discussed in Chapter 2.5.2, is used to isolate transport signals associated with synoptic processes. There is extensive discussion of the influence of mean and eddy components of the atmospheric circulation on seasonal variations of CO₂, including vertical and horizontal spatial structure, zonal and time average column integrated transport, and sensitivity to vertical coordinate. Analysis of covariance of baroclinic waves with ecosystem scale metabolism is carried out to determine the influence of synoptic storms in middle latitudes, where the bulk of the terrestrial biosphere resides, on the seasonality of atmospheric CO₂ in middle and high latitudes, where vegetation is sparse (a phenomenon that will be referred to as "meridional sloshing of CO₂"). A conceptual diagram that summarizes key interactions between baroclinic waves and CO₂ mixing ratio is provided at the end of Chapter 3.

3.2 The Zonal Mean Circulation - Streamfunctions

Before analyzing atmospheric transport of CO₂ by mean and eddy circulations, the large scale atmospheric circulation operating between equator and pole is described. The global atmospheric circulation transports high energy air from equatorial regions to polar regions. This includes poleward flow of high energy parcels of air and equatorward flow of low energy parcels. Due to

the turbulent nature of the atmosphere, parcel trajectories vary widely, and it becomes necessary to describe the circulation in an averaged sense by computing zonal and temporal means over a sufficiently long period. Pauluis et al. [2008] give an excellent overview of global mean circulations calculated from the NCEP-NCAR Reanalysis on p , θ , and θ_e . In this section, calculations of streamfunctions made by Pauluis et al. [2008] are repeated using GEOS4-1.25x1 to illustrate key points and determine whether circulations in GEOS4-1.25x1 are consistent with NCEP-NCAR reanalysis.

3.2.1 *Streamfunction on Terrain Following Surfaces (η)*

The Eulerian mean circulation is a common technique for describing the atmospheric circulation. It is produced by averaging the flow on constant pressure, geopotential height, or terrain following coordinates. The circulation is conceptually and quantitatively similar in all cases. Since transport in PCTM is calculated on the terrain following coordinate η , calculate of the Eulerian mean streamfunction Ψ is performed on η , where Ψ_η is defined as:

$$\Psi_\eta(\eta_0, \phi) = \frac{1}{\tau} \int_0^\tau \int_0^{2\pi} \int_0^{p_s} H(\eta_0 - \eta) v a \cos \phi \frac{dp}{g} d\lambda dt. \quad (3.1)$$

Here, η_0 is some reference value of η from 0 to 1 in increments of 0.1, p is pressure, ϕ is latitude, τ is the time period over which the average is computed, λ is longitude, a is Earth's radius, v is the meridional velocity, g is the gravitational acceleration, and $H(x)$ is the Heavyside function, with $H(x) = 1$ for $x \geq 0$ and $H(x) = 0$ for $x < 0$.

Plots of Ψ effectively show zonally averaged vertical and meridional velocity, together in one diagram. Lines of constant Ψ cannot intersect the Earth's surface; if they did, that would imply a flow of air across the Earth's surface. Similarly, lines of constant Ψ cannot extend upward into space. Figure 3.1 shows the annual mean Ψ_η as a function of latitude for GEOS4-1.25x1 for 2005.

The annual mean circulation consists of a three cell structure in both hemispheres: the Hadley cell in the tropics, the Ferrel cell in mid-latitudes, and the polar cell at high latitudes. The Hadley and polar cells, with air parcels moving poleward at high altitude and equatorward at low altitude, are direct circulations that transport energy toward the poles. Deep rising motion occurs near the

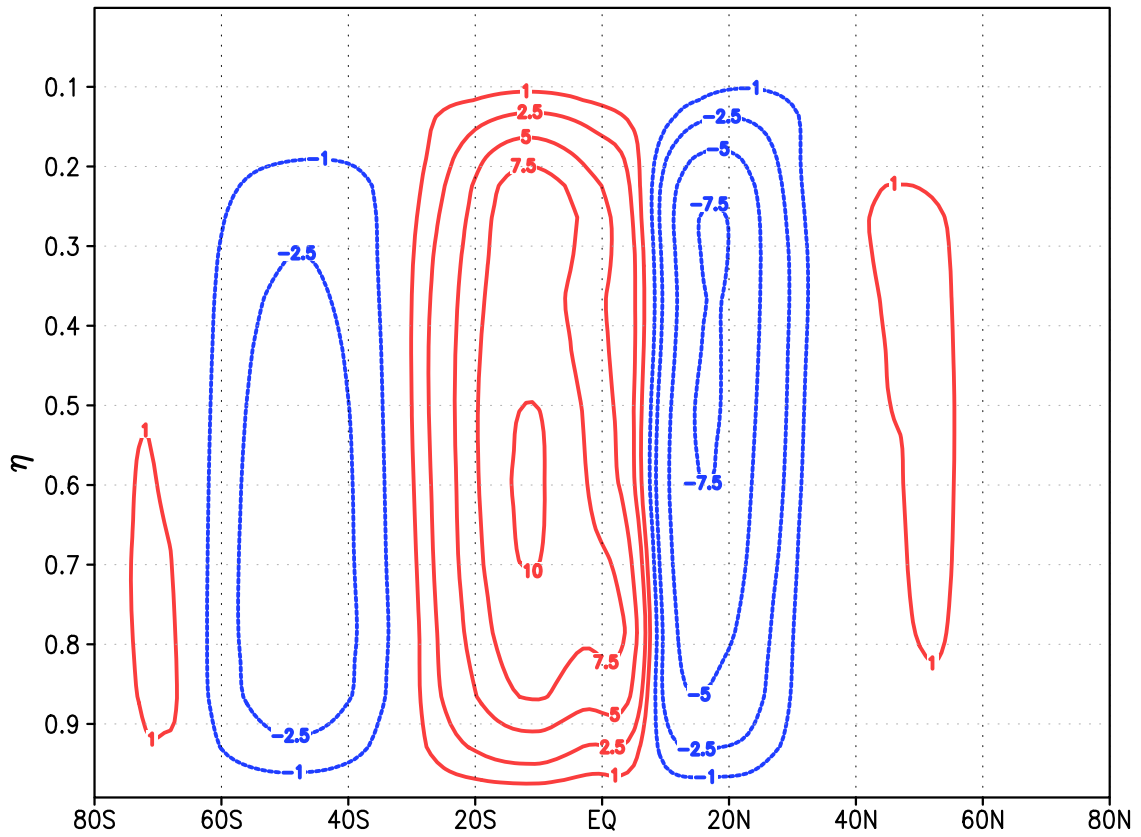


Figure 3.1: The global mean circulation computed on Eta surfaces from GEOS4-1.25x1 for 2005. Contour interval is $2.5 \times 10^{10} \text{ kg s}^{-1}$. Solid red contours are positive values of Ψ and correspond counterclockwise circulations, with northward flow at low levels and southward flow at high levels. Dashed blue contours are negative values of Ψ and correspond to clockwise circulations, with southward flow at low levels and northward flow at high levels.

equator in the annual mean, with sinking motion on either side in the sub-tropics. The zonal band of deep rising motion shifts north and south seasonally with the Inter-Tropical Convergence Zone (ITCZ) and the position of the sun. The strongest vertical motion occurs near $\eta = 0.5$, which roughly corresponds to the middle troposphere, or 500 mb. The polar cells, in comparison, are very weak in the annual mean. The Ferrel Cell, an indirect circulation (energy transport is from low to high energy) in mid-latitudes, is strongest in the Southern Hemisphere, and corresponds to poleward flow near the surface and equatorward flow at high altitude that together transport energy towards the equator. Comparison to streamfunctions computed from NCEP-NCAR Reanalysis [Pauluis et

al., 2008] indicates that the general circulation is slightly stronger in GEOS4-1.25x1.

Synoptic scale eddies, which result from baroclinic instability in the unstable symmetric circulation, are not apparent in the Eulerian mean circulation. Eddies transport more energy toward the poles than the Ferrel cell transports toward the equator such that total energy transport in the mid-latitudes is poleward. The Ferrel cell is a response of the MMC to energy and momentum transport by synoptic eddies. Energy transport acts to cool the subtropics, inducing the sinking branch of the Ferrel cell, and warm higher latitudes, inducing the rising branch of the Ferrel cell. Eddy transport of angular momentum causes the Ferrel cell to adjust the meridional branches of the circulation; i.e., angular momentum transport out of the subtropics to middle latitudes is balanced in the MMC by Coriolis acceleration associated with an equatorward component of the Ferrel Cell.

3.2.2 *Streamfunction on θ*

The mean circulation can also be described through averaging on isentropic surfaces. The streamfunction on θ , Ψ_θ , is defined by

$$\Psi_\theta(\theta_0, \phi) = \frac{1}{\tau} \int_0^\tau \int_0^{2\pi} \int_0^{p_s} H(\theta_0 - \theta) v a \cos \phi \frac{dp}{g} d\lambda dt. \quad (3.2)$$

This is identical to Equation 3.1 except η_0 has been replaced with θ_0 . Figure 3.2 shows the annual mean streamfunction on θ , which looks very different from η . Direct circulations extend from the Equator all the way to the poles. Since the atmosphere is statically stable and θ is monotonic with height, it can be said that the isentropic circulation is characterized by poleward flow at high altitudes and equatorward return flow near the Earth's surface. Radiative cooling causes θ to decrease during poleward flow aloft while sensible heating causes θ to increase during the equatorward return flow near the surface. Strong diabatic heating by solar radiation, latent heat release, and sensible heating cause cross-isentropic flow and deep upward vertical motion in the tropics, while strong radiative cooling causing cross-isentropic flow and subsidence at high latitudes and the subtropics. Ferrel cells do not appear in the isentropic circulation.

To understand why isentropic coordinates exhibit poleward transport at all latitudes while

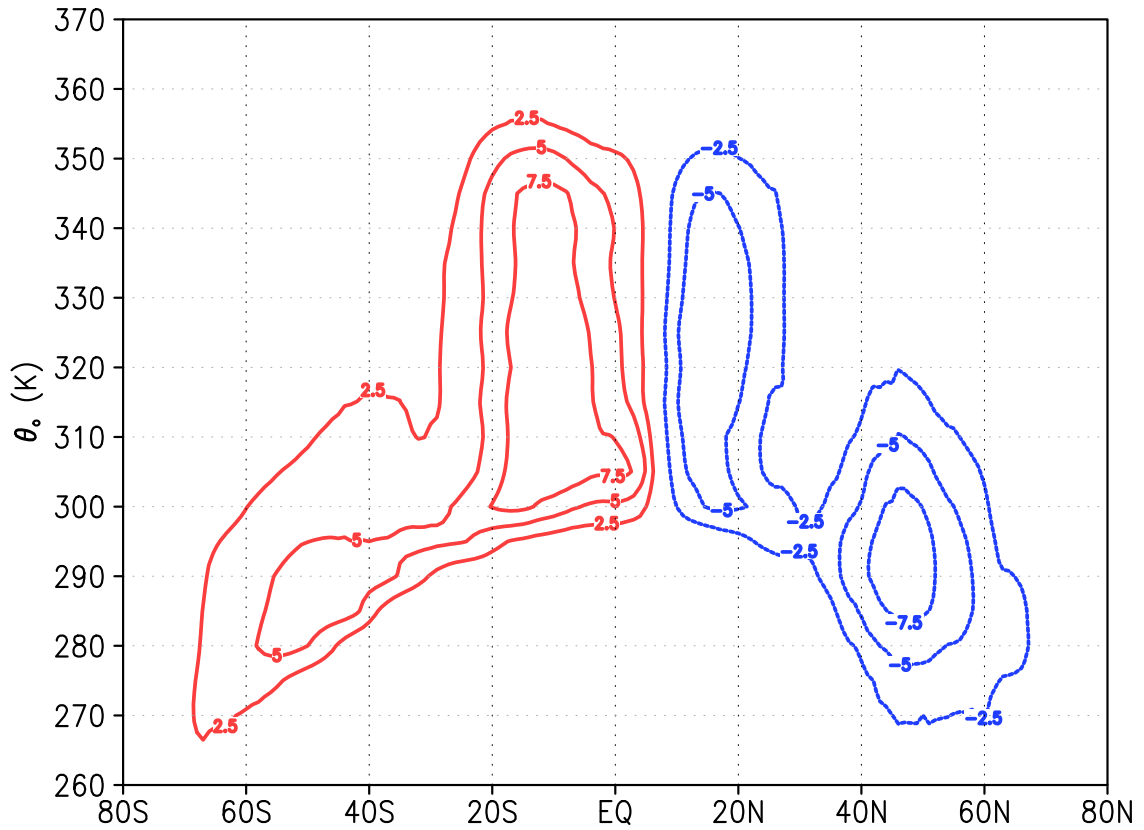


Figure 3.2: Same as Figure 3.1, except computed on potential temperature surfaces.

Eulerian coordinates exhibit poleward transport everywhere except mid-latitudes, we write the following equation for mass transport using eddy decomposition technique described in Chapter 2:

$$[mv] = [m][v] + [m^*v^*], \quad (3.3)$$

where m is the pseudo-density and v is the meridional wind. The first term on the RHS of Equation 3.3 is the product of the zonally averaged pseudo-density with the zonally averaged meridional wind. The second term arises from correlated fluctuations of the pseudo-density and meridional wind. The first term represent mass transport by the mean flow, which is supplemented by eddy mass flux when variations of meridional wind are correlated strongly enough with variations of pseudo-density.

Transport by the zonally averaged flow, $[m][v]$, dominates the circulation in the tropics where

variations of mass are small because of weak temperature gradients. This leads to small values of m^* on both η and θ and the eddy mass flux is trivially small in the tropics. In the mid-latitudes, however, the zonally averaged meridional wind is small because of geostrophic balance. Eddy mass flux dominates mass transport in midlatitudes because stationary and baroclinic waves force large variations of mass and hence m^* becomes large. Variations of mass on η are still too small, however, to stand out in Eulerian averaged circulations, and consequently the zonally averaged flow dominates the Eulerian circulation as seen in Figure 3.1. Variations of mass are large on isentropic surface such that $[m^*v^*]$ takes over from the zonally averaged flow. Variations of mass are much larger on θ than η because, as discussed in Chapter 2, isentropic circulations are more indicative of parcel trajectories, where potential temperature of an air parcel is approximately conserved in the absence of condensation.

3.2.3 Streamfunction on θ_e

While energy transport on θ is poleward in both hemispheres, the isentropic flow is only approximately conserved because of strong sources of potential temperature. In particular, the Northern Hemisphere mid-latitudes experience fairly severe cross isentropic flow near 40°N (streamlines are vertical) due to latent heat release by condensation and precipitation along stormtracks (see Figure 3.2). This source of potential temperature is due to latent heat release associated with moist air parcels. θ_e , defined in Chapter 2.5.3, includes a contribution from the latent heat content of water vapor so that, unlike in θ , phase transitions from vapor to liquid are conserved.

The streamfunction on θ_e , Ψ_{θ_e} , is defined as:

$$\Psi_{\theta_e}(\theta_{e0}, \phi) = \frac{1}{\tau} \int_0^\tau \int_0^{2\pi} \int_0^{p_s} H(\theta_{e0} - \theta_e) v a \cos \phi \frac{dp}{g} d\lambda dt. \quad (3.4)$$

This is identical to Equation 3.2 except θ_0 has been replaced with θ_{e0} . The use of the Heavyside function is key here; θ_e is non-monotonic (θ_e tends to decrease with height near the surface and then increase in the upper troposphere) and therefore has multiple instances throughout a vertical column. The Heavyside function accounts for this non-monotonicity so that mass transport along a

θ_e surface with multiple instances is additive.

Figure 3.3 shows the annual mean streamfunction on θ_e , which looks similar to θ except for a few key differences. First, accounting for moisture effects has strongly reduced the tendency for

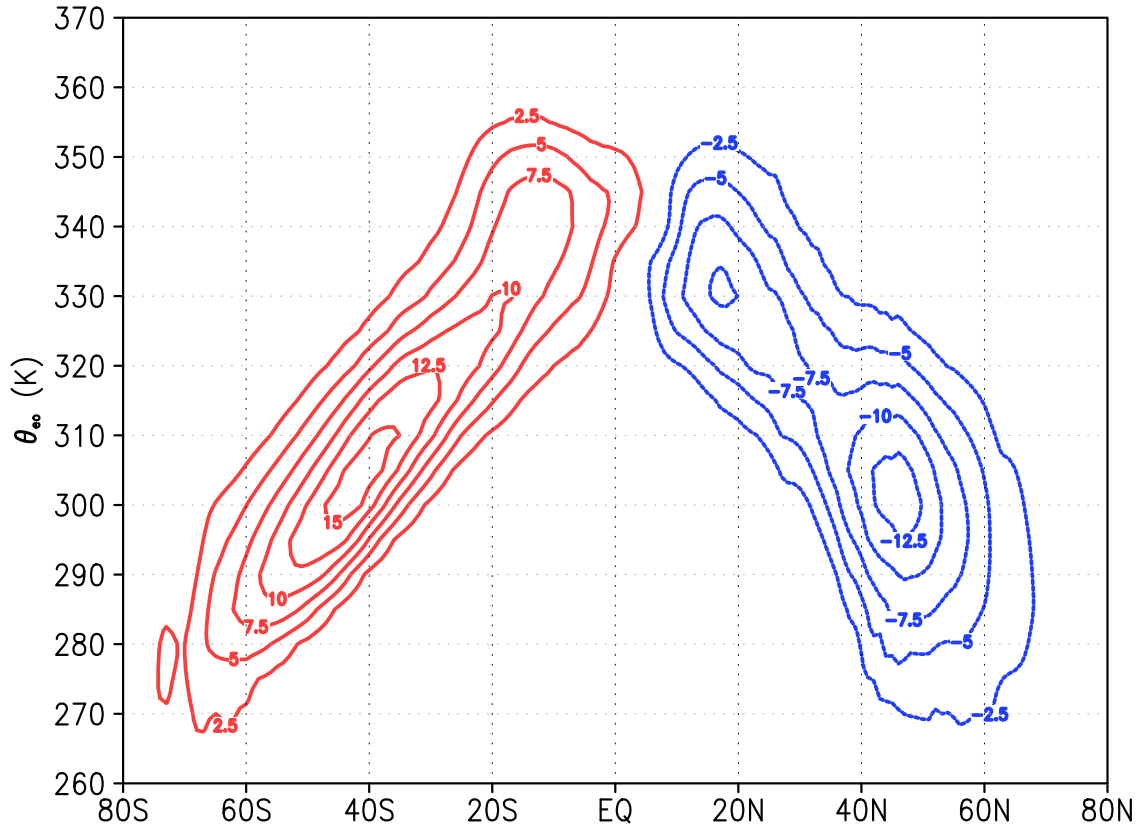


Figure 3.3: Same as Figure 3.2, except computed on equivalent potential temperature surfaces.

strong cross-isentropic flow, and hence vertical streamlines, in middle latitudes. The streamlines have a stronger tendency to be oriented horizontally (horizontal streamlines, or constant θ_e , implies conservation of θ_e) than before, although radiative cooling (sensible heating) during poleward (equatorward) flow aloft (near the surface) causes some downward tilt from equator to pole. Second, and perhaps most important, calculations of Pauluis et al [2008] show that total mass transport on θ_e is approximately twice that on θ . The authors use the joint distribution of mass transport on θ and θ_e to show that the additional mass transport corresponds to a low-level poleward flow of warm moist air with high θ_e indicative of air parcels that are nearly convectively unstable. The circulation is

strongest in mid-latitudes along the stormtrack where synoptic scale eddies advect low-level warm moist air upward and poleward before subsiding over the poles. It is also worth noting that the potential temperature of the surface equatorward return flow increases at a faster rate on θ_e because of surface evaporation.

To summarize, GEOS4 analysis is consistent with NCEP-NCAR analysis. The enhanced circulation in Figure 3.3 is due to latent heat release by moist rising air in synoptic eddies. These results show that mass transport by synoptic eddies is actually stronger when accounting for moist processes embedded within stormtracks. It is therefore crucial to account for moist processes when describing CO₂ transport by synoptic eddies.

3.3 Energy Transport

The atmospheric heat engine operating between the equator and poles is an important vehicle for tracer transport. If streamfunctions provide insight into what the general circulation looks like, eddy decomposition describes how zonally symmetric and asymmetric components of the general circulation move energy and tracer around. Interpretation of the general circulation is also sensitive to the vertical coordinate; as will be shown later, eddy decomposition and hence tracer transport by different components of the circulation is also sensitive to vertical coordinate. Such sensitivity will ultimately aid perception of important mechanisms that govern meridional CO₂ transport.

The streamfunction calculated on θ_e suggests that the mid-latitude circulation is driven strongly by asymmetries from the zonally symmetric circulation (i.e., eddies). To illustrate the relative importance of heat transport by eddies compared to the zonally symmetric circulation, eddy decomposition is used to parse moist static energy ($h = c_p T + gz + Lq$, where T is temperature, g is gravity, z is altitude, and L is latent heat) transport to mean, transient, and stationary terms as discussed in

Chapter 2.5.2 according to the expression:

$$\begin{aligned}
2\pi a \cos \phi \int_{\zeta_{sfc}}^{\zeta_{top}} \overline{[m_{\zeta} v_{\zeta} h_{\zeta}]} \frac{d\zeta}{g} &= 2\pi a \cos \phi \int_{\zeta_{sfc}}^{\zeta_{top}} \overline{[(mv)_{\zeta}]} \overline{[h_{\zeta}]} \frac{d\zeta}{g} \\
&+ 2\pi a \cos \phi \int_{\zeta_{sfc}}^{\zeta_{top}} \overline{[(mv)_{\zeta}^* h_{\zeta}^*]} \frac{d\zeta}{g} \\
&+ 2\pi a \cos \phi \int_{\zeta_{sfc}}^{\zeta_{top}} \overline{[(mv)_{\zeta}]} \overline{[h_{\zeta}]} \frac{d\zeta}{g} \\
&+ 2\pi a \cos \phi \int_{\zeta_{sfc}}^{\zeta_{top}} \overline{[(mv)_{\zeta}^* h_{\zeta}^*]} \frac{d\zeta}{g}. \tag{3.5}
\end{aligned}$$

Equation 3.5 gives units of energy transport in PW. As mentioned at the end of Section 2.5.2, the third and fourth terms on the RHS of Equation 3.5 will collectively be referred to as transport by transient eddies.

Moist static energy is essentially a measure of the energy within an air parcel due to potential energy, sensible heat or internal energy, and latent heating. Moist static energy transport is calculated on η , θ , and θ_e , vertically integrated according to Equation 3.5, and plotted in Figure 3.4. Positive values indicate northward transport and negative values indicate southward transport. Energy transport peaks in middle latitudes in both hemispheres near 45°N and crosses zero near the equator, indicating the atmospheric heat engine is moving energy away from low latitudes and into high latitudes.

Interpretation of energy transport by mean and eddy terms is sensitive to vertical coordinate and somewhat misleading. When calculated on η (Figure 3.4A), the MMC (mean circulation) dominates transport out of the subtropics through the Hadley Cell. Transport by the MMC at lower latitudes is actually stronger during individual seasons, but this transport largely cancels in the annual mean. Eddies dominate transport in the annual mean in mid-latitudes, with transient eddies important in both hemispheres. While transient and stationary waves contribute equally in the NH, eddies are dominated by transient eddies in the SH due to the large percentage of ocean coverage.

Eddy transport is much weaker on θ and almost non-existent on θ_e . In general, transport by the MMC is dominant in the isentropic framework. These results are misleading, however, because h and θ_e are closely related by $c_p T d \ln \theta_e \approx dh$, where T is the temperature of the condensation

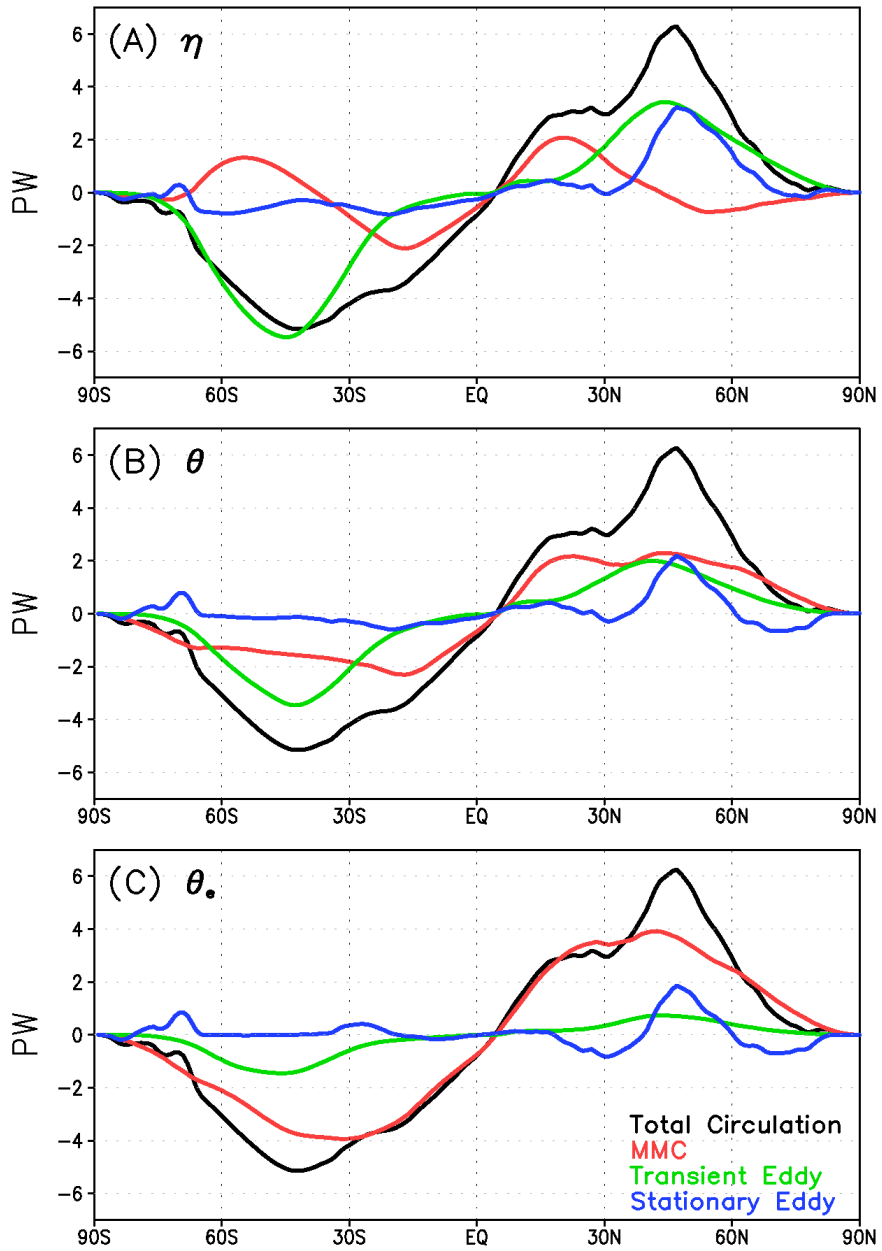


Figure 3.4: Annual mean transport of moist static energy by various components of the mid-latitude circulation. Energy has units of PW month^{-1}

level, and are thus very strongly correlated in the lower troposphere. Because θ_e and h within air parcels are both conserved during adiabatic vertical motion, and synoptic eddies tend to follow the path of isentropes during moist ascent along stormtracks, zonal and temporal perturbations of h are

approximately zero when calculated on θ_e such that “eddy” transport of h becomes small in the isentropic framework. It is therefore more convenient to use Eulerian coordinates such as η when describing energy or heat transport by baroclinic waves.

3.4 Seasonal Covariance of Baroclinicity and Ecosystem Metabolism

The motivation behind including eddy decomposition of energy transport in this study is to show how seasonal variations of meridional transport of energy and heat correspond with plant growth and decay. To this end, the seasonal distribution of eddy transport of h , as calculated on η , is plotted in black in Figure 3.5. Transport of h is much more vigorous during winter (DJF) than summer (JJA) in the NH due to the strong meridional temperature gradient. By comparison, there is relatively little seasonal change in eddy transport in the SH. The green line in Figure 3.5 represents zonally averaged NEE as simulated by SiB. NEE has the largest seasonality in northern mid-latitudes where the bulk of global land area resides and ecosystem metabolism is limited by seasonal variations in solar radiation. During DJF there is net respiration of CO_2 to the atmosphere due to a strong reduction in GPP (both GPP and respiration are strongly reduced, but respiration exceeds GPP in winter). During JJA there is net uptake of CO_2 from the atmosphere due to photosynthetic assimilation. NEE is much weaker in the SH where GPP and respiration are more in balance seasonally. While the tropics are the most biologically active part of the planet, seasonality of zonally averaged NEE is small due to cancellation of respiration and GPP. Synoptic transport of h is correlated with ecosystem metabolism in the NH because large-scale baroclinicity and photosynthesis are both driven seasonally by variations in solar radiation. Baroclinic wave activity, as depicted by eddy energy transport in Figure 3.5, is enhanced in winter when respiration and decomposition dominates ecosystem metabolism, and is suppressed in summer when photosynthesis dominates.

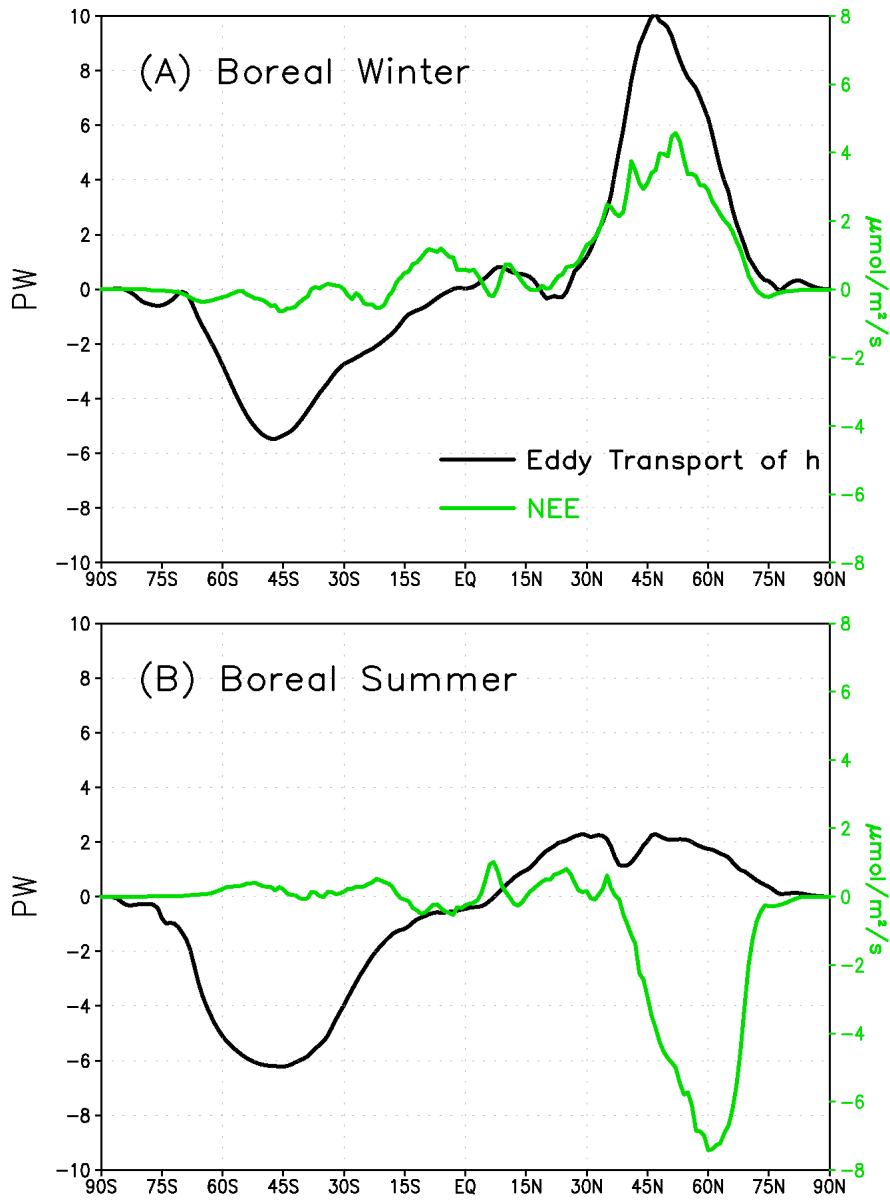


Figure 3.5: Seasonal covariance of moist static energy transport (h , black line) and zonally-monthly averaged terrestrial net ecosystem exchange (NEE, green line) for boreal winter (A, Dec-Jan-Feb) and boreal summer (B, Jun-Jul-Aug). NEE is plotted as a zonal mean in units of $\mu\text{mol m}^{-2} \text{s}^{-1}$ on the right y-axis.

3.5 Meridional Transport of CO_2 by Mean and Eddy Circulations

This section provides analysis of the influence of covariance of heat transport and surface fluxes of CO_2 on meridional transport of CO_2 . Eddy decomposition is used to assess how transport

by eddy and mean circulations contribute separately to CO₂ seasonality in northern middle and polar latitudes. Total average meridional transport at an arbitrary level ζ is calculated according to the expression

$$2\pi a \cos \phi \frac{M_c}{M_{air}} \overline{[m_\zeta v_\zeta C_\zeta]} \frac{d\zeta}{g}, \quad (3.6)$$

giving units of PgC K⁻¹ month⁻¹, where M_c is the molecular weight of carbon and M_{air} is the molecular weight of air [Note that the time average over one month is taken but that Equation 3.6 is multiplied by the number of seconds in a month to get these units]. Mean and eddy components of transport are calculated the same way with total transport decomposed according to Equation 2.16 in Chapter 2. Equation 3.6 is used to show vertical distributions of CO₂ transport. The zonal mean is removed to discuss spatial distributions of transport (this analysis assumes zonal wind is zero). The vertically integrated distributions of eddy and mean transport is also analyzed. Column integrated meridional transport is calculated in units of PgC month⁻¹. The equation for CO₂ transport is similar to that discussed above for h transport:

$$\begin{aligned} 2\pi a \cos \phi \frac{M_c}{M_{air}} \int_{\zeta_{sfc}}^{\zeta_{top}} \overline{[m_\zeta v_\zeta C_\zeta]} \frac{d\zeta}{g} &= 2\pi a \cos \phi \frac{M_c}{M_{air}} \int_{\zeta_{sfc}}^{\zeta_{top}} \left[\overline{(mv)_\zeta} \right] \left[\overline{C_\zeta} \right] \frac{d\zeta}{g} \\ &+ 2\pi a \cos \phi \frac{M_c}{M_{air}} \int_{\zeta_{sfc}}^{\zeta_{top}} \left[\overline{(mv)_\zeta^* C_\zeta^*} \right] \frac{d\zeta}{g} \\ &+ 2\pi a \cos \phi \frac{M_c}{M_{air}} \int_{\zeta_{sfc}}^{\zeta_{top}} \left[\overline{(mv)_\zeta} \right] \left[\overline{C_\zeta} \right] \frac{d\zeta}{g} \\ &+ 2\pi a \cos \phi \frac{M_c}{M_{air}} \int_{\zeta_{sfc}}^{\zeta_{top}} \left[\overline{(mv)_\zeta^* C_\zeta^*} \right] \frac{d\zeta}{g}. \end{aligned} \quad (3.7)$$

Again, the third and fourth terms on the RHS of Equation 3.7 are referred to as transient eddies.

3.5.1 CO₂ Transport by the MMC

Seasonal variations in the vertical distribution of CO₂ transport by the MMC, as calculated on θ_e , are summarized in Figure 3.6. Mean poleward and equatorward CO₂ transport are in opposite directions within a vertical column throughout the year in northern latitudes. Transport is strongest during winter (Figure 3.6B) and tends to dominate the annual mean signal (Figure 3.6A). Transport

during summer (Figure 3.6C) resembles the winter pattern except that transport throughout the column is weaker and occurs at higher θ_e due to warmer temperatures.

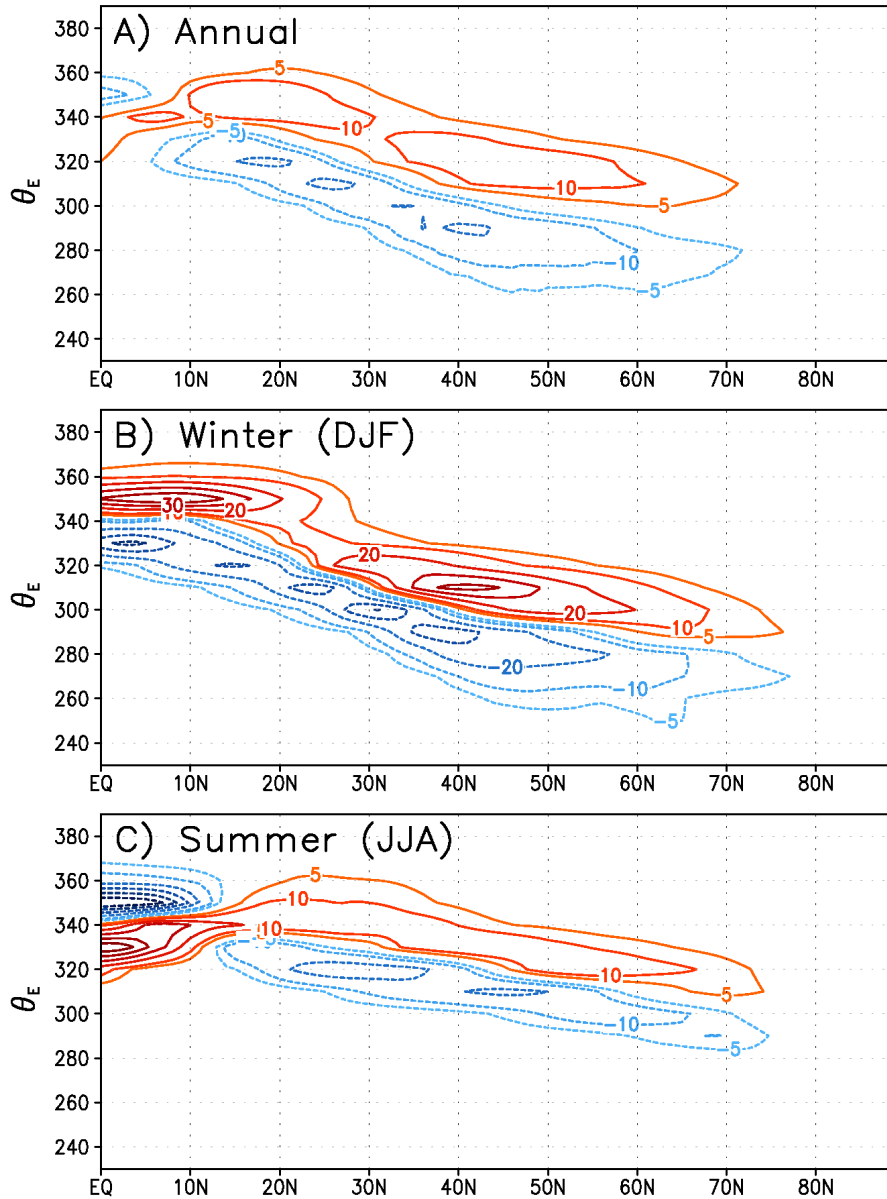


Figure 3.6: Diagnosis of vertical distribution of atmospheric CO₂ transport by the MMC on θ_e in the annual mean (A) and during boreal winter (B) and summer (C). Red (blue) contours indicate poleward (equatorward) transport. Units are PgC K⁻¹ month⁻¹

The pattern of seasonal transport by the MMC is explained to some degree by the mean distribution of atmospheric CO₂ and meridional mass fluxes, which are plotted together in Figure 3.7.

During boreal winter (Figure 3.7B), for example, the northern mid-latitudes are a source region for

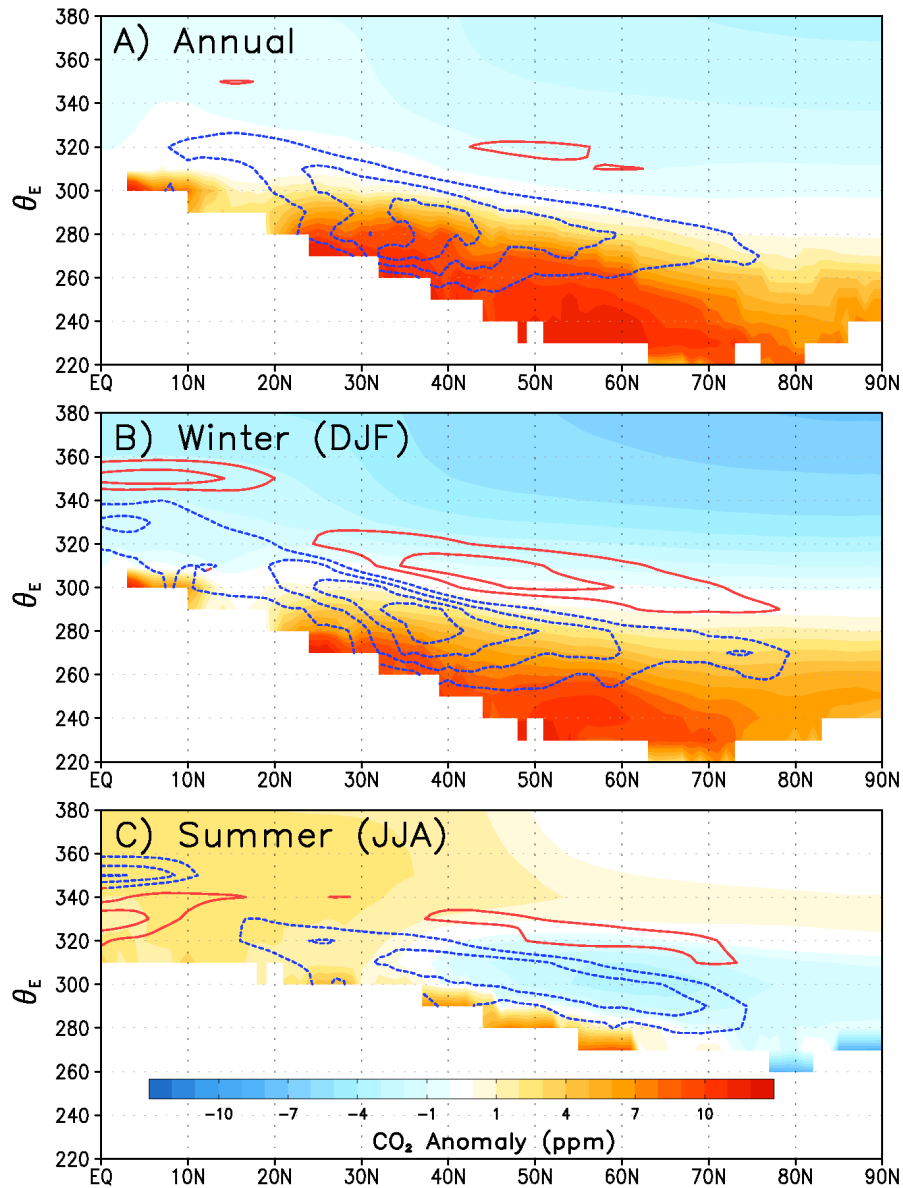


Figure 3.7: Zonal and monthly mean distribution of CO₂ (shaded) and mass flux (contours) in the annual mean (A) and during boreal winter (B) and summer (C). Shaded values are represented by the colorbar in (C), where the hemispheric mean has been subtracted (hence “CO₂ anomaly”). Contour intervals of mass fluxes are 0.05 Pg s⁻¹ K⁻¹. Red solid (blue dashed) contours correspond to poleward (equatorward) flow.

atmospheric CO₂ through ecosystem respiration (see Figure 3.5A) and fossil fuel emission such that CO₂ accumulates near the surface (dark red shading) and decreases vertically into the upper

atmosphere (shading tapers from dark red near 50°N and 260K to yellow and blue upward and outward; note that red values indicate CO₂ that is high relative to the column mean, i.e. positive CO₂ anomaly, and blue shading indicates low CO₂ relative to the column mean). As expected from Section 3.2, θ_e is not continuous from equator to pole because of surface evaporation and sensible heating of air parcels moving equatorward along the surface [Pauluis et al., 2008]. Also, because θ_e slopes upward and poleward toward cold air, there is net gain in altitude following θ_e poleward (with loss in altitude due to radiational cooling of 1°C day⁻¹). It should be noted that, over the course of a typical synoptic storm (3-5 days), this cross-isentropic flow is likely to have an impact on the results; however, the focus in Part 1 is on the difference in CO₂ transport by synoptic eddies when moist processes are included in the analysis.

Red and blue contours in Figure 3.7 indicate the mean poleward and equatorward meridional mass flux, respectively. According to Figure 3.7B, transport by the MMC during boreal winter leads to mean poleward transport of relatively low CO₂ (with respect to the vertical mean) at large θ_e (corresponding approximately to the upper troposphere in an isentropically stable atmosphere) and equatorward transport of relatively high CO₂ at small θ_e (near the surface), consistent with Miyazaki et al. [2008]. Poleward transport of low CO₂ by the MMC during boreal winter is indicated by red contours in Figure 3.6B. Equatorward transport of high CO₂ is indicated by blue contours.

Mean mass circulation during boreal summer occurs in the same sense as winter transport (see red and blue contours in Figure 3.7C); during summer, however, the equator-to-pole temperature gradient is strongly reduced and the strength of the atmospheric circulation weakens. At the same time, warmer temperatures and increased precipitation create a sink region for atmospheric CO₂ in the mid-latitudes through enhanced photosynthetic uptake (see Figure 3.5B), causing reversal in the large-scale vertical CO₂ gradient north of ~30°N (except near the surface because of deep convective uplifting of low CO₂ [see Miyazaki et al., 2008]).

3.5.2 *CO₂ Transport by Synoptic Eddies*

As this section is the focus of Part 1, it is longer and therefore organized into subsections based on the spatial structure being characterized. Other subsections, including “Cyclonic Case Study” and “Significance of Eddy Transport” are aimed at clarifying mechanisms associated with eddy transport.

Vertical distribution of Eddy Transport

Interpretation of transport on θ_e reveals that transport by synoptic eddies is weaker than mean transport by several orders of magnitude, but poleward through most of the troposphere in northern latitudes (north of 30°N) in the annual mean (Figure 3.8A). Poleward transport by synoptic eddies is strongest during boreal winter (Figure 3.8B) with peak transport near 45°N near $\theta_e = 300$ K. During boreal summer (Figure 3.8C) there is convergence of poleward and equatorward eddy transport near 60°N due to net biological uptake of CO₂. Opposing directions of transport in the column south of 30°N, most noticeable during boreal winter, are a result of transport by monsoonal circulations in tropical latitudes, which are manifested in stationary waves due to deviations from the zonal mean circulation and characterized by offshore flow during winter.

Eddy transport is forced through covariance between perturbations (temporal and zonal) to the mean circulation and to mean CO₂. Positive (negative) perturbations to the mean circulation represent anomalous poleward (equatorward) mass flux, with poleward flow of warm moist air ($\theta_e > \sim 280$ K) representing WCBs and equatorward flow of cold dry air ($\theta_e < \sim 280$ K) representing DIs. Anomalous mass flux along θ_e causes corresponding perturbations to mean CO₂ (with respect to latitude). Because CO₂ decreases northward on θ_e throughout much of the troposphere in the annual mean (Figure 3.7A), anomalous poleward mass flux causes positive perturbations of CO₂. Poleward transport in the annual mean and during boreal winter is a result of positive covariance of anomalous mass flux and CO₂. Equatorward transport north of 60°N during summer, on the other hand, is a result of negative covariance. Negative covariance and thus equatorward transport

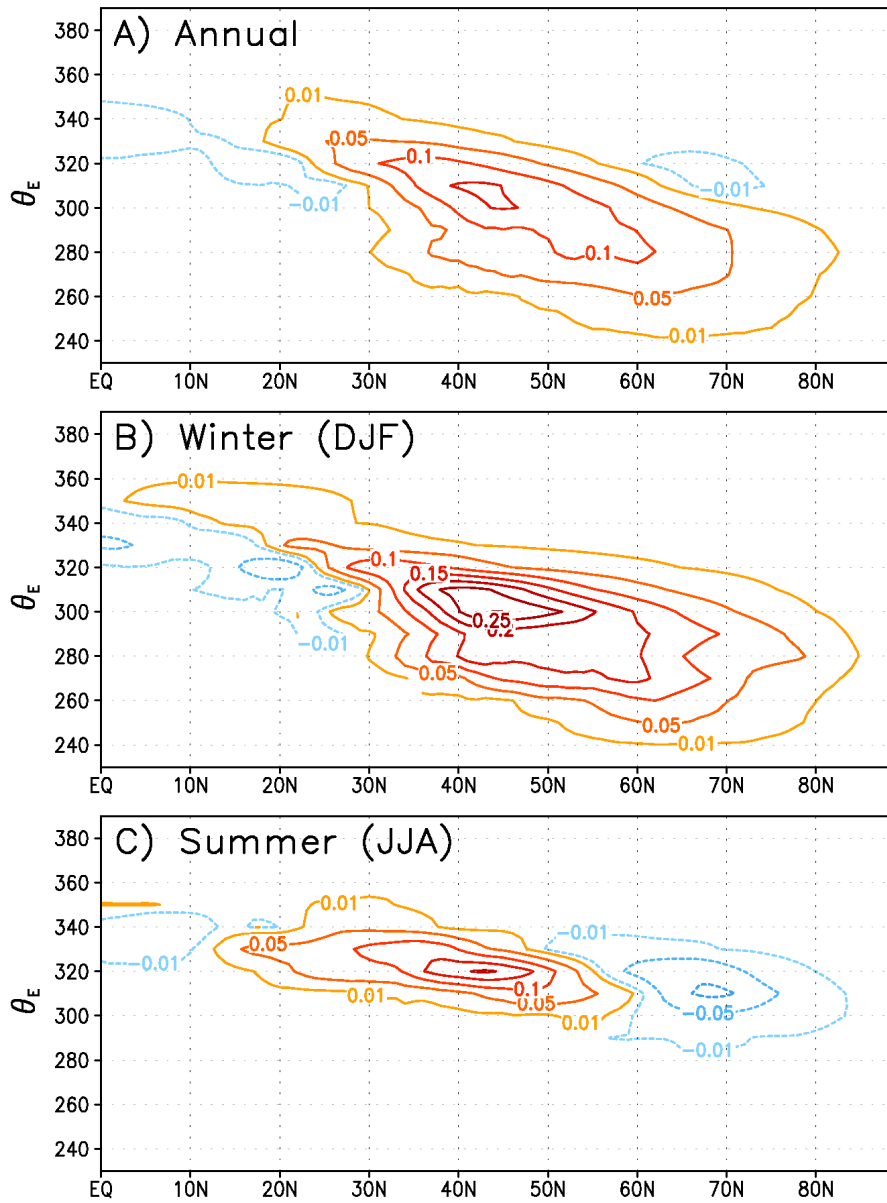


Figure 3.8: Diagnosis of vertical distribution of atmospheric CO₂ transport by synoptic eddies (stationary and transient waves combined) on θ_e in the annual mean (A) and during boreal winter (B) and summer (C). Red (blue) contours indicate poleward (equatorward) transport. Units are PgC K⁻¹ month⁻¹

result primarily from changes in the sign of meridional CO₂ gradients. These results suggest that CO₂ transport by eddies is trivially small when compared to transport by mean circulations; as will be discussed later in this section, however, eddy transport is actually strongly non-trivial when

integrated in the column.

Cyclonic Case Study

Examination of a particular case illustrates the eddy transport mechanism. A composite surface map (Figure 3.9A) shows an extratropical cyclone that passed over the continental United States on 13 January 2005. A low- pressure system is centered over Lake Michigan, with corresponding warm and stationary fronts (solid red line and red-blue line, respectively) passing into New England and a cold front (solid blue line) over the Great Plains extending to Mexico. In the warm sector of the cyclone (southeast United States) there is poleward flow (depicted by wind vectors at surface stations pointing north) of warm moist air (temperatures from 10-20°C, high dewpoints). Following the classic mid-latitude cyclone [Cooper et al., 2001; Stohl et al., 2001], this air follows a WCB, rises above the surface warm front, and spreads into Canada and the Atlantic. In the cold sector is equatorward flow (wind vectors point south) of cold dry air out of Canada (temperatures from -10-0°C, low dewpoints), which descends behind the cold front.

Figure 3.9B shows the cyclone influence on meridional CO₂ transport at $\theta_e = 300\text{K}$. Since poleward moving air originates at subtropical latitudes where air is warmer and moister than equatorward moving air, θ_e intersects the surface at higher latitude in the warm sector ($\sim 42^\circ\text{N}$) than the cold sector ($\sim 27^\circ\text{N}$). The primary pattern is for equatorward mass flux of low CO₂ air in the cold sector and poleward flux of high CO₂ air in the warm sector. As equatorward moving air sinks it crosses many pressure levels and creates large anomalous mass fluxes. Cold sector transport is dry; q is zero on θ_e and equatorward transport is equal on θ (not shown) and θ_e surfaces. Similarly, poleward moving air crosses many pressure levels during moist ascent, with equally large anomalous mass fluxes. ***Warm sector transport is moist and q is nonzero; since θ_e conserves energy in the presence of latent heating by condensation while θ gains energy, θ_e is more indicative of parcel trajectories along moist conveyors.*** This portion of eddy transport is parsed to the mean term when diagnosed on θ , reducing eddy CO₂ transport by nearly half (see discussion below). Because co-

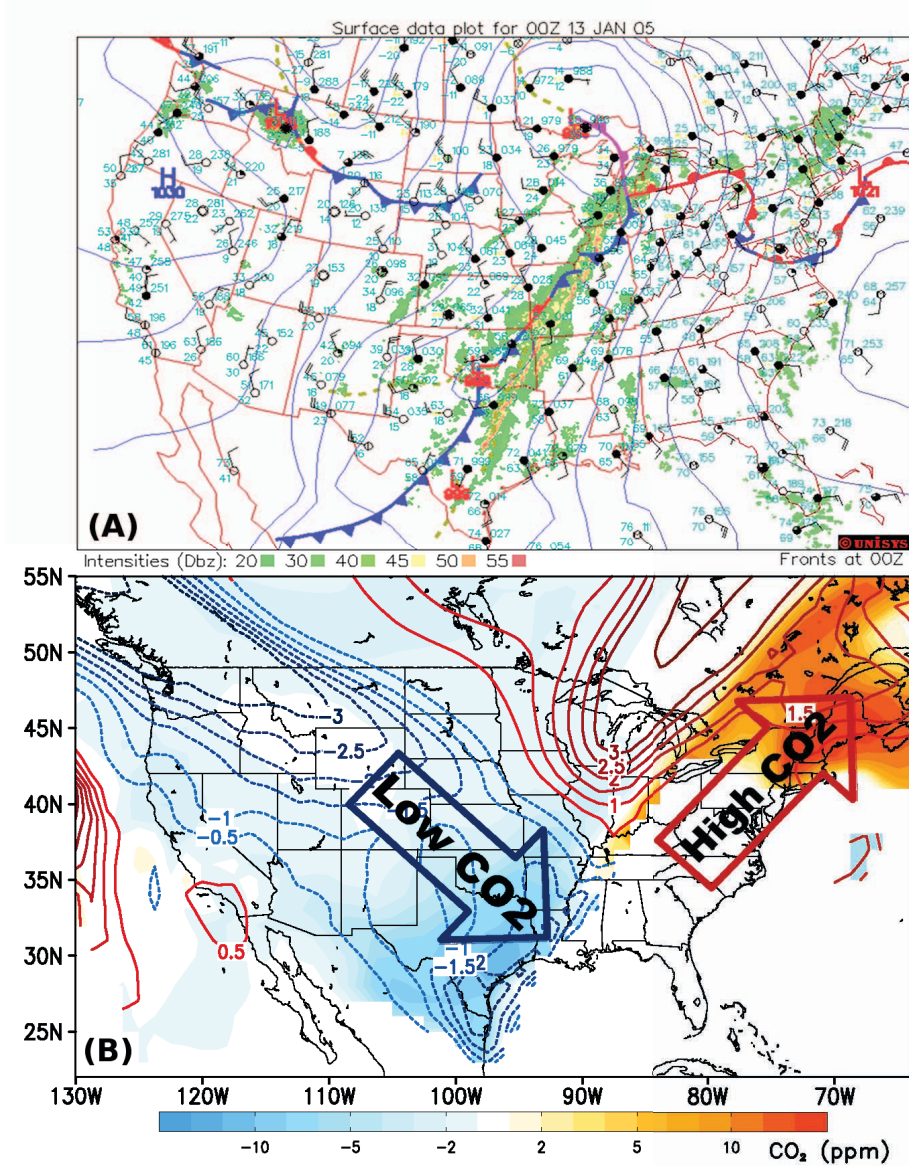


Figure 3.9: Case study from 13 Jan 2005 showing an example of eddy CO_2 transport associated with a typical mid-latitude cyclone. The surface composite map in (A) is reproduced with permission of Unisys Corporation (c) 2011. Model output of anomalous CO_2 (ppm, shaded) and mass flux ($1 \times 10^{-4} \text{ kg m}^{-1} \text{ K}^{-1}$, contour) along $\theta_e = 300 \text{ K}$ is plotted in (B). Taken from Parazoo et al., [2011]

variance of CO_2 and mass flux is positive in the warm and cold sectors in the time and zonal mean at $\theta_e = 300 \text{ K}$, net eddy transport over North America is poleward. Eddy transport over Eurasia, as well as along other θ_e surfaces, has different latitudinal origins, with corresponding transport dependent

on the latitudinal CO_2 gradient and the amount of convective instability of θ_e , but follows the same principle.

Cloudiness Associated with Eddy Transport

Migrating cyclones responsible for CO_2 advection also cause a great deal of precipitation and cloudiness. In the case illustrated above, radar (color filled stippling in Figure 3.9B) indicates observed precipitation and filled surface stations cloudiness. Radar shows that precipitation during this day occurs primarily near cold and warm fronts. Surface station analysis indicates that moist conveyors in the warm sector are also very cloudy. ***Covariance among condensing air (i.e. clouds), precipitation, CO_2 , and heat transport means that CO_2 transport along the east side of baroclinic waves will be hidden from satellite observing systems.*** Transport along the DI, however, is dry and sunny (open surface stations) and detectable by satellites.

Significance of Eddy Transport

While covariance of zonal and temporal anomalies of mass flux and CO_2 are positive and thus poleward on average for stationary and transient waves, there are many instances of net equatorward transport of CO_2 by eddies, as seen for example over the Great Lakes in Figure 3.9B. It is useful to calculate the correlation coefficient of the data series used to calculate the eddy terms to get a sense of the persistence of positive correlations of mass flux and CO_2 . A plot of the annual mean correlation coefficient for transient and stationary waves is shown in Figure 3.10.

The average correlation is positive throughout the northern atmosphere, consistent with predominantly poleward transport in Figure 3.8A. Stationary waves exhibit correlations between mass flux and CO_2 deviations of about 0.25 in northern middle latitudes and values close to 0.4-0.5 at higher northern latitudes. Correlations within transient waves peak near 30-50°N and are closer to 0.1. Higher correlations in stationary waves suggest a stronger and more systematic correspondence between mass flux and CO_2 deviations, with net flow dominated by poleward transport of CO_2 .

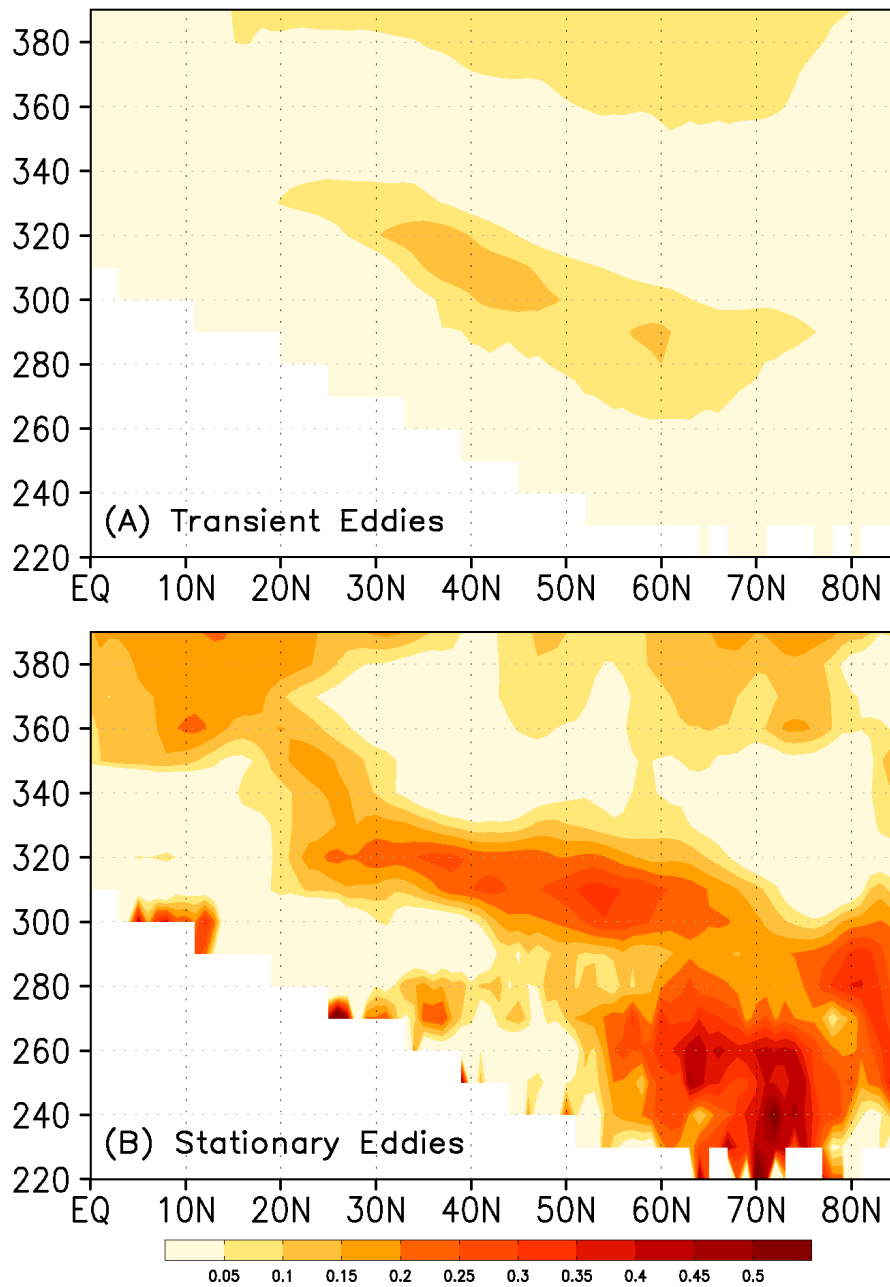


Figure 3.10: Annual mean correlation coefficient of mass flux and CO₂ deviations for (A) transient eddies and (B) stationary eddies (bottom plot), plotted as a function of θ_e . Colorbar is the correlation coefficient.

Low correlations in transient waves in the annual mean suggest that transport by traveling cyclones is noisy and mixed between poleward and equatorward transport. Eddy correlations have some seasonality with maximum values attained during boreal winter, but are not significantly different in

shape or magnitude from the annual mean (not shown). These results suggest that eddy transport is poleward throughout the column in the annual average as a result of (1) persistent positive CO₂ anomalies throughout the year due to fossil fuel emissions and (2) strong transport, respiration, and fossil fuel during boreal winter (Figure 3.8B).

Horizontal Distribution of Eddy Transport

The previous discussion, including case studies, has facilitated understanding of some of the key underlying mechanisms responsible for the pattern of predominantly poleward eddy CO₂ transport in the NH. The next step is discussion of the longitudinal distribution of time-averaged column integrated eddy transport. This analysis will provide an idea of the horizontal extent of zonally averaged eddy terms discussed in Figure 3.8. The spatial distribution of column integrated stationary and transient waves is plotted in Figure 3.11.

Patterns of eddy CO₂ transport emerge over spatial scales of 1000's of km's. Comparison to a climatology of WCBs presented in Figure 3 of Eckhard et al. [2004] suggests that dominant patterns of combined poleward CO₂ transport by stationary and transient eddies (Figure 3.11A) are coincident with climatologically favorable regions for WCBs. Like WCBs, CO₂ transport tends to follow a northward and eastward track originating in subtropical latitudes (~20-30°N), peaking in middle latitudes (~40-50°N), and terminating at the southern base of the polar vortex (~70°N). The most favorable regions tend to originate over land (e.g., southern portion of the United States and Tropical Asia) and terminate over the eastern portion of the adjacent ocean (e.g., Pacific Ocean and Atlantic Ocean, respectively).

Poleward eddy transport is also coincident with regions of strong fossil fuel emission (e.g., industrial Northeast U. S., China and Japan, and Europe). It appears that synoptic eddies transport a large portion of the worlds fossil fuel emissions into the Arctic every year. This result will be explored in more detail in Section 3.6.

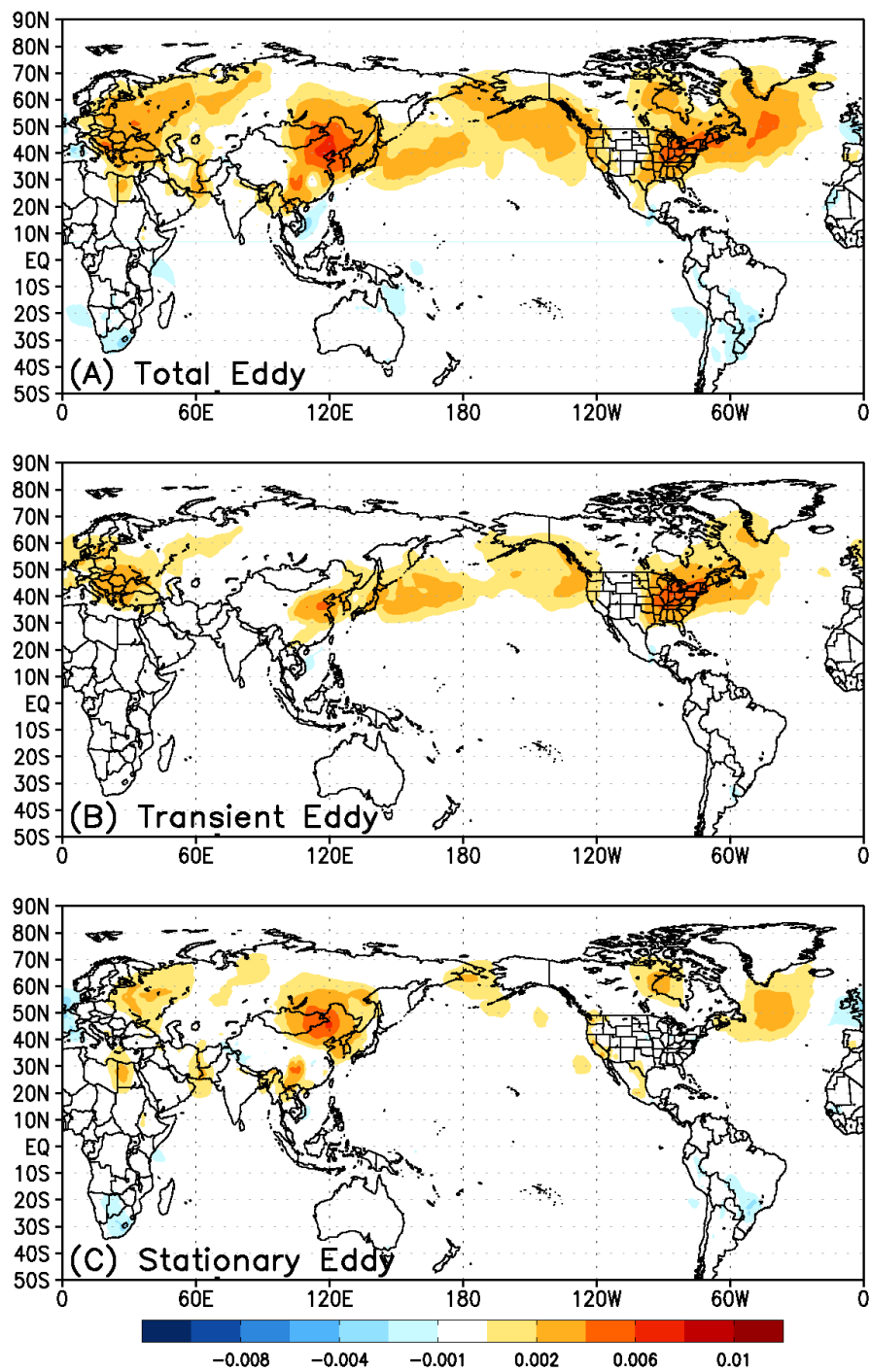


Figure 3.11: The annual mean spatial distribution of column integrated transport by (A) transient and stationary eddies, (B) transient eddies and (C) stationary eddies. The colorbar for each plot is shown at the bottom in units of PgC month^{-1}

3.5.3 Vertically Integrated Transport

Column integrated transport in the annual mean and during boreal winter and summer are shown in Figure 3.12. In the annual mean, total transport in the column is equatorward south of

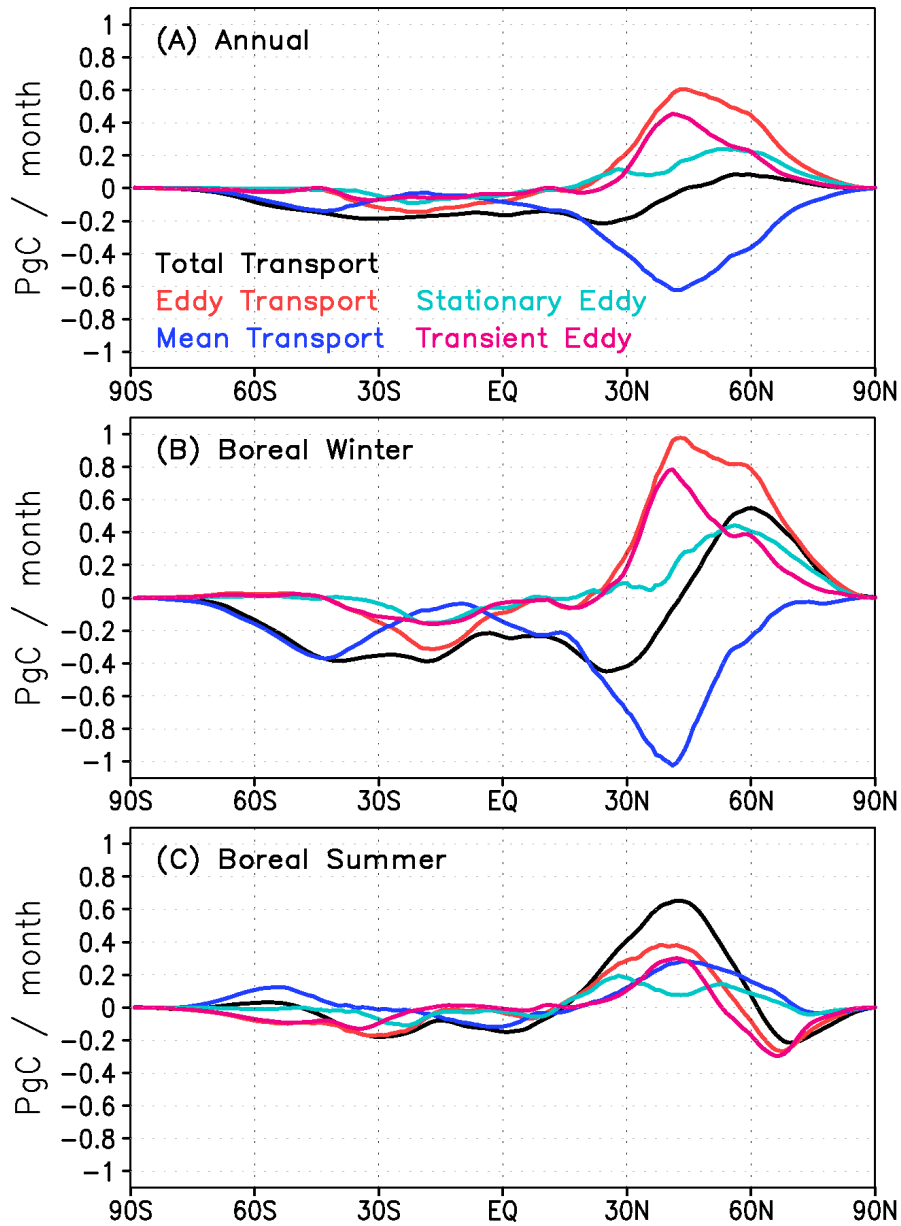


Figure 3.12: Column integrated transport in the annual mean (A) and during boreal winter (B) and summer (C). Total transport (black line) is parsed into transport by total eddy (red, transient + stationary), transient eddy (magenta), stationary eddy (cyan) and mean (blue) components.

45°N and poleward north of 45°N (Figure 3.12A). Since net terrestrial biological surface flux is zero in the annual mean due to forced balance between GPP and respiration, net transport in the annual mean primarily reflects transport of fossil fuels out of northern mid-latitudes. Seasonal transport is, however, much larger and more strongly influenced by seasonal biology. Transport during boreal winter (Figure 3.12B), for example, is reminiscent of annual mean transport in pattern but much stronger in amplitude due to strong decomposition and respiration in the same zone as fossil fuel emissions. Transport during boreal summer (Figure 3.12C) leads to convergence of CO₂ near 60° where strong terrestrial uptake occurs.

Vertically integrated transport by the MMC gives insight into the interplay of the strong vertical CO₂ gradient and the single overturning cell exhibited in the mean circulation field on θ_e shown in Figures 3.6 and 3.7. While poleward and equatorward transport by the MMC are large, they largely cancel one another with smaller residual equatorward transport in the annual mean with maximum equatorward transport of -0.6 PgC month⁻¹. During summer, residual mean transport is poleward in the column integral, reflecting the change in sign of the vertical CO₂ gradient. Net eddy transport, however, is poleward throughout the column (Figure 3.8) and in the column integral (Figure 3.12) in the annual mean. Although eddy transport is orders of magnitude smaller than mean transport within a single moist isentropic layer, it is poleward through the entire column. ***Annual mean transport by synoptic eddies is therefore systematically opposed in the column by transport by the MMC.*** Poleward eddy transport peaks at 0.6 PgC month⁻¹ in the annual mean and 1.0 PgC month⁻¹ during boreal winter. Partitioning of eddy transport to stationary and transient components reveals similar patterns to those discussed in the spatial plots of Figure 3.11, namely that eddy transport is dominated by transient eddies at lower latitudes and determined equally by transient and stationary eddies at higher latitudes.

3.5.4 Dependence on Vertical Coordinate

Although PCTM is run on a terrain following coordinate system, partitioning of transport to eddy and mean components is sensitive to vertical coordinate. To demonstrate this, eddy and mean CO_2 transport are diagnosed on η , θ_e and θ coordinate systems as discussed in the beginning of this section and in Chapter 2.5.3, column integrated as in Figure 3.12, and plotted as annual means in Figure 3.13. Note that column integrated transport along coordinates which are monotonic with height (η and θ at all latitudes and θ_e outside the tropics) is equal and therefore conserved. There is,

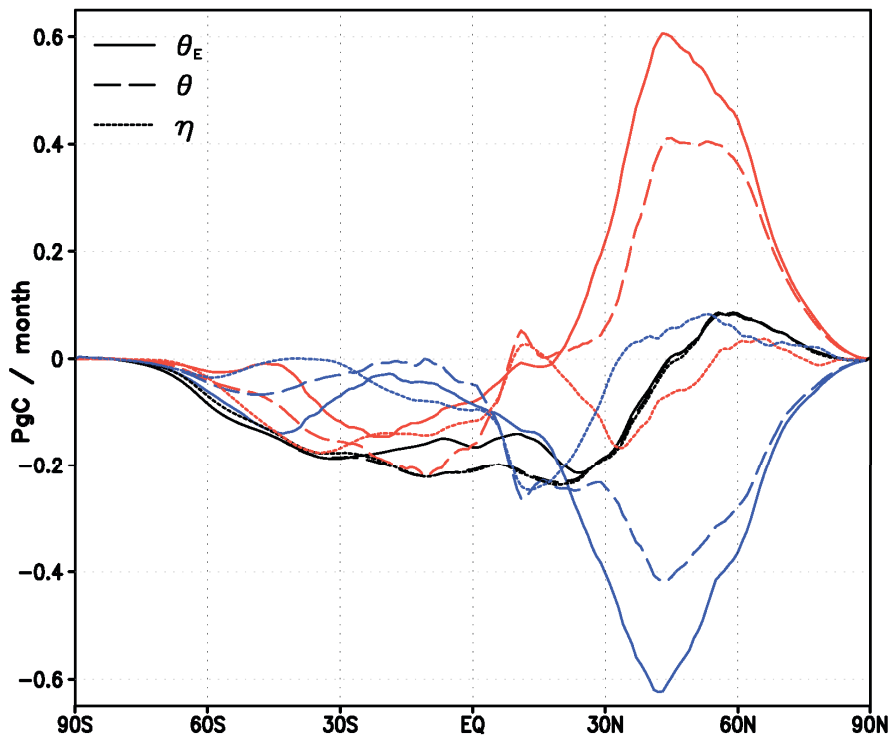


Figure 3.13: Column integrated transport in the annual mean as a function of vertical coordinate. Transport is calculated on moist isentropic surfaces (θ_e , solid line), dry isentropic surfaces (θ , dashed line), and terrain following surfaces (η , dotted line). Total transport (black) is partitioned to transport by eddy (red) and mean (blue) components.

however, a small error in θ_e in the tropics where a mid-tropospheric minimum in θ_e occurs. If total mass and CO_2 are conserved in a column at any given latitude, total transport will (and should) be independent of coordinate system. This error has been investigated and is attributed to small errors

in mass conservation when regridding in the tropics from monotonic η to non-monotonic θ_e . The primary implication is for mean transport; vertically distributed mean transport is unaffected, but vertically integrated mean transport is by 0.5 PgC in the tropics.

Outside of this small error in the tropics, total transport is conserved and therefore independent of coordinate system. *The partitioning of total transport to eddy and mean components, however, is strongly sensitive to vertical coordinate.* Focusing on the northern mid-latitudes with transport on θ_e the reference (solid lines), eddy transport decreases by nearly half when calculated on θ (red dashed line). Because total transport is conserved, decreased poleward transport by eddies in a θ framework is compensated by decreased equatorward transport by the MMC (dashed blue line).

Mass transport on θ_e includes a large contribution from moist air rising within stormtracks [Pauluis et al., 2008], while averaging on dry coordinate systems such as θ misses entirely this contribution. As demonstrated in Figure 3.13, the corresponding transport ends up in the mean term and in the annual mean case of CO_2 transport strongly reduces CO_2 transport attributed to eddies. The vertical component of motion gained from latent heat release in condensing moist air is therefore critical for describing tracer transport by moist ascent within synoptic waves. Transport due to latent heat release is most important in regions of condensing air such as moist conveyors in the warm sector of extratropical cyclones. For example, in the cold dry sector of the case study shown in Figure 3.9 (west side of a typical baroclinic wave), water vapor (q) is near zero, θ_e is reduced to θ , and equatorward transport is equal on θ and θ_e . Warm sector transport, however, is moist and q is nonzero. While θ_e conserves energy in the presence of latent heating by condensation, θ gains energy. As seen in Figure 3.13, this portion of eddy transport is parsed to the mean term when transport is diagnosed on θ . As a result, column integrated transport by eddies is strongly reduced on θ .

While eddy and mean transport patterns behave very similarly due to the Lagrangian nature of parcel following coordinates such as θ and θ_e , transport in an Eulerian framework such as the

terrain following coordinate η provides an entirely different interpretation of transport within an atmospheric fluid. Column integrated eddy transport on η (red dotted line) actually opposes eddy transport on isentropes. The same phenomenon occurs in the case of mean transport. Both terms are nearly an order of magnitude smaller than their isentropic counterparts.

To demonstrate the effect of an Eulerian framework on interpretation of CO₂ transport, vertical distributions of CO₂ and mass flux are calculated on θ_e and η . Annual mean vertical profiles are shown in Figure 3.14. The annual mean CO₂ distribution is clearly sensitive to coordinate system. In the Lagrangian framework, CO₂ gradients are very strong with respect to latitude and height and carry potential for large eddy CO₂ fluxes in response to baroclinic instabilities in the flow (Figure 3.14A). In the Eulerian framework, CO₂ gradients are extremely weak and carry little capacity for strong transport by eddies (Figure 3.14B). While η is tied to the surface and has little variability in space, θ_e is strongly sensitive to moisture and heating and is highly variable in time and space. θ_e surfaces tilt upward towards cold air. This means parcels of air traveling along isentropes start in polluted boundary layers where CO₂ mixing ratios are enhanced for much of the year due to fossil fuel emission and respiration and rise upward and poleward along stormtracks out of polluted boundary layers into the free troposphere where CO₂ mixing ratios are depleted relative to the surface. CO₂ therefore decreases from equator to pole following θ_e but increases following η .

The diagram in Figure 3.15 further illustrates this paradox. A vertical cross section of the atmosphere is shown for the midlatitudes from 20-70°N (north and poleward is to the left) from the surface up to the tropopause. For the purpose of this argument, attention is focused on the polar front and the red and blue air streams in the center of the diagram where extratropical cyclones and anticyclones occur. Dashed lines are not exact but can be thought of as isentropes, which are tilted upward and poleward. From our discussion of CO₂ distributions in the Eulerian framework it was shown that CO₂ tends to build up near the surface with peak values north of 50°N. From an Eulerian framework along for example the surface, poleward moving air flows, on average, directly into CO₂ enriched air from the south such that CO₂ depleted air is carried poleward. This results

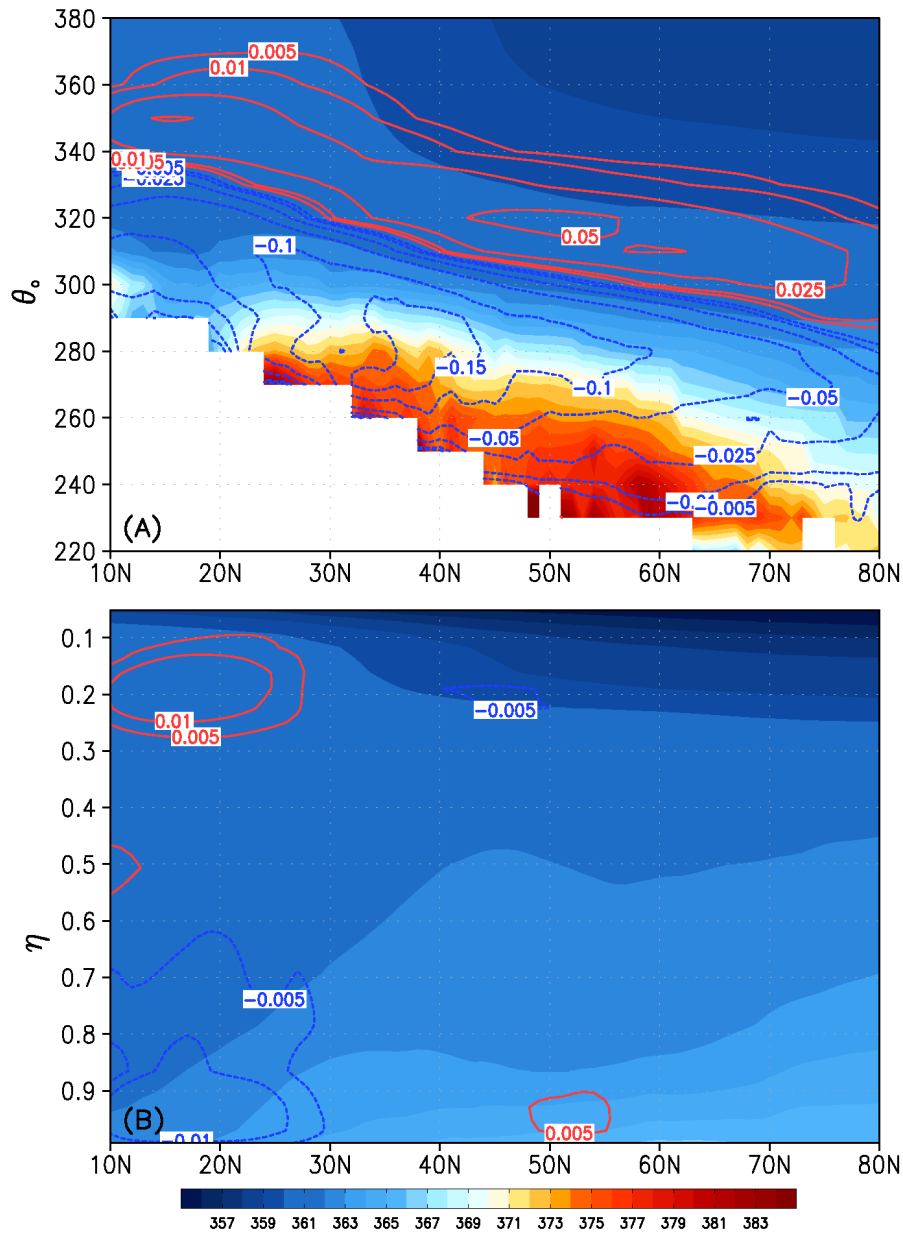


Figure 3.14: Zonal and month mean distribution of CO₂ (shaded) and meridional mass flux (contours) in the annual mean on θ_e (A) and η (B). The colorbar for CO₂ (in ppm) is shown on the bottom. CO₂ is plotted on the same scale.

in negative covariance of CO₂ and mass flux and net eddy CO₂ transport is equatorward, as shown in the dashed red line near 30°N in Figure 3.13. From a Lagrangian perspective of isentropes, poleward moving air follows the red line of rising warm air (the slope of which depends on whether

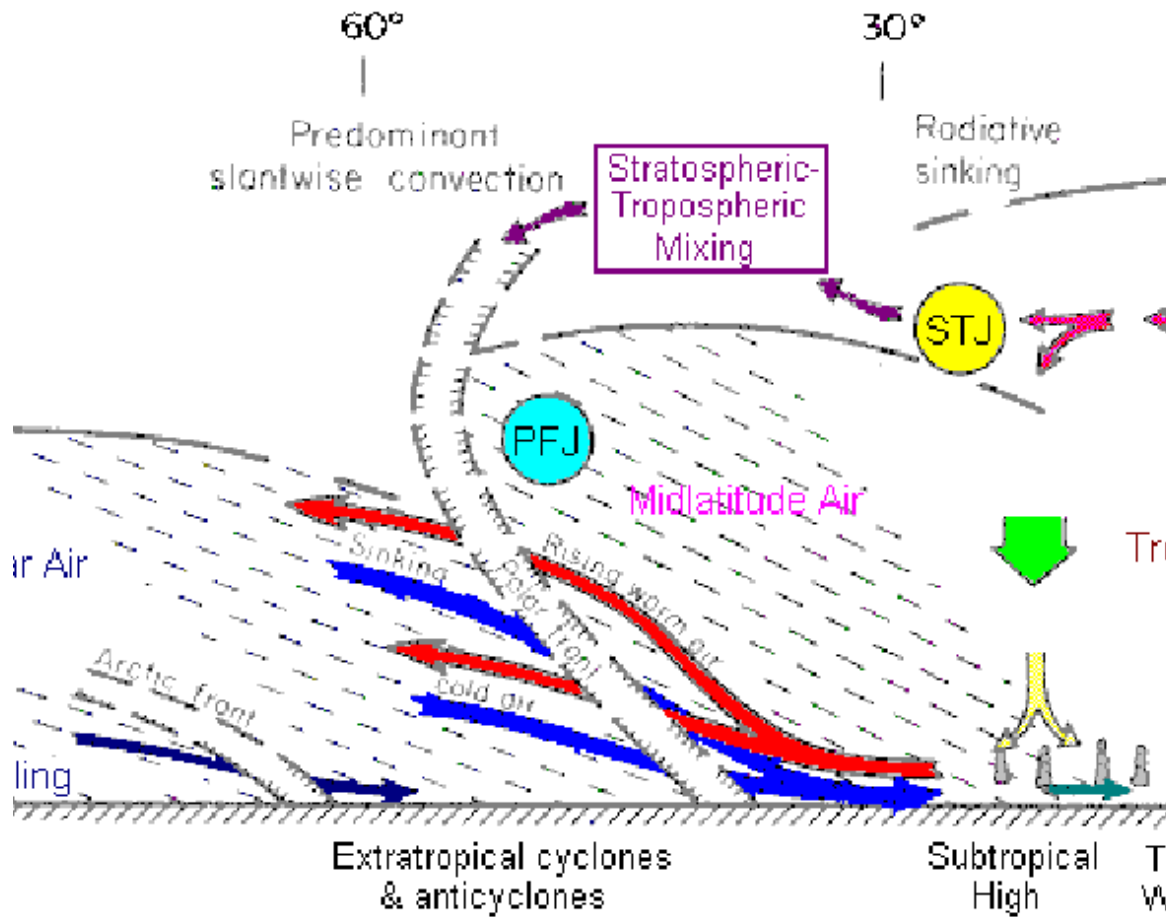


Figure 3.15: Diagram of isentropic surfaces and air streams along polar front (courtesy <http://www-das.uwyo.edu/geerts/cwx/notes/chap01/tropo.html>).

θ or θ_e is used) and flows, on average, directly out of CO_2 enriched air near the surface into the free troposphere such that CO_2 enriched air is carried poleward. This parcel following flows results in positive covariance of CO_2 and mass flux and net eddy CO_2 transport is poleward, as shown in the solid red line in Figure 3.13.

The importance of moist processes and slantwise ascent for transporting CO_2 enriched air out of the mid-latitude boundary layer and into the Arctic is demonstrated more precisely on moist isentropes. By including the moist contribution due to moist rising air in stormtracks, it can be said that, each year, synoptic eddies transport nearly all of the world's fossil fuel emissions into the Arctic ($0.6 \text{ PgC/month} \times 12 \text{ month} = 7.2 \text{ PgC / year}$, which is roughly equal to total annual fossil

fuel emissions used in this study). If eddy transport were instead diagnosed on dry isentropes, nearly one third of this transport would be unaccounted for (see Figure 3.13).

3.6 Seasonal Variations

Meridional transport strongly mediates the seasonal cycle of CO₂ in mid-latitudes and amplifies it in high latitudes, accounting for most of the observed seasonality at sites like Barrow, Alaska and Alert, Canada [Fung et al., 1983]. Comparison of satellite observed vegetation with modeled transport implies that atmospheric mixing produces signals at high latitudes where vegetation is sparse [Fung et al., 1987]. To convey the influence of eddy and mean transport on seasonality in the Arctic from a θ_e perspective, the seasonal cycle of the atmospheric CO₂ tendency (tendencies in ppm month⁻¹ are approximated by dividing Equation 1 through by zonal and time averaged surface pressure) binned by latitude into the Arctic and mid-latitudes is plotted as a function of eddy transport, mean transport and surface flux tendencies (Figure 3.16).

CO₂ seasonality is stronger in the Arctic despite weak surface fluxes (Figure 3.16A). This is driven strongly by synoptic eddies and therefore moist synoptic storms. Polar seasonality is strongly opposed by the mean meridional circulation, with net equatorward transport (at all northern latitudes) from September-June and poleward transport during summer. The same transport processes responsible for seasonality in the Arctic also strongly damp the seasonal cycle in mid-latitudes to about 50% of the seasonality implied by NEE, with eddy transport of similar magnitude to fossil fuel emissions during summer and fall (Figure 3.16B). Eddy transport tends to lead mean transport by 2-4 weeks during summer in the Arctic.

3.7 Conceptual Diagram

Results of Part 1 of this study are summarized in Figure 3.17. Synchrony of baroclinic waves with terrestrial ecosystem metabolism governs “meridional sloshing” of CO₂ between middle and high latitudes, which modulates seasonality at mid-latitudes and amplifies seasonality at high

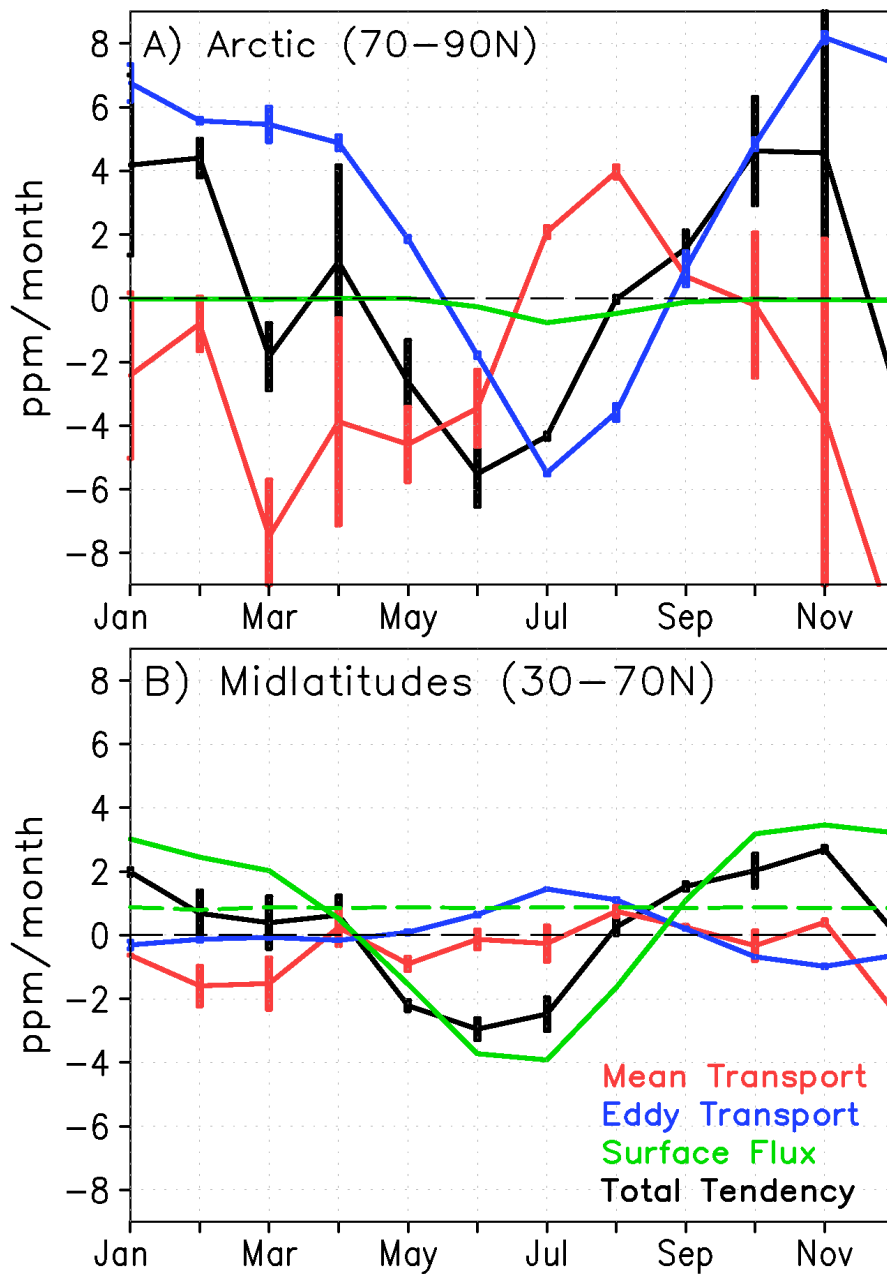


Figure 3.16: Column integrated seasonal CO_2 budget tendencies (ppm month^{-1}) on θ_e binned into (A) high latitudes and (B) mid-latitudes. Transport by transient and stationary eddies is plotted in blue, mean meridional transport in red, the total CO_2 tendency in black, and the total surface flux of carbon from land, ocean, and fossil fuels in green. The fossil fuel tendency is plotted as a dashed green line. The sum of individual tendencies (red, blue and green lines) is equal to the total tendency (black line). Error bars represent the root mean squared error for the two years of averaging used. Taken from Parazoo et al., [2011]

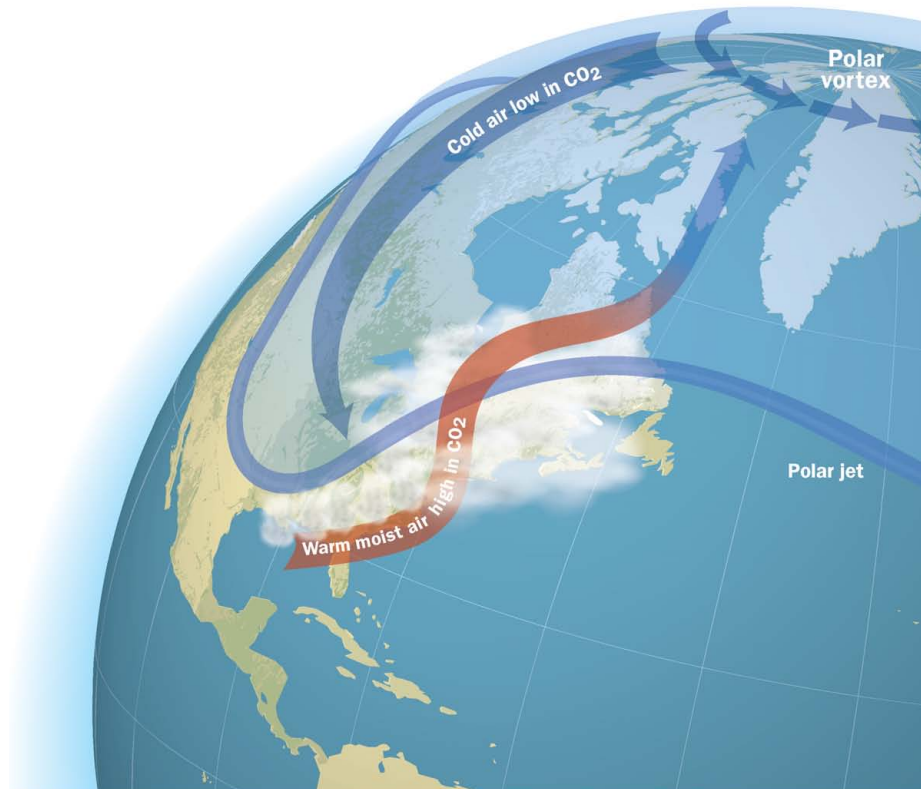


Figure 3.17: Illustration of important CO₂ transport mechanisms associated with a baroclinic wave. Adapted from Parazoo et al. [2011]

latitudes. Poleward flow of warm moist air, high in CO₂ relative to high latitudes, is swept along moist isentropic surfaces along the east side of baroclinic waves. As this air is forced up over the polar front along the mid-latitude stormtrack, high CO₂ air is dumped into the polar vortex and a huge comma-shaped cloud forms. Poleward flow is compensated by equatorward flow of cold dry air, low in CO₂ relative to low latitudes. This air descends from high polar altitudes into lower latitudes from the vortex along the surface in the western trough portion of the baroclinic wave. Mean polar flow, not depicted graphically in this study, opposes transport by synoptic eddies with net equatorward transport of CO₂ during winter.

3.8 Discussion and Conclusions from Part 1

Synoptic weather systems transport a large amount of CO₂ north and south in mid-latitudes, up to 1 PgC month⁻¹ during winter when baroclinic waves ramp up. As a result, seasonality is strongly damped in mid-latitudes and amplified in the Arctic. To put this in perspective, synoptic eddies transport more CO₂ out of mid-latitudes than is emitted by fossil fuels. Furthermore, simulations suggest that nearly one third of this transport is contained in clouds, which are a large source of uncertainty in most global models. The total amount of CO₂ transported by synoptic eddies is therefore most likely sensitive to model choice and should be better resolved as models become more skilled at representing important eddy processes such as frontal circulation, moist convection and precipitation. Because eddies mediate seasonality in northern latitudes, it is critical that inversion scientists (modelers and observationalists) consider seasonal meridional transport, and the underlying mechanisms, carefully.

Sensitivity of eddy transport to factors such as storm track position, seasonal tendencies in CO₂ mixing ratio and the pattern of seasonal change in surface CO₂ flux over the globe poses a challenging task for inversion modelers. Additionally, interpretation of synoptic variations in continental records requires accurate simulation of frontal weather systems [Geels et al., 2004; Wang et al., 2007; Parazoo et al., 2008] and moist conveyors. As discussed in Chapter 3 and by Corbin et al. [2006], moist processes associated with synoptic weather systems hide much of the dynamics from satellites, and likely from other observing systems [e.g., aircraft flask samples, Stephens et al., 2007]. Additionally, warm conveyors transport CO₂ and other trace gases into the polar vortex where they are more likely to be hidden from passive satellite instruments during polar winter. Continuous in-situ records can supplement airborne and remotely observed measurements during inclement weather, but only at a few locations. This fair-weather bias in measurements puts stringent requirements on models of moist transport. We therefore recommend that inversion modelers pay special attention to modeling of wet synoptic storms in addition to in-situ and satellite observations, with particular attention given to factors such as grid spacing (e.g., frontal circulations

better resolved with finer grid spacing), representation of moist convection along fronts and within the warm sector of cyclones, and assimilation of observations of moisture. Simulations using multi-scale modeling frameworks such as the Goddard MMF [Tao et al., 2009] are a feasible approach in the short term for improving the representation of CO₂ transport by moist processes.

Regional inversion modelers in particular should pay special attention to the vast amounts of seasonal transport by synoptic storms. It is important to correctly represent large-scale meridional CO₂ gradients flowing over regional domains because interaction with synoptic waves generates a source of variability that may confound flux attribution [Keppel-Aleks et al., 2010]. It is not surprising, given the unobserved and unresolved nature of moist synoptic transport, that Schuh et al. [2010] find that the annual sink over N. A. varies by ~30% when lateral boundary conditions are prescribed from two different global transport models. Because of large meridional transport by synoptic eddies, regional inversions should carefully account for meridional advection at north and south borders when prescribing lateral boundary conditions.

Furthermore, it is possible that interannual variability in eddy (or mean) transport, in response for example to teleconnection patterns such as the North Atlantic Oscillation [e.g., Hurrell, 1995], has contributed to trends in CO₂ seasonality in the Arctic [e.g., Keeling et al., 1996; Randerson et al., 1997]. Keeling et al. [1996] reported that the seasonal cycle of CO₂ increased in amplitude by 40% in the Arctic from the early 1960's to the mid-90's. While the study also provided evidence that increased seasonality is linked to global warming and increased uptake by plants, a subsequent investigation by Randerson et al. [1997] showed that such large trends in uptake couldn't be explained by CO₂ fertilization alone, and that other processes must also contribute. Given the large year-to-year changes in the amount of mass transported back and forth between middle and polar latitudes, and the possible link between global warming, NAO index, and winter storm strength, it is reasonable to expect that trends in seasonal exchange of CO₂ between middle and polar latitudes may contribute to trends in seasonal CO₂ in the Arctic. While such analysis is beyond the scope of this study, it is an excellent topic for future studies.

Finally, it is worth exploring in more detail to what degree synoptic transport into the polar vortex influences equatorward moving air at a later point in time. Previous studies show that point emissions of tracer can scatter widely north, south, and across ocean basins through interaction with baroclinic waves [e.g., Cooper et al., 2001, 2004]. It is common, for example, for baroclinic waves to advect polluted Asian air into the Arctic. A portion of this air is advected back south into N. A. with the same system, but the rest mixes in the polar vortex. Counter to intuition CO₂ anomalies in air arriving at mid-latitude sites from the north may actually reflect fluxes that occurred earlier to the south, and mixing with the polar vortex scrambles any coherent link between the longitudinal origin of poleward and equatorward moving air.

Chapter 4

SENSITIVITY OF MOIST SYNOPTIC TRANSPORT OF CO₂ TO CHANGING METEOROLOGICAL DATA

Part 1 of this study, presented in Chapter 3, showed that CO₂ transport by moist synoptic storms in northern mid-latitudes is significant and intimately tied to frontal and moist processes. Because of much of the transport by synoptic eddies is tied up in clouds and moist processes, which are typically poorly resolved in global models, a significant portion of eddy transport (approximately one-third) is likely to be poorly represented in most global transport models and systematically unobserved by satellites. Because a much of CO₂ transport is unobserved, there is need for models of moist transport to represent synoptic transport processes with high fidelity. Part 2 of this study seeks to quantify the total difference in CO₂ transport by moist synoptic storms using several different transport formulations. Of particular interest is sensitivity of meridional transport by synoptic storms to grid spacing and fine-scale vertical mixing by moist convection and PBL turbulence. It is entirely possible that transport differences exist but are mostly random and largely cancel out over long enough time scales. It is just as likely, however, that systematic transport differences exist, in which case transport errors are more prone to be aliased into inverse estimates of CO₂ flux.

In order to quantify uncertainty associated with resolved and unresolved synoptic processes, I include analysis of meridional transport of seasonally varying CO₂ using a global transport model, identical surface fluxes and initial conditions, and transport driven by four reanalysis products from GEOS-DAS (described in Chapter 2.3). Using a common transport model (PCTM), transport differences arise strictly from differences in meteorological forcing and grid, unlike in some previous

studies such as TransCom which also differ in transport algorithms. With confirmation in Chapter 3 of the importance of moist synoptic processes for carbon transport, transport is diagnosed strictly along θ_e surfaces.

4.1 Introduction

Model projections of climate change depend critically on accurate predictions of carbon sources and sinks [Friedlingstein et al., 2006; IPCC, 2007]. Inverse methods combine information from atmospheric models and CO₂ mixing ratio measurements to provide process-based and observed constraint to source and sink estimates. This “top-down” approach is useful at global scales but mostly unsuccessful to date at regional scales where information about underlying processes is contained [Baker et al., 2006]. While in-situ and spaced-based measurement constraints have improved in quantity and quality in recent years, strong sensitivity to transport error continues to be a key limitation at regional scales [Gurney et al., 2004; Houweling et al., 2010]. For example, seasonal and diurnal covariance between ecosystem metabolism and vertical transport in the atmosphere is a strong determinant of vertical structure in CO₂ (the CO₂ “rectifier effect,” Denning et al. [1995, 1996, 1999]). Numerical treatment of subgrid-scale vertical mixing is a leading source of uncertainty in CO₂ inverse models [Denning et al., 1999; Yi et al., 2004; Helliker et al., 2004; Baker et al., 2005; Yang et al., 2007; Stephens et al., 2007]. As discussed in Chapter 3, transport by baroclinic waves is another process that controls the distribution of CO₂ on seasonal time scales.

The global CO₂ observing system has grown to include continuous records at continental locations close to terrestrial sources. These records allow quantitative flux estimation at finer spatial scales than previously possible [e.g., Law et al., 2003; Peylin et al., 2005; Zupanski et al., 2007; Lauvaux et al., 2008; Schuh et al., 2009], but feature much greater variance at synoptic scales. Interpretations of these variations require accurate simulation of structure, timing, and vertical motions associated with synoptic waves and frontal weather systems [Geels et al., 2004; Hurwitz et al., 2004; Wang et al., 2007; Parazoo et al., 2008].

Tracer transport by baroclinic waves is associated with large- and small-scale features. Representation of large-scale features (~ 1000 km's) in numerical models, such as the position and timing of a baroclinic wave, is strongly dependent on grid spacing, with finer grid spacing leading to improved representation of features within a wave. Model inter-comparison studies show that simulations at higher spatial resolution produce better match with observed synoptic variations at northern mid-latitudes sites [Geels et al., 2007; Patra et al., 2008; Ahmadov et al., 2009].

Unfortunately, certain features associated with synoptic waves occur at scales smaller than most global inverse models (1° globally or coarser, ~ 100 km) can resolve. Frontal ascent of tracer, for example, is typically confined to a 60 km wide region [Donnel et al., 2001], is therefore unresolved down to grid spacing of 10 km or less (assuming at least 6 grid points are needed to sufficiently resolve atmospheric features). Additionally, transport by moist convection and turbulent mixing typically occur at scales smaller (< 10 km) than most atmospheric models can resolve. These processes are solved instead through parameterization, which is highly variable between models, not as easily constrained in meteorological reanalysis as resolvable flows, and therefore highly uncertain. It is unclear what role slantwise vertical transport by synoptic storms plays in top-down CO_2 flux estimates, but because vertical mixing, surface CO_2 flux intensity, and CO_2 spatial gradients are tightly linked in inverse calculations, errors in vertical mixing translate into errors in vertical CO_2 distribution and thus CO_2 flux estimates [Stephens et al., 2007]. For example, models in TransCom3 that trap more CO_2 near the surface due to weak vertical mixing tend to have larger estimates of the strength of the NH terrestrial sink.

In the era of remotely-sensed observations of trace gas from satellites, an additional complication arises because the strongest horizontal gradients in CO_2 occur along frontal boundaries that are typically hidden from orbital sensors by clouds [Corbin et al., 2006]. Corbin et al. [2008] analyzed simulated column-mean CO_2 using a clear-sky sampling regime along hypothetical satellite orbits and found that systematic sampling errors of up to 1.5 ppm in the seasonal mean were caused by cloud masking of frontal CO_2 gradients. Covariance of synoptic transport with surface CO_2 flux

is likely to cause errors in top-down flux estimates if not represented correctly in transport models. Since a portion of the synoptic signal is unobserved, it is important to quantify model sensitivity to these processes, especially if eddy CO₂ transport out of northern mid-latitudes (meridional eddy CO₂ flux is proportional to all of worlds fossil fuel emissions) is as strong as suggested by model estimates in Chapter 3.

Model-intercomparisons that use a common experimental protocol are a useful way to evaluate model sensitivity of eddy CO₂ transport to model parameters. To test for sensitivity to meteorological forcing, forward simulations of CO₂ are run using a common tracer transport model (PCTM) and identical surface fluxes, but with transport driven by four reanalysis products from GEOS-DAS. Mass fluxes of CO₂ are calculated on θ_e from the four reanalysis products (discussed in Chapter 2.3) and corresponding CO₂ distributions (as determined by PCTM), and then decomposed into mean and eddy components to isolate transport by synoptic storms in the eddy term. Model sensitivity to synoptic storms is quantified as the model spread (in units of PgC) in the diagnostic eddy transport calculations.

I also attempt to explain the resulting model spread of eddy transport as a function of key differences between reanalysis products. As discussed in Section 2.3, these products are different primarily in (1) native grid spacing and (2) physical parameterization of sub-grid scale vertical mixing. This experiment therefore aims to isolate differences in grid spacing and vertical mixing as the primary cause of differences in eddy CO₂ transport.

Large sensitivity of simulated eddy CO₂ transport to meteorological forcing motivates the use of inversion framework to test the effect of transport sensitivity on CO₂ flux estimation (see Chapter 5). This effort is of little use to model developers, however, unless an estimate of model fidelity in simulating synoptic scale variability of CO₂ is provided. A small section of this Chapter is reserved for comparison CO₂ output from PCTM to observed variations. In particular, these comparisons provide (1) a diagnostic for the accuracy of transport simulations and (2) indication that model uncertainty in eddy transport is a result of improved representation and resolution of

physical processes as models move towards higher fidelity. Because the strongest variability, and likely strongest model sensitivity, tends to occur within the PBL, model comparisons are made to well-calibrated in-situ measurement sites at northern mid-latitude continental (close to terrestrial CO₂ flux) and remote (far from terrestrial CO₂ flux) locations. The 12 sites chosen for this study are described in more detail in Parazoo et al. [2008]. Lag-correlations are used as a measure of correlation and timing (or phase) of synoptic variations. Hourly data is used, and seasonal and diurnal variations are removed from time series of modeled and observed CO₂ using a butterworth filter.

This Chapter is organized as follows. Model-observation comparison is shown in Section 4.2. Discussion of transport sensitivity is the primary focus of the first half of Section 4.3. This research also seeks to identify key differences between models that may be responsible for uncertainties in eddy transport. Possible explanations for transport uncertainty are discussed in the latter half of Section 4.4. Discussion and concluding remarks are provided in Section 4.5.

4.2 Comparison to Observations

Modeled variability at synoptic scale is fairly well correlated with observations at zero time lag with an average correlation among all sites and models of $r=0.496$ (see Figure 4.1). The strongest correlations occur at remote sites (ZEP, PAL; $r=0.66$) and coastal sites (MHD, SBL; $r=0.64$). Weaker correlations occur over continental terrestrial sites (e.g., LEF, CDL, and WPL), which tend to be more sensitive to surface fluxes. Overall correlations vary only slightly between models, with $r = 0.476$ for GEOS4-2.5x2, $r = 0.482$ for GEOS4-1.25x1, $r = 0.509$ for GEOS5-1.25x1, and $r = 0.517$ for GEOS5-0.67x0.5, although model dependence of correlation is probably better interpreted on a site-to-site basis. Relative to a select set of continuous observations, day-to-day variability is generally more realistic in GEOS5-0.67x0.5.

These plots provide little indication of the amplitude of day-to-day variability at these locations. To demonstrate amplitude differences between models relative to observations, modeled

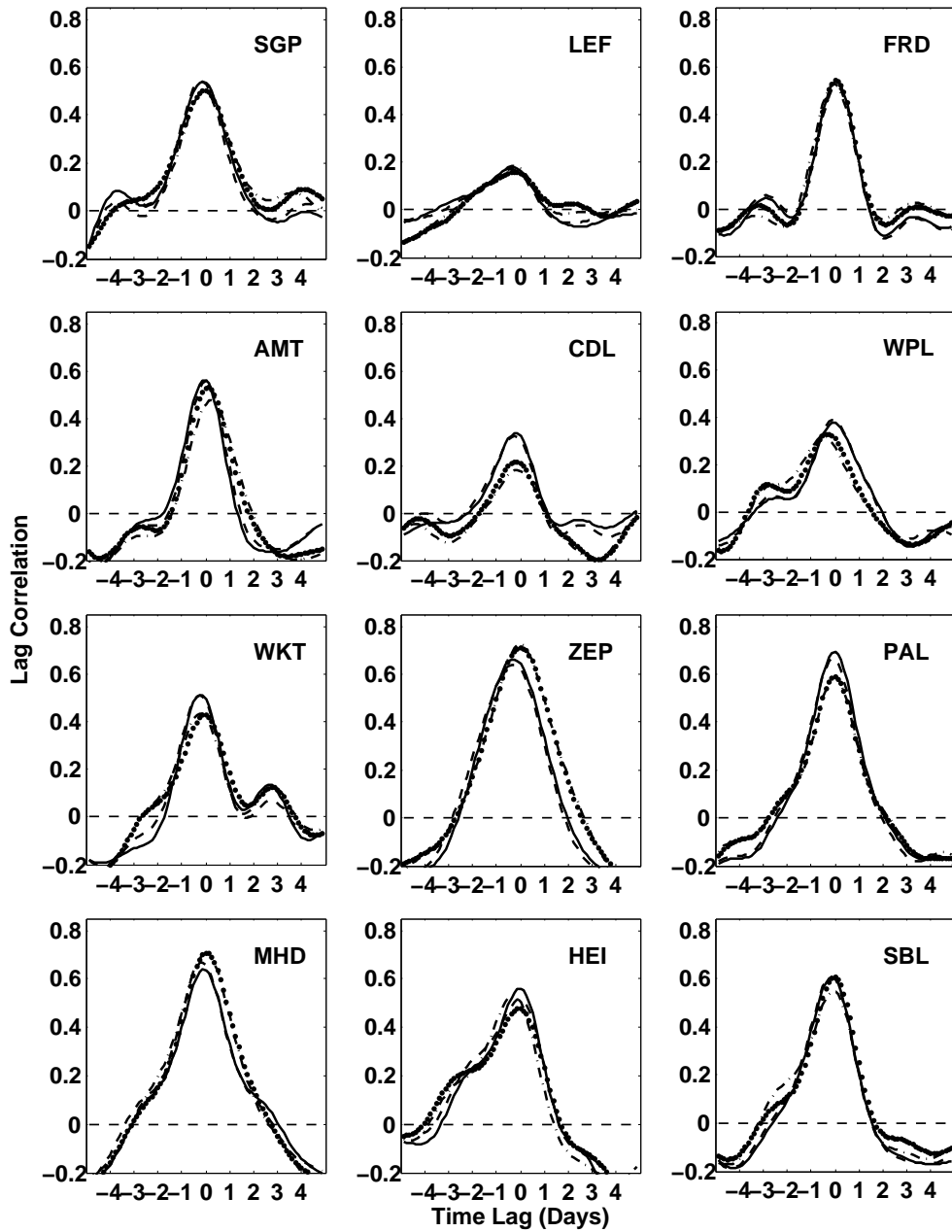


Figure 4.1: Lag Correlations between model and observations at mid-latitude sites in North America and Europe. The four line styles refers to the model used in the correlation, where GEOS5-0.67x0.5 is solid, GEOS5-1.25x1 as dashed, GEOS4-1.25x1 is dotted, and GEOS4-2.5x2 is dash-dotted. These same line styles are used in the remaining figures in the Chapter.

and observed surface CO₂ mixing ratios are plotted for a 30-day period in January 2005 at LEF in Figure 4.2. While the timing and structure of synoptic features is consistent between models and

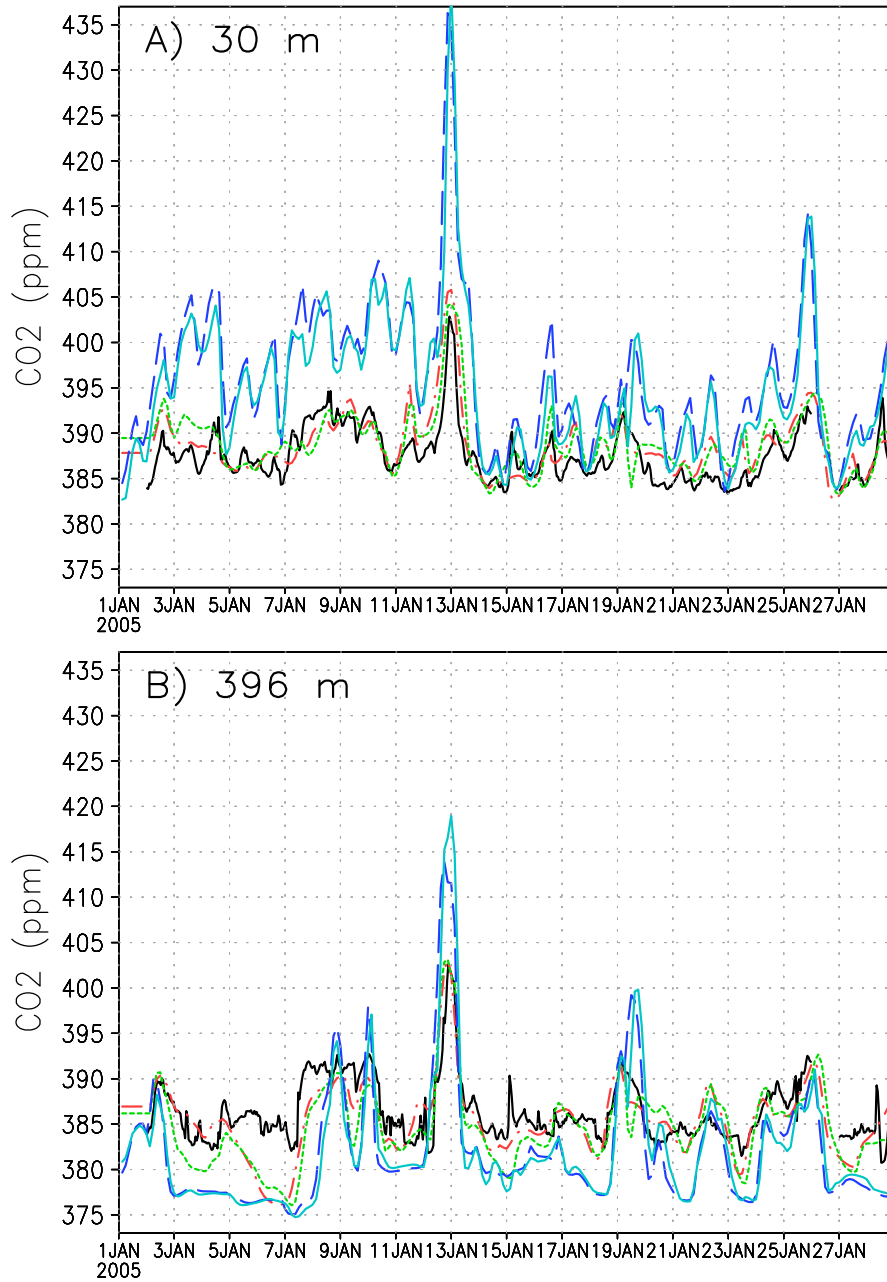


Figure 4.2: Modeled and observed CO₂ mixing ratio from January 1-30, 2005 at a site in northern Wisconsin (LEF) (A) 30 m above the surface (lowest model level, 50 m) and (B) 396 m above the surface (3rd model level in GEOS4 and 5th model level in GEOS5, ~ 500 m). Observations are plotted in black. Line styles for models are the same as in Figure 4.1

observations at 30 m and 396 m above the surface, the amplitude of GEOS5 is significantly over-estimated relative to observations, while GEOS4 is more in line with the observed amplitude. In GEOS5, CO₂ is high near the surface (relative to observations at 30 m) and low at the fifth model level (relative to observations at 396 m); this suggests that GEOS5 is sufficiently mixing CO₂ out of the boundary layer.

Although more extensive analysis of model spread in amplitude and correlation relative to observations would be useful, I will cut off the analysis here and summarize by mentioning that these strong differences in amplitude occur at most of the other mid-latitude and boreal sites during winter, especially at higher latitudes, but that model error in amplitude is significantly smaller during summer. Differences due to surface fluxes have been eliminated through the use of a common surface flux between models; model-to-model differences can be explained only by differences in transport. Whether model-to-model differences in correlation and amplitude at synoptic timescales can be attributed to differences in a certain feature of atmospheric transport (transport by eddies vs mean circulations), and more specifically to differences to vertical mixing and grid spacing, is the subject of the remainder of this Chapter.

4.3 Model Differences in CO₂ Transport by Eddy and Mean Circulations

Total column transport in the annual mean is approximately conserved between models (a small exception exists at low latitudes), with net northward transport north of 50°N and net southward transport south of 50°N (Figure 4.3A). Eddy transport is poleward in both hemispheres and opposed by mean transport, which is strongly southward in northern latitudes in the annual mean. Eddy and mean transport peak in northern mid-latitudes, consistent with strong terrestrial breathing of the planet and industrial emissions, and during boreal winter when baroclinic waves are most active. Mean transport in the column is a small residual of cancellation between strong poleward transport aloft and equatorward transport near the surface; eddy transport is weak but poleward through most of the troposphere and hence is of same order of magnitude as due to the mean merid-

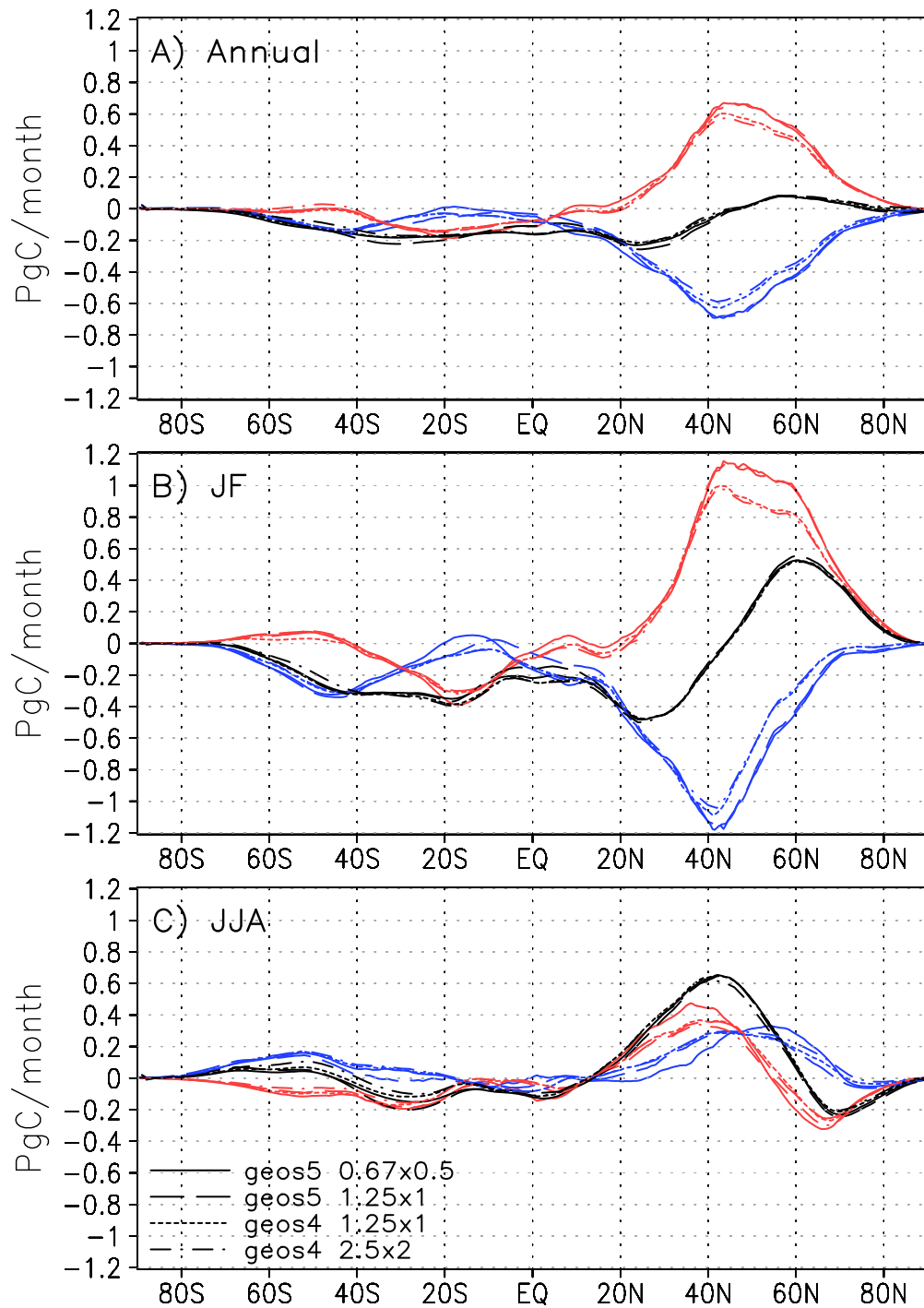


Figure 4.3: Total column integrated CO₂ transport (black) partitioned into transport by the mean circulation (blue) and synoptic eddies (baroclinic + stationary waves, red) in the annual mean (A) and during boreal winter (Jan-Feb, B) and summer (Jun-Jul-Aug, C).

ional circulation in the vertical integral [Parazoo et al., 2011].

There are important differences in model partitioning of meridional transport into eddy and mean components. Eddy transport differences between GEOS4 and GEOS5 are as large as $0.1 \text{ PgC month}^{-1}$ from $40\text{-}60^\circ\text{N}$ in the annual mean (Figure 4.3A), representing difference of 15-20% relative to peak transport. Seasonal differences are sometimes twice as large; for example, differences up to $0.2 \text{ PgC month}^{-1}$ from $40\text{-}60^\circ\text{N}$ occur during boreal winter (Figure 4.3B) and $0.2 \text{ PgC month}^{-1}$ from $35\text{-}40^\circ\text{N}$ during boreal summer (Figure 4.3C). Eddy transport is weaker in GEOS4 than GEOS5 and weakest in GEOS4-2.5x2. Eddy transport differences between the two GEOS4 resolutions and between the two GEOS5 resolutions are generally small in mid-latitudes. To conserve total meridional transport in the column, increased northward eddy transport (for example in GEOS5) is compensated by increased southward mean transport at the same latitude.

The contribution of eddies to seasonal tendencies of CO_2 in the Arctic (defined as $70\text{-}90^\circ\text{N}$, tendencies have units of ppm month^{-1}) is shown in Figure 4.4A. Since eddy tendencies are calculated for the polar cap, with meridional exchange occurring with mid-latitudes at 70°N , positive tendencies represent net eddy transport from mid-latitudes into the Arctic (vice versa for negative tendencies). Model differences of $\sim 1 \text{ ppm month}^{-1}$ occur throughout the year, with all models contributing positively from September-May and negatively from June-August. Eddy exchange between middle and polar latitudes is strongest in GEOS5-0.67x0.5 during all months, and therefore contributes most strongly to seasonality in the Arctic. The weakest eddy exchange occurs in GEOS4 during winter and in GEOS4-1.25x1 and GEOS5-1.25x1 during summer.

Model differences are smaller in magnitude ($\sim 0.5 \text{ ppm month}^{-1}$) in mid-latitudes ($30\text{-}70^\circ\text{N}$) but account for a larger percentage of total eddy transport (Figure 4.4B). Unlike the Arctic, where net meridional exchange occurs only at the southern boundary (i.e., 70°N), mid-latitude exchange occurs at two boundaries (30°N and 70°N). Caution must therefore be taken when interpreting the cause of mid-latitude tendencies; positive tendencies, for example, can result from equatorward transport out of the Arctic and/or poleward transport out of mid-latitudes. As in the Arctic, eddy

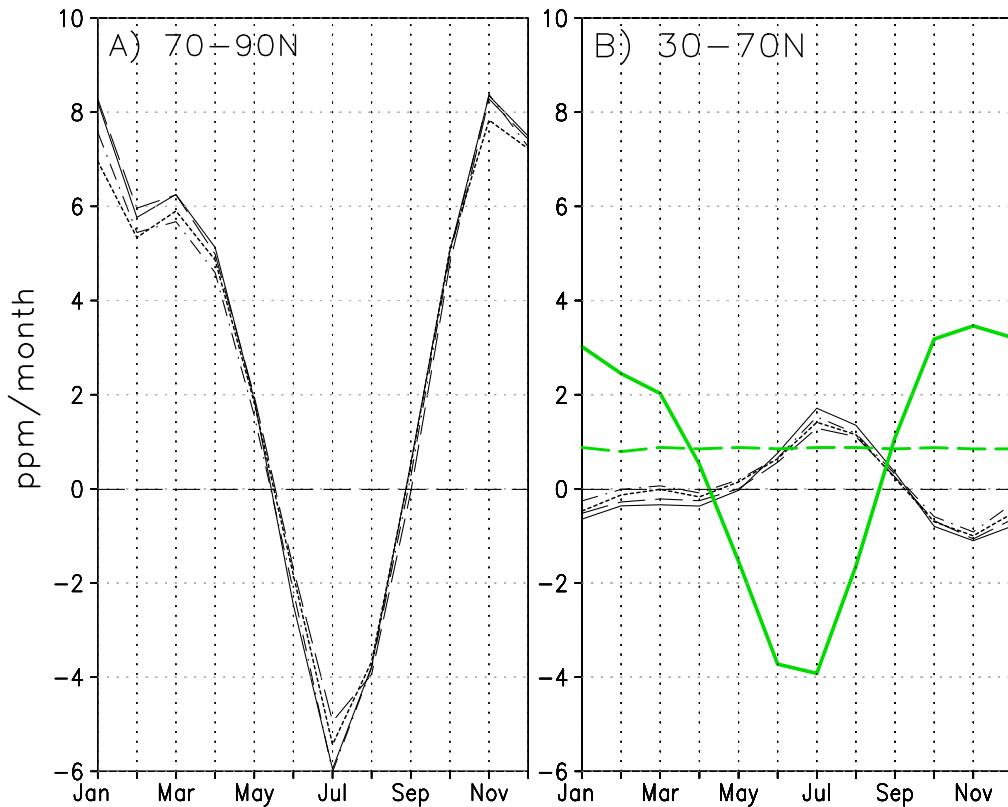


Figure 4.4: Column integrated seasonal CO₂ budget tendencies (ppm month⁻¹) for eddies binned into high latitudes (70-90°N, A) and mid-latitudes (30-70°N, B). Tendencies due to total surface flux (green solid) and fossil fuel emissions (green dashed) are shown in (B).

transport is strongest in GEOS5-0.67x0.5, with peak positive tendencies in July of ~ 1.75 ppm month⁻¹ and peak negative tendencies during November of ~ 1.1 ppm month⁻¹. In all model cases, eddy transport is weakest from January to April, with tendencies of ~ 0.5 ppm month⁻¹ in GEOS5-0.67x0.5 but zero net tendency in GEOS4-2.5x2. Put another way, coarse grid models (such as GEOS4-2.5x2) suggest zero net eddy transport out of mid-latitudes (poleward transport at 30°N equals poleward transport at 70°N) during the first third of the year while the finer grid model (such as GEOS5-0.67x0.5) suggest up to 0.5 ppm month⁻¹ net eddy transport out of mid-latitudes.

Model dependence of transport out of mid-latitudes by differential eddy transport at the north and south “borders” is likely to be misinterpreted by regional inverse models if north and south lateral boundary conditions aren’t properly accounted for; this is because CO₂ mixing ratios observed

within a regional domain have contributions from outside the domain, and will therefore be attributed to the incorrect fluxes within the domain. It is even worse considering that the tendency due to eddies is sometimes twice the fossil fuel signal ($0.9 \text{ ppm month}^{-1}$, dashed green line in Figure 4.4B). For example, transport by GEOS5-0.67x0.5 is nearly $1.75 \text{ ppm month}^{-1}$ during July alone. *The large tendency due to eddies requires model fidelity in handling atmospheric mixing at synoptic scales; unfortunately, even models of very similar architecture experience eddy transport differences of up to $0.5 \text{ ppm month}^{-1}$, or half the tendency due to fossil fuels, for much of the year.*

Synoptic eddies are composed of transient and stationary waves. The primary difference is that stationary waves are anchored geographically by season while transient waves arise from baroclinic instability within stationary waves. Because baroclinic instability in transient waves leads to fine scale circulations which may be unresolved and moist processes (such as convection) which must often be parameterized, transport by transient waves is more uncertain than stationary waves. In this study, this uncertainty arises primarily from differences in grid spacing and vertical mixing schemes. To determine if there is indeed more uncertainty in transient waves than in stationary waves, annual and seasonal mean transport by each component is plotted in Figure 4.5.

Transient and stationary waves transport CO_2 poleward in the annual mean (Figure 4.5A), with peak transport by transient waves near 40°N and stationary waves near 55°N . Transient waves dominate the total eddy signal from $30\text{-}60^\circ\text{N}$ in the annual mean (Figure 4.5A), with peak transport during winter (Figure 4.5B). During summer (Figure 4.5C) there is convergence of CO_2 near 50°N due to poleward transport from the south and equatorward transport from the north. This convergence is coincident with peak biological uptake (see Figure 3.5B). Transport by transient waves from $40\text{-}60^\circ\text{N}$ increases by $\sim 0.08 \text{ PgC month}^{-1}$ from GEOS4-2.5x2 to GEOS5-0.67x0.5 in the annual mean, with differences between GEOS4 models and GEOS5 models ~ 0.02 and $\sim 0.04 \text{ PgC month}^{-1}$, respectively. Transport differences are as large as $\sim 0.15 \text{ PgC month}^{-1}$ from $40\text{-}60^\circ\text{N}$ during winter and $\sim 0.11 \text{ PgC month}^{-1}$ from $60\text{-}70^\circ\text{N}$ during summer.

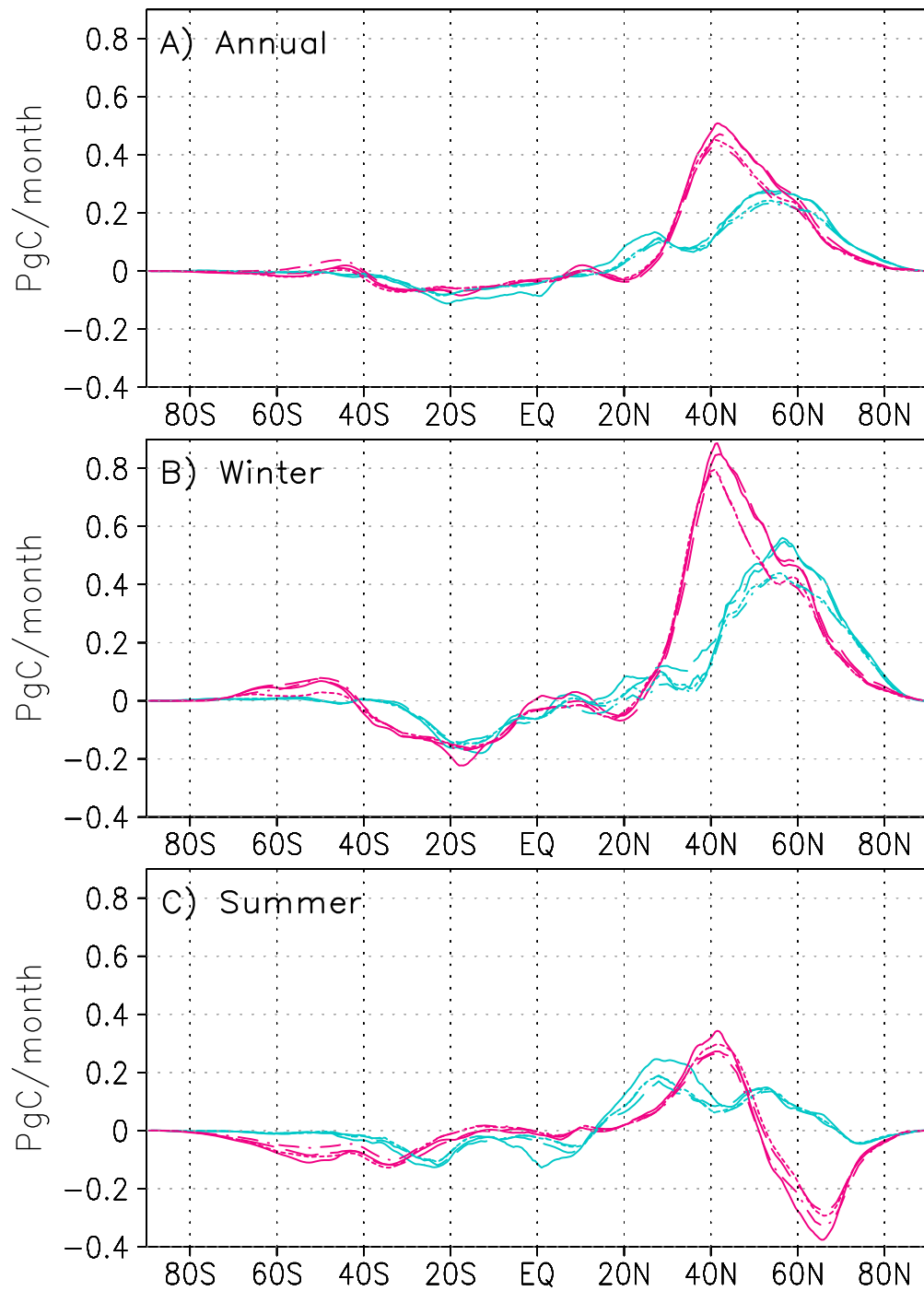


Figure 4.5: CO₂ transport by stationary waves (cyan) and baroclinic waves (magenta) along θ_e in the annual mean (A) and during boreal winter (B) and boreal summer (C).

Transport by stationary waves near 50°N increases by $\sim 0.05 \text{ PgC month}^{-1}$ from GEOS4-2.5x2 to GEOS5-0.67x0.5 in the annual mean (Figure 4.5A), with differences between GEOS4 models and GEOS5 models trivially small. Transport differences are as large as $\sim 0.15 \text{ PgC month}^{-1}$ from 50-70°N during winter and $\sim 0.11 \text{ PgC month}^{-1}$ near 30°N during summer (Figure 4.5C). ***Counter to my hypothesis, stationary waves experience a similar range of uncertainty as transient waves in this test.*** Although differences in total eddy transport between the GEOS5 models are small in the annual mean (Figure 4.3A), assessment of the transient and stationary wave components reveals that non-trivial differences (errors of up to 0.1 PgC/month, or 15% of annual fossil fuel emissions) exist in transient waves near peak amplitude (40°N) that largely cancel when added to stationary waves.

Eddy transport is stronger in the GEOS5 models, but comparison of horizontal structure reveals that geographic patterns and magnitudes of transport are very similar between models (Figure 4.6). In all models, patterns of eddy transport emerge over similar spatial scales (1000's km's) and regions. Comparison to a climatology of WCBs in Figure 3 of Eckhardt et al. [2004] suggests that dominant patterns of poleward eddy transport are coincident with climatologically favorable regions for WCBs. Like WCBs, CO₂ transport tends to follow a northward and eastward track originating in subtropical latitudes, peaking in mid-latitudes, and terminating 72 hours later to the east and toward the Arctic. The most favorable regions tend to originate over land (e.g., southern part of the United States and Tropical Asia) and terminate over the eastern portion of the adjacent ocean (e.g., Pacific and Atlantic Oceans, respectively). Strong eddy transport in Europe isn't consistent with the starting point for WCBs, but strong surface fluxes combined the migration of the North American WCB into Europe after 72 hours might explain this. The major difference in models is largely a result of differing magnitudes of transport in favorable synoptic regions, for example over Europe (GEOS5 models dominate) and boreal Canada (GEOS5-1.25x1 dominates).

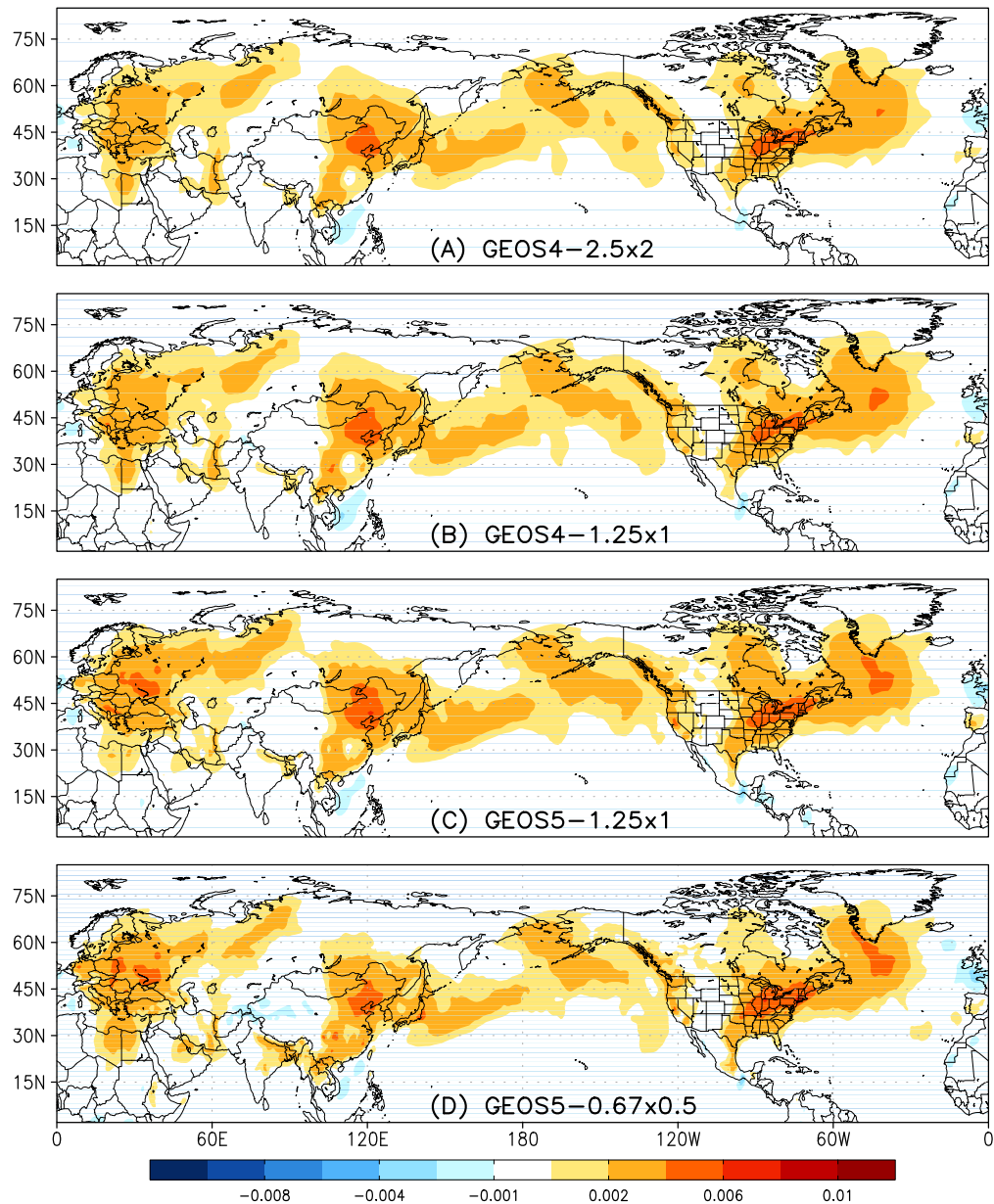


Figure 4.6: Spatial structure of annual mean column integrated CO_2 transport by synoptic eddies along θ_e for GEOS4-2.5x2 (A), GEOS4-1.25x1 (B), GEOS5-1.25x1 (C) and GEOS5-0.67x0.5 (D). The colorbar is shown in units of PgC month^{-1} .

4.4 Reasons for Model Differences in Eddy CO_2 Transport

Comparison of model characteristics helps explain uncertainty in model eddy transport. Because GEOS4 models differ only in horizontal grid spacing, the difference between GEOS4-2.5x2

and GEOS4-1.25x1, although small, can be explained purely due to regridding of GEOS4-1.25x1 to the coarser grid of GEOS4-2.5x2. Differences in transport between GEOS5 models can also be explained through differences in grid spacing, although data assimilation procedures (meteorology is reanalyzed in GEOS5-1.25x1 but only analyzed in GEOS5-0.67x0.5) and model updates between 5.1.0 and 5.2.0 (high latitude diurnal cycle) may also contribute. Transport differences between GEOS4-1.25x1 and GEOS5-1.25x1 are not as straightforward because several major differences between GEOS4 and GEOS5 exist. First, although grid spacing is the same in GEOS4-1.25x1 and GEOS5-1.25x1, the native grid of GEOS5-1.25x1 is $0.67^\circ \times 0.5^\circ$ (i.e., GEOS5-1.25x1 is run at $0.67^\circ \times 0.5^\circ$ with transport fields saved at reduced resolution). Second, there are differences in cumulus convection and cloud mixing parameterizations. Third, vertical resolution in the troposphere is nearly two times that of GEOS4. Fourth, the number and type of data assimilated per cycle is not consistent between models. Finally, data assimilation schemes are not the same.

Model differences due to data assimilation are not possible to test in this study because transport simulations are run offline from parent models. Differences due to grid spacing, however, are more straightforward to test. An example of the effect of grid spacing is shown in Figure 4.7. As discussed in the Introduction, large-scale features associated with synoptic waves and “CO₂ weather” show up in both fine and coarse grid models. GEOS5-0.67x0.5 (Figure 4.7A), however, does a much better job resolving finer scale features and magnitudes. The most obvious difference between models in this example is in Western Siberia where wave-like features associated with stronger horizontal gradients in column CO₂ occur in GEOS5-0.67x0.5, but are strongly smoothed in GEOS4-2.5x2. A similar effect is also seen in the N. Atlantic. Additionally, CO₂ tends to build up more in the column in the Amazon in GEOS5-0.67x0.5.

Although interactions with resolved scales is not straightforward to analyze, I can use the model to speculate about the effect of differences in vertical mixing due to cumulus convection and turbulent mixing on CO₂ transport. I start by looking at differences in vertical mass fluxes by cumulus convection and turbulent mixing in GEOS4 and GEOS5. These fluxes are plotted as a function of

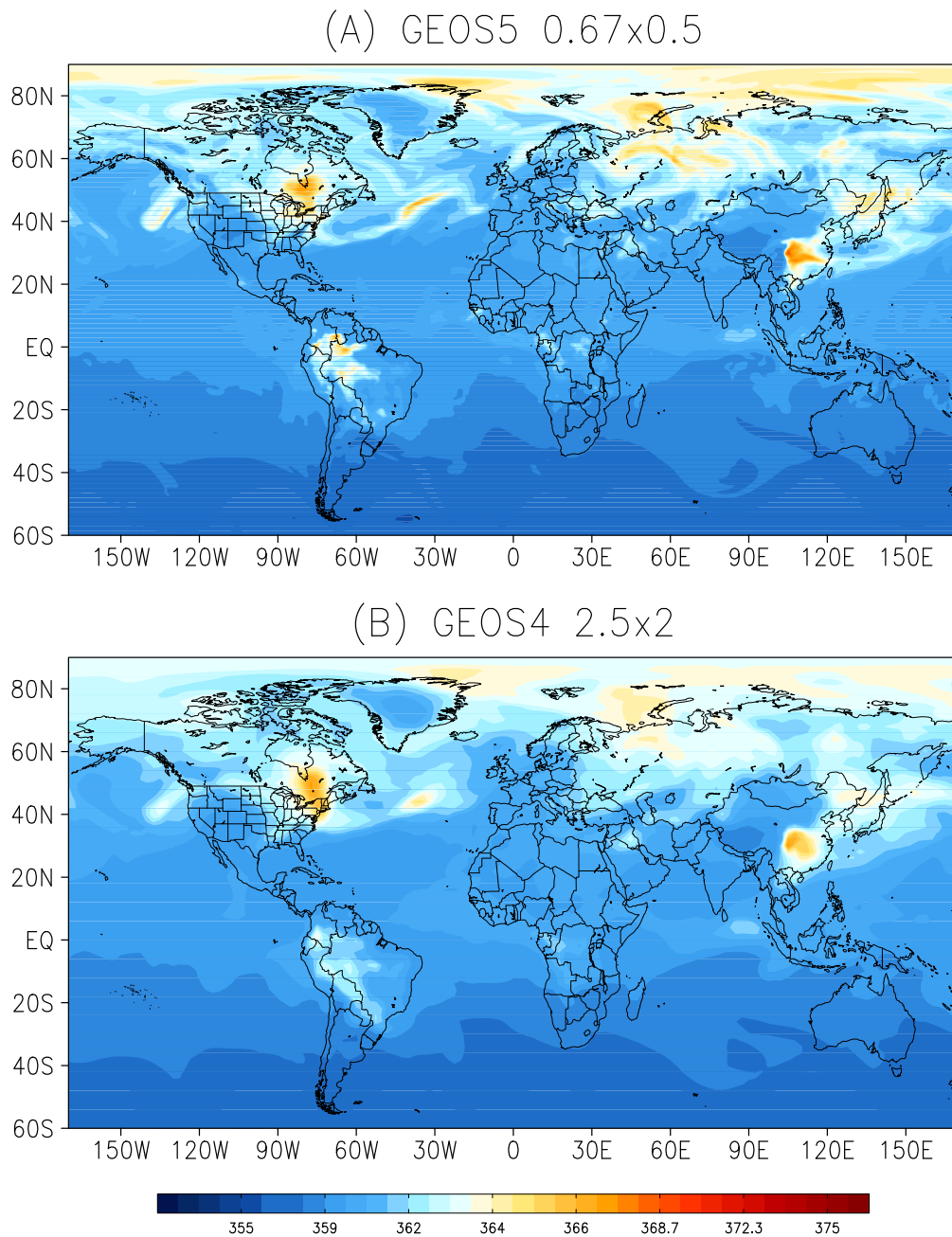


Figure 4.7: Column CO_2 snapshots on 10 January 2005 for GEOS5-0.67x0.5 (a) and GEOS4-2.5x2 (b)

η and averaged in northern mid-latitudes (30-70°N) in Figure 4.8. Turbulent mixing (Figure 4.8A) and cumulus convection (Figure 4.8B) in GEOS5 are consistently weaker than GEOS4 throughout the column in northern mid-latitudes, with cumulus mass flux nearly twice as weak. There are also

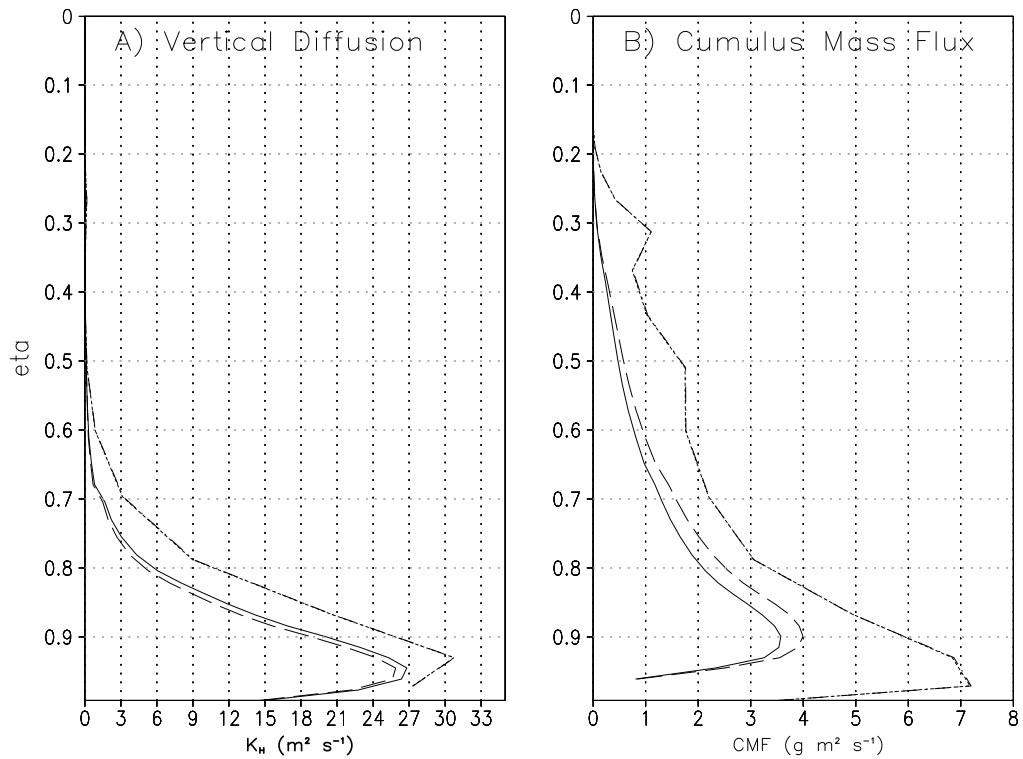


Figure 4.8: Zonal-annual mean values for vertical diffusion (A) and cumulus mass flux (B) binned into mid-latitudes (30-70°N) and plotted as a function of the terrain following coordinate η for each reanalysis product. These values are taken directly from the driver files used to force vertical mixing in PCTM. GEOS4 lines are identical and lie directly over one another.

smaller differences in vertical mixing between GEOS5-1.25x1 and GEOS5-0.67x0.5. Weak vertical mixing in mid-latitudes in GEOS5 is consistent with results published by Ott et al. [2009], who found that single column model application of RAS significantly underestimates convective mass flux relative to CRMs for several case studies of mid-latitude convective storms, resulting in weaker vertical transport of trace gases. The question is whether reduced vertical mixing in GEOS5 is a cause for enhanced meridional CO₂ transport from middle to polar latitudes.

Figure 4.9 shows model differences in annual mean CO₂ along η in northern mid-latitudes. The vertical gradient of CO₂ in the PBL from the surface to about $\eta = 0.7$ is stronger in GEOS5, where GEOS5 exceeds GEOS4 near the surface by 0.5-1.0 ppm with model convergence of CO₂ in the free troposphere. Weak vertical mixing in GEOS5 has likely trapped CO₂ in the PBL and en-

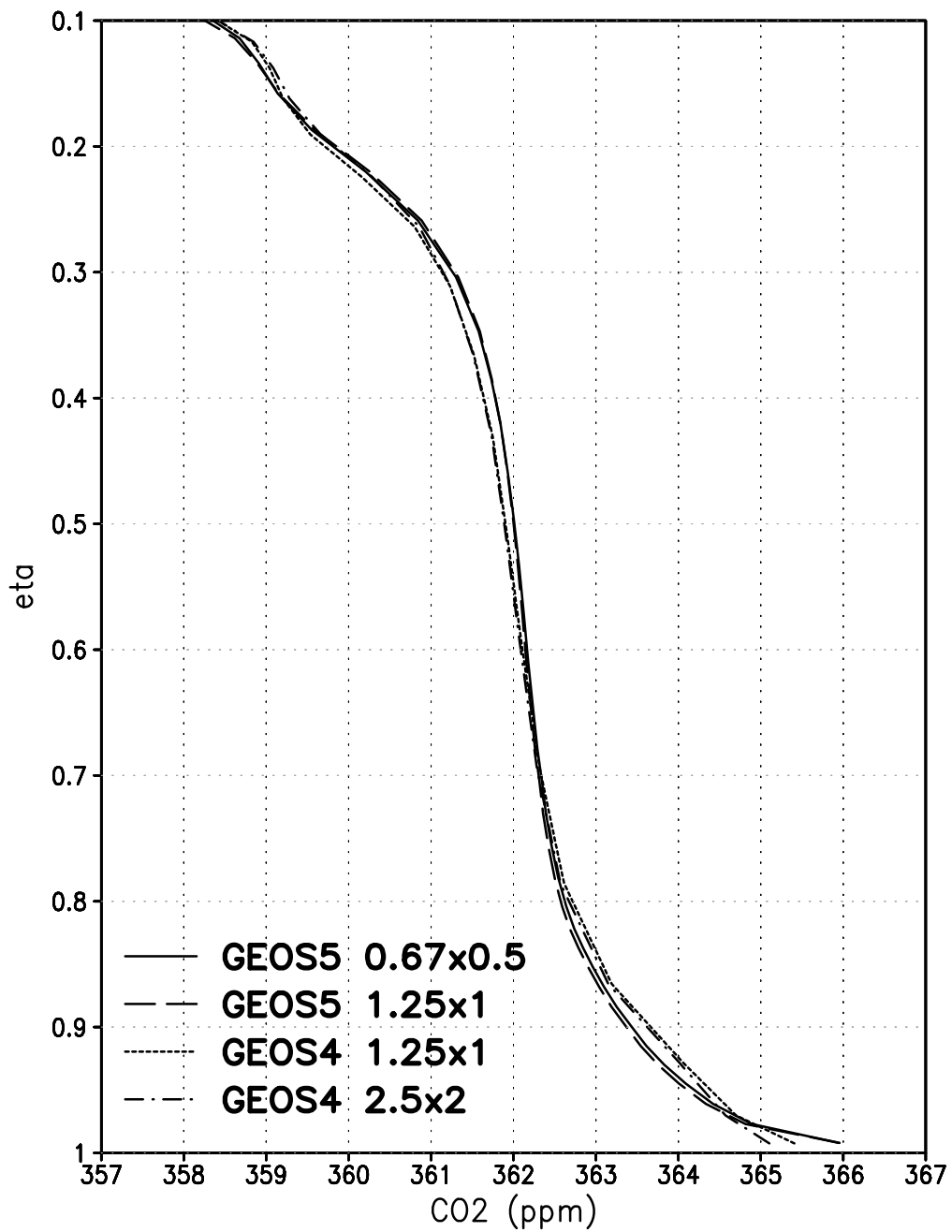


Figure 4.9: Zonal-annual mean CO₂ mixing ratio (ppm) binned into mid-latitudes (30-70°N) and plotted as a function of η .

hanced CO₂ variability near the surface. This increased variability, in turn, enhances the likelihood of strong temporal and zonal perturbation to CO₂, hence driving increased eddy transport out of the

PBL. Figure 4.10 shows that the difference in eddy transport between GEOS4-1.25x1 and GEOS5-1.25x1 lies primarily at lower levels, near $\theta_e = 270$ K, indication that eddy transport is stronger in GEOS5-1.25x1 near the surface.

Without isolating individual synoptic events, it is difficult to use these results to conclude which model factor (i.e. grid spacing or near-scale vertical mixing) is more important for enhanced eddy CO₂ transport in GEOS5 relative to GEOS4. However, the following implications regarding eddy CO₂ transport may be made. First, eddy CO₂ transport depends strongly on interactions of anomalous mass fluxes (weather) with vertical and horizontal CO₂ gradients. Results show that, on average, near-scale vertical mixing is weaker in GEOS5, with mixing by cumulus convection in GEOS5 about half that of GEOS4 and mixing by PBL turbulence only about 10% weaker, and that this is associated with stronger vertical gradients in CO₂. It is mixing of this background gradient by eddies that matters for eddy CO₂ transport. This leaves two possible explanations for enhanced eddy CO₂ transport in GEOS5: (1) the vertical CO₂ gradient is more than large enough to compensate for weak transport by cumulus convection in synoptic storms, or (2) it is not near-scale vertical mixing in extratropical cyclones that matters most for eddy CO₂ transport, but slow, slantwise ascent of CO₂ out of the PBL along moist isentropic surfaces, which occurs at larger scales than vertical mixing by cumulus convection and is therefore more likely to be resolved on the 50 km grid of GEOS5. Both of these explanations are plausible, and help explain how eddy CO₂ transport can be larger despite weaker near-scale vertical mixing. This also lends support to the argument that vertical and horizontal grid spacing matter for resolving transport by synoptic storms (although moist processes associated with slantwise ascent must still be parameterized). These results do imply, however, that synoptic storms feed strongly off vertical CO₂ gradients, and so it is important to represent near-scale vertical mixing correctly at the very least as a primer for transport by synoptic storms.

Differences in poleward flow of warm moist air out of the subtropics may also contribute to enhanced eddy CO₂ transport in GEOS5. Moist ascent in mid-latitudes is implied in arguments by Pauluis et al. [2008, 2009] that there is a large poleward transport of warm moist air out of

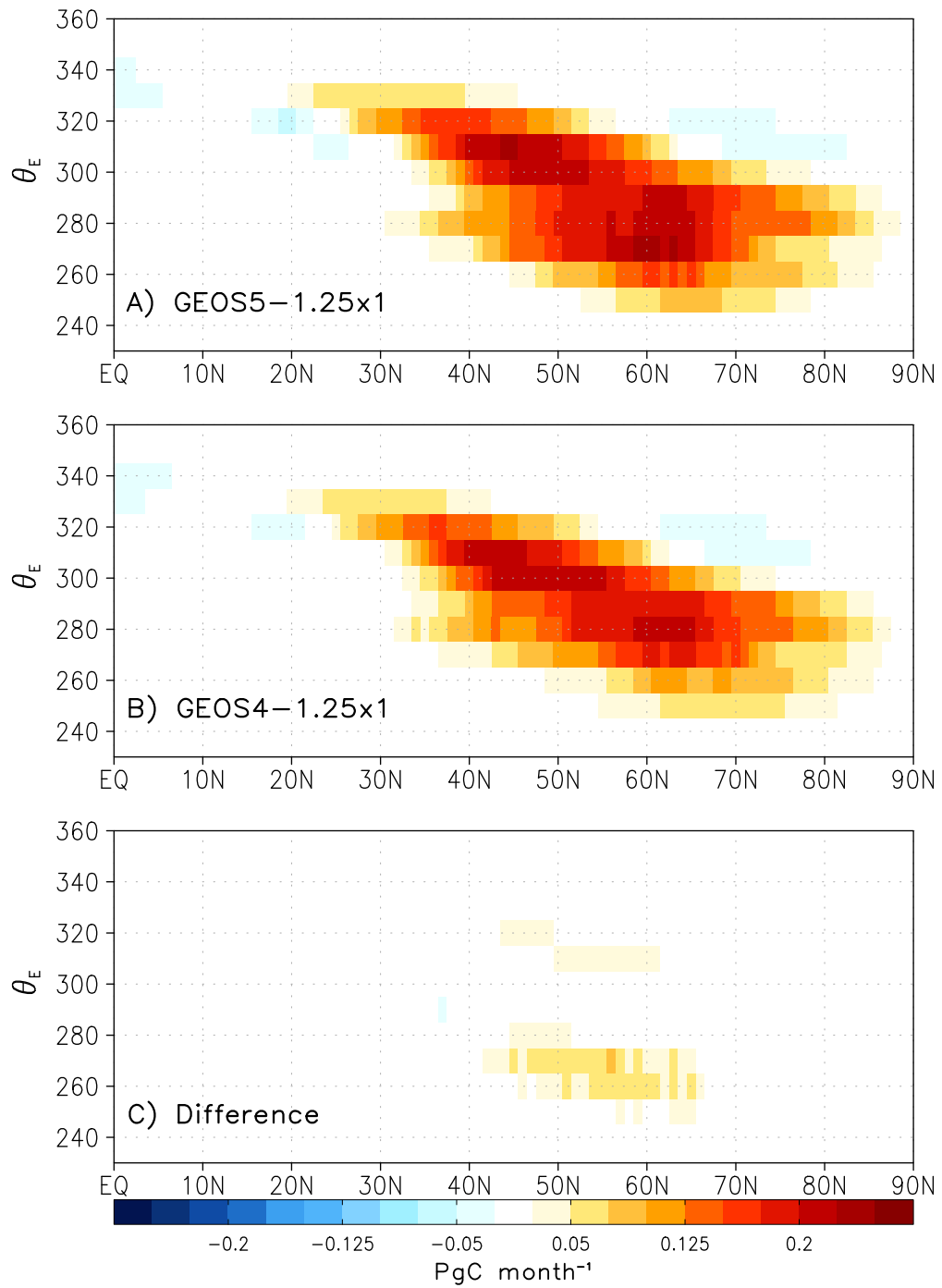


Figure 4.10: Eddy CO₂ transport by GEOS5-1.25x1 (A) and GEO4-1.25x1 (B). Difference in eddy transport between models are shown in (C).

the subtropics into mid-latitudes where air parcels become convectively unstable and ultimately saturated through poleward and upward flow through stormtracks. Figure 4.11 shows mass transport along three important airstreams of the general circulation: low-level flow of warm moist air (red line), low-level flow of cold dry air (blue line), and upper-level flow of warm dry air (black line). These airstreams are determined using the joint distribution of mass transport of dry and moist isentropes as described in Eqns. 5a-5c in Pauluis et al. [2009] and add to zero at every latitude.

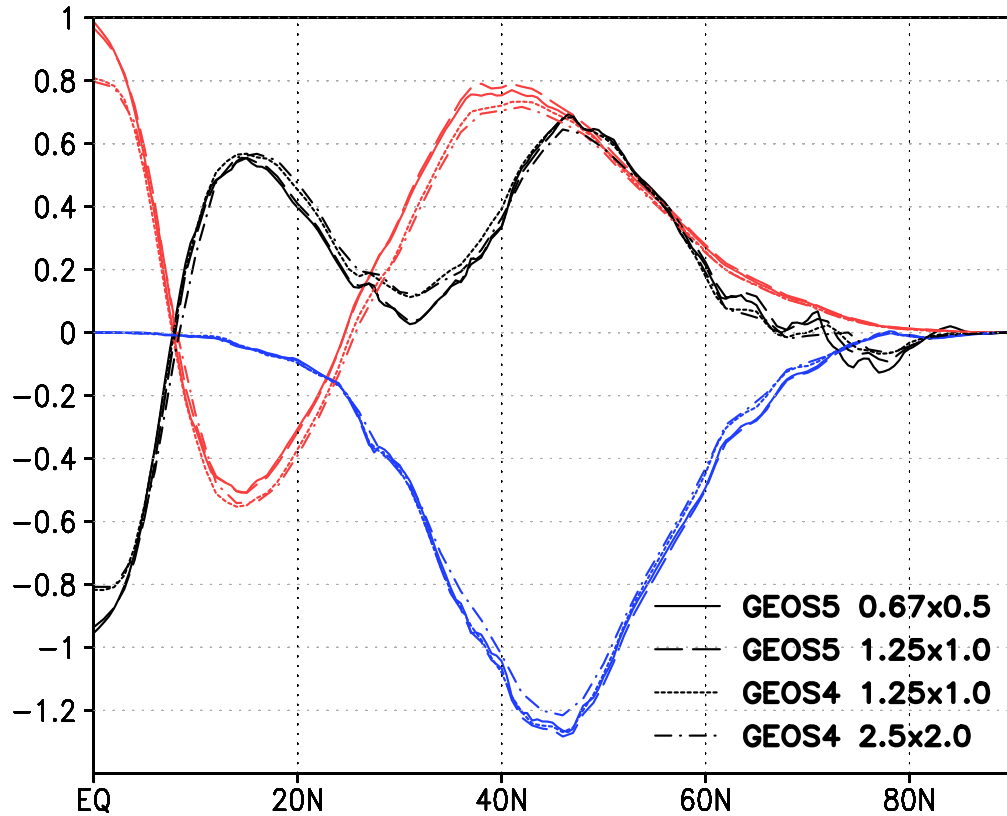


Figure 4.11: Mass transport of low-level cold dry air (blue line), low-level warm moist air (red line), and upper-level warm dry air (black line) as defined in Eqs. (5a)-(5c) of Pauluis et al. [2009].

The most important result in Figure 4.11 is the model difference in low-level poleward flow of warm moist air near 40°N. This airstream supplies much of the energy necessary for moist slantwise ascent within baroclinic eddies. This analysis suggests that GEOS5 transports more mass poleward along moist airstreams than GEOS4, and thus the moist circulation is stronger in GEOS5.

Strong poleward flow of warm moist air is compensated by strong equatorward flow of cold dry air. Since upward and poleward eddy transport of CO₂ is intimately tied to the moist circulation [e.g., Parazoo et al., 2011], a stronger moist circulation in GEOS5 (a likely result of new data assimilation techniques, number and type of data assimilated, and finer horizontal and vertical grid spacing in the parent grid) helps explain enhanced eddy transport of CO₂. Similarly, the stronger moist circulation in GEOS5-1.25x1 relative to GEOS5-0.67x0.5 (Figure 4.11) given the same mean vertical CO₂ profile (Figure 4.9) may help explain differences in transport by stationary and transient waves within GEOS5, with the difference in moist circulation explained by reanalysis of more observations in GEOS5-1.25x1 compared to GEOS5-0.67x0.5.

4.5 Discussion and Conclusions from Part 2

Eddy CO₂ transport from a global tracer model is analyzed using identical surface fluxes and tracer transport code, but with transport driven by four reanalysis products that differ primarily in (1) grid spacing and (2) fine-scale vertical mixing. Analysis on θ_e reveals differences at synoptic scales. Differences in eddy transport at northern mid-latitudes reach 0.1 PgC month⁻¹ in the annual mean and up to 0.2 PgC month⁻¹ during boreal winter and summer. The weakest overall eddy transport occurs in the coarsest resolution model GEOS4-2.5x2, which reduces transport (relative to GEOS5-0.67x0.5) out of mid-latitudes by as much as 0.5 ppm month⁻¹ and consequently reduces the eddy component of polar seasonality by as much as 1 ppm month⁻¹. These estimates of uncertainty in eddy transport are likely conservative given the use of identical model boundary conditions and similarity between analysis products. The tendency for eddy transport θ_e to decrease as grid spacing and fine-scale vertical mixing increase suggests that systematic differences between analysis products may result in persistent differences in tracer transport by moist synoptic storms.

Additionally, in the context of fossil fuel emissions these eddy transport differences are potentially significant. Fossil fuels are prescribed using the dataset described by Andres et al. [1996], which has a total global emission of 6.17 PgC year⁻¹, or ~ 0.5 PgC month⁻¹. With this dataset as

a reference, an annual mean eddy transport bias of $0.1 \text{ PgC month}^{-1}$ represents 20% of the global fossil fuel inventory and up to 40% when transport biases reach $0.2 \text{ PgC month}^{-1}$ during winter and summer. The problem is even worse relative to fossil fuel inventories in northern mid-latitudes. This uncertainty in eddy transport, combined with sensitivity of regional flux estimates to lateral boundary conditions [e.g., Schuh et al. 2010], requires that regional inversions carefully account for meridional advection at north and south boundaries, preferably using observed distributions of CO_2 at lateral boundaries.

In the same way that systematic model underestimates of nocturnal boundary layer mixing degrade the utility of nocturnal continuous measurements of CO_2 for inverse flux estimates (i.e., models have difficulty simulating nocturnal buildup of CO_2 and so nocturnal measurements in the continental PBL are often excluded from inversions, see Law et al., [2008]), biases in synoptic transport of CO_2 might degrade the utility of continuous or satellite measurements of CO_2 along fronts. Comparison to continuous measurements, for example, has shown that overall models in this study correctly simulate the phase and pattern of synoptic variability, but that GEOS5 in particular has the tendency during winter to overestimate the amplitude of synoptic variability near the surface. In general, inter-model comparison studies show that models tend to do a better job of simulating the timing of variability at diurnal and synoptic scales than the amplitude [e.g., Patra et al., 2008; Law et al., 2008]. While no direct correlation between CO_2 amplitude and vertical mixing was made in this study, results imply that weak vertical mixing in GEOS5, in particular by moist convection, plays a role in enhancing the amplitude of synoptic variability by trapping CO_2 in the PBL throughout northern mid-latitudes, which is then acted on by slow, slantwise ascent along moist conveyors. To test for implications of amplitude errors on inverse flux estimation, future studies could invert for CO_2 flux for an isolated synoptic event using GEOS4 and GEOS5, compare CO_2 flux estimates, and then explain resulting differences by comparing vertical CO_2 distributions before and after the synoptic event. This test could be extended to isolate vertical mixing along fronts as the primary cause of flux errors by using two weather products of the same resolution and with identical initial

conditions prior to the onset of the synoptic event, but with different vertical mixing.

It is more likely, as discussed in Chapter 3, that CO₂ variations associated with synoptic moist dynamics will be mostly unobserved by satellites. CO₂ transport at synoptic scales may therefore be systematically unresolved *and* unobserved. Given the importance of transport by synoptic weather systems [Parazoo et al., 2008], the covariance of horizontal CO₂ gradients with rising, moist, cloudy air, and the resulting temporal sampling bias in CO₂ mixing ratio distributions [Corbin et al., 2008], significant flux estimation errors may be incurred due solely to unobserved transport, even if transport were perfect. It would be interesting to see how excluding column CO₂ data from moist synoptic storm systems using some kind of cloud screening technique might bias inverted surface fluxes given OSSEs using (1) the same transport model to generate and invert synthetic satellite data, and (2) different models to generate and invert synthetic data. These experiments are carried out in Chapter 5.

It is important to keep in mind that total meridional transport in northern mid-latitudes is the same in all simulations and therefore reduced transport of CO₂ by eddies in GEOS4 must be compensated for by reduced transport by mean circulations. This means transport by the mean circulation experiences the same total bias between GEOS4 and GEOS5 as transport by baroclinic waves, albeit for different reasons. Unlike transport by moist baroclinic storms, measurements of transport by the mean circulation are less likely to experience fair weather bias (assuming dry conditions are more prevalent), and therefore mean transport is better constrained by continuous and flask observations at the surface, satellite measurements of column CO₂, and vertical profiling by aircraft. Because of the large uncertainty in mean transport and the opposing flows of CO₂ throughout the column discussed in Chapter 3, these fair weather measurements are crucial for constraining flow in dry parts of the atmosphere.

A question raised by Pauluis et al. [2009] is whether midlatitude ascent occurs primarily through rapid convective events such as thunderstorms or slower slantwise ascent in baroclinic eddies. Eddy decomposition on θ_e strongly suggests that slantwise ascent plays a critical role in overall

midlatitude ascent. Furthermore, the moist circulation is slightly stronger in GEOS5 given a weaker cumulus mass flux. This raises questions as to what combination of factors sets the moist circulation in GEOS5 apart from that of GEOS4. Data assimilation techniques almost certainly play a role but it is likely finer grid spacing (horizontally and vertically) in GEOS5 is able to better resolve cyclonic circulations, frontal structure, and slantwise ascent along moist conveyors within baroclinic eddies. Eddy transport is only weakly sensitive to winds that have been regridded to coarse resolution (e.g., GEOS4-1.25x1 to GEOS4-2.5x2) or sampled from finer grids (e.g., grid points in GEOS5-1.25x1 are sampled from GEOS5-0.67x0.5). It is therefore more important to run models and generate reanalysis at the finest possible grid spacing in order to resolve fine-scale synoptic features. Future studies should examine sensitivity of eddy transport to grid spacing, with a fixed vertical mixing scheme, by running GCMs at multiple grid spacing from 250 km down to 50 km or finer if possible.

Eddy decomposition is a valuable tool for assessing tracer models via the statistics of eddy CO₂ transport along the moist synoptic pathway. This technique could almost certainly be applied to other tracers to assess forward or inverse models. It could also be used to investigate the validity of moist convection in mid-latitudes in global models relative to observations and/or cloud resolving models. Even at 50 km grid spacing convective scales are far from resolved. Ott et al. [2009] show that vertical mixing in GEOS5 is weak compared to a cloud-resolving model, but that parameters within the GEOS5 convection scheme could be optimized to improve vertical transport by convective storms. We have seen that weak vertical mixing in GEOS5 traps CO₂ in the PBL, where it accumulates over time. Eventually moist processes within baroclinic waves, unobserved by satellites, sweeps the CO₂ upward and poleward. Future studies should examine sensitivity of eddy transport within a high resolution global model such as GEOS5 to vertical mixing, with other factors such as grid spacing and CO₂ flux held constant, and then compare the amplitude of CO₂ variations to continuous measurements at different levels in the PBL (e.g., tall towers), to vertical profiles measurement by aircraft (e.g., HIPPO), and to column measurements (e.g., TCCON or satellite). We might find that some schemes do better than others, likely with seasonal and geographic depen-

dence, but that ultimately a multi-scale modeling framework such as the Goddard-MMF [Tao et al., 2009] is needed to explicitly represent moist convection and vertical mixing of tracer within GCM sized grid cells.

Chapter 5

IMPLICATIONS OF TRANSPORT BIAS FOR INVERSE FLUX ESTIMATION

Part 1 (Chapter 3) showed that moist synoptic storms drive meridional sloshing of CO₂ between middle and polar latitudes, which in turn strongly modulates the seasonality of atmospheric mixing ratios of CO₂ in northern latitudes, and that much of this transport is likely to be unobserved by satellites. Part 2 (Chapter 4) showed that CO₂ transport by moist synoptic weather systems is significantly different when driven by different weather products that are architecturally very similar but have key differences in horizontal grid spacing and the strength of fine-scale vertical mixing. Part 3 extends analysis in Parts 1 and 2 by using a top-down inversion approach to test for flux estimation errors due to systematic differences in transport between GEOS4 and GEOS5.

5.1 Introduction

The primary goal of CO₂ inversions is quantification of source and sink patterns at fine spatial and temporal scales that are as consistent as possible with CO₂ mixing ratio observations. Such inverse estimates provide independent information on flux distributions that can then be compared with “bottom-up” estimates. Inversions may also be used in an OSSE framework to provide specific information about instrument design needed to meet certain science objectives. For example, future satellite missions use OSSEs to determine specifics about orbit, averaging kernels (i.e., vertical weighting functions), and measurement precision that may be needed to measure certain flux signals (e.g., increasing emissions due to permafrost melt) produced by the Earth system. Baker et al. [2010] is an example of an OSSE designed to quantify carbon source and sink information that

could be provided by column CO₂ measurements from OCO-2.

A possible source of flux estimation error in OSSEs lies in the atmospheric transport model. Transport models, which are typically run at global resolutions of 50 km or greater for inversion studies, are responsible for communicating between flux and measurement. Many atmospheric processes, however, occur at scales much smaller than most atmospheric models can resolve (e.g., cumulus convection, PBL mixing, frontal convergence). Sub-grid scale processes must be calculated through parameterization. These processes, in particular fine scale vertical mixing, are an important and well known source of uncertainty for tracer transport models [Denning et al., 1999; Yi et al., 2004; Yang et al., 2007; Stephens et al., 2007].

It follows then that fluxes estimated directly from CO₂ observations through simulated transport, such as is done in inversion studies, will be impacted by transport error. Transport errors that are more random than systematic could be assumed to average out over long enough time scales, in which case flux errors would also tend to average out. If, however, transport errors are biased in a systematic way (underestimated vertical mixing, phase difference of day-to-day variability due to synoptic processes, poorly represented PBL heights) that is correlated with the phenomenon of interest, then corresponding errors in flux estimation should also be expected (assuming other components of the inversion system are not biased in a different direction).

Chapter 4 set out to determine whether differences in CO₂ transport by GEOS4 and GEOS5 existed and to what degree errors were systematic and biased or purely random. Comparison of simulations to surface based CO₂ mixing ratio observations showed good agreement in the timing of synoptic events. A diagnosis of net meridional transport by synoptic eddies was, however, strongly sensitive to the analysis product. For example, eddy transport was stronger in GEOS5 by up to 0.1 PgC yr^{-1} in the annual mean and with absolute differences close to 0.2 PgC yr^{-1} in northern mid-latitudes during boreal winter and summer. This so-called “eddy” component of mid-latitude transport was shown to be most strongly sensitive to (1) grid spacing, with enhanced transport on finer grids and (2) the representation of fine scale vertical mixing by PBL turbulence and moist con-

vection. Given that these reanalysis products are similar in architecture and run through a common transport model, it is likely that these are conservative estimates for the magnitude of transport bias to be expected.

The obvious question at this point is whether transport bias is aliased into errors in flux estimation vis-a-vis CO₂ inversion. Baker et al. [2010] tested the effect of transport errors on flux estimation by generating synthetic satellite retrievals with one transport model and inverting the retrievals with the same model but with stored meteorology offset by 18 hours. The result was significant degradation of 7-day flux improvements in the optimization. Houweling et al. [2010] also tested for the effect of transport errors on inversion of satellite data, but instead of using the same model offset in time, entirely different transport models were used to generate satellite data and to run the inversion. This technique better quantifies errors due to biased transport or systematic differences in transport. Although seasonal differences in column CO₂ were shown to be small (~ 0.5 ppm), the errors were correlated in space and caused flux estimation errors large enough that high precision satellite missions such as A-SCOPE might be limited in their ability to reduce uncertainties in flux estimates and meet science objectives of high accuracy at regional scales.

In this chapter, inversion techniques are utilized as in Houweling et al. [2010] to test for flux estimation errors that may result from transport bias. The approach is to generate synthetic satellite measurements of column CO₂ using a transport model driven by reanalysis at fine resolution and invert the synthetic data using the same transport model but driven by reanalysis at relatively coarse resolution. GEOS4 is used as coarse resolution reanalysis and GEOS5 as the fine resolution reanalysis. As discussed in Section 2.6.2, column CO₂ will be sampled from forward simulations of PCTM along a GOSAT like orbit. Control experiments are also needed to make sure that (1) the optimization technique, in this study MLEF (discussed in more detail in Chapter 2.6.3), is accurate and robust to random measurement errors, (2) enough satellite observations are available after cloud screening to provide a reasonable solution given realistic conditions, and (3) temporal sampling biases due to cloud screening of column CO₂ (discussed in Corbin et al. [2009]) don't significantly

bias flux estimates. This last point will help determine if clear sky data from a GOSAT like instrument is enough to constrain flux estimates without significant bias. Control experiments will use transport driven by the same reanalysis product, GEOS4, to generate and invert synthetic satellite data. Given the simplicity of these control cases, so-called “sink recovery” experiments are added to determine whether the inversion can detect realistic carbon sinks hidden within satellite data, as a test to see whether slowly varying sinks that resemble real world processes can be detected in column CO₂ data by the inversion algorithm.

In addition to transport bias, the accuracy of any inversion technique is limited by the optimization technique. Any given optimization algorithm searches for the best combination of surface fluxes that is consistent with observations by minimizing a cost function (see Equation 2.23). In ensemble data assimilation, the solution that best minimizes the cost function is obtained from a sample of the total range of possible solutions. The ensembles are therefore an approximation to the full analytical solution. More ensembles facilitate convergence of this “reduced rank” solution to the full solution but at greater computational expense. Since a major benefit of ensemble data assimilation is computational savings and the ability to process large amounts of data, tradeoff is needed between computational expense and accuracy. Zupanski et al. [2007] show that approximating the full solution does not have obvious detrimental impact on the solution and is worth the saved computational cost. The concepts of an “information matrix” and the DFS were discussed in Chapter 2.6.3 as guides for determining an appropriate number of ensembles. Tests based on this criteria demonstrate that 200 ensembles and assimilation windows of 14 days are adequate for flux recovery.

For details regarding the inversion framework, including prior estimates, the observation operator, description of the optimization technique and bias estimation strategy, covariance smoothing, flux and uncertainty calculations, and basic description of terminology, please refer to Chapter 2.6. Note that results in this chapter are presented either as net flux over the land (terrestrial NEE) or ocean (air-sea exchange). There are a total of six experiments in this study, with experiments be-

coming progressively more challenging for the inversion. The first two (Experiment 1 and 2, Section 5.2) are control experiments, designed to test for flux errors that arise given perfect transport and unbiased truth. The next two (Experiments 3 and 4, Section 5.3) are designed to test whether hypothetical sources and sinks can be recovered from satellite data, given perfect transport and biased truth. The last two (Experiments 5 and 6, Section 5.4) test for flux errors that arise given biased transport and two different scenarios of truth.

5.2 Control Experiments - Perfect Transport

For simplicity, true fluxes are defined with $\beta_{GPP} = \beta_{RESP} = \beta_{OCEAN} = 0$ so that truth is unbiased. Satellite data is generated using forward runs of GEOS4-2.5x2, and then inverted using ensembles of GEOS4-2.5x2 transport. In the absence of any errors in the ensemble approximation or significant temporal sampling biases after cloud screening, the inversion will know the satellite data is unbiased and return analyzed fluxes that are equal to the priors. Two experiments are run: one in which all satellite data is retained (Experiment 1), and one in which satellite data is retained only during sunny conditions (Experiment 2). In a real inversion clouds and aerosol in the atmospheric column contaminate measurements of column CO_2 and these points must be discarded. Cloud contamination is assessed using cloud optical depth (τ) from MERRA, with data thrown out if $\tau > 0.3$. So, by introducing cloud screening in Experiment 2, the OSSEs are tested for sensitivity to (1) less observations and (2) observations that experience fair weather bias.

5.2.1 *Experiment 1: Perfect Transport, Unbiased Truth, and no Cloud Screening*

Annual mean errors in terrestrial NEE are shown at pixel scale for Experiment 1 in Figure 5.1. Since SiB is annually balanced ($GPP = RESP$), prior estimates of terrestrial NEE are zero in the annual mean. Therefore, in a perfect inversion or the case that the ensemble solution has converged to a theoretically optimal solution obtained using the Kalman Filter approach (Zupanski et al., 2007), analyzed fluxes should also be zero in the annual mean. As can be seen, the inversion is not perfect,

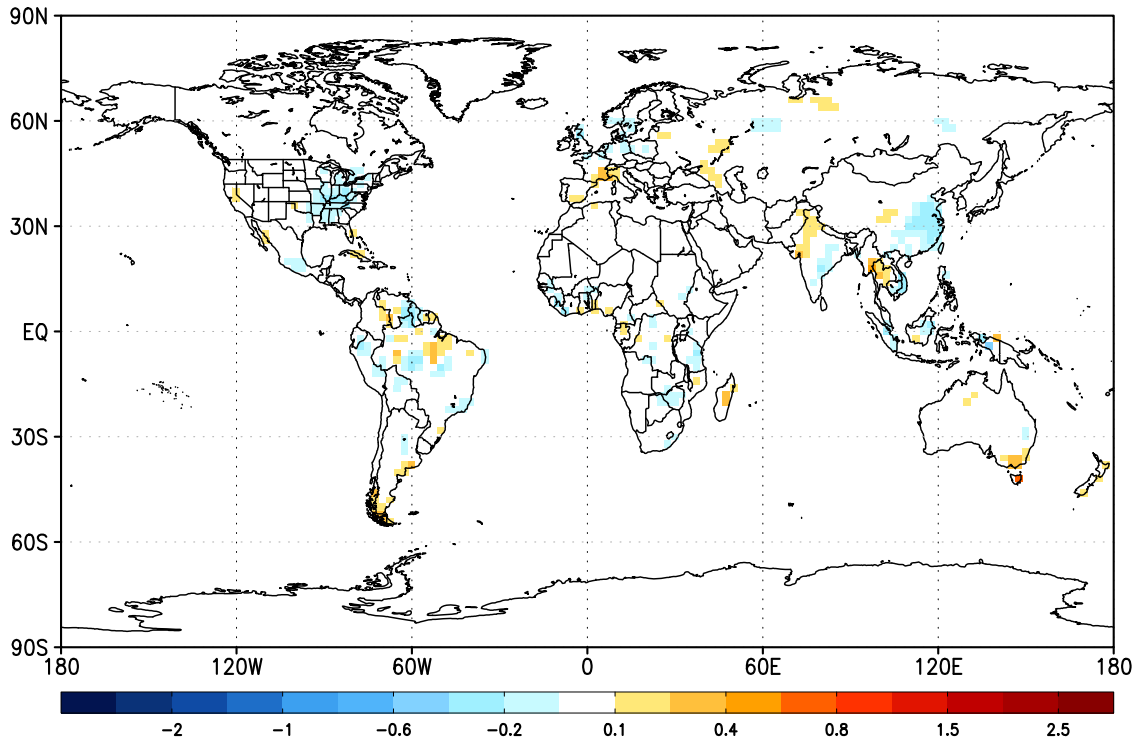


Figure 5.1: Annual mean errors in terrestrial NEE in units of $\mu\text{moles m}^{-2} \text{s}^{-1}$ at pixel scale ($2.5^\circ \times 2^\circ$) for Experiment 1.

and non-zero, but nevertheless small, flux errors emerge. While it is unlikely that these flux errors are due to data constraints considering the large size of the observation vector in this control case, testing is needed to determine sensitivity to the size of the observation vector. These errors could also be due to the ensemble approximation; a simple test would be to rerun the inversion with a different set of ensembles and see if similar errors emerge (not done). Annual mean flux errors do not have any obvious coherent spatial structure and could be interpreted as random in this experiment. These results are helpful confirmation that the inversion is stable and doesn't produce extremely biased flux estimates.

It could be argued that these annual mean flux errors are a convenient result of cancellation of larger seasonal errors. Seasonal flux errors are therefore plotted in Figure 5.2. For comparison to annual mean fluxes, seasonal fluxes are plotted on the same scale as in Figure 5.1. Larger differences between true and analyzed fluxes exist at seasonal time scales than in the annual mean, especially

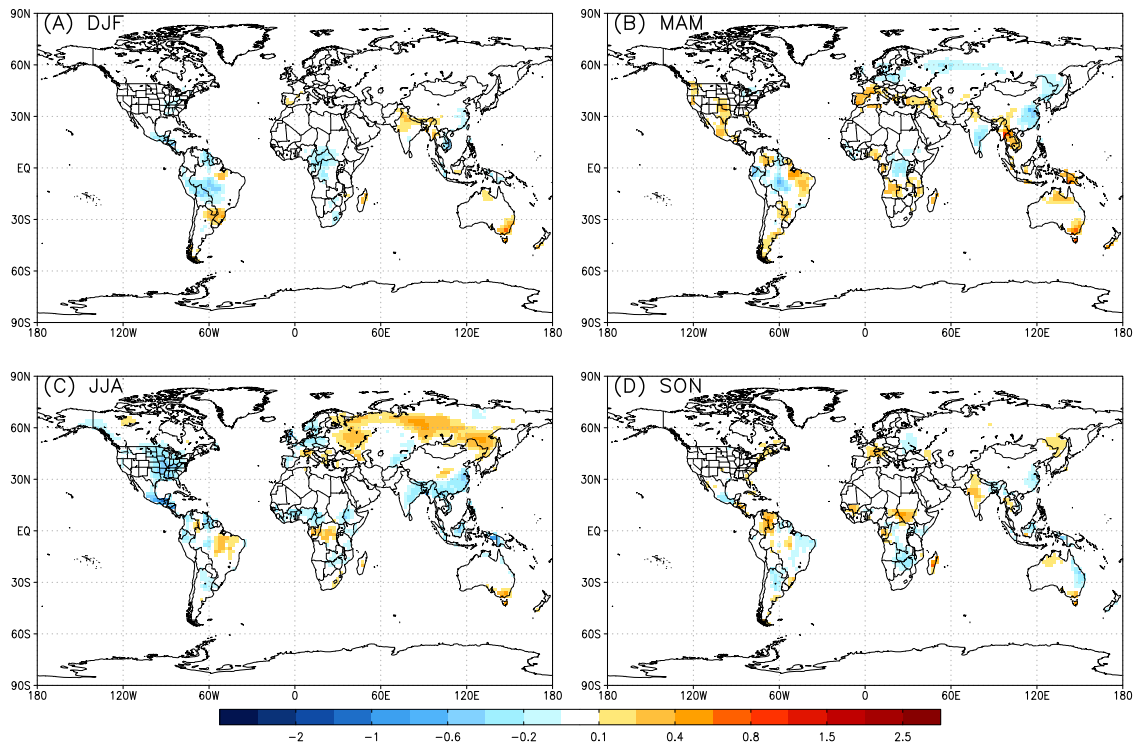


Figure 5.2: Similar to Figure 5.1 except plotted as a function of season for Experiment 1: (a) boreal winter, or December-January-February (DJF), (b) boreal spring, or March-April-May (MAM), (c) boreal summer, or June-July-August (JJA), and (d) boreal fall, or September-October-November (SON). The colorbar has the same scale as in Figure 5.1.

during boreal summer. The major feature that stands out in the seasonal plot is summer efflux out of boreal Asia and uptake in eastern N. America. These are clearly non-random features that largely cancel in the annual mean. Flux errors during the remaining seasons are much smaller and seemingly less systematic.

To get a sense of the relative size of flux errors, seasonal errors are compared directly to priors (Figure 5.3) and divided by the priors (Figure 5.4) as a measure of percent error, where purple colors (values close to zero) indicate small errors relative to the priors and red colors (values close to one) indicate large errors. Together, Figures 5.3 and 5.4 demonstrate that flux errors are typically small throughout the year in northern mid-latitudes where seasonal NEE is strong, but that large errors can occur in particular in eastern Europe during boreal Spring (Figure 5.4B) and in the southeast

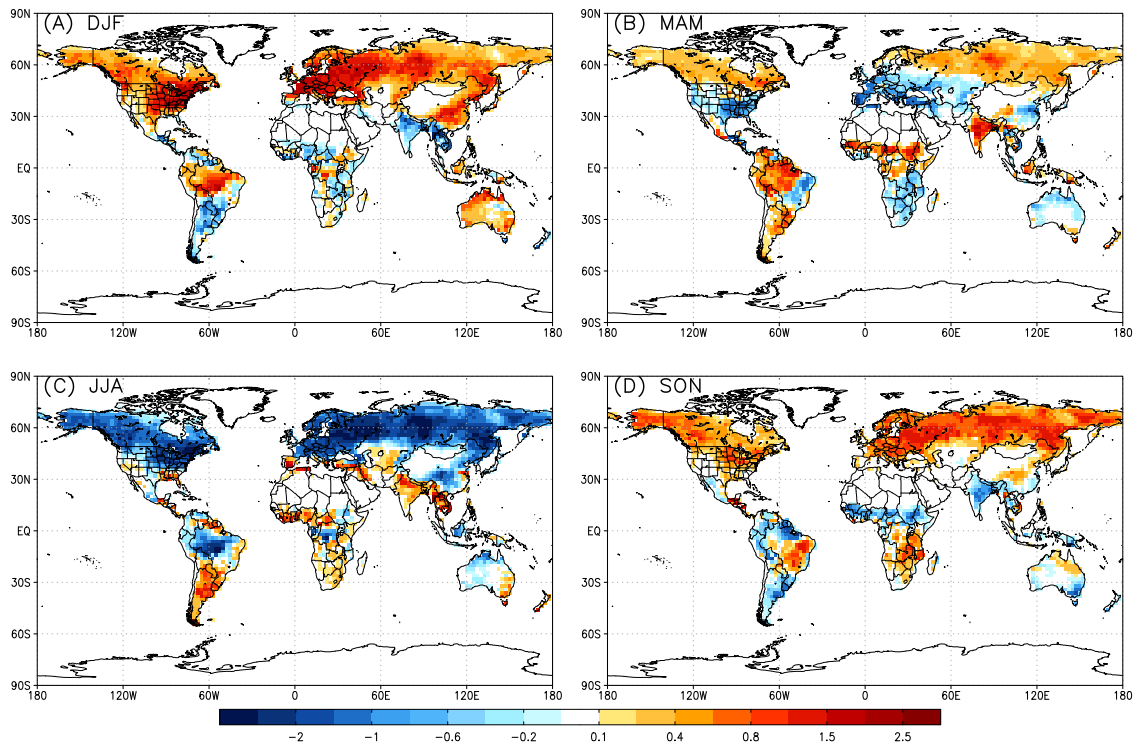


Figure 5.3: Seasonal distribution of prior estimate of terrestrial NEE, plotted on the same scale as Figure 5.1. These priors are used for all experiments in this chapter.

North America during boreal Summer (Figure 5.4C). Comparison of red values in Figure 5.4 to priors in Figure 5.3 indicates that, although the large relative errors tend to occur where priors are weak (deserts, savanna, mountains), errors can also be large in productive regions (southeast North America).

Prescribed and analyzed uncertainties for terrestrial NEE, along with uncertainty reductions, are calculated using the covariance matrix according to Equation 2.27 and plotted in Figure 5.5. The prescribed error covariance is calculated by assuming prior *GPP* and *RESP* components have uncertainties of $\sigma = 0.2$, where σ represents the standard deviation. This prior uncertainty on the component fluxes is somewhat generous, but is chosen such that the vast amounts of satellite data can help steer the optimized fluxes away from the priors. As seen in Figure 5.5A, the prescribed error covariance produces uncertainties over land regions that scale with terrestrial NEE. As expected, the

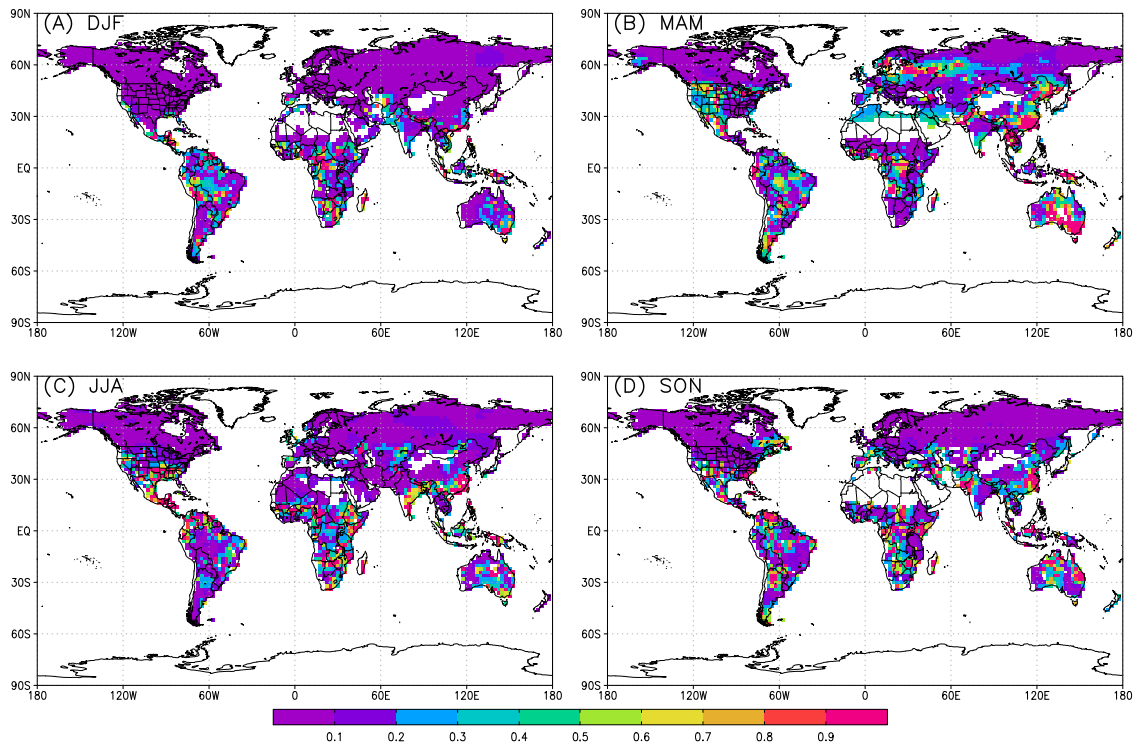


Figure 5.4: Seasonal flux errors for Experiment 1 plotted as a fraction of the prior.

largest uncertainties occur over tropical regions where component fluxes of *GPP* and *RESP* are largest.

As discussed in Lokupitiya et al. [2008], cross-correlations in the covariance matrices become diagonally dominant after a few cycles, despite strong smoothing at the first cycle, as error covariances learn from the observations. Lokupitiya et al. [2008] also showed that variance (diagonal terms of covariance matrix), and hence uncertainty, is most strongly reduced in regions where observations are dense. When constrained by surface observations, the analyzed error covariance is most strongly reduced in northern mid-latitudes. As can be seen in Figure 5.5 B and C, however, uncertainties are strongly reduced at all latitudes in the assimilation of satellite observations and propagation of error covariance forward in time to the next assimilation cycle. According to Figure 5.5C, uncertainty is reduced by about 70-80% globally. Keeping in mind the simplicity of the first experiment, this is a very encouraging result.

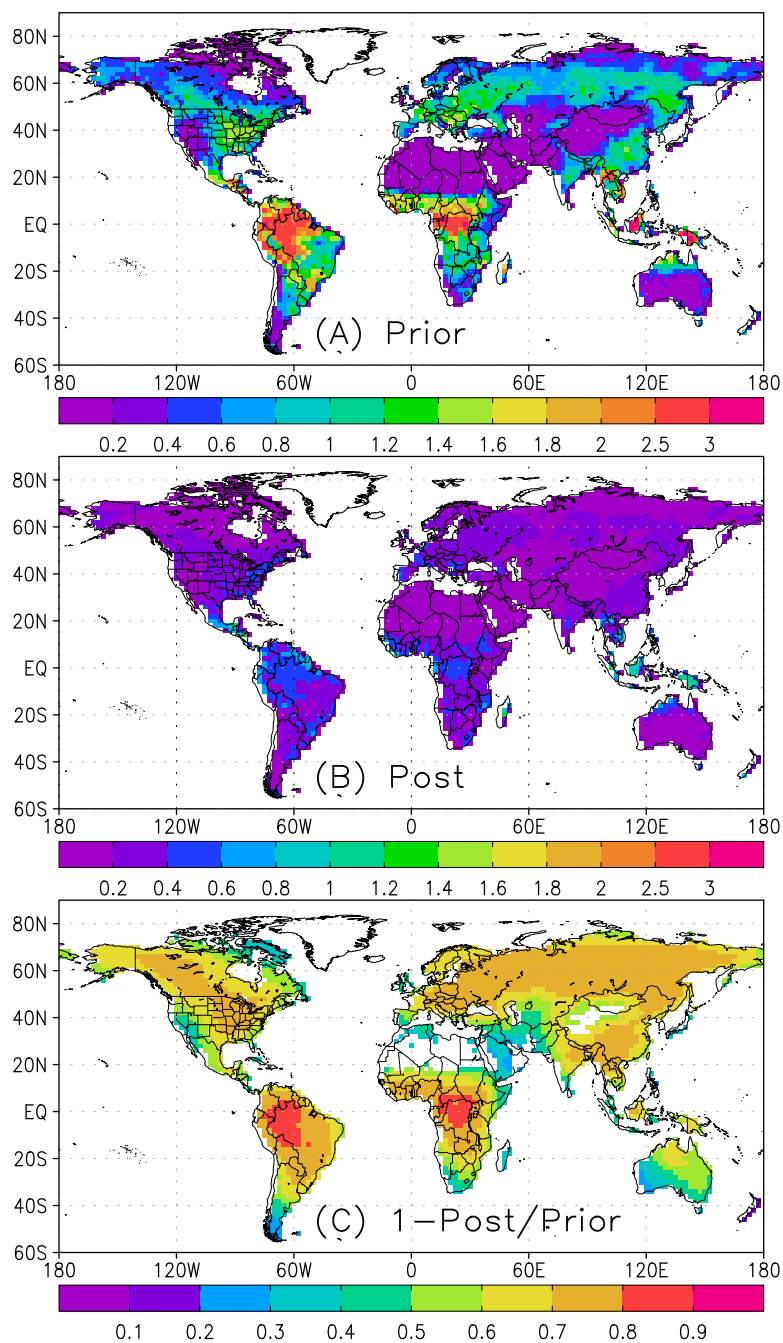


Figure 5.5: Annual mean uncertainties in Experiment 1 for (a) prior and (b) analyzed flux (units of $\mu\text{moles m}^{-2} \text{s}^{-1}$). Uncertainty reduction for terrestrial NEE is shown in the bottom plot (c).

Annual mean flux errors over the ocean are shown in Figure 5.6. Unlike in SiB, ocean fluxes are not annually balanced and thus priors and truth are non-zero in the annual mean (see Figure 5.7).

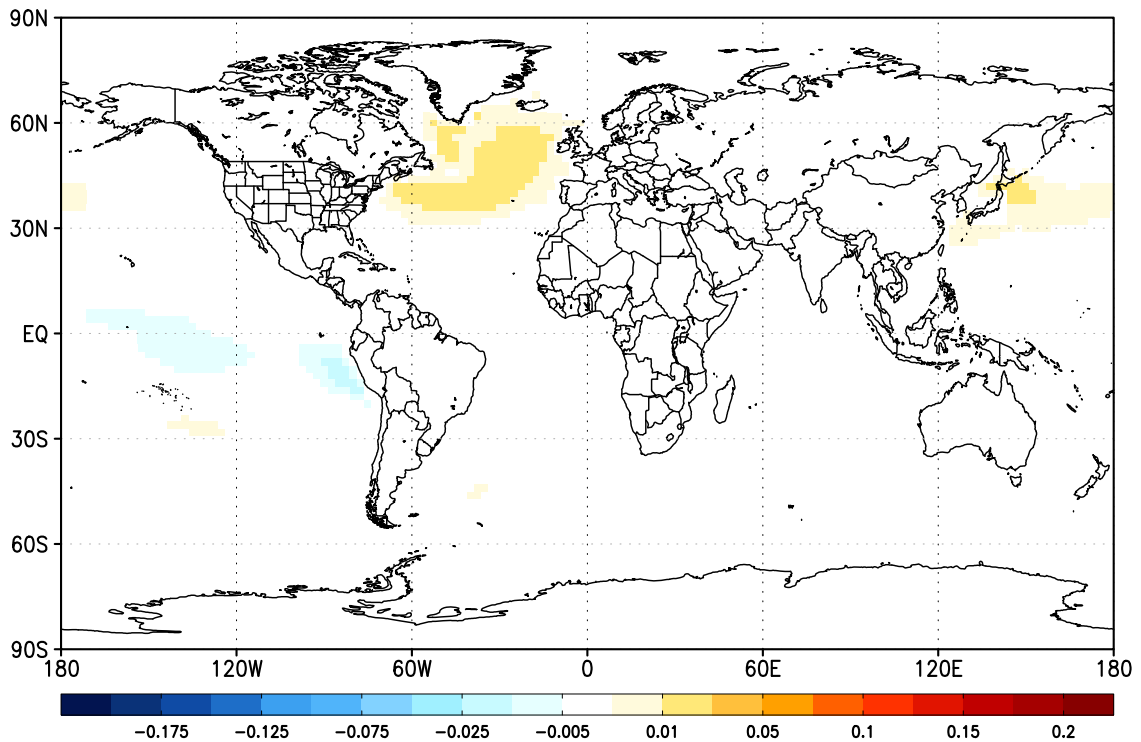


Figure 5.6: Same as Figure 5.1 but for air-sea exchange for Experiment 1. Note difference in scale between land and ocean.

As was the case for terrestrial NEE, inversion for air-sea exchange is not perfect, but errors are small and tend to scale with annual mean ocean flux priors. It is possible that small ocean flux errors result from ocean fluxes being too weak to be detected in the satellite data by the inversion, and that analyzed fluxes over the ocean are constrained more by the priors than satellite data. This phenomenon will be discussed in more detail later in Section 5.3 when the inversion is forced to recover hypothetical biases in air-sea exchange.

As with terrestrial NEE, it is possible that small residual fluxes in the annual mean are a result of cancellation of larger seasonal fluxes. Seasonal flux errors are therefore plotted in Figure 5.8. No large cancellation between seasons is apparent, most likely because seasonality of air-sea exchange is very weak (i.e., there is little change in magnitude or sign of fluxes within a given region). These results show that annual mean errors are dominated by net efflux in the northern Pacific and Atlantic during boreal winter and spring. Comparison to seasonal prior air-sea exchange, plotted in

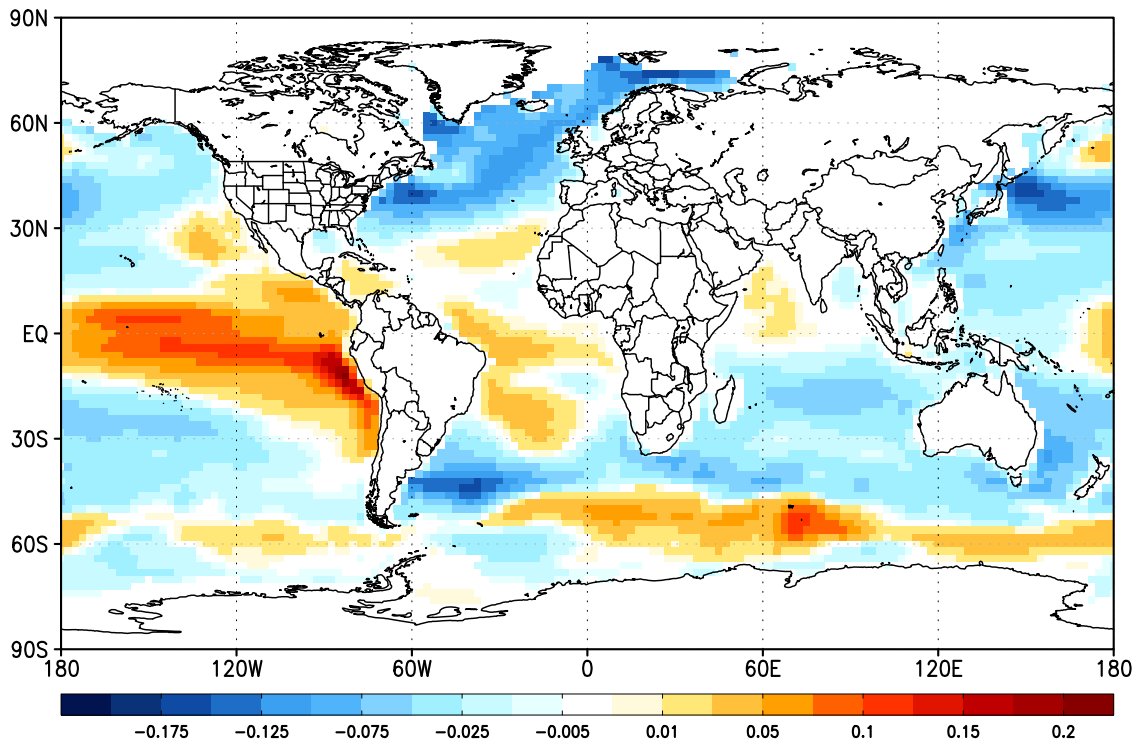


Figure 5.7: Same as Figure 5.6 but for prior air-sea exchange.

Figure 5.9, shows that the winter and spring errors in the north Pacific and Atlantic scale slightly with an uptake feature in the Gulf Stream. Air-sea exchange errors are divided by ocean priors in Figure 5.10. Ocean flux errors are mostly small and trivial (blue shading), with the largest errors approximately 20% of the prior. Errors are smallest where ocean exchange is strongest, and largest where ocean exchange is weakest.

Prescribed and analyzed uncertainties for air-sea exchange, along with uncertainty reductions, are calculated using the covariance matrix according to Equation 2.29 and plotted in Figure 5.11. The prescribed error covariance is calculated by assuming ocean priors have an uncertainty of $\sigma = 0.1$. By design, ocean flux estimates are more heavily weighted towards the priors. The prescribed error covariance produces reasonable looking uncertainties over ocean regions that scale with the largest air-sea exchanges (Figure 5.11A). Although not comparable in reduction to terrestrial NEE, and despite the weaker flux signal, uncertainties over the ocean are still strongly

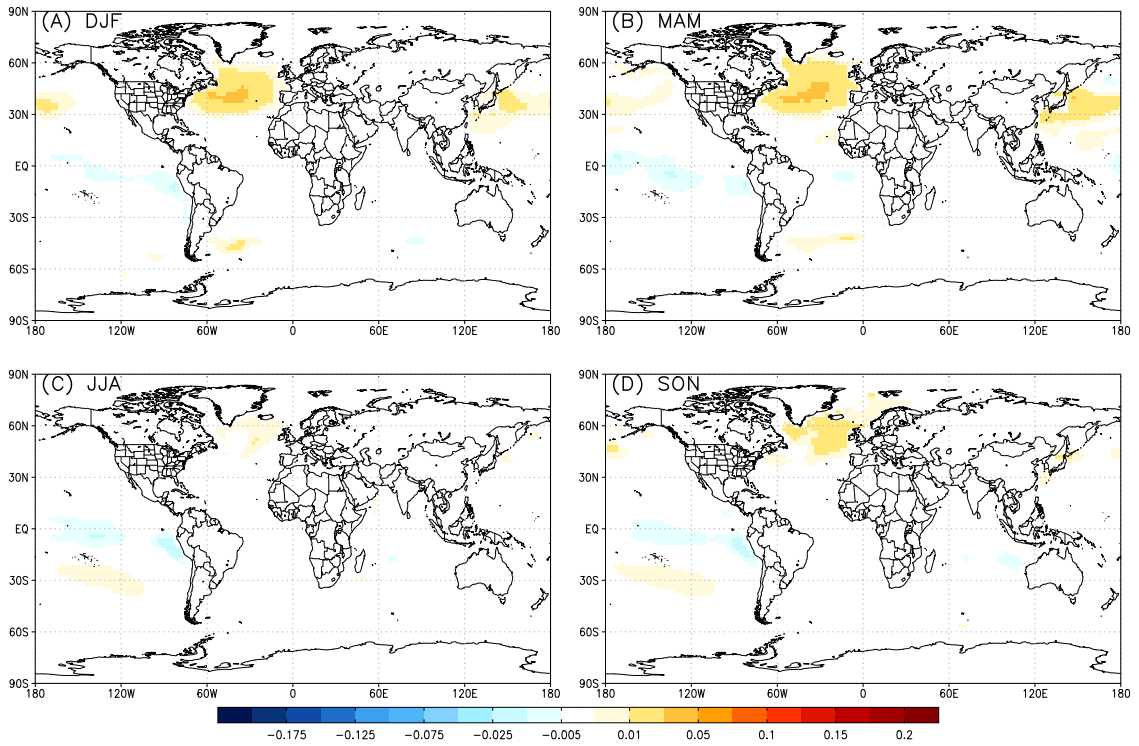


Figure 5.8: Similar to Figure 5.6 for Experiment 1, except plotted as a function of season (a) DJF, (b) MAM, (c) JJA, and (d) SON. The colorbar has the same scale as in Figure 5.6.

reduced at global scale in the process of assimilation of satellite observations (Figure 5.11B). According to Figure 5.5C, uncertainty is reduced by 40-50% globally. This result is encouraging, but not as much so as the uncertainty reduction for terrestrial NEE.

5.2.2 Experiment 2: Perfect Transport, Unbiased Truth, and Cloud Screening

Experiment 2 is the same as Experiment 1 except that satellite data is screened for clouds. More importantly, column CO₂ data from moist synoptic storm systems is excluded. This means that a large number of points are discarded and the observation constraint is greatly reduced from Experiment 1 (e.g., see Figure 2.2). Cloud screening is performed by sampling forward model runs only when $\tau_{cld} < 0.3$. While it is more realistic to use observed cloud distributions (for comparison of MERRA clear-sky fraction to estimates from CALIOP, see Section 2.6.2), here τ_{cld} is prescribed from MERRA to be consistent with weather driver data used in this study. Note that aerosols also

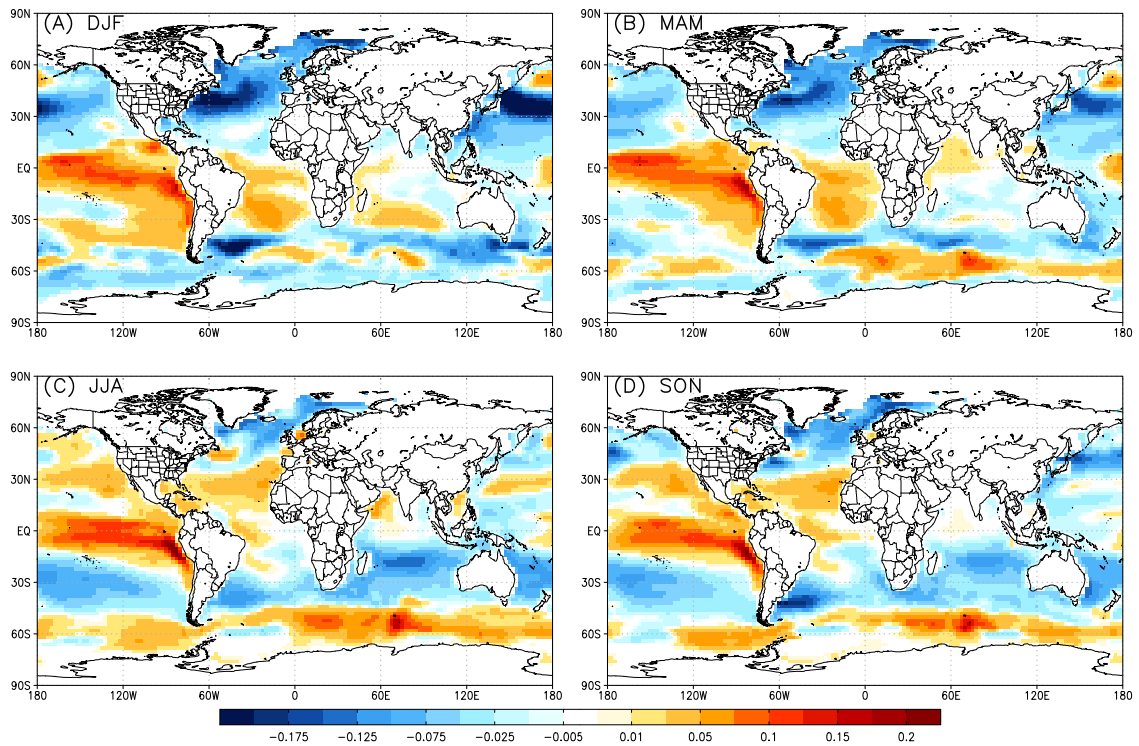


Figure 5.9: Same as Figure 5.8 except for air-sea exchange priors.

contaminate satellite measurements but are not considered in this study.

Annual mean errors in terrestrial NEE are shown at pixel scale for Experiment 2 in Figure 5.12. The largest errors are incurred over the tropics where cloud screening eliminates most of the data (see Figure 2.1B and 2.2). Flux errors are actually reduced over N. America and China relative to Experiment 1, but become more positively biased in Europe, especially Spain and France.

Seasonal errors (Figure 5.13) are by comparison much larger. Tropical regions experience large errors during all seasons. Europe experiences large positive bias during boreal spring and summer. Large seasonal errors occur over N. America (positive bias during summer, negative bias the remainder of the year) that cancel in the annual mean. Boreal and temperate Eurasia continue to experience very little error throughout the year. In general, seasonal errors in Experiment 2 are more spatially coherent than in Experiment 1. Data reduction hasn't simply relaxed the solution to the priors. Fair weather bias in measurements has steered the solution away from errors due to ensemble

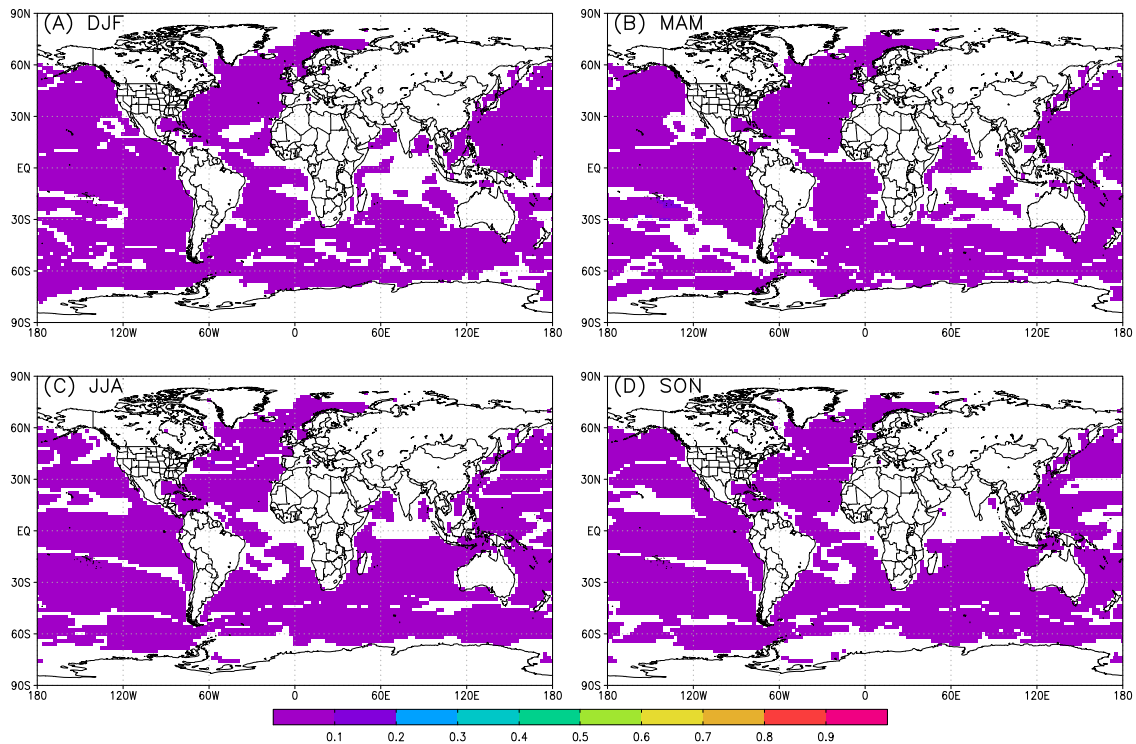


Figure 5.10: Seasonal errors in air-sea exchange in Experiment 1 plotted as a fraction of the prior.

approximation (large number of unknowns estimated through small number of ensembles), most notably toward positive bias during summer in northern temperate and boreal latitudes. A possible explanation for this is that the inversion thinks poleward transport of CO_2 by synoptic eddies is reduced because transport in the warm moist sector of extra-tropical cyclones largely hidden from satellite detection by clouds (nearly 80% of points in eastern N. America and Europe are thrown out in summer), and so the inversion compensates by introducing a source of CO_2 during summer in N. America and Europe. Further testing is needed to test this hypothesis.

Uncertainty is not as strongly reduced in Experiment 2 (50-60% globally, see Figure 5.14B and C) because there is much less data for the information matrix in Equation 2.25 to learn from. However, considering the huge reductions of satellite data, especially in the Amazon where clouds are prevalent all year, substantial reductions in uncertainty are nevertheless achieved. Flux errors over the ocean are actually much weaker than when cloud screening isn't applied (also not shown).

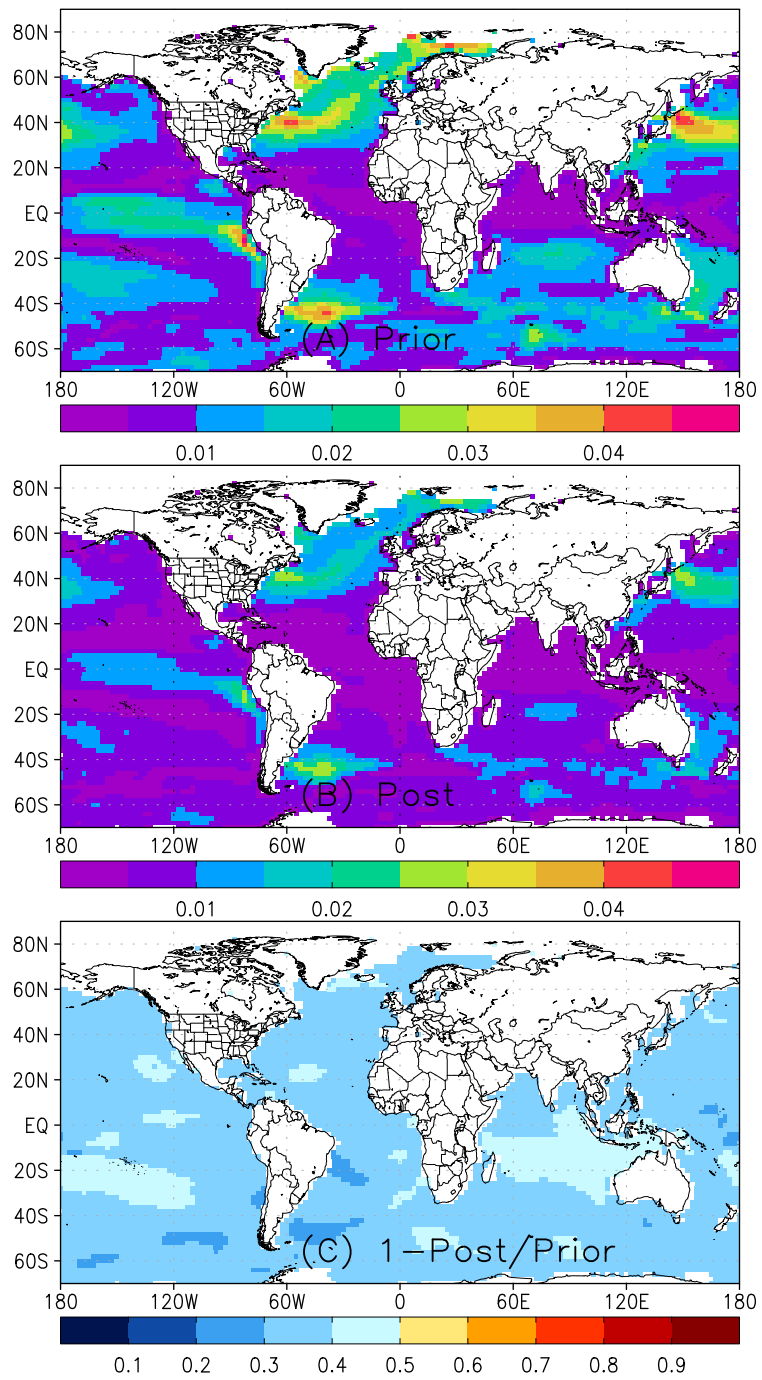


Figure 5.11: Annual mean uncertainties in Experiment 1 for (a) prior and (b) analyzed air-seas exchange. Uncertainty reduction is shown in the bottom plot (c).

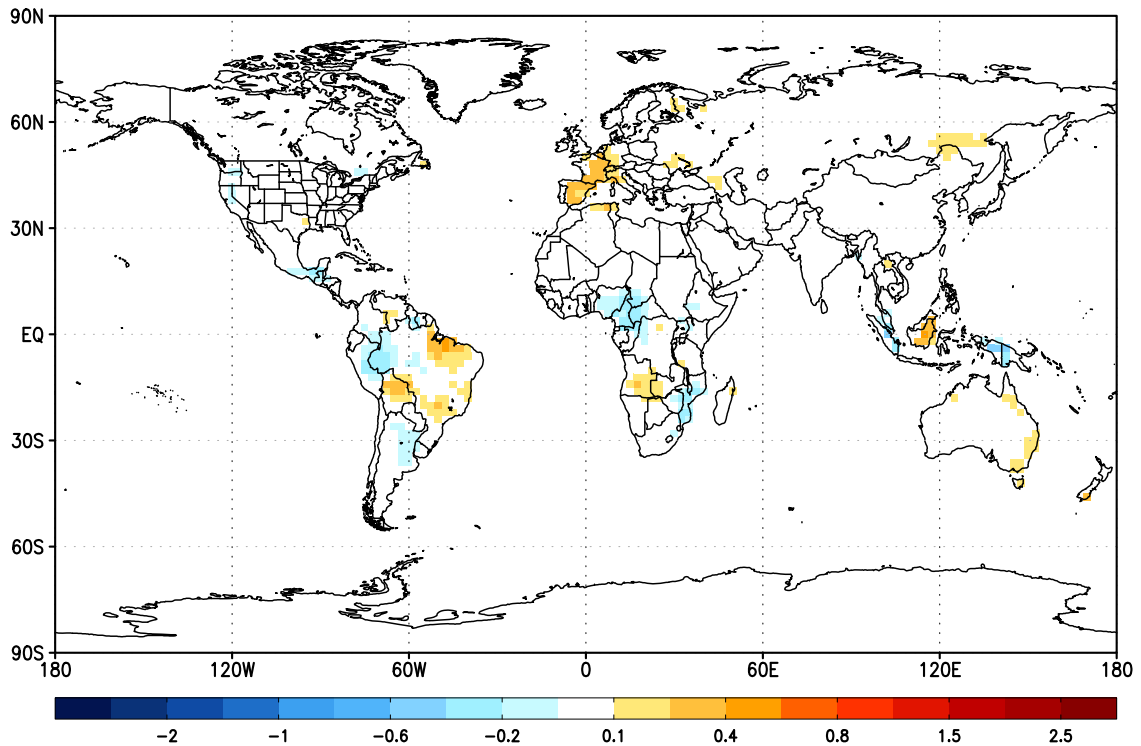


Figure 5.12: Same as Figure 5.1 except for Experiment 2.

This is most likely because there is so little information over the ocean (e.g., Figure 2.1) that the inversion is forced to relax to the priors.

5.2.3 Aggregation of Experiments 1 and 2 up to TransCom Regions

Flux errors (and uncertainties) are often correlated in space due to (1) spatial smoothing applied to the covariance matrix during the first assimilation cycle, (2) transport patterns that emerge from the prevailing wind, and (3) spatial coherence of vegetation type. Uncertainties are also highly anti-correlated in space so it is useful to aggregate up to larger regions to reduce the uncertainty of flux errors. A common practice for global scale inversion experiments is to aggregate fluxes up to continental-sized basis functions that reflect both geographical and mechanical elements (see Figure 5.15). These regions, referred to as TransCom regions, are constructed based on land cover type classification. In this way, flux errors over large regions can be related (albeit crudely) to land

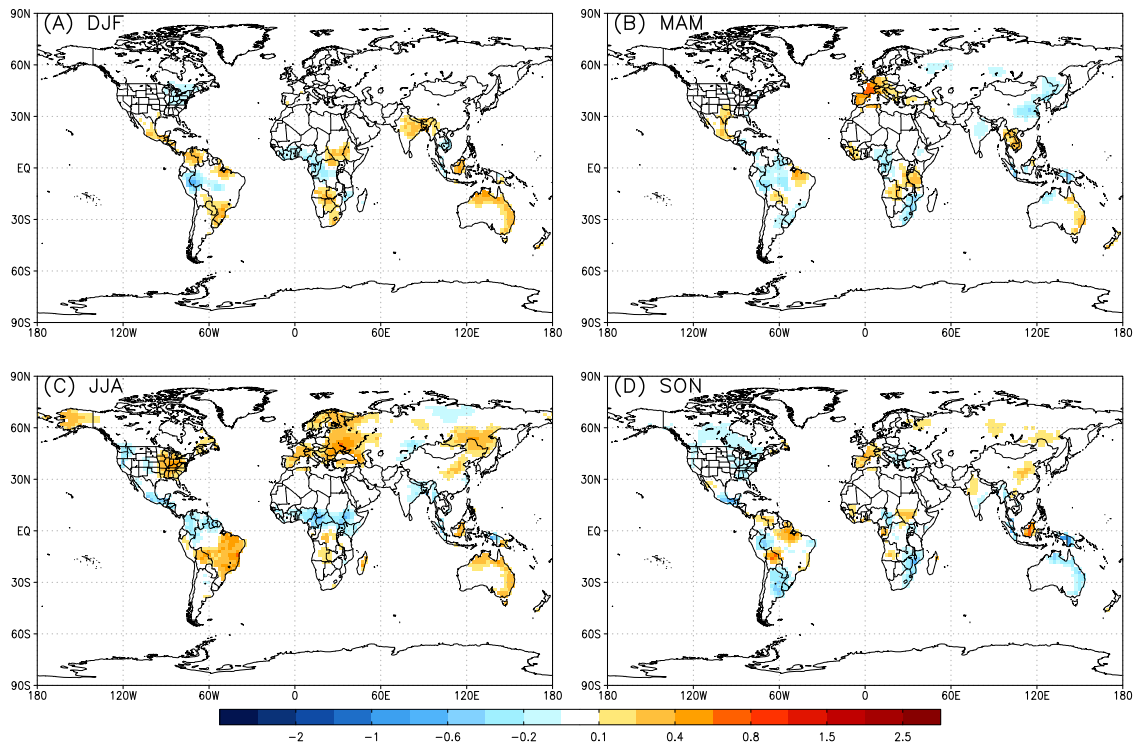


Figure 5.13: Flux errors plotted as a function of season for Experiment 2: (a) boreal winter, or December-January-February (DJF), (b) boreal spring, or March-April-May (MAM), (c) boreal summer, or June-July-August (JJA), and (d) boreal fall, or September-October-November (SON). The colorbar has the same scale as in Figure 5.12.

cover type classification.

Annual flux and uncertainty estimates for Experiments 1 and 2 are aggregated up, binned into TransCom regions (11 land and 11 ocean), and converted to GtC year^{-1} in Figure 5.16 according to Equations 2.30-2.33. Note that since total annual prior (also truth in this case) terrestrial NEE is zero at every pixel (SiB3 balances *GPP* and *RESP* in an annual cycle), aggregation up to TransCom regions also results in zero net flux. Total annual prior air-sea exchange is non-zero at pixel and TransCom scale.

In Experiment 1, recovered fluxes of terrestrial NEE are close to zero when aggregated up, never more than $0.15 \text{ GtC year}^{-1}$ away from zero and, except for Australia, always within 1σ (see Equation 2.30) of the truth. This is good; the simplified inversion does not create annual fluxes

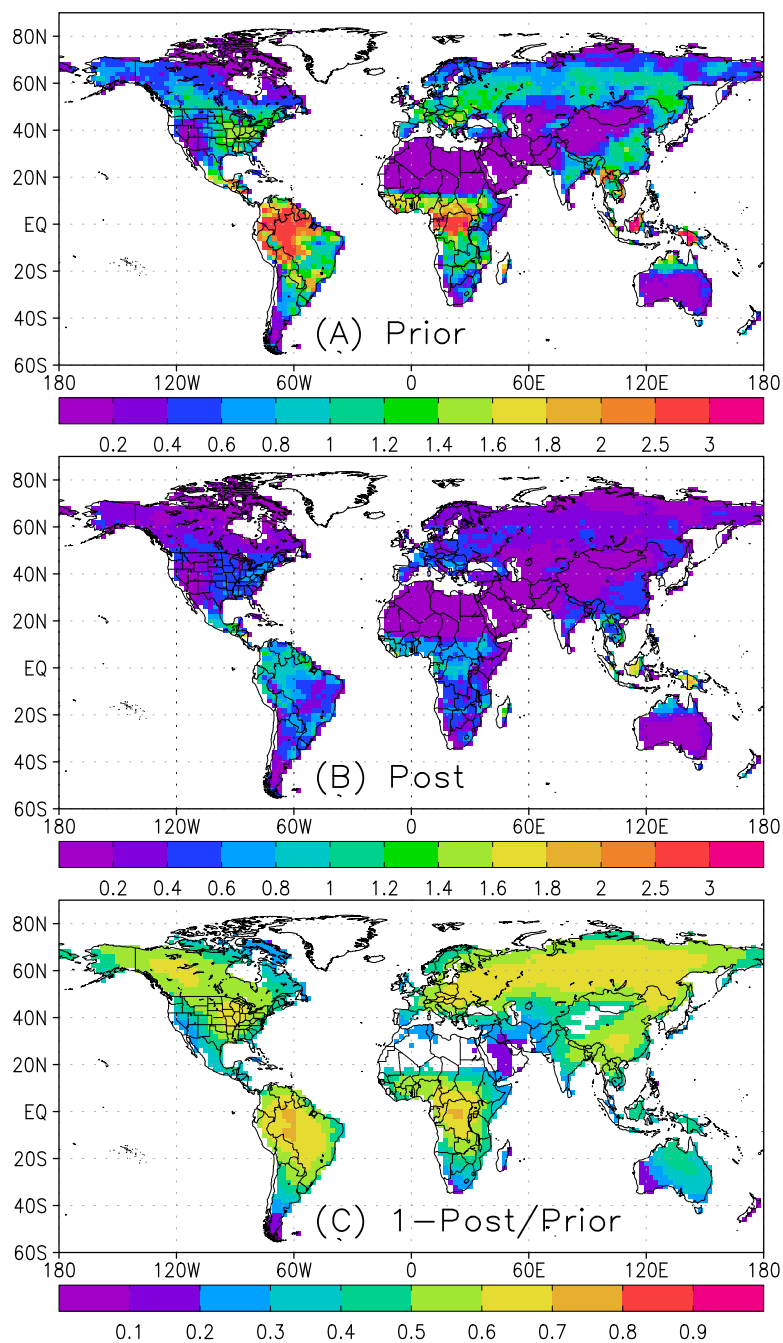


Figure 5.14: Annual mean uncertainties in Experiment 2 for (a) prior and (b) analyzed flux. Uncertainty reduction for terrestrial NEE is shown in the bottom plot (c).

that are significantly biased from the truth. The same is true for air-sea exchange, which has an even tighter uncertainty. Overall, there tends to be negative bias in terrestrial NEE in Experiment 1,

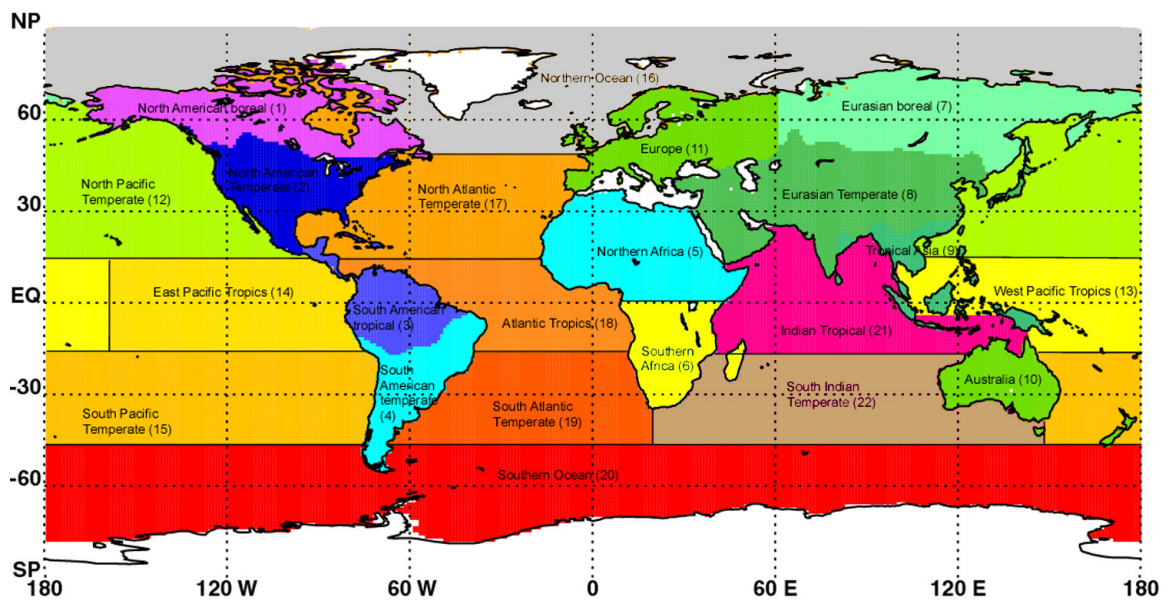


Figure 5.15: TransCom basis functions.

which is dominated by negative biases in the tropics and Temperate N. America.

Cloud screening in Experiment 2 doesn't change annual TransCom sized fluxes significantly, but there are some very noticeable and important differences from Experiment 1. First, reduction of satellite data increases posterior uncertainty of flux estimates. While fluxes in most regions are within 1σ of the truth, flux errors in Australia and Europe reach $\sim 0.1 \pm 0.115$ and 0.25 ± 0.245 GtC year^{-1} , respectively, and are 1σ away from the truth. N. Africa is within 1σ of the truth but incurs an error of nearly 0.2 ± 0.350 GtC year^{-1} due to cloud screening. Ocean flux estimates are closer to the truth in Experiment 2 than Experiment 1 because data reduction has given more weight to priors. The total land flux has a positive bias of 0.3 ± 1.2 GtC year^{-1} , which is about 10% of the total annual global sink. The total land bias is dominated by positive bias in Europe, Eurasian Boreal, and Australia.

The effect of screening column CO_2 data from moist synoptic storms in mid-latitudes and other cloudiness associated with day-to-day weather in the tropics through cloud screening is more obvious in seasonal plots of flux errors from Experiments 1 and 2 (Figure 5.17), where Experi-

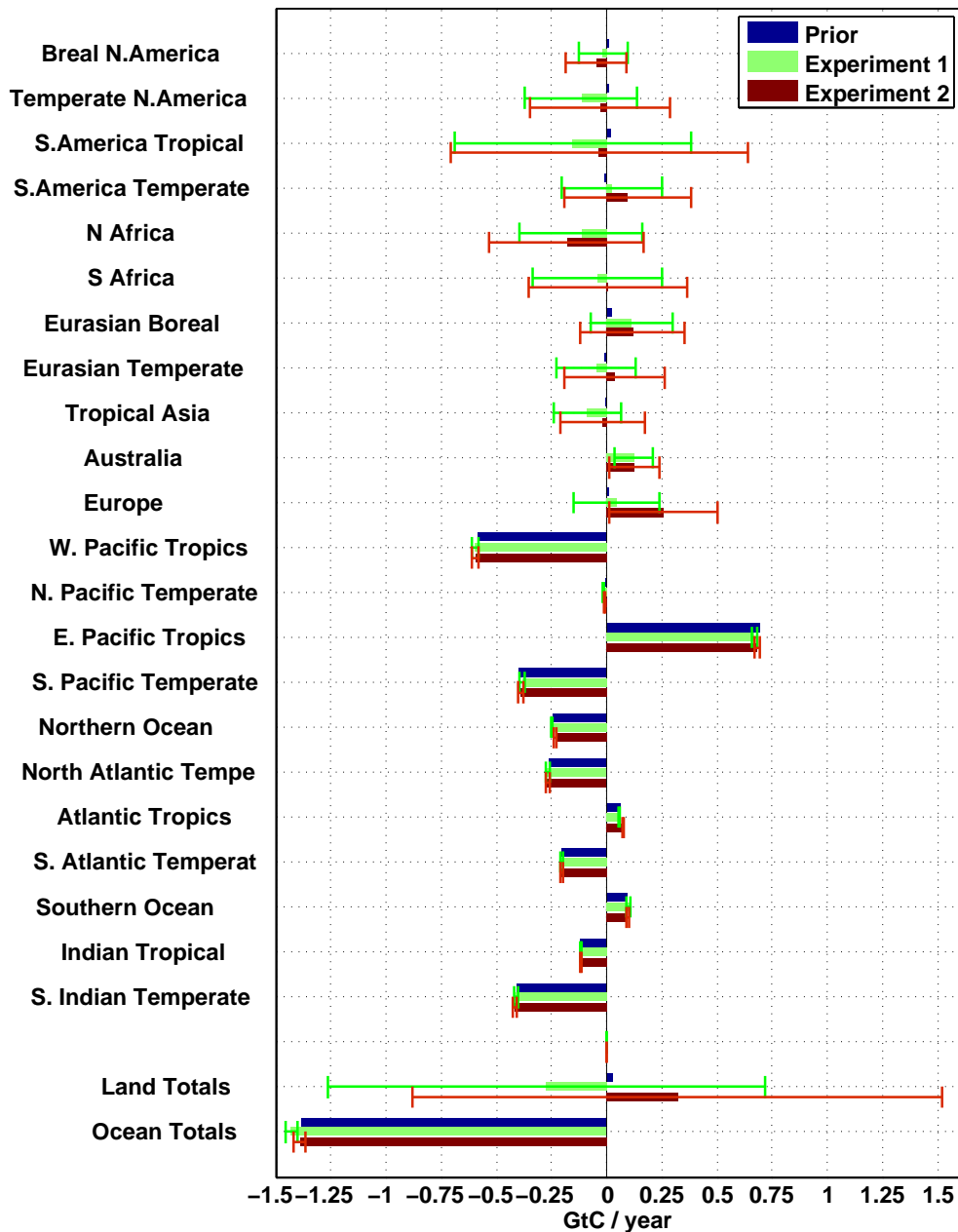


Figure 5.16: Bar plot of total annual fluxes from prior (dark blue), and recovered fluxes from Experiment 1 (green) and 2 (red) with corresponding posterior uncertainty estimates (error bars), aggregated up to TransCom Regions (see Figure 5.15), in GtC year^{-1} . The top 11 regions correspond to land, the next 11 regions correspond to ocean, and the bottom two regions correspond to total land and ocean.

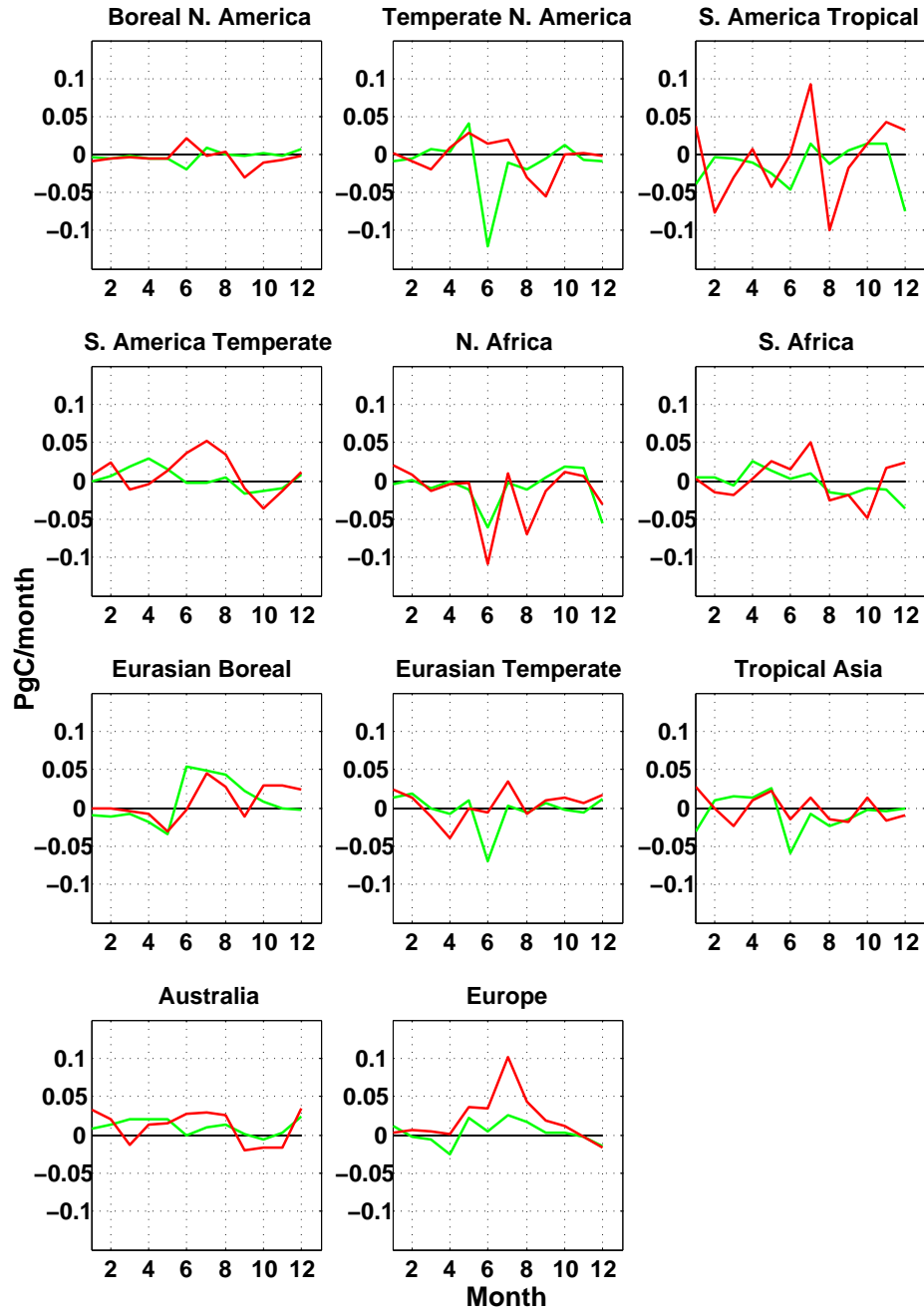


Figure 5.17: Seasonal flux errors for TransCom land regions 1-11 for Experiment 1 (green) and Experiment 2 (red), plotted in GtC month^{-1} .

ment 1 is plotted in green and Experiment 2 in blue to be consistent with Figure 5.16. The pattern for northern boreal and temperate latitudes (Boreal and Temperate N. America, Eurasian Boreal

and Temperate, and Europe) for Experiment 2 is positive bias during summer (consistent with Figure 5.13) relative to Experiment 1 and small to net zero error, negative bias during transition seasons, and little to no bias during winter. The strongest positive bias, 0.1 PgC, occurs during summer in Europe. The largest errors at northern latitudes also tend to occur during summer, suggesting that cloud screening becomes more detrimental for flux estimation during the growing season when component fluxes are larger. While there are no obvious patterns for flux errors in the tropics, flux errors are nevertheless larger on average at monthly time scales when cloud screening is applied.

This section has established a baseline level of flux retrieval error to be expected from ensemble optimization of satellite data using very simple experiments. Experiment 1 estimated spatial and seasonal errors due to intrinsic problems with the ensemble optimization method (Experiment 1). Experiment 2 established the degree of degradation of these intrinsic errors through cloud screening (Experiment 2). The results showed that the inversion is fairly robust to random measurement errors, but not necessarily data reductions that introduce fair weather bias into the measurements.

5.3 Bias Recovery and Perfect Transport

The next step is to test whether the inversion can recover realistic looking carbon sinks hidden within satellite data. To simulate a real world situation that the inversion might encounter, true fluxes (i.e., those fluxes used in the generation of synthetic measurements) are prescribed from realistic carbon processes that cause a net annual sink of ~ 3 GtC over land. While this prescribed global land sink is realistic, the underlying processes are slowly varying and produce fluxes that are small relative to background fluxes. For example, terrestrial NEE varies strongly in time and space due in large part to variations of solar radiation, which varies in time at diurnal, synoptic, and seasonal scales and in space as a function of latitude and season. Prescribed sinks are assumed to be small but persistent such that, over time, the inversion sees through background noise and recovers low signal-to-noise information.

As discussed in Chapter 2.6.1, hypothetical truths are generated by assuming that background

fluxes are systematically biased by processes not modeled well in SiB. Processes that bias model estimates of GPP include underestimation of available nitrogen, forest management, agricultural land use, and CO_2 fertilization. An example of a process that biases $RESP$ is forest regrowth. These persistent processes are represented by the multiplicative correction factors β_{GPP} and β_{RESP} , which were set to zero in control experiments. To generate hypothetical truth from these processes, β_{GPP} and β_{RESP} are prescribed according to the maps in Figure 5.18. GPP (Figure 5.18A), for example, is enhanced ($\beta_{GPP} > 0$) in this hypothetical world in (1) northern mid-latitude terrestrial forests in the northeastern temperate N. America and Europe and (2) tropical regions of S. America, Africa, and Asia. Processes that control long-term and persistent enhancement of GPP include nitrogen deposition in the eastern N. America, agricultural land use in Europe, and CO_2 fertilization in the tropics. To simulate regrowing forests in northeastern Temperate N. America that result from forests still recovering from agricultural abandonment and forests harvested before 1980, respiration (Figure 5.18) is reduced by 5% ($\beta_{RESP} = -0.05$), since by definition a regrowing forest is one in which $RESP$ lags GPP .

Biases in air-sea exchange are also included in this experiment (Figure 5.18C) as a function of latitude, with enhancement of flux in northern middle and high latitudes, reduction of flux at tropical latitudes, and strong reduction of flux at southern middle and high latitudes. Relative to annual mean air-sea exchange shown in Figure 5.7, these biases enhance uptake in the north Pacific and Atlantic Oceans (deepening mixed layers), reduce outgassing in the tropics and especially in the eastern Pacific (enhanced upwelling during La Nina), and reduce outgassing in the Southern Ocean (enhanced circulation during climate change relaxes back to conditions typical of a pre-industrial climate).

Like in the control experiments, the bias recovery experiments assume that β 's are initially unknown in the priors by setting $\beta_{GPP} = \beta_{RESP} = \beta_{OCEAN} = 0$. Experiment 3 assumes that true β 's are constant throughout the year. Experiment 4 assumes β 's vary in space and time and are perturbed with a random 10% noise. This added complexity is necessary considering that β 's,

which represent slowly varying processes in the real world, may be persistent but are likely not constant in time or smooth in space.

5.3.1 Experiment 3: Perfect Transport, Constant and Unperturbed Biases, and Cloud Screening

Maps of total annual true and recovered fluxes are shown at pixel scale in Figure 5.19. By design, the truth (Figure 5.19A) contains net sinks in the annual mean in temperate N. America, Europe, and tropical S. America, Africa, and Asia. **Recovered sinks are similar in both pattern and magnitude**, most notably in the eastern United States and throughout the tropics (Figure 5.19B).

According to Figure 5.19, there are several outstanding differences between the true and recovered fluxes, most noticeably in western Europe, the east coast of S. America, S. Africa, and eastern Australia. These errors are especially apparent in a map of the difference between recovered and true fluxes shown in Figure 5.20. Flux errors are largest where artificial sinks are prescribed.

Total annual recovered sinks, along with prior and true fluxes as reference, are aggregated up to TransCom regions and shown as bar plots with posterior uncertainty estimates in Figure 5.21. Flux recovery is evaluated by comparing recovered fluxes (red bar) with true fluxes (green bar). Recovered and true fluxes have good agreement in Temperate N. America, S. America Tropical, S. Africa, and Tropical Asia. The recovered flux in Temperate N. America is nearly indistinguishable from the true flux. Comparison of bias recovery in Experiment 3 with unbiased recovery in Experiments 1 and 2 (see Figure 5.16) shows that recovered fluxes for the most part stay true to the satellite data. It is very encouraging, for example, that recovered fluxes are closer to the truth than the prior. In regions where substantial sinks are prescribed such as Temperate N. America, S. America Tropical, and N. Africa, flux estimates are certain to within 1σ of having the correct sign (i.e., source vs sink). These posterior uncertainty estimates need to be interpreted carefully, however, as they are strongly dependent on prior uncertainty, and in some cases 1σ is greater than $0.5 \text{ GtC year}^{-1}$ and therefore not that certain (e.g., S. America Tropical). The seasonality of recovered fluxes in

TransCom regions is shown in Figure 5.22. Prior fluxes in Temperate N. America are eventually pulled towards the truth in late summer and fall. The large sink in S. America Tropical is $\sim 100\%$ recovered from the onset of data assimilation.

Some noteworthy errors are also apparent in recovery of TransCom scale sinks. Like in Experiments 1 and 2, recovered fluxes have a strong positive bias relative to the truth in Australia, Europe and Tropical Asia. In fact, the primary difference in these regions from Experiment 2 is that the positive bias is amplified (only slightly in Europe but by nearly $0.2 \text{ GtC year}^{-1}$ in Australia and $0.1 \text{ GtC year}^{-1}$ in Tropical Asia). The recovered flux over Europe suggests a net source when actually the true flux is a sink. The seasonal distribution of the European sink recovery shows that Europe stays close to the prior for almost the entire year, and is at least 1σ away from the truth for much of the year. The recovered solution should always fall somewhere between the prior and true flux, but this is not always the case (e.g., N. Africa in the annual mean and S. Africa at the end of the year) due to errors discussed in Experiments 1 and 2.

The total recovered land sink is nearly 20% less than the true sink (not shown), with the positive bias dominated by errors in Australia, Europe, and Tropical Asia. The total land error represents a net global source of carbon of about $0.6 \text{ GtC year}^{-1}$, half of which comes from baseline errors established in the previous section (see Figure 5.16, red bar under “Land Totals” representing total annual retrieved terrestrial flux). So, about 0.3 GtC comes from intrinsic errors and cloud screening; the remaining error, 0.3 GtC , is likely not detected by the inversion because slowly varying sinks are hidden within large diurnal and seasonal background fluxes. Recovered ocean fluxes aren’t significantly different from priors, in part because prior uncertainty over the ocean is much smaller.

That errors in Experiment 3 tend to be only slightly amplified relative to Experiment 2, especially in Australia and Tropical Asia, suggests that baseline errors aren’t necessarily proportional to the size of hidden sink. This is good news for inversions assuming that prior fluxes are relatively well modeled. It suggests that atmospheric signals due to slowly varying processes aren’t strongly

hidden from the inversion by intrinsic errors in the inverse method, clouds, or random measurement error. This doesn't, however, take into account flux errors that might be incurred due to incorrect prescription of fossil fuel fluxes, systematic measurement error, or noisy looking or seasonally varying β s. Experiment 4 tests this last point.

5.3.2 *Experiment 4: Perfect Transport, Seasonal and Noisy Biases, and Cloud Screening*

Seasonality is added to β s in Figure 5.18 through a sinusoidal function with peak amplitude during boreal summer such that fluxes in northern latitudes are most strongly biased during the active part of the growing season. To represent this seasonal dependence, constant β s are divided into 12 monthly values and then multiplied by the function $1 + 0.5\cos(x + \pi)$. This has the effect of changing regional sinks by a few percent, but increasing the total land sink only very slightly from 2.253 to 2.305 PgC month⁻¹. β s are then multiplied by white gaussian noise with $\mu = 0$ and $\sigma = 0.1$ using the *rnorm*(..) function in *FORTTRAN*. Maps of true and recovered fluxes are shown at pixel scale in Figure 5.23. Recovered sinks are again similar in both pattern and magnitude, and overall not much different from Experiment 3. The recovered fluxes aren't as noisy as the true fluxes due to (1) covariance smoothing in the first run and (2) smoothing out of noisy flux patterns by atmospheric mixing. It is likely, however, that small scale variations in the β s could be recovered more accurately with surface measurements that are close to the sources and sinks. Recovered fluxes aggregated up to TransCom regions (Figure 5.24) are also consistent with Experiment 3.

5.4 **Biased Transport**

The previous experiments have established baseline flux estimation errors that result from (1) intrinsic problems associated with ensemble optimization and (2) degradation of internal errors due to cloud screening. Despite these baseline errors, the inversion is able to recover nearly 80% of a 3

GtC sink hidden within satellite data, which is good but leaves room for improvement. This recovery assumes, however, that the transport model perfectly simulates atmospheric winds. This assumption can be made because the transport model, which can be driven by any offline reanalysis product, is used twice in the experiment: the first use (step one) is in forward simulations for generating synthetic satellite data, the second use (step two) is in inverse calculations through an ensemble of forward simulations determined by a random sampling of β 's with 20% prior uncertainty (or standard deviation of 0.2σ). In the “perfect” transport experiments, the same reanalysis product is used in both steps.

In this Section, biased transport experiments are carried by using one reanalysis product in the first step (synthetic data) and a different reanalysis product in the second step (inversion). GEOS5-0.67x0.5 are used to produce synthetic measurements, where realistic four-dimensional CO₂ output is sampled using the same GOSAT orbital ephemeris in the previous experiments. These synthetic retrievals are then inverted using transport driven by the coarse grid of GEOS4-2.5x2. As discussed in Chapter 4, these models produce similar looking variations of CO₂ at synoptic timescales, but annual mean eddy transport is stronger in GEOS5-0.67x0.5 by about 20%. The approach here is to sample column CO₂ mixing ratios from the higher resolution simulations and then assess how these mixing ratios are interpreted by an inversion that then uses coarse resolution transport to translate synthetic measurements from another model back to surface flux distributions. If variations of column CO₂ are systematically different between transport models, fluxes estimated by the inversion will be different from surface fluxes going into synthetic measurements, and flux estimation errors will result.

Two experiments are run: Experiment 5, where unbiased truth (priors with β 's set to zero) is run through GEOS5-0.67x0.5 to generate synthetic satellite data, and Experiment 6, where biased truth (priors with monthly varying non-zero β 's added to generate annual sinks) is run through GEOS5-0.67x0.5. Experiment 5 is therefore related to Experiment 2 in that the same fluxes are used, but different in that fluxes are run through a different transport model. Experiment 6 is related

to Experiment 4 for the same reason.

5.4.1 *Experiment 5: Biased Transport, Unbiased Truth, and Cloud Screening*

Annual mean errors in terrestrial NEE are shown at pixel scale in Figure 5.25. ***Large, spatially coherent flux errors emerge on a global scale due to differences in transport between GEOS4 and GEOS5.*** In particular, sinks appear over N. America and tropical Asia while net sources emerge over Europe and temperate and boreal Asia. S. America and S. Africa have strongly opposing sources and sinks. Annual errors in Experiment 5 are significantly larger than those in Experiment 2.

It is even worse on seasonal timescales (Figure 5.26), especially during boreal summer. In most regions, similar patterns are seen throughout the year. For example, sinks consistently arise in N. America, sources in Europe, and strongly opposing sources and sinks in S. America and Africa, regardless of season. ***The summer sink in N. America in particular is in stark contrast to the summer source created when cloudy points were removed in Experiment 2.*** There tend to be seasonal variations of sources and sinks in boreal Eurasia, with zero net flux during winter, sinks during spring, a strong source during summer, and back to a sink during fall.

These results are aggregated up to TransCom regions and compared to experiments with perfect transport in Figure 5.27. The key result here is that flux errors are small at continental scale, with truth contained within the 1σ bounds of the posterior uncertainty, when transport is unbiased and all satellite points are included (Experiment 1). When cloud screening is applied similar errors occur, except flux errors grow large enough in Australia and Europe that the truth is no longer contained within 1σ (Experiment 2). With the exception of Europe and Australia, the inversion incurs mostly small errors when given realistic satellite data and a perfect transport model. When transport is biased, however, much larger continental scale flux errors occur. In the cases of Boreal N. America, Temperate N. America, Eurasian Temperate, Australia, and Europe, flux errors are large and certain enough that the truth is no longer contained within 1σ of the recovered flux. ***The***

largest flux errors occur in Europe and Temperate N. America, amounting to 0.51 ± 0.256 and $-0.41 \pm 0.324 \text{ GtC year}^{-1}$, respectively.

The seasonal cycles of true and recovered fluxes for TransCom land regions are shown in Figure 5.28. Recovered fluxes have the same seasonality as the truth, but are sometimes characterized by fluctuations about the truth. While flux errors accumulate in the annual mean as shown in Figure 5.27 over certain regions such as Europe, Eurasian Temperate, Temperate N. America, and Boreal N. America, other regions, such as S. America Tropical (and the tropics in general) have large seasonal errors that cancel in the annual mean.

5.4.2 Experiment 6: Biased Transport, Biased Truth, and Cloud Screening

Annual errors due to biased transport and biased truth (i.e., monthly varying sinks) are shown in Figure 5.29. Errors due solely to biased transport are seen by comparing the green bar from Experiment 4 (perfect transport) with the red bar from Experiment 6 (biased transport). The largest errors (relative to Experiment 4) are in S. America Tropical ($\sim 0.2 \text{ GtC year}^{-1}$ source), S. America Temperate ($\sim 0.3 \text{ GtC year}^{-1}$ sink), N. Africa ($\sim 0.4 \text{ GtC year}^{-1}$ source), Tropical Asia ($\sim 0.25 \text{ GtC year}^{-1}$ sink), and Europe ($\sim 0.35 \text{ GtC year}^{-1}$ source). Posterior uncertainty estimates are actually larger in a few regions when transport is biased. This is because the uncertainty is a function of the variance of β times component flux estimates. Flux estimates in most regions are slightly larger (or more wrong) in the case of biased transport, and so uncertainty also increases slightly.

The seasonal cycle of true and recovered fluxes for TransCom land regions for the case of biased truth is shown in Figure 5.30. Like in Experiment 5, recovered fluxes have the same seasonality as the truth with some fluctuation superimposed by transport bias. Also like Experiment 5, posterior uncertainty decreases in time relative to the prior. In most cases, the truth is contained within 1σ of the posterior uncertainty. Flux estimates in some regions such as Tropical Asia, Boreal N. America, and Eurasian Temperate are just outside the truth. Europe is a fairly extreme outlier in this experiment and is close to 2σ away from the truth during the summer. This means that the

retrieved flux is positively biased 95% of the time and that the inversion recovers the true flux less than 5% of the time. In other words, given the wrong transport, fluxes retrieved during summer will be positively biased at least 95% of the time.

Seasonal flux errors (recovered minus true) for TransCom land regions are plotted for Experiments 5 and 6 in Figure 5.31. With the exception that Experiment 5 estimates strong summer drawdown in Boreal and Temperate N. America, the seasonality of flux errors is consistent between biased transport experiments. It seems the need for a strong sink in the biased transport model is satisfied by the N. American sink imposed in the satellite data in Experiment 6.

5.5 Discussion and Conclusions from Part 3

This chapter consists of a comparison of end-to-end OSSEs with perfect and biased transport to test for flux estimation errors in the MLEF inversion framework. All flux estimates were optimized using MLEF inversion of synthetic satellite data with 3 ppm random measurement error. In the so-called perfect transport OSSEs, which consisted of experiments with and without hypothetical carbon sinks hidden within satellite data, the same transport model (PCTM driven by GEOS4-2.5x2) was used to generate and invert synthetic data. Because of the possibility that systematic errors in transport, such as those discussed in Chapter 4, are aliased into errors in inverse estimates of surface flux, a third set of so-called biased transport OSSEs were run in which synthetic satellite data was generated using a global mesoscale model (PCTM driven by GEOS5-0.67x0.5) and inverted using a coarse resolution global model (PCTM driven by GEOS4-2.5x2).

The perfect transport OSSEs are robust to random measurement errors and are able to recover small but reasonable looking sinks hidden within satellite data. The robustness of the inversion to random measurements errors results from the tendency for random errors to average out over time (in contrast to biased measurement errors, which are not discussed in this study). Larger flux estimation errors are incurred in the perfect transport OSSEs when column CO₂ data is excluded due to cloud contamination. There is a tendency in northern latitudes, most notably in Europe, for posi-

tive surface flux biases during the growing season, suggesting that synthetic satellite measurements must also have positive bias when data from moist synoptic storms is excluded. This is consistent with temporal sampling errors in atmospheric CO₂ mixing ratio calculated by Corbin et al. [2008] who show, along with Parazoo et al. [2008], that satellite data becomes enriched with CO₂ during the growing season primarily due to masking of large horizontal CO₂ gradients from satellites by clouds. These simple perfect transport OSSEs have demonstrated the tendency for fair weather bias in satellite measurements in northern mid-latitudes to be aliased in flux inversions as spatially coherent positively biased surface fluxes of up to 0.1 PgC month⁻¹ but at the very worst no more than 0.257 ± 0.245 PgC year⁻¹.

Nevertheless, the inversion recovers realistic looking sinks hidden in satellite data despite (1) errors that result from excluding data in moist synoptic storms, (2) large and high frequency background noise, (3) random measurement errors of 3 ppm, and (4) monthly varying sources and sinks that contain random spatial noise. The best sink recovery occurs in the Amazon, where satellite data is all but eliminated by clouds. Further investigation is needed, but two possible explanations are (1) weak Coriolis and slow mixing timescales enhance atmospheric memory of nearby sources and sinks, thus increasing the odds that a satellite will sample a non-cloudy and information containing pixel, and (2) information over S. America is eventually propagated offshore where the chance of cloud contamination is reduced. Because the sinks are slowly varying and persistent throughout the year, and the MLEF framework is designed to propagate state vectors and error covariance matrices forward in time between assimilation cycles, optimized fluxes are able to learn from a years worth of satellite data and converge within reasonable distance of the true fluxes.

Biased transport leads to additional errors in flux estimation at all latitudes. The largest annual errors occur in northern temperate and boreal latitudes, including Boreal and Temperate N. America, Eurasian Temperate, and Europe. For example, the inversion estimates a 0.5 ± 0.256 GtC year⁻¹ source in Europe (nearly double the error due to cloud screening) and 0.41 ± 0.324 GtC year⁻¹ sink in Temperate N. America (almost no error due to cloud screening) even though no such

sources or sinks are prescribed in the satellite data. Other regions that don't experience large annual errors actually experience large opposing seasonal errors that cancel. Flux errors are equally large when sinks are added to the synthetic satellite data. The inversion is confident to 1σ that 5 out of the 11 land regions contain sources or sinks of CO_2 that don't exist in the true fluxes. These flux error estimates are likely to be conservative given that the (1) two analysis products used in the biased transport OSSE are similar in architecture and (2) same chemistry transport model is used to generate and invert synthetic satellite data.

Flux errors caused by biased transport present a real challenge for inversion modelers and, as discussed in a similar study by Houweling et al. [2010], put stringent requirements on the performance of transport models. Theoretically, transport errors could be accounted for in the observation covariance matrix. This is currently done in in-situ inversions in response to high uncertainty of nocturnal boundary layer dynamics by strongly reducing the precision of nocturnal continuous measurements [e.g., Lokupitiya et al., 2008]. This solution is less than ideal, however, as these measurements are essentially filtered from the inversion and therefore contribute almost no information to flux optimization. A far more desirable solution is to use observed information about vertical tracer profiles (e.g., correlation of vertical profile of CO_2 with CO) to learn about mixing schemes and make necessary adjustments.

This raises the question as to whether there are certain aspects of model development that could and/or should receive priority. With regard to this study, are there certain systematic differences between GEOS4-2.5x2 and GEOS5-0.67x0.5 that cause large pixel- and continental- scale flux errors? For example, Chapter 4 discussed two important differences between these models: (1) systematically weaker vertical mixing in GEOS5-0.67x0.5 and (2) finer grid spacing and therefore better resolution of baroclinic waves. Although eddy transport differences are significant during winter, results from this chapter indicate that flux errors in northern mid-latitudes are very small during winter; thus, winter transport bias might not matter for CO_2 flux estimation. However, large eddy transport errors also occur during summer, and we saw that annual mean flux errors are

dominated by errors during summer when component fluxes and fine-scale vertical mixing by deep convection are at peak. It is therefore possible that weak vertical mixing in GEOS5-0.67x0.5 during summer contributes significantly to flux errors. This is certainly consistent with many previous studies [e.g., Stephens et al., 2007] who found that vertical mixing and surface flux estimation are strongly related. Future studies could do a much better job isolating the primary source of error by inverting satellite data with a model that has the capability of running a multiple grid spacing with vertical mixing held constant, and vice-versa.

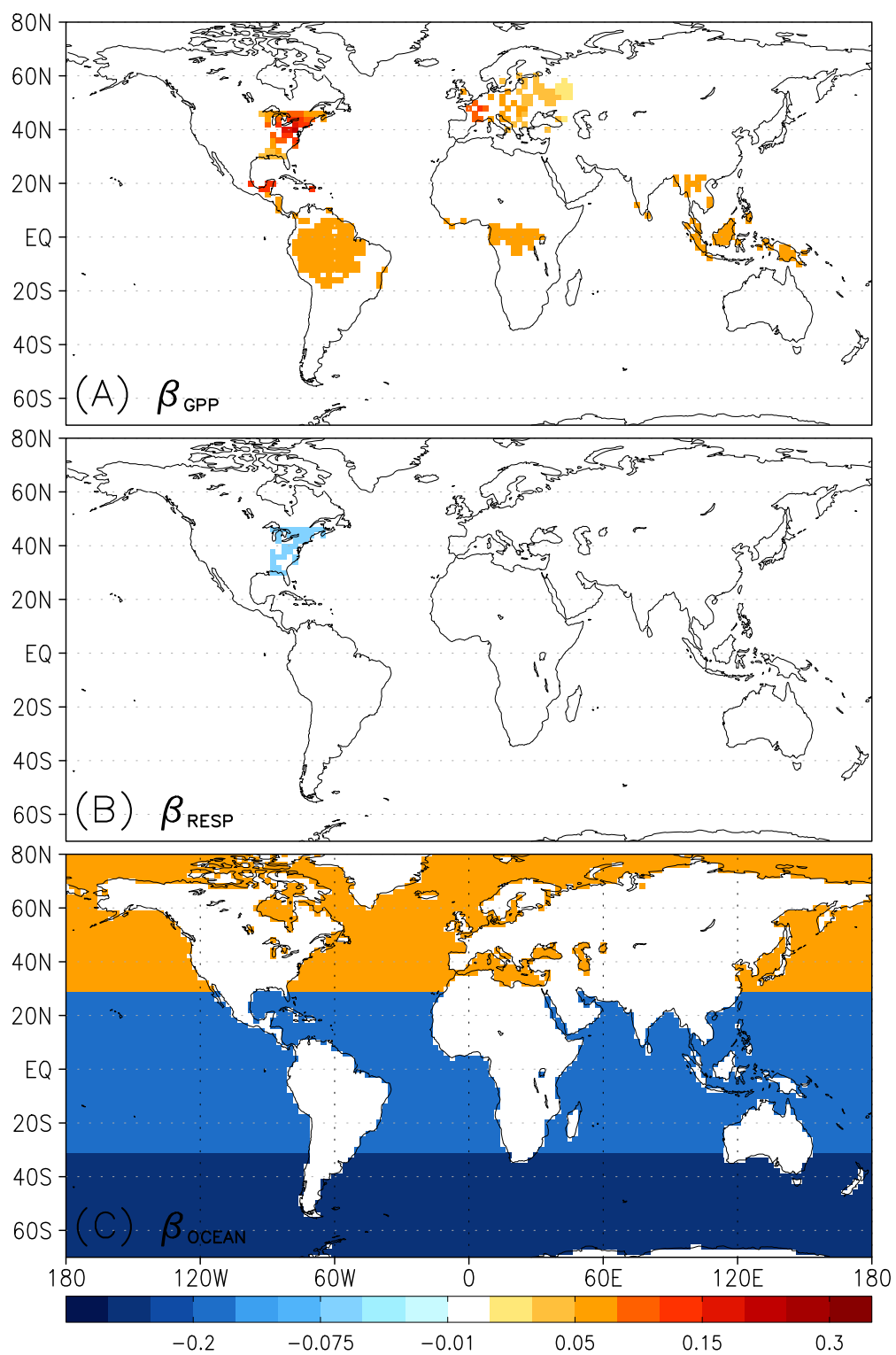


Figure 5.18: Multiplicative correction factors β_{GPP} (a), β_{RESP} (b), and β_{OCEAN} (c).

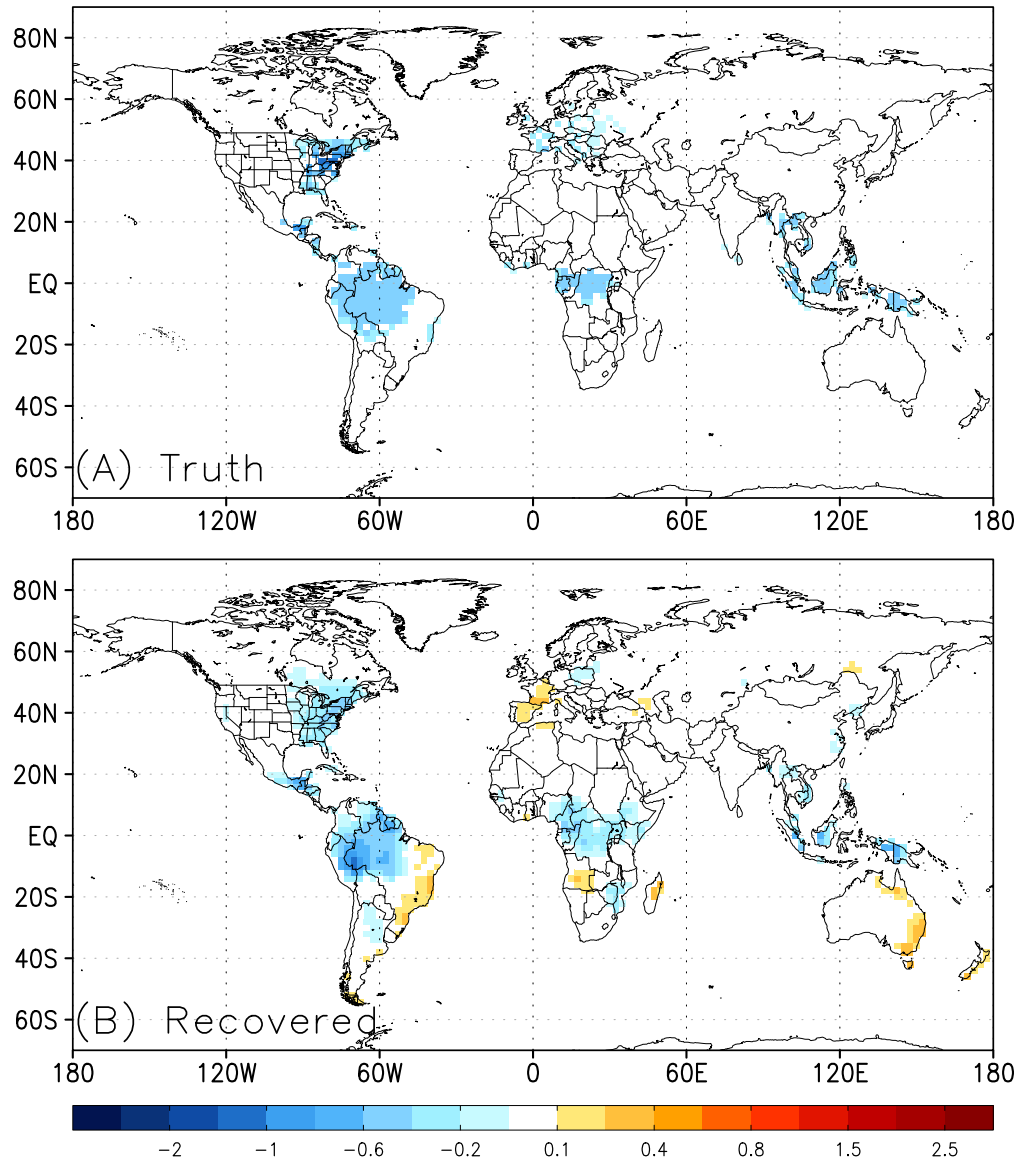


Figure 5.19: True (a) and recovered (b) annual mean terrestrial NEE in $\mu\text{moles m}^2 \text{s}^{-1}$ for Experiment 3.

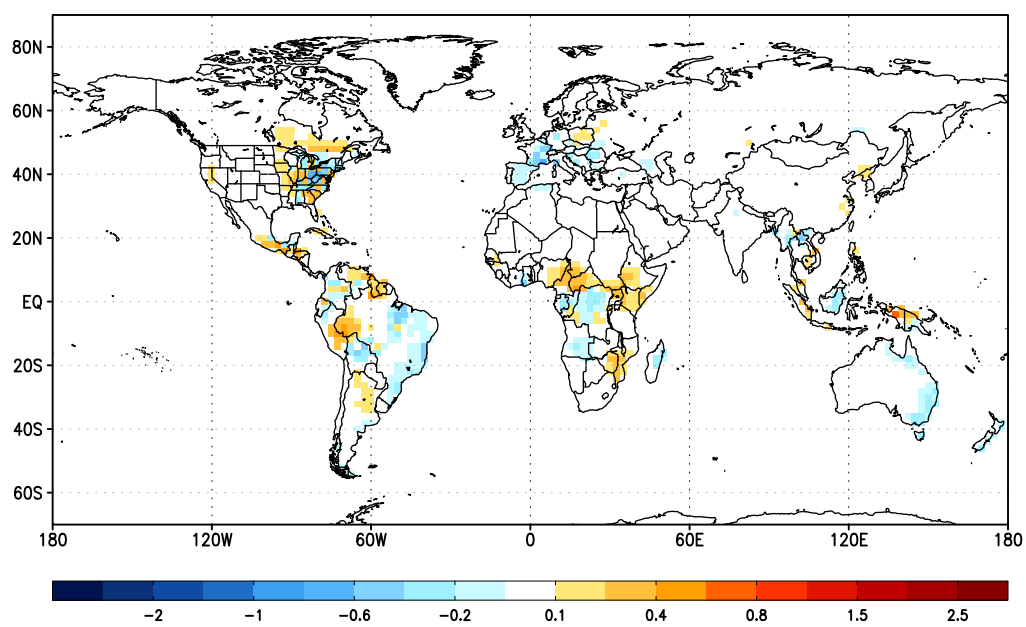


Figure 5.20: Difference between true and recovered annual mean flux, in $\mu\text{moles m}^2 \text{s}^{-1}$, for Experiment 3.

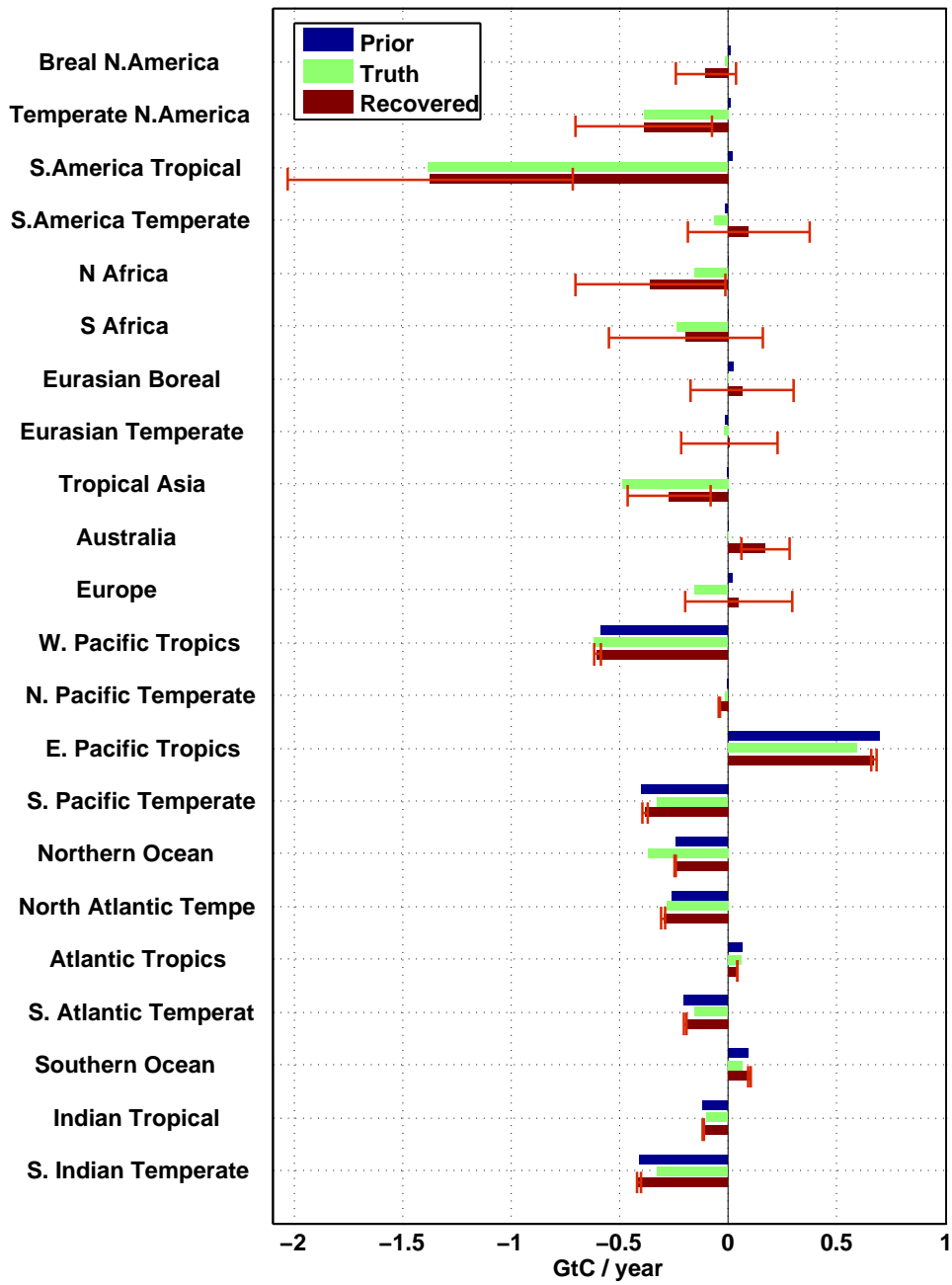


Figure 5.21: Bar plot of annual prior flux (dark blue), true flux (green), and recovered flux (red), aggregated up to TransCom regions like Figure 5.16, and plotted in GtC year^{-1} for Experiment 3. Posterior uncertainty is plotted in red.

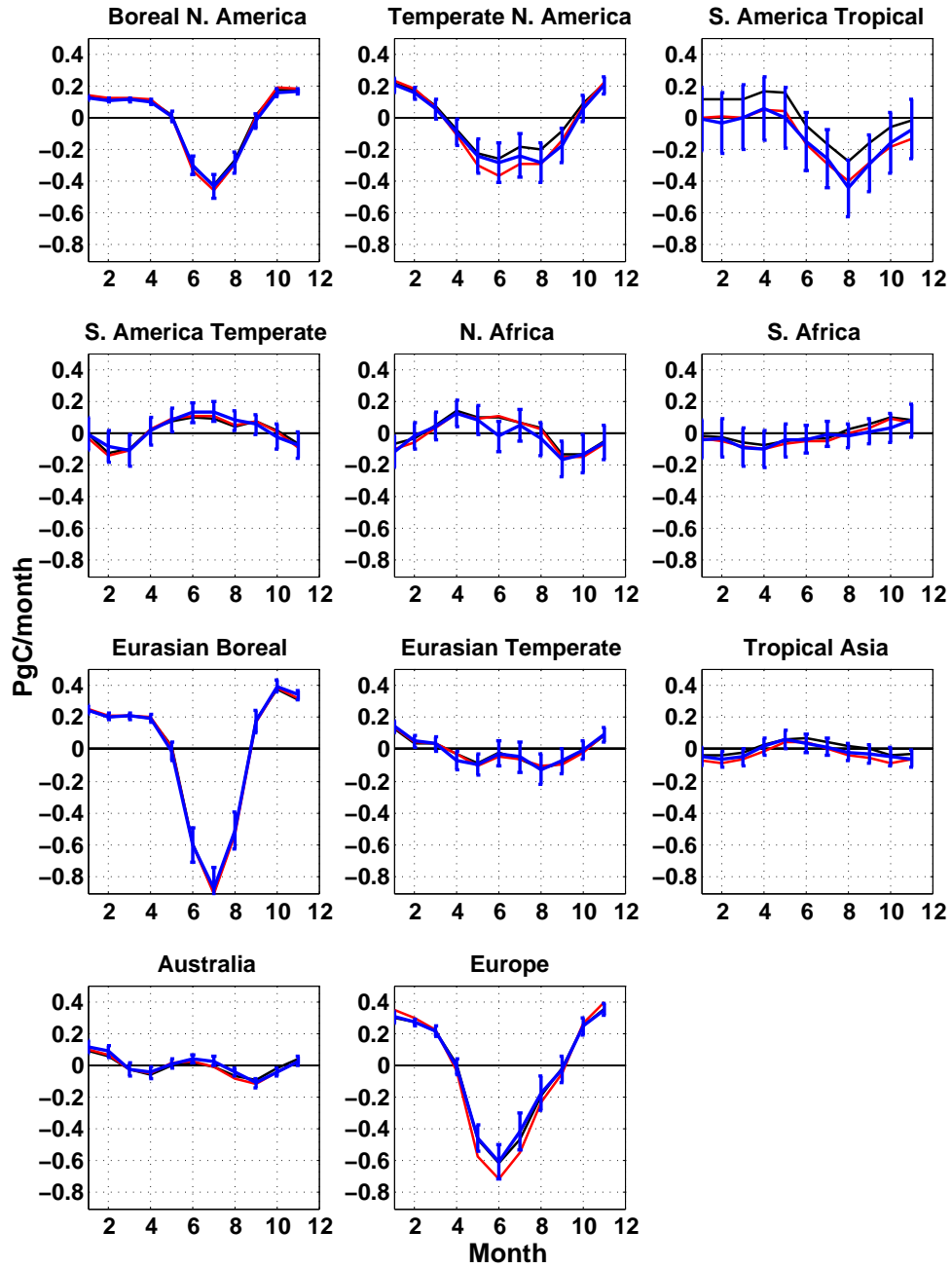


Figure 5.22: Seasonal cycle of prior (black), true (red), and recovered (blue) TransCom fluxes for Experiment 3 (biased truth) for land regions 1-11, plotted in GtC month^{-1} . Posterior (red) uncertainties are plotted as error bars.

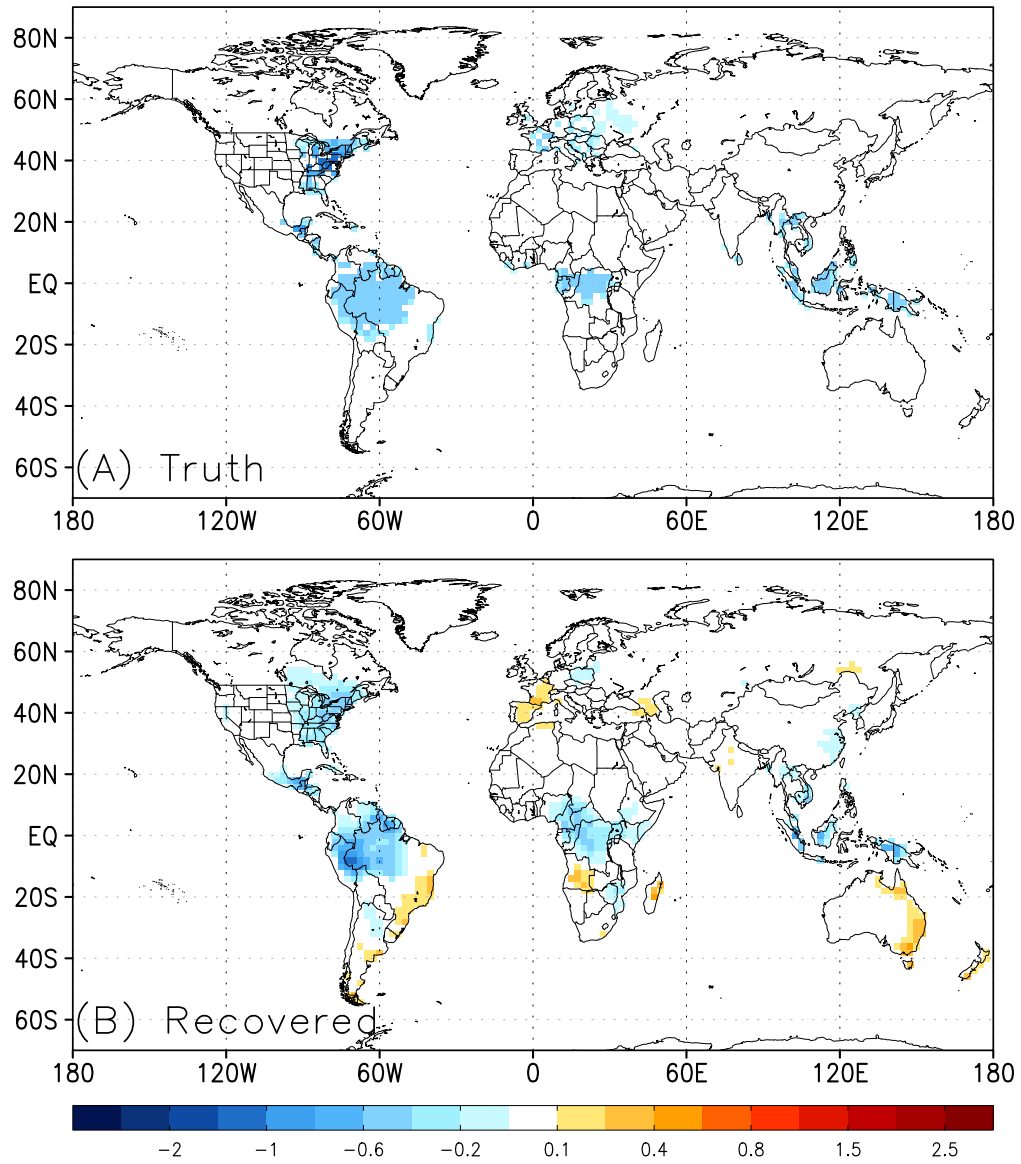


Figure 5.23: True (a) and recovered (b) annual mean terrestrial NEE in $\mu\text{moles m}^2 \text{s}^{-1}$ for Experiment 4.

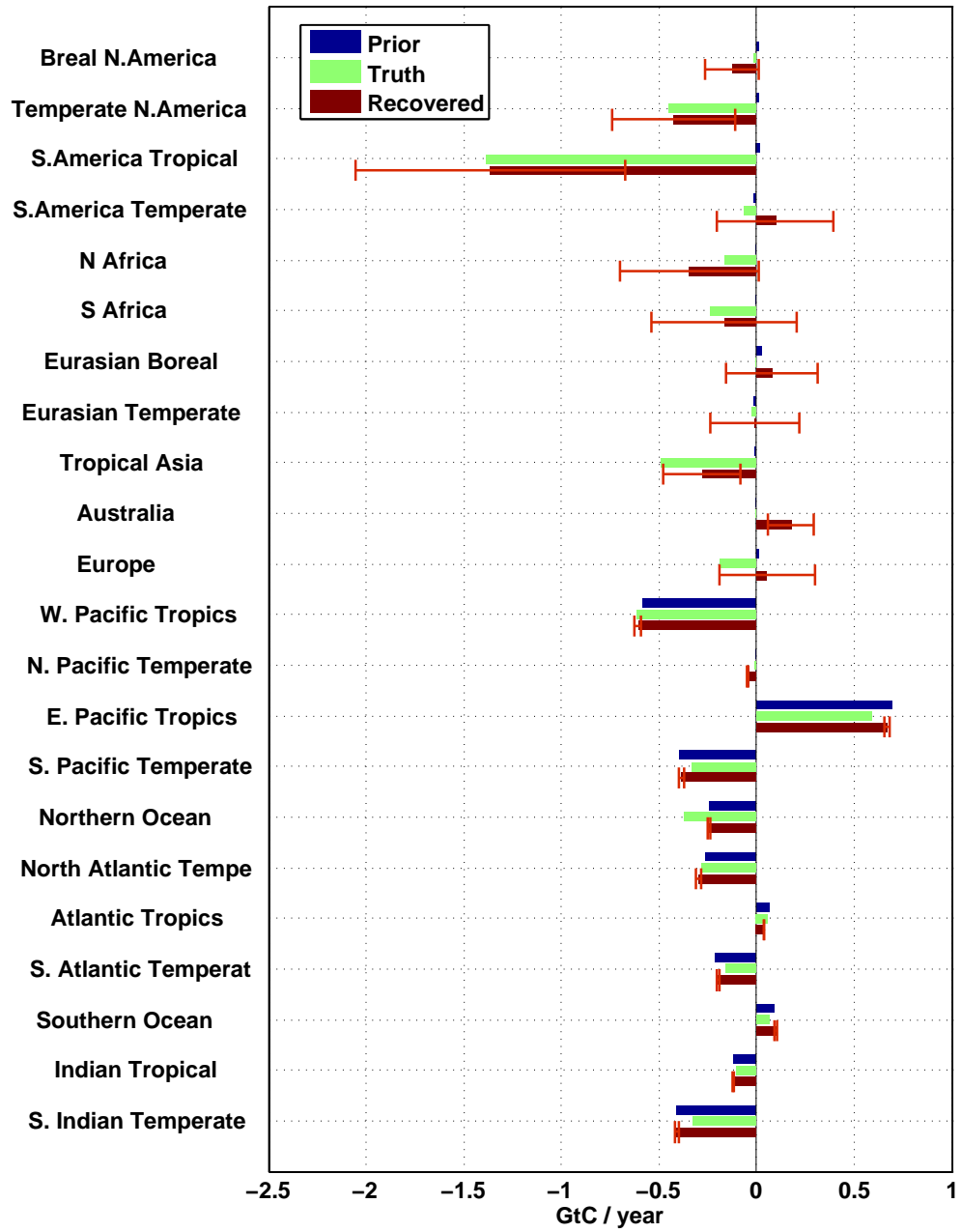


Figure 5.24: Bar plot of annual prior flux (dark blue), true flux (green), and recovered fluxes (red) for Experiment 4.

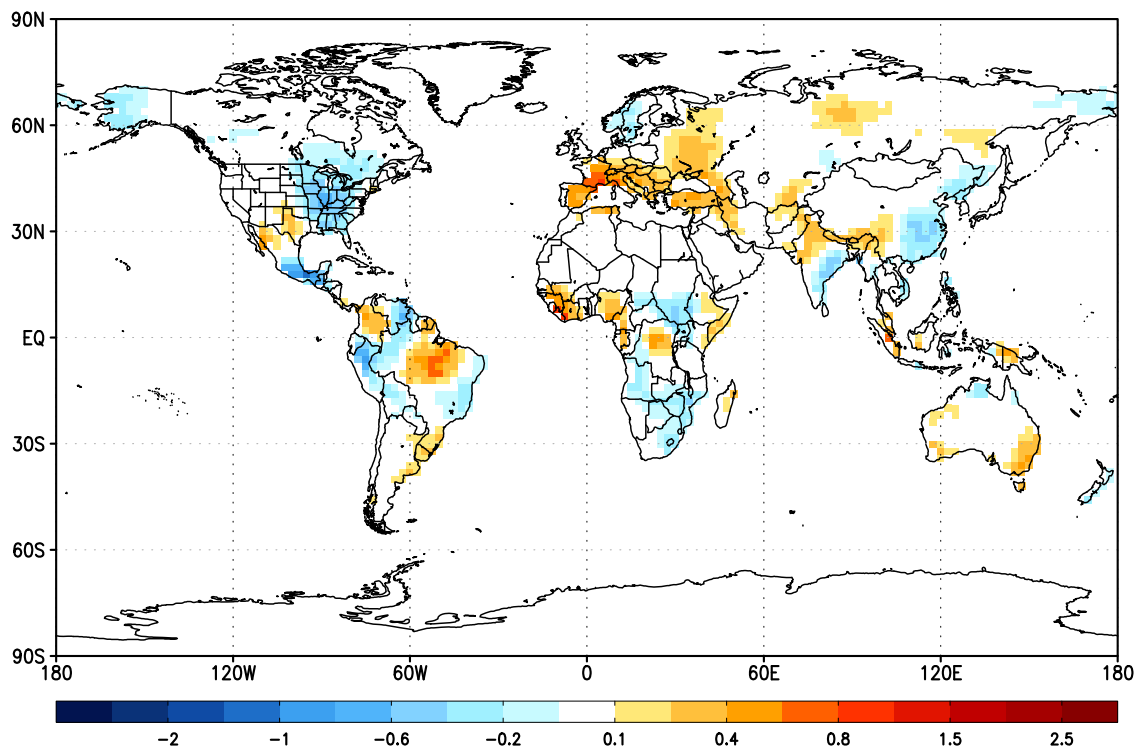


Figure 5.25: Annual mean flux errors over land for Experiment 5 (unbiased truth), plotted in $\mu\text{moles m}^{-2} \text{s}^{-1}$ at pixel scale ($2.5^\circ \times 2^\circ$).

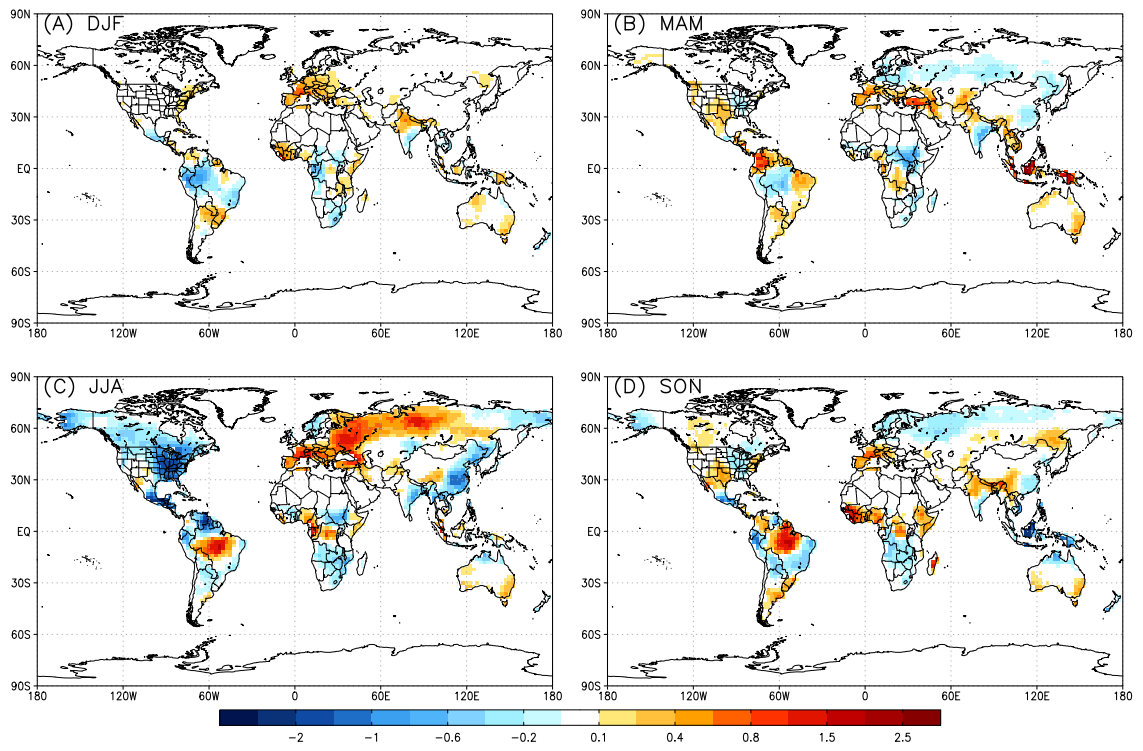


Figure 5.26: Seasonal flux errors over land for Experiment 5 (same units and scale as Figure 5.25).

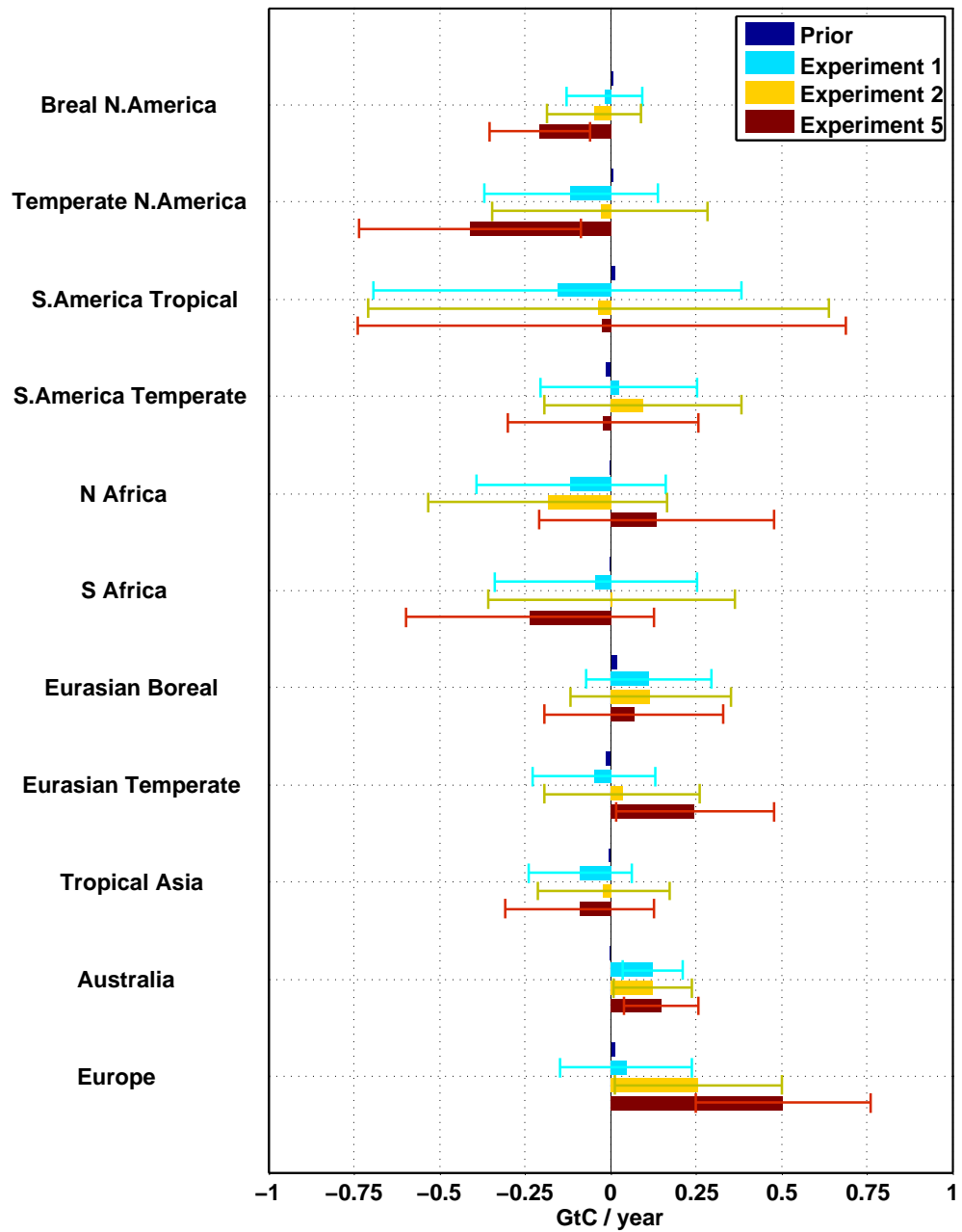


Figure 5.27: Bar plot of annual prior (dark blue), flux errors from Experiment 1 (light blue, perfect transport and no cloud screening), Experiment 2 (yellow, perfect transport and cloud screening), and Experiment 5 (red, biased transport and cloud screening), aggregated up to TransCom land regions and plotted in GtC year^{-1} .

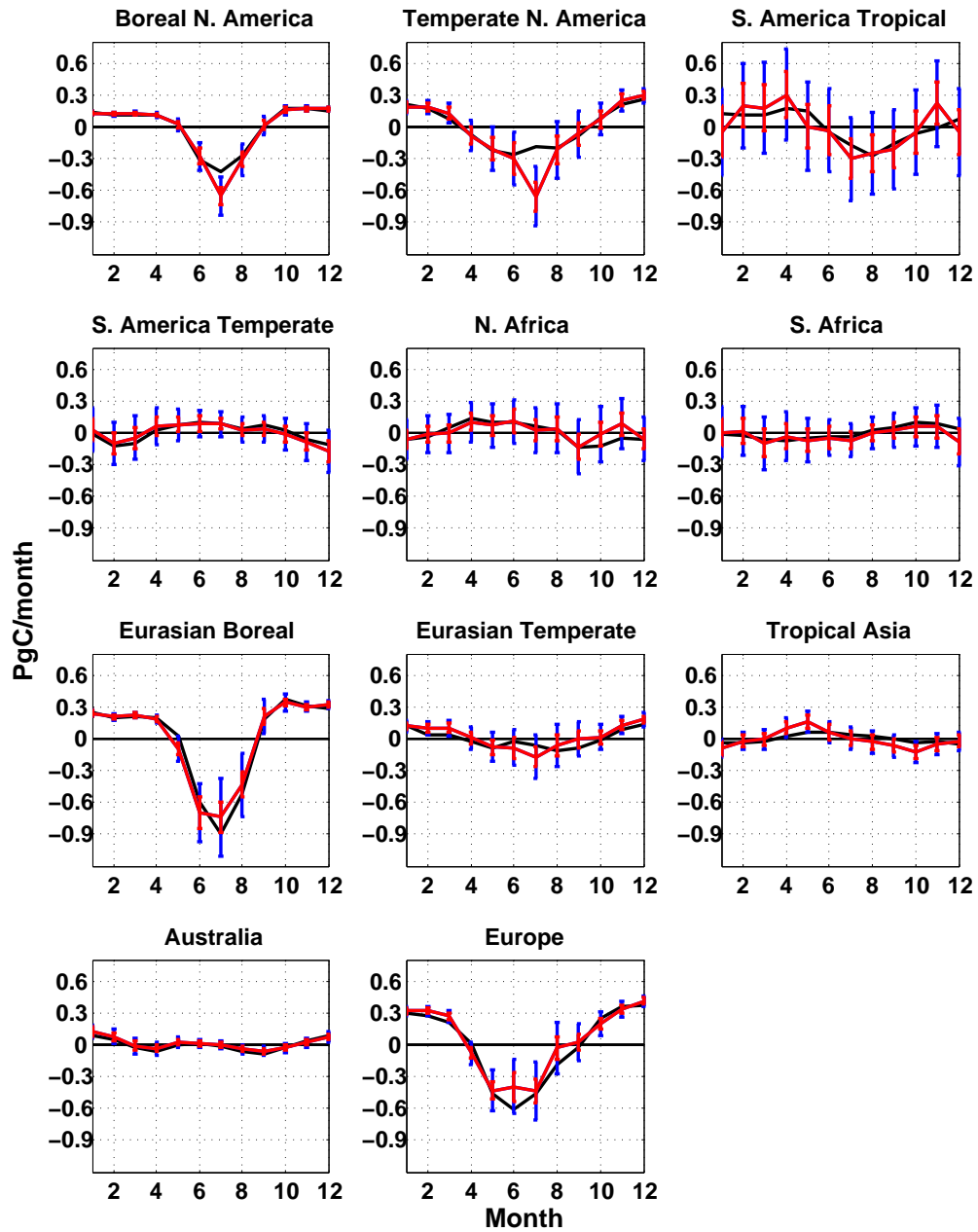


Figure 5.28: Seasonal cycle of true (black) and recovered (red) TransCom fluxes for Experiment 5 (unbiased truth) for land regions 1-11, plotted in GtC month^{-1} . Prior (blue) and posterior (red) uncertainties are plotted as error bars.

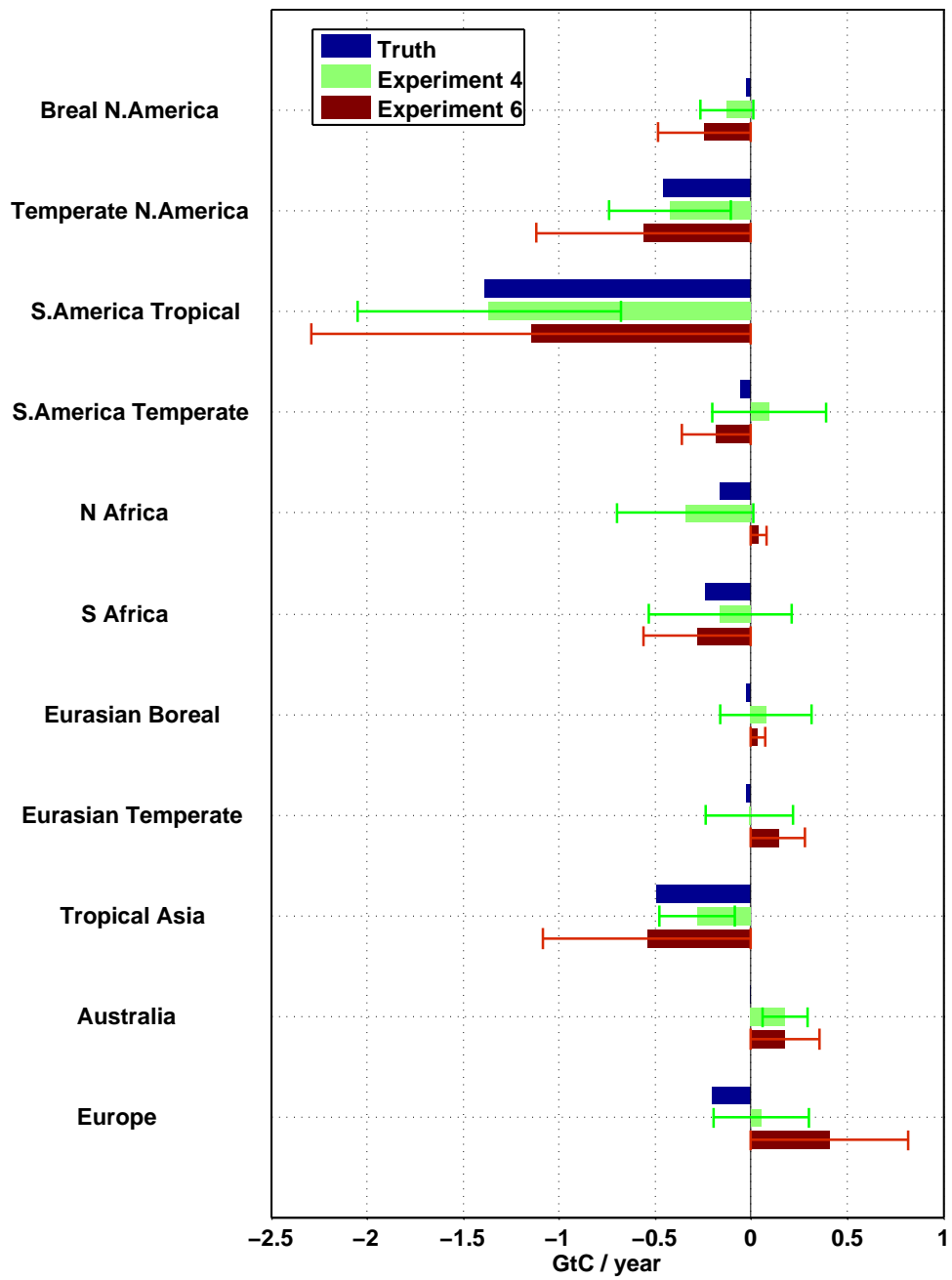


Figure 5.29: Bar plot of annual prior (dark blue), flux errors from Experiment 4 (green, perfect transport and monthly varying sinks), and Experiment 6 (red, biased transport and monthly varying sinks), aggregated up to TransCom land regions and plotted in GtC year^{-1} .

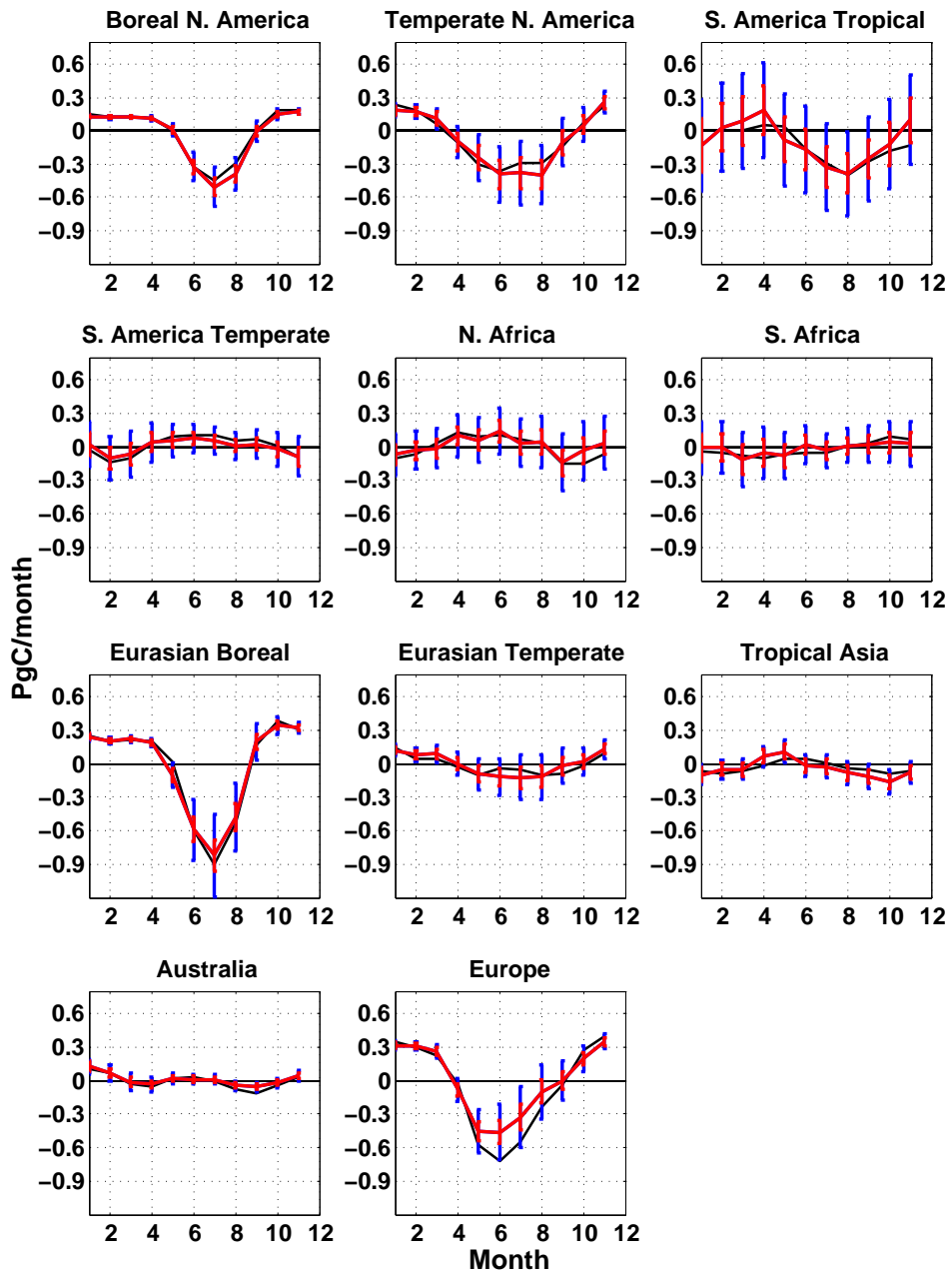


Figure 5.30: Seasonal cycle of true (black) and recovered (red) TransCom fluxes for Experiment 6 (biased truth) for land regions 1-11, plotted in GtC month^{-1} . Prior (blue) and posterior (red) uncertainties are plotted as error bars.

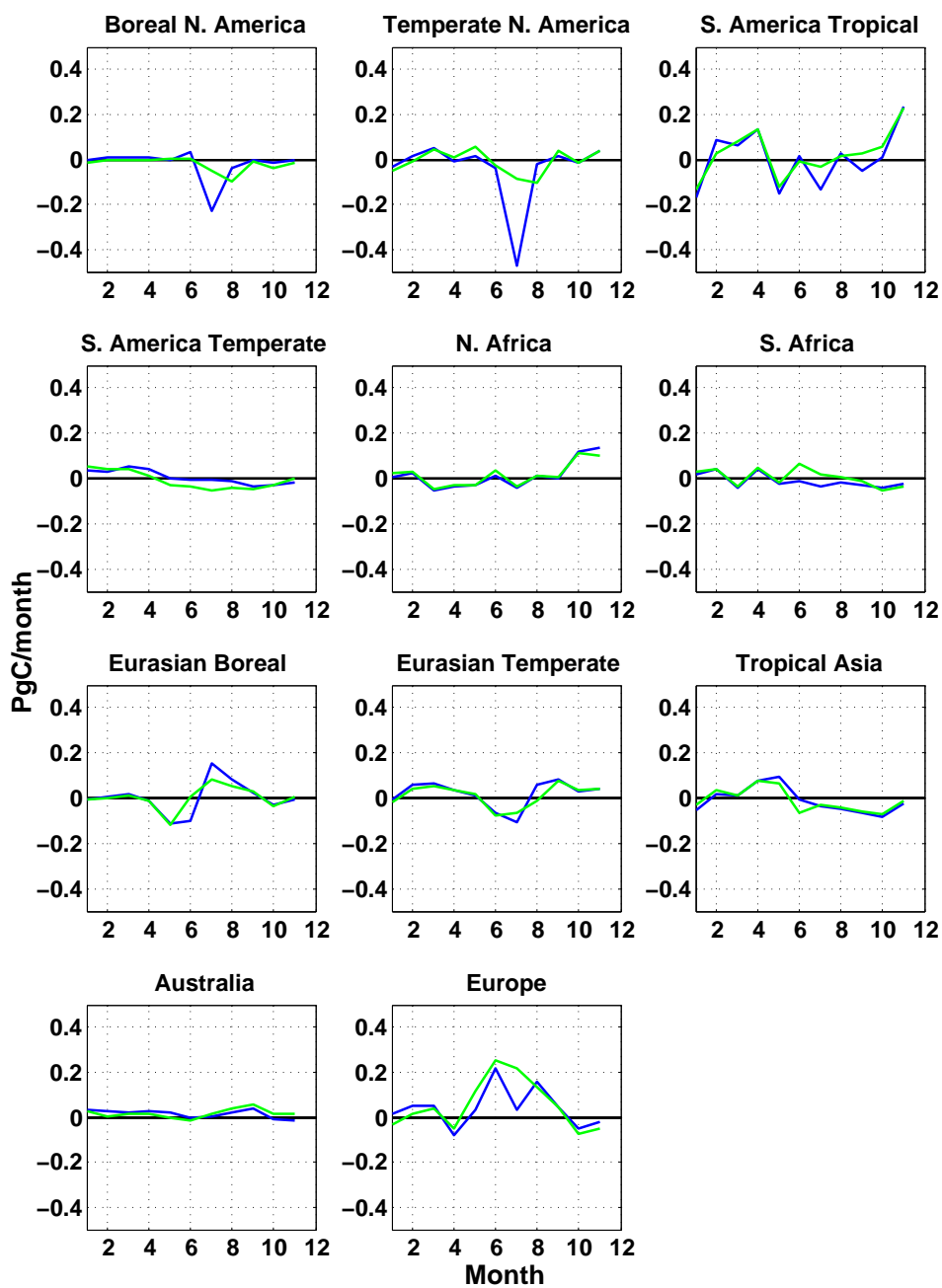


Figure 5.31: Seasonal flux errors for TransCom land regions 1-11 for Experiment 5 (blue) and Experiment 6 (green), plotted in GtC month^{-1} .

Chapter 6

CONCLUSIONS AND FUTURE WORK

Mass transport along moist isentropic surfaces on baroclinic waves represents an important component of the atmospheric heat engine that operates between the equator and poles. This is also an important vehicle for tracer transport, and is correlated with ecosystem metabolism because large-scale baroclinicity and photosynthesis are both driven seasonally by variations in solar radiation. This research has pursued a dynamical framework for explaining atmospheric transport of CO₂ by synoptic weather systems at middle and high latitudes. A global model of atmospheric tracer transport, driven by meteorological analysis in combination with a detailed description of surface fluxes, is used to create time varying CO₂ distributions in the atmosphere. Simulated mass fluxes of CO₂ are decomposed into a zonal monthly mean component and deviations from the monthly mean in space and time. Mass fluxes of CO₂ are described on moist isentropic surfaces in order to include transport along frontal systems in the eddy terms rather than in the mean.

The resulting transport of CO₂ in moist conveyors and dry intrusions accounts for significant exchanges of CO₂ of up to 1 PgC month⁻¹ between middle and high northern latitudes. Through seasonal covariance with ecosystem metabolism, synoptic eddies modulate the seasonality of CO₂ mixing ratio in northern latitudes by damping seasonality in the biologically active mid-latitudes to 50% of that implied by NEE while strongly amplifying seasonality in the Arctic. Meridional fluxes of CO₂ are of comparable magnitude as biological and anthropogenic surface exchange of CO₂ and thus require careful consideration in (inverse) modeling of the carbon cycle. An additional complication arises in that transport along stormtracks is correlated with rising, moist, cloudy air

along frontal clouds and moist conveyors, which systematically hide this CO₂ transport from satellites. Continuous in-situ records can supplement airborne and remotely observed measurements during inclement weather, but only at a few locations. This fair-weather bias in measurements puts stringent requirements on models of moist transport.

Tracer transport by frontal systems and moist processes is associated with sub-grid scale processes (e.g., moist convection and PBL turbulence) that are typically poorly represented in global inverse models and may therefore be a source of error for inverse estimates of CO₂ flux. Sensitivity in meridional transport is investigated by calculating model spread in eddy transport by a global model driven by four analysis products from the Goddard EOS Data Assimilation System for 2005 in combination with identical surface fluxes. Eddy transport is found to be highly variable between simulations, with significant seasonal biases of up to 0.2 PgC, representing up to 50% of fossil fuel emissions. The analysis products used are architecturally very similar and these bias estimates are therefore conservative. Comparison to in-situ CO₂ measurements suggest that differences in grid spacing and vertical mixing by moist convection and PBL turbulence are important causes for the large model spread, but more analysis is needed (e.g., comparison to observed vertical profiles of CO and CO₂, model sensitivity experiments holding grid spacing or vertical mixing constant) to gauge fidelity of CO₂ transport at finer grid spacing.

To test for aliasing of transport bias into inverse flux estimates, synthetic satellite data is (1) generated by sampling forward simulations driven by reanalysis at 50 km grid spacing using the GOSAT orbital ephemeris and (2) inverted using transport driven by reanalysis at 200 km grid spacing. The MLEF ensemble filtering method is used to optimize fluxes. When the same transport model is used to generate and invert satellite retrievals, the inversion framework is able to recover realistic looking sinks imposed in the data. When similar transport models containing different vertical mixing and grid spacing are used, flux estimates are highly biased at pixel and continental scale at all latitudes. The most significant errors are the 0.5 ± 0.256 GtC year⁻¹ source in Europe and a 0.41 ± 0.324 GtC year⁻¹ sink in Temperate N. America. About half of the total error in

the biased transport experiment is attributed to sampling biases that occur in northern temperate and boreal latitudes during the growing season as a result of exclusion of column CO₂ data from moist synoptic storm systems. There are also large seasonal errors in tropical regions. Errors due to transport bias are likely to be conservative.

Key results are highlighted below...

- The prominence of tracer transport by synoptic systems is illustrated more clearly when formulated on moist isentropic surfaces
- Transport, principally in synoptic storms, strongly damps the seasonality of CO₂ mixing ratio in northern mid-latitudes to about half that implied by net ecosystem exchange, while amplifying seasonality in the Arctic
- Column integrated meridional fluxes of CO₂ in synoptic eddies are of similar magnitude to anthropogenic surface fluxes of CO₂ in northern mid-latitudes
- CO₂ transport along the east side of baroclinic waves is likely to be largely unobserved by satellites due to correlations of rising condensing air, precipitation, CO₂, and heat transport
- Model differences in meridional fluxes of CO₂ by synoptic storms is significant, up to 50% of fossil fuel emissions
- Inversion of synthetic satellite data using ensemble methods and bias parameter estimation produced realistic looking sinks, up to 80% of global land sink of 3 GtC year⁻¹, assuming underlying transport is unbiased
- Nearly 100% of sinks are recovered in the Amazon despite large reductions in column CO₂ data due to cloud contamination
- Sampling errors in column CO₂ in northern mid-latitudes cause small but spatially coherent flux estimation errors during summer in this test

- Transport biases strongly affect inverse estimates of sources and sinks

Sensitivity of eddy transport to factors such as storm track position, frontal weather systems, seasonal tendencies in CO₂ mixing ratio and the pattern of seasonal change in surface CO₂ flux over the globe poses a challenging task for inversion modelers. This study has addressed implications of frontal weather systems for the atmospheric carbon cycle and demonstrated the need to represent these systems with high fidelity. It could not however link uncertainty in transport to a single factor, making it difficult to make specific recommendations for future modeling efforts. Future studies would therefore do well to use a global model capable of running at multiple grid spacings and/or with multiple vertical mixing schemes to examine sensitivity of eddy transport to (1) vertical mixing with grid spacing held constant and (2) grid spacing with vertical mixing held constant. Such a model could be applied rather easily in an ensemble inversion framework, in which an adjoint is not required, to test for aliasing of a single factor into surface flux errors.

This work has touched on the influence of storm track position on transport by moist synoptic storms. It is observed, for example, that storm track position shifts north and south with annular modes and quite possibly climate change. Using a dry dynamical core of an AGCM, Butler et al. [2010] show that heating in the tropical troposphere might lead to a poleward shift of extratropical storm tracks. Enhancement of moist isentropic circulations with global warming are also possible, as shown in work by [Laliberte and Pauluis, 2010].

BIBLIOGRAPHY

- Abramowitz, M. and I. A. Stegun, 1965: *Handbook of Mathematical Functions*. Dover. 1046 pp.
- Abshire, J. B., H. Riris, G. Allan, X. Sun, J. Chen, S. R. Kawa, J.-P. Mao, M. Stephen, and J. F. Burris, 2007: Laser Sounder for Global Measurement the CO₂ Concentrations in the Troposphere from Space. In *14th Coherent Laser Radar Conference*, Snowmass, CO, USA.
- Ahmadov, R., C. Gerbig, R. Kretschmer, S. Korner, C. Rodenbeck, P. Bousquet, and M. Ramonet, 2009: Comparing high resolution WRF-VPRM simulations and two global CO₂ transport models with coastal tower measurements of CO₂. *Biogeosciences*, **6**, 807–817.
- Amiro, B. D., J. B. Todd, B. Wotton, K. A. Logan, M. D. Flannigan, B. J. Stocks, J. A. Mason, D. L. Martell, and K. G. Hirsch, 2001: Direct carbon emission from Canadian forest res, 1959-1999. *Can. J. For. Res.*, **31**, 512–525.
- Andres, R. J., G. Marland, I. Fung, and E. Matthews, 1996: 1 degrees x 1 degrees distribution of carbon dioxide emissions from fossil fuel consumption and cement manufacture, 1950-1990. *Global Biogeochem. Cy.*, **10**, 419–429.
- Aumann, H. H. and R. J. Pagano, 1994: Atmospheric Infrared Sounder on the Earth Observing System. *Optical Engineering*, **33**, 776–784.
- Baker, D. F., H. Bosch, S. C. Doney, D. O'Brien, and D. S. Schimel, 2010: Carbon source/sink information provided by column CO₂ measurements from the Orbiting Carbon Observatory. *Atmos. Chem. Phys.*, **10**, 4145–4165.
- Baker, D. F., R. M. Law, K. R. Gurney, P. Rayner, P. Peylin, A. S. Denning, P. Bousquet, L. Bruhwiler, Y.-H. Chen, P. Ciais, I. Y. Fung, M. Heimann, J. John, T. Maki, S. Maksyutov, K. Masarie, M. Prather, B. Pak, S. Taguchi, and Z. Zhu, 2006: TransCom 3 inversion intercomparison: Impact of transport model errors on the interannual variability of regional CO₂ fluxes, 1988-2003. *Global Biogeochem. Cy.*, **20**, GB1002, 10.1029/2004GB002439.
- Baker, I. A., S. Denning, N. Hanan, L. Prihodko, M. Uliasz, P. Vidale, K. Davis, and P. Bakwin, 2003: Simulated and observed fluxes of sensible and latent heat and CO₂ at the WLEF-TV tower using SiB2.5. *Global Change Biol.*, **9**, 1262–1277.
- Bakwin, P. S., P. P. Tans, D. F. Hurst, and C. Zhao, 1998: Measurements of carbon dioxide on very tall towers: Results of the NOAA/CMDL program. *Tellus*, **50B**, 401–415.

- Baldocchi, D., E. Falge, L. Gu, R. Olson, D. Hollinger, and et al., 2001: FLUXNET: a new tool to study the temporal and spatial variability of ecosystem-scale carbon dioxide, water vapor and energy flux densities. *Bull. Amer. Meteor. Soc.*, **82**, 2415–2434.
- Barford, C. C., S. C. Wofsy, M. L. Goulden, J. W. Munger, E. H. Pyle, and et al., 2001: Factors controlling long- and short-term sequestration of atmospheric CO₂ in a mid-latitude forest. *Science*, **294**, 2415–2434.
- Berkowitz, C. M., P. H. Daum, C. W. Spicer, and K. M. Busness, 1996: Synoptic patterns associated with the flux of excess ozone to the western North Atlantic. *J. Geophys. Res.*, **101**, 28923–28933.
- Bethan, S., G. Vaughan, C. Gerbig, A. Volz-Thomas, H. Richer, and D. A. Tiddeman, 1998: Chemical air mass differences near fronts. *J. Geophys. Res.*, **103**, 13413–13434.
- Bloom, S., A. da Silva, and D. Dee, 2005: Documentation and Validation of the Goddard Earth Observing System (GEOS) Data Assimilation System Version 4. Technical Report Series on Global Modeling and Data Assimilation. Technical report, NASA. Tech. Rep. 104606 V26.
- Bosilovich, M. G., S. D. Schubert, M. Rienecker, R. Todling, M. Suarez, J. Bacmeister, R. Gelaro, G.-K. Kim, I. Stajner, and J. Chen, 2006: NASAs Modern Era Retrospective-analysis for Research and Applications. *U.S. CLIVAR Variations*, **4**, 5–8.
- Bousquet, P., P. Peylin, P. Ciais, P. Friedlingstein, C. Lequere, and P. Tans, 2000: Interannual CO₂ sources and sinks as deduced by inversion of atmospheric CO₂ data. *Science*, **290**, 1342–1346.
- Bovensmann, H., J. P. Burrows, M. Buchwitz, J. Frerick, S. Nol, V. V. Rozanov, K. V. Chance, and A. H. P. Goede, 1999: SCIAMACHY - Mission Objectives and Measurement Modes. *J. Atmos. Sci.*, **56**, 1271–1280.
- Bruhwyler, L. P., A. M. Michalak, W. Peters, D. F. Baker, and P. Tans, 2005: An improved Kalman Smoother for atmospheric inversions. *Atmos. Chem. Phys.*, **5**, 1891–1923.
- Canadell, J. G., C. L. Quere, M. R. Raupach, C. B. Field, E. T. Buitenhuis, P. Ciais, T. J. Conway, N. P. Gillett, R. A. Houghton, and G. Marland, 2007: Contributions to accelerating atmospheric CO₂ growth from economic activity, carbon intensity, and efficiency of natural sinks. *Proc. Nat. Acad. Sci.*, **104**, 18866–18870.
- Carlson, T., 1981: Speculations on the movement of polluted air to the Arctic. *Atmos. Environ.*, **15**, 1473–1477.
- Carlson, T. S., 1998: *Mid-latitude Weather Systems*. Am. Meteorol. Soc.
- Chan, D., C. W. Yuen, K. Higuchi, A. Shashkov, J. Liu, J. Chen, and D. Worthy, 2004: On the CO₂ exchange between the atmosphere and the biosphere: the role of synoptic and mesoscale processes. *Tellus*, **56B**, 194–212.
- Chen, B., J. M. Chen, J. Liu, D. Chan, K. Higuchi, and A. Shashkov, 2004: A vertical diffusion scheme to estimate the atmospheric rectifier effect. *J. Geophys. Res.*, **109**, D04306, doi:10.1029/2003JD003925.

- Chen, P. and W. A. Robinson, 1992: Propagation of planetary waves between the troposphere and stratosphere. *J. Atmos. Sci.*, **49**, 2533–2545.
- Chevallier, F., F.-M. Breon, and P. J. Rayner, 2007: Contribution of the Orbiting Carbon Observatory to the estimation of CO₂ sources and sinks: Theoretical study in a variational data assimilation framework. *J. Geophys. Res.*, **112**, D09307, doi:10.1029/2006JD007375.
- Chevallier, F., M. Fisher, P. Peylin, S. Serrar, P. Bousquet, F.-M. Breon, A. Chedin, and P. Ciais, 2005: Inferring CO₂ sources and sinks from satellite observations: Method and application to TOVS data. *J. Geophys. Res.*, **110**, D24309, doi:10.1029/2005JD006390.
- Chevallier, F., S. Maksyutov, P. Bousquet, F.-M. Breon, R. Saito, Y. Yoshida, and T. Yokota, 2009: On the accuracy of the CO₂ surface fluxes to be estimated from the GOSAT observations. *Geophys. Res. Lett.*, **36**, L19807, doi:10.1029/2009GL040108.
- Chdin, A., R. Saunders, A. Hollingsworth, N. A. Scott, M. Matricardi, J. Etcheto, C. Clerbaux, R. Armante, and C. Crevoisier, 2003: The feasibility of monitoring CO₂ from high-resolution sounders. *J. Geophys. Res.*, **108**, doi:10.1029/2001JD001443.
- Chdin, A., S. Serrar, R. Armante, N. A. Scott, and A. Hollingsworth, 2002: Signatures of annual and seasonal variations of CO₂ and other greenhouse gases from NOAA/TOVS observations and model simulations. *J. Climate*, **15**, 95–116.
- Clarke, L. C. and R. J. Renard, 1965: Experiments in numerical objective frontal analysis. *Mon. Wea. Rev.*, **93**, 547–556.
- Collatz, G. J., J. T. Ball, C. Grivet, and et al., 1991: Physiological and environmental regulation of stomatal conductance, photosynthesis, and transpiration: A model that includes a laminar boundary layer. *Agr. Forest Meteorol.*, **54**, 107–136.
- Collatz, G. J., M. Ribas-Barbo, and J. A. Berry, 1992: Coupled photosynthesis-stomatal conductance model for leaves of C₄ plants. *Aust. J. Plant Physiol.*, **19**, 519–538.
- Collins, W. D., M. Blackmon, C. M. Bitz, G. B. Bonan, C. S. Bretherton, J. A. Carton, P. Chang, S. Doney, J. J. Hack, J. T. Kiehl, T. Henderson, W. G. Large, D. McKenna, and B. D. Santer, 2006: The Community Climate System Model: CCSM3. *J. Climate*, **11**, 21222143.
- Cooper, O. R., C. Forster, D. Parrish, M. Trainer, E. Dunlea, T. Ryerson, G. Hubler, F. Fehsenfeld, D. Nicks, J. Holloway, J. de Gouw, C. Warneke, J. M. Roberts, F. Flocke, and J. Moody, 2004: A case study of transpacific warm conveyor belt transport: Influence of merging airstreams on trace gas import to North America. *J. Geophys. Res.*, **109**, D23S08, doi:10.1029/2003JD003624.
- Cooper, O. R., J. L. Moody, D. D. Parrish, M. Trainer, J. S. Holloway, T. B. Ryerson, G. Hubler, F. C. Fehsenfeld, S. J. Oltmans, and M. J. Evans, 2002: Trace gas composition of mid-latitude cyclones over the western North Atlantic Ocean: A conceptual model. *J. Geophys. Res.*, **107**, 10.1029/2001JD000901.
- Cooper, O. R., J. L. Moody, D. D. Parrish, M. Trainer, T. B. Ryerson, J. S. Holloway, G. Hubler, F. C. Fehsenfeld, S. J. Oltmans, and M. J. Evans, 2001: Trace gas signatures of the airstreams within North Atlantic cyclones: Case studies from the North Atlantic Regional Experiment (NARE 97) aircraft intensive. *J. Geophys. Res.*, **106**, 5437–5456.

- Corbin, K. D., K. D., A. S. Denning, J.-W. Wang, L. Lu, L. Prihodko, and I. T. Baker, 2008: Possible representation errors in inversions of satellite CO₂ retrievals. *J. Geophys. Res.*, **113**, D02301, doi:10.1029/2007JD008716.
- Corbin, K. D. and A. S. Denning, 2006: Using continuous data to estimate clear-sky errors in inversion of satellite CO₂ measurements. *Geophys. Res. Lett.*, **33**, L12810, doi:10.1029/2006GL025910.
- Cox, P. M., R. A. Betts, C. D. Jones, S. A. Spall, and I. J. Totterdell, 2000: Acceleration of global warming due to carbon-cycle feedbacks in a coupled climate model. *Nature*, **408**, 184187.
- Crisp, D., R. M. Atlas, F.-M. Breon, L. R. Brown, J. P. Burrows, P. Ciais, B. J. Connor, S. C. Doney, I. Y. Fung, D. J. Jacob, C. E. Miller, D. O'Brien, S. Pawson, J. T. Randerson, P. Rayner, R. J. Salawitch, S. P. Sander, B. Sen, G. L. Stephens, P. P. Tans, G. C. Toon, P. O. Wennberg, S. C. Wofsy, Y. L. Yung, Z. Kuang, B. Chudasama, G. Sprague, B. Weiss, R. Pollock, D. Kenyon, and S. Schroll, 2004: The Orbiting Carbon Observatory (OCO) mission. *Adv. Space Res.*, **34**, 700–709.
- Davis, K. J., P. S. Bakwin, C. Yi, B. W. Berger, C. Zhao, R. M. Teclaw, and J. G. Isebrands, 2003: The annual cycle of CO₂ and H₂O exchange over a northern mixed forest as observed from a very tall tower. *Global Change Biol.*, pages 1278–1293.
- Denman, K. L. and et al., 2007: *IPCC Climate Change 2007: The Physical Science Basis*. Cambridge Univ. Press.
- Denning, A. S., J. G. Collatz, C. Zhang, D. A. Randall, J. A. Berry, and et al., 1996a: Simulations of terrestrial carbon metabolism and atmospheric CO₂ in a general circulation model. Part 1: Surface carbon fluxes. *Tellus*, **48B**, 521–542.
- Denning, A. S., I. Y. Fung, and D. Randall, 1995: Latitudinal gradient of atmospheric CO₂ due to seasonal exchange with land biota. *Nature*, **376**, 240–243.
- Denning, A. S., M. Holzer, K. R. Gurney, M. Heimann, R. M. Law, P. J. Rayner, I. Y. Fung, S.-M. Fan, S. Taguchi, P. Friedlingstein, Y. Balkanski, J. Taylor, M. Maiss, and I. Levin, 1999: Three-dimensional transport and concentration of SF₆A model intercomparison study (TransCom 2). *Tellus*, **51B**, 266297.
- Denning, A. S., M. Nicholls, L. Prihodko, I. Baker, P. Vidale, K. Davis, and P. Bakwin, 2003: Simulated variations in atmospheric CO₂ over a Wisconsin forest using a coupled ecosystem-atmosphere model. *Global Change Biol.*, **9**, 1241–1250.
- Denning, A. S., D. A. Randall, G. J. Collatz, and P. J. Sellers, 1996b: Simulations of terrestrial carbon metabolism and atmospheric CO₂ in a general circulation model. Part 2: Spatial and temporal variations of atmospheric CO₂. *Tellus*, **48B**, 453–567.
- Doney, S. C., I. Lima, J. K. Moore, K. Lindsay, M. J. Behrenfeld, T. K. Westberry, N. Mahowald, D. M. Glover, and T. Takahashi, 2009: Skill metrics for confronting global upper ocean ecosystem-biogeochemistry models against field and remote sensing data. *J. Mar. Systems*, **76**, 95–112.

- Doney, S. C., K. Lindsay, I. Fung, and J. John, 2006: Natural variability in a stable 1000 year coupled climate-carbon cycle simulation. *J. Climate*, **19**, 3033-3054.
- Donnell, E. A., D. J. Fish, and E. M. Dicks, 2001: Mechanisms for pollutant transport between the boundary layer and the free troposphere. *J. Geophys. Res.*, **106**, 7847-7856.
- Douglass, A. R. and S. R. Kawa, 1999: Contrast between 1992 and 1997 high-latitude spring Halogen Occultation Experiment observations of lower stratospheric HCl. *J. Geophys. Res.*, **104**, 739-754.
- Douglass, A. R., M. R. Schoeberl, R. B. Rood, and S. Pawson, 2003: Evaluation of transport in the lower tropical stratosphere in a global chemistry and transport model. *J. Geophys. Res.*, **108**, doi:10.1029/2002JD002696.
- Eady, E. T., 1949: Long waves and cyclone waves. *Tellus*, **1**, 33-52.
- Eckhardt, S., A. Stohl, H. Wernli, P. James, C. Forster, and N. Spichtinger, 2004: A 15-year climatology of warm conveyor belts. *J. Climate*, **17**, 219-237.
- Eguchi, N. and T. Yokota, 2008: Investigation of clear-sky occurrence rate estimated from CALIOP and MODIS observations. *Geophys. Res. Lett.*, **35**, L23816, doi:10.1029/2008GL035897.
- Eliassen, A., 1983: The Charney-Stern theorem on barotropic-baroclinic instability. *Pure Appl. Geophys.*, **121**, 563-572.
- Emanuel, K. A., 1988: Observational evidence of slantwise convective adjustment. *Mon. Wea. Rev.*, **116**, 1805-1816.
- Engelen, R. J., A. S. Denning, K. R. Gurney, and TransCom3 modelers, 2002: On error estimation in atmospheric CO₂ inversions. *J. Geophys. Res.*, **107**, 4635, doi:10.1029/2002JD002195.
- Eugster, W. and S. Siegrist, 2000: The influence of nocturnal CO₂ advection on CO₂ flux measurements. *Basic and Applied Ecology*, **1**, 177-188.
- Fan, S., M. Gloor, J. Mahlman, S. Pacala, J. Sarmiento, T. Takahashi, and P. Tans, 1998: A large terrestrial carbon sink in North America implied by atmospheric and oceanic carbon dioxide data and models. *Science*, **282**, 442-446.
- Farquhar, G. D., S. von Caemmerer, and J. A. Berry, 1980: A biochemical model of photosynthetic CO₂ assimilation in C₃ plants. *Planta*, **14**, 78-90.
- Fischer, H. and et al., 2002: Synoptic tracer gradients in the upper troposphere over central Canada during the Stratosphere-Troposphere Experiments by Aircraft Measurements 1998 summer campaign. *J. Geophys. Res.*, **107**, 4064, doi:10.1029/2000JD000312.
- Fjørtoft, R., 1950: Application of integral theorems in deriving criteria of stability for laminar flows and for the baroclinic circular vortex. *Geophys. Publ.*, **17**. No. 6.
- Flammer, C., 1957: *Spheroidal Wave Functions*. Stanford University Press. 84 pp.

- Friedlingstein, P., P. Cox, R. Betts, L. Bopp, W. von Bloh, V. Brovkin, P. Cadule, S. Doney, M. Eby, I. Fung, G. Bala, J. John, C. Jones, F. Joos, T. Kato, M. Kawamiya, W. Knorr, K. Lindsay, H. D. Matthews, T. Raddatz, P. Rayner, C. Reick, E. Roeckner, K.-G. Schnitzler, R. Schnur, K. Strassmann, A. J. Weaver, C. Yoshikawa, and N. Zeng, 2006: Climate-Carbon Cycle Feedback Analysis: Results from the C4MIP Model Intercomparison. *J. Climate*, **19**, 3337–3353.
- Fung, I., S. C. Doney, K. Lindsay, and J. John, 2005: Evolution of carbon sinks in a changing climate. *Proc. Nat. Acad. Sci.*, **102**, 201211.
- Fung, I., K. Prentice, E. Matthews, J. Lerner, and G. Russell, 1983: Three-dimensional tracer model study of atmospheric CO₂: Response to seasonal exchanges with the terrestrial biosphere. *J. Geophys. Res.*, **88**, 1281–1294.
- Fung, I. Y., C. J. Tucker, and K. C. Prentice, 1987: Application 290 of Advanced Very High Resolution Radiometer vegetation index to study atmosphere-biosphere exchange of CO₂. *J. Geophys. Res.*, **92**, 2999–3015.
- Geels, C., S. C. Doney, R. Dargaville, J. Brandt, and J. H. Christensen, 2004: Investigating the sources of synoptic variability in atmospheric CO₂ measurements over the Northern Hemisphere continents: A regional model study. *Tellus*, **56B**, 35–50.
- Geels, C., M. Gloor, P. Ciais, P. Bousquet, P. Peylin, A. T. Vermeulen, R. Dargaville, T. Aalto, J. Brandt, J. H. Christensen, and et al., 2007: Comparing atmospheric transport models for future regional inversions over Europe Part 1: Mapping the atmospheric CO₂ signals. *Atmos. Chem. Phys.*, **7**, 3461–3479.
- Gerbig, C., J. C. Lin, S. C. Wofsy, B. C. Daube, A. E. Andrews, B. B. Stephens, P. S. Bakwin, and C. A. Grainger, 2003: Toward constraining regional-scale fluxes of CO₂ with atmospheric observations over a continent: 1. Observed spatial variability from airborne platforms. *J. Geophys. Res.*, **108**, doi:10.1029/2002JD003018.
- Gloor, M., P. Bakwin, D. Hurst, L. Lock, and R. Draxler, 2001: What is the concentration footprint of a tall tower? *J. Geophys. Res.*, **106(17)**, 831–840.
- Gruber, N., M. Gloor, S. E. Mikaloff-Fletcher, S. C. Doney, S. Dutkiewicz, M. J. Follows, M. Gerber, A. R. Jacobson, F. Joos, K. Lindsay, D. Menemenlis, A. Mouchet, S. A. Muller, J. L. Sarmiento, and T. Takahashi, 2009: Oceanic sources, sinks, and transport of atmospheric CO₂. *Global Biogeochem. Cy.*, **23**, GB1005.
- Gurney, K. R., Y.-H. Chen, T. Maki, S. R. Kawa, A. Andrews, and Z. Zhu, 2005: Sensitivity of atmospheric CO₂ inversions to seasonal and interannual variations in fossil fuel emissions. *J. Geophys. Res.*, **110**, D10308, doi:10.1029/2004JD005373.
- Gurney, K. R., R. M. Law, A. S. Denning, P. J. Rayner, D. Baker, P. Bousquet, L. Bruhwiler, Y.-H. Chen, P. Ciais, S. Fan, I. Y. Fung, M. Gloor, M. Heimann, K. Higuchi, J. John, E. Kowalczyk, T. Maki, S. Maksyutov, P. Peylin, M. Prather, B. C. Pak, J. Sarmiento, S. Taguchi, T. Takahashi, and C.-W. Yuen, 2003: Transcom 3 inversion intercomparison: 1. Annual mean control results and sensitivity to transport and prior flux information. *Tellus*, **55B**, 555–579.

- Gurney, K. R., R. M. Law, A. S. Denning, P. J. Rayner, D. Baker, P. Bousquet, L. Bruhwiler, Y.-H. Chen, P. Ciais, S. Fan, I. Y. Fung, M. Gloor, M. Heimann, K. Higuchi, J. John, T. Maki, S. Maksyutov, K. Masarie, P. Peylin, M. Prather, B. C. Pak, J. Randerson, J. Sarmiento, S. Taguchi, T. Takahashi, and C.-W. Yuen, 2002: Towards robust regional estimates of CO₂ sources and sinks using atmospheric transport models. *Nature*, **415**, 626–630.
- Gurney, K. R., R. M. Law, A. S. Denning, P. J. Rayner, B. C. Pak, D. Baker, P. Bousquet, L. Bruhwiler, Y.-H. Chen, P. Ciais, I. Y. Fung, M. Heimann, J. John, T. Maki, S. Maksyutov, P. Peylin, M. Prather, and S. Taguchi, 2004: Transcom 3 inversion intercomparison: Model mean results for the estimation of seasonal carbon sources and sinks. *Global Biogeochem. Cy.*, **18**, GB1010, doi:10.1029/2003GB002111.
- Gurney, K. R., D. Mendoza, Y. Zhou, M. Fischer, S. de la Rue du Can, S. Geethakumar, and C. Miller, 2009: The Vulcan Project: High resolution fossil fuel combustion CO₂ emissions fluxes for the United States. *Environ. Sci. Technol.*, **43**, doi:10.1021/es900806c.
- Hack, J. J., 1994: Parameterization of moist convection in the National Center for Atmospheric Research community climate model (CCM2). *J. Geophys. Res.*, **99**, 5551–5568.
- Hanan, N. P., J. A. Berry, S. B. Verma, E. A. Walter-Shea, A. E. Suyker, G. G. Burba, and A. S. Denning, 2005: Testing a model of CO₂, water and energy exchange in Great Plains tall-grass prairie and wheat ecosystems. *Agr. Forest Meteorol.*, **131**, 162179.
- Hansen, M. C., R. S. DeFries, J. R. G. Townshend, and et al., 2000: Global land cover classification at 1km spatial resolution using a classification tree approach. *Int. J. Remote Sens.*, **21**, 1331–1364.
- Heimann, M., 2001: Atmospheric Inversion Calculations Performed for IPCC Third Assessment Report Chapter 3 (The carbon cycle and atmospheric CO₂). Technical report, Max-Planck-Inst. Fr Biogeochem., Jena, Germany.
- Helliker, B. R., J. A. Berry, A. K. Betts, P. S. Bakwin, K. J. Davis, A. S. Denning, J. R. Ehleringer, J. B. Miller, M. P. Butler, and D. M. Ricciuto, 2004: Estimates of net CO₂ flux by application of equilibrium boundary layer concepts to CO₂ and water vapor measurements from a tall tower. *J. Geophys. Res.*, **109**, D20106, doi:10.1029/2004JD004532.
- Higuchi, K., D. Worthy, D. Chan, and A. Shashkov, 2003: Regional source/sink impact on the diurnal, seasonal and inter-annual variations in atmospheric CO₂ at a boreal forest site in Canada. *Tellus*, **55B**, 115–125.
- Hinzman, L. D., N. D. Bettez, W. R. Bolton, F. S. Chapin, M. B. Dyrurgerov, C. L. Fastie, B. Griffith, R. D. Hollister, A. Hope, H. P. Huntington, and et al., 2005: Evidence and implications of recent climate change in northern Alaska and other arctic regions. *Clim. Change*, **72**, 251298.
- Holtlag, A. A. M. and B. A. Boville, 1993: Local versus non-local boundary layer diffusion in a global climate model. *J. Climate*, **6**, 1825–1842.
- Houghton, R. A., 1999: The annual net flux of carbon to the atmosphere from changes in land use 1850-1990. *Tellus*, **51B**, 298–313.

- Houweling, S., I. Aben, F.-M. Breon, F. Chevallier, N. Deutscher, R. Engelen, C. Gerbig, D. Griffith, K. Hungerschofer, R. Macatangay, J. Marshall, J. Notholt, W. Peters, and S. Serrar, 2010: The importance of transport model uncertainties for the estimation of CO₂ sources and sinks using satellite measurements. *Atmos. Chem. Phys.*, **10**, 9981–9992.
- Houweling, S., F.-M. Breon, I. Aben, C. Rodenbeck, M. Gloor, M. Heimann, and P. Ciais, 2004: Inverse modeling of CO₂ sources and sinks using satellite data: a synthetic inter-comparison of measurement techniques and their performance as a function of space and time. *Atmos. Chem. Phys.*, **4**, 523–538.
- Houweling, S., T. Kaminski, F. Dentener, J. Lelieveld, and M. Heimann, 1999: Inverse modelling of methane sources and sinks using the adjoint of a global transport model. *J. Geophys. Res.*, **104**, 26137–26160.
- Hu, Y. and K. K. Tung, 2001: Interannual and decadal variations of planetary wave activity, stratospheric cooling, and northern hemisphere annular mode. *J. Climate*, **15**, 1659–1673.
- Huang, H.-P. and W. A. Robinson, 1998: Two-dimensional turbulence and persistent zonal jets in a global barotropic model. *J. Atmos. Sci.*, **55**.
- Huffman, G. J., R. F. Adler, M. Morrissey, D. T. Bolvin, S. Curtis, R. Joyce, B. McGavock, and J. Susskind, 2001: Global precipitation at one degree daily resolution from multi-satellite observations. *J. Hydrometeorol.*, **2**, 3650.
- Hungerschofer, K., F.-M. Breon, P. Peylin, F. Chevallier, P. Rayner, A. Klonecki, S. Houweling, and J. Marshall, 2010: Evaluation of various observing systems for the global monitoring of CO₂ surface fluxes. *Atmos. Chem. Phys.*, **10**, 10503–10520.
- Hurwitz, M. D., D. M. Ricciuto, P. S. Bakwin, K. J. Davis, W. Wang, C. Yi, and M. P. Butler, 2004: Transport of carbon dioxide in the presence of storm systems over a Northern Wisconsin Forest. *J. Atmos. Sci.*, **61**, 607–618.
- Ingmann, P., 2009: A-SCOPE, Advanced space carbon and climate observation of planet earth: Report for Assessment. Technical Report SP-1313/1, ESA communication production of ce, Noordwijk, The Netherlands.
- Intergovernmental Panel on Climate Change, 2001: *Climate Change 2001: The Scientific Basis. Contribution of the Working Group I to the Third Assessment Report of the Intergovernmental Panel on Climate Change*, Houghton, J. T. et al., eds. Cambridge and New York: IPCC.
- Intergovernmental Panel on Climate Change, 2007: *Climate Change 2007: The Physical Science Basis, Contribution from Working Group I to the Fourth Assessment Report of the Intergovernmental Panel on Climate Change*, edited by S. Solomon et al. Cambridge Univ. Press, Cambridge, U.K.
- Jones, P. W., 1999: First- and Second-Order Conservative Remapping Schemes for Grids in Spherical coordinates. *Mon. Wea. Rev.*, **127**, 2204–2210.
- Kaminski, T., M. Heimann, and R. Giering, 1999: A coarse grid three dimensional global inverse model of the atmospheric transport. Inversion of the transport of CO₂ in the 1980s. *J. Geophys. Res.*, **104**, 18555–18581.

- Kaminski, T., P. J. Rayner, M. Heimann, and I. G. Enting, 2001: On aggregation errors in atmospheric transport inversions. *J. Geophys. Res.*, **106**, 4703–4715.
- Kanamitsu, M., W. Ebisuzaki, J. Woollen, K.-S. Yang, J. J. Hnilo, M. Fiorino, and G. L. Potter, 2002: NCEP-DOE AMIP-II reanalysis (R-2). *Bull. Amer. Meteor. Soc.*, **83**, 1631–1643.
- Kawa, S. R., D. J. E. III, S. Pawson, and Z. Zhu, 2004: Global CO₂ transport simulations using meteorological data from the NASA data assimilation system. *J. Geophys. Res.*, **109**, D18312, doi:10.1029/2004JD004554.
- Keeling, C. D., J. F. S. Chin, and T. P. Whorf, 1995: Increased activity of northern vegetation inferred from atmospheric CO₂ measurements. *Nature*, **382**, 146–149.
- Keppel-Aleks, G., P. O. Wennberg, and T. Schneider, 2011: Sources of variations in total column carbon dioxide. *Atmos. Chem. Phys.*, **10**, 30569–30611.
- Khvorostyanov, D. V., P. Ciais, G. Krinner, and S. A. Zimov, 2008: Vulnerability of east Siberia's frozen carbon stores to future warming. *Geophys. Res. Lett.*, **35**, L10703, doi:10.1029/2008GL033639.
- Kiehl, J. T., J. J. Hack, G. B. Bonan, B. A. Boville, D. L. Williamson, and P. J. Rasch, 1998: The National Center for Atmospheric Research Community Climate Model: CCM3. *J. Climate*, **11**, 1131–1149.
- Kuo, Y.-H., M. A. Shapiro, and E. G. Donall, 1991: The interaction between baroclinic and diabatic processes in a numerical simulation of a rapidly intensifying extratropical marine cyclone. *Mon. Wea. Rev.*, **119**, 368–384.
- Kuze, A., H. Suto, M. Nakajima, and T. Hamazaki, 2010: Thermal and near infrared sensor for carbon observation Fourier-transform spectrometer on the Greenhouse Gases Observing Satellite for greenhouse gas monitoring. *Applied Optics*, **48**, 6716–6733.
- Large, W. G. and S. G. Yeager, 2004: Diurnal to decadal global forcing for ocean and sea ice models: the data sets and flux climatologies. *NCAR Technical Note*. NCAR/TN-460+STR 111 pp.
- Lauvaux, T., O. Pannekoucke, C. Sarrat, F. Chevallier, P. Ciais, J. Noilhan, and P. J. Rayner, 2009: Structure of the transport uncertainty in mesoscale inversions of CO₂ sources and sinks using ensemble model simulations. *Biogeosciences*, **6**, 1089–1102.
- Law, R. M., Y.-H. Chen, K. R. Gurney, and TransCom 3 Modellers, 2003: TransCom 3 CO₂ inversion intercomparison: 2. Sensitivity of annual mean results to data choices. *Tellus*, **55B**, 580–595.
- Law, R. M., P. J. Rayner, L. P. Steele, and I. G. Enting, 2002: Using high temporal frequency data for CO₂ inversions. *Global Biogeochem. Cy.*, **16**, doi:10.1029/2001GB001593.
- Le Quere, C., M. R. Raupach, J. G. Canadell, G. Marland, and et al., 2009: Trends in the sources and sinks of carbon dioxide. *Nature Geoscience*, **2**, 831–836.
- Li, Q., H. F. Graf, and M. A. Giorgetta, 2006: Stationary planetary wave propagation in northern hemisphere winter - climatological analysis of the refractive index. *Atmos. Chem. Phys. Disc.*, **6**, 9033–9067.

- Li, Q., D. J. Jacob, T. D. Fairlie, H. Liu, R. M. Yantosca, and R. Martin, 2002: Stratospheric versus pollution influences on ozone at Bermuda: Reconciling past analysis. *J. Geophys. Res.*, **107**, 10.1029/2002JD002138.
- Lin, B.-D., 1982: The behavior of winter stationary planetary waves forced by topography and diabatic heating. *J. Atmos. Sci.*, **39**, 1206–1226.
- Lin, S.-J., 2004: A Vertically Lagrangian finite-volume dynamical core for global models. *Mon. Wea. Rev.*, **132**, 2293–2307.
- Lin, S. J. and R. B. Rood, 1996: Multidimensional flux-form semi-Lagrangian transport schemes. *Mon. Wea. Rev.*, **124**, 2046–2070.
- Lock, A. P., A. R. Brown, M. R. Bush, G. M. Martin, and R. N. B. Smith, 2000: A new boundary layer mixing scheme. Part I: Scheme description and single-column model tests. *Mon. Wea. Rev.*, **138**, 3187–3199.
- Lokupitiya, R. S., D. Zupanski, A. S. Denning, S. R. Kawa, K. R. Gurney, and M. Zupanski, 2008: Estimation of global CO₂ fluxes at regional scale using the maximum likelihood ensemble iter. *J. Geophys. Res.*, **113**, D20110, doi:10.1029/2007JD009679.
- Lorenz, E. N., 1955: Available potential energy and the maintenance of the general circulation. *Tellus*, **2**, 157–167.
- Lorenz, E. N., 2006: Reflections on the conception, birth, and childhood of numerical weather prediction. *Annu. Rev. Earth Planet. Sci.*, **34**, 37–45.
- Los, S. O., G. J. Collatz, P. J. Sellers, and et al., 2000: A global 9-yr biophysical land surface dataset from NOAA AVHRR data. *J. Hydrometeor.*, **1**, 183–199.
- Louis, J., M. Tiedtke, and J. Geleyn, 1982: A short history of the pbl parameterization at ecmwf. In *Proceedings of the ECMWF Workshop on Planetary Boundary Layer Parameterization*, page 5980, Reading, United Kingdom, ECMWF.
- Mahowald, N., C. Luo, J. D. Corral, and C. Zender, 2003: Interannual variability in atmospheric mineral aerosols from a 22-year model simulation and observational data. *J. Geophys. Res.*, **108**, 4352.
- Manning, A. C. and R. F. Keeling, 2006: Global oceanic and land biotic carbon sinks from the Scripps atmospheric oxygen flask sampling network. *Tellus*, **58B**, 95116.
- Matsuno, T., 1970: Vertical propagation of stationary planetary waves in the winter northern hemisphere. *J. Atmos. Sci.*, **27**, 871–883.
- McNeil, B. I., R. J. Matear, R. M. Key, J. L. Bullister, and J. L. Sarmiento, 2003: Anthropogenic CO₂ uptake by the ocean based on the global chlorofluorocarbon data set. *Science*, **299**, 235239.
- Merrill, J. T. and J. L. Moody, 1996: Synoptic meteorology and transport during the North Atlantic Regional Experiment (NARE) intensive: Overview. *J. Geophys. Res.*, **101**, 28903–28921.

- Michalak, A. M., L. Bruhwiler, and P. P. Tans, 2004: A geostatistical approach to surface flux estimation of atmospheric trace gases. *J. Geophys. Res.*, **109**, D14109, doi:10.1029/2003JD004422.
- Miller, C. E., D. Crisp, P. L. DeCola, S. C. Olsen, J. T. Randerson, A. M. Michalak, A. Alkhaled, P. Rayner, D. J. Jacob, P. Suntharalingam, D. B. A. Jones, A. S. Denning, M. E. Nicholls, S. C. Doney, S. Pawson, H. Boesch, B. J. Connor, I. Y. Fung, D. O'Brien, R. J. Salawitch, S. P. Sander, B. Sen, P. Tans, G. C. Toon, P. O. Wennberg, S. C. Wofsy, Y. L. Yung, and R. M. Law, 2007: Precision requirements for space-based XCO₂ data. *J. Geophys. Res.*, **112**, D10314, doi:10.1029/2006JD007659.
- Miyazaki, K., P. K. Patra, M. Takigawa, T. Iwasaki, and T. Nakazawa, 2008: Global-scale transport of carbon dioxide in the troposphere. *J. Geophys. Res.*, **113**, D15301, doi:10.1029/2007JD009557.
- Miyazaki, Y. and et al., 2003: Synoptic-scale transport of reactive nitrogen over the western Pacific in spring. *J. Geophys. Res.*, **108**, 8788, doi:10.1029/2002JD003248.
- Moody, J. L., J. C. Davenport, T. Merrill, S. J. Oltmans, D. D. Parrish, J. S. Holloway, H. Levy II, G. L. Forbes, M. Trainer, and M. Buhr, 1996: Meteorological mechanisms for transporting O₃ over the western North Atlantic Ocean: A case study for August 24-29, 1993. *J. Geophys. Res.*, **101**, 29213–29227.
- Moore, J. K., S. C. Doney, and K. Lindsay, 2004: Upper ocean ecosystem dynamics and iron cycling in a global 3-D model. *Global Biogeochem. Cy.*, **18**, GB4028. doi:10.1029/2004GB002220.
- Moorthi, S. and M. J. Suarez, 1992: Relaxed Arakawa-Schubert: A parameterization of moist convection for general circulation models. *Mon. Wea. Rev.*, **120**, 978–1002.
- Murakami, T., 1965: Energy cycle of the stratospheric warming in early 1958. *J. Meteor. Soc. Japan*, **43**, 262–283.
- Nielson, J., 2000: Documentation for the Three-Dimensional Parameterized Chemistry and Transport Model. Emergent Information Technologies, Inc. Technical report, NASA Goddard Space Flight Center.
- NOAA GMD, Boulder, Colorado, 2009: GLOBALVIEW-CO₂: Cooperative Atmospheric Data Integration Project - Carbon Dioxide. [Also available on Internet via anonymous FTP to ftp.cmdl.noaa.gov, Path: ccg/co2/GLOBALVIEW].
- O'Brien, D. M. and R. M. Mitchell, 1990: Zones of feasibility for retrieval of surface pressure from observations of absorption in the A-band of oxygen. Technical report, CSIRO Div. Atmos. Res., Aspendale.
- O'Neill, A. and C. E. Youngblut, 1982: Stratospheric warmings diagnosed using the transformed eulerian-mean equations and the effect of the mean state on wave propagation. *J. Atmos. Sci.*, **39**, 1370–1386.
- Ott, L. E., J. Bacmeister, S. Pawson, K. Pickering, G. Stenchikov, M. Suarez, H. Huntrieser, M. Loewenstein, J. Lopez, and I. Xueref-Remy, 2009: Analysis of convective transport and parameter sensitivity in a single column version of the Goddard earth observation system, version 5, general circulation model. *J. Atmos. Sci.*, **66**, 627–646.

- Pacala, S. and R. Socolow, 2004: Stabilization Wedges: Solving the Climate Problem for the Next 50 Years with Current Technologies. *Science*, **305**, 968–972.
- Pacala, S. W., G. C. Hurtt, D. Baker, P. Peylin, R. A. Houghton, and et al., 2001: Consistent land- and atmosphere-based U.S. carbon sink estimates. *Science*, **292**, 2316–2320.
- Parazoo, N. C., A. S. Denning, J. A. Berry, A. Wolf, D. A. Randall, S. R. Kawa, O. Pauluis, and S. C. Doney, 2011: Moist synoptic transport of CO₂ along the mid-latitude storm track. *Geophys. Res. Lett.*, **38**, L09804, doi:10.1029/2011GL047238.
- Parazoo, N. C., A. S. Denning, R. Kawa, K. Corbin, R. Lokupitia, I. Baker, and D. Worthy, 2008: Mechanisms for synoptic transport of CO₂ in the midlatitudes and tropics. *Atmos. Chem. Phys.*, **8**, 7239–7254.
- Parrish, D. D., J. S. Holloway, R. Jakoubek, M. Trainer, T. B. Ryerson, G. Hubler, F. C. Fehsenfeld, J. L. Moody, and O. R. Cooper, 2000: Mixing of anthropogenic pollution with stratospheric ozone: A case study from the North Atlantic wintertime troposphere. *J. Geophys. Res.*, **105**, 24363–24374.
- Patra, P. K., R. M. Law, W. Peters, C. Rodenbeck, M. Takigawa, C. Aulagnier, I. Baker, D. J. Bergmann, P. Bousquet, J. Brandt, and et al., 2008: TransCom model simulations of hourly atmospheric CO₂: Analysis of synoptic-scale variations for the period 2002–2003. *Global Biogeochem. Cy.*, **22**, GB4013, doi:10.1029/2007GB003081.
- Pauluis, O., A. Czaja, and R. Korty, 2008: The global atmospheric circulation on moist isentropes. *Science*, **321**, 1075–1078, DOI: 10.1126/science.1159649.
- Pauluis, O., A. Czaja, and R. Korty, 2010: The global atmospheric circulation on moist isentropic coordinates. *J. Climate*, **23**, DOI:10.1175/2009JCLI2789.1, 3077–3093.
- Peixoto, J. P. and A. H. Oort, 1992: *Physics of Climate*. AIP Press.
- Peters, W. and et al., 2007: An atmospheric perspective on North American carbon dioxide exchange: Carbon tracker. *Proc. Nat. Acad. Sci.*, **104**, 18925–18,930.
- Peters, W., J. B. Miller, J. Whitaker, A. S. Denning, A. Hirsch, M. C. Krol, D. Zupanski, L. Bruhwiler, and P. P. Tans, 2005: An ensemble data assimilation system to estimate CO₂ surface fluxes from atmospheric trace gas observations. *J. Geophys. Res.*, **110**, D24304, doi:10.1029/2005JD006157.
- Peylin, P., D. Baker, P. Bousquet, J. Sarmiento, P. Ciais, and P. Monfray, 2002: Influence of atmospheric transport uncertainty on annual mean versus seasonal inversions of atmospheric CO₂ data. *J. Geophys. Res.*, **107**, 4385, doi:10.1029/2001JD000857.
- Peylin, P., P. Bousquet, C. L. Quere, S. Sitch, P. Friedlingstein, G. McKinley, N. Gruber, P. Rayner, and P. Ciais, 2005: Multiple constraints on regional CO₂ flux variations over land and oceans. *Global Biogeochem. Cy.*, **19**, GB1011, doi:10.1029/2003GB002214.
- Phillips, N., 1958: Geostrophic errors in predicting the appalachian storm of november 1950. *Geophysica*, **6**, 389–405.

- Prados, A. I., R. R. Dickerson, B. G. Doddridge, P. A. Milne, J. L. Moody, and J. T. Merrill, 1999: Transport of ozone and pollutants from North America to the North Atlantic Ocean during the 1996 AEROCE Intensive Experiment. *J. Geophys. Res.*, **104**, 26219–26234.
- Randall, D. A., D. A. Dazlich, C. Zhang, A. S. Denning, P. J. Sellers, C. J. Tucker, L. Bounoua, J. A. Berry, G. J. Collatz, C. B. Field, S. O. Los, C. O. Justice, and I. Fung, 1996: A revised land surface parameterization (SiB2) for GCMs. Part III: The Greening of the Colorado State University General Circulation Model. *J. Climate*, **9**, 738–763.
- Randerson, J. T., G. R. van der Werf, L. Giglio, G. J. Collatz, and P. S. Kasibhatla, 2006: Global Fire Emissions Database, Version 2 (GFEDv2). Dataset from Oak Ridge National Laboratory Distributed Archive Center, Oak Ridge, Tennessee, U.S.A.
- Rayleigh, L., 1880: On the stability, or instability, of certain fluid motions. *Proc. Lond. Math. Soc.*, **11**, 57–70.
- Rayner, P., I. Enting, R. Francey, and R. Langenfelds, 1999: Reconstructing the recent carbon cycle from atmospheric CO₂, d13C and O₂/N₂ observations. *Tellus*, **51B**, 213–232.
- Rayner, P. J., R. M. Law, D. M. O'Brien, T. M. Butler, and A. C. Dilley, 2002: Global observations of the carbon budget 3. Initial assessment of the impact of satellite orbit, scan geometry, and cloud on measuring CO₂ from space. *J. Geophys. Res.*, **107**, doi:10.1029/2001JD000618, 2002.
- Rayner, P. J. and D. M. O'Brien, 2001: The utility of remotely sensed CO₂ concentration data in surface source inversions. *Geophys. Res. Lett.*, **28**, 1751–178.
- Rhines, P., 1975: Waves and turbulence on a beta-plane. *J. Fluid Mech.*, **69**, 417–443.
- Rienecker, M. M., M. J. Suarez, R. Gelaro, R. Todling, J. Bacmeister, E. Liu, M. G. Bosilovich, S. D. Schubert, L. Takacs, G.-K. Kim, S. Bloom, J. Chen, D. Collins, A. Conaty, A. da Silva, and et al., 2010: MERRA - NASA's Modern-Era Retrospective Analysis for Research and Applications. *J. Climate*, pages doi: 10.1175/JCLI-D-11-00015.1.
- Rodenbeck, C., S. Houweling, M. Gloor, and M. Heimann, 2003: CO₂ flux history 1982–2001 inferred from atmospheric data using a global inversion of atmospheric transport. *Atmos. Chem. Phys.*, **3**, 1919–1964.
- Rotman, D. A., J. R. Tannahill, D. E. Kinnison, P. S. Connell, D. Bergmann, D. Proctor, J. M. Rodriguez, S. J. Lin, R. B. Rood, M. J. Prather, P. J. Rasch, D. B. Considine, R. Ramarosan, and S. Kawa, 2001: Global Modeling Initiative assessment model: Model Description, integration, and testing of the transport shell. *J. Geophys. Res.*, **106**, 1669–1691.
- Salmon, R., 1998: *Lectures on Geophysical Fluid Dynamics*. Oxford University Press. 378 pp.
- Schimel, D. S., J. I. House, K. A. Hibbard, P. Bousquet, P. Ciais, P. Peylin, B. H. Braswell, M. J. Apps, D. Baker, A. Bondeau, J. Canadell, G. Churkina, W. Cramer, A. S. Denning, C. B. Field, P. Friedlingstein, C. Goodale, M. Heimann, R. A. Houghton, J. M. Melillo, B. M. III, D. Murdiyarso, I. Noble, S. W. Pacala, I. C. Prentice, M. R. Raupach, P. J. Rayner, R. J. Scholes, W. L. Steffen, and C. Wirth, 2001: Recent patterns and mechanisms of carbon exchange by terrestrial ecosystems. *Nature*, **414**, 169–172.

- Schubert, W. H. and M. T. Masarik, 2006: Potential vorticity aspects of the MJO. *Dynam. Atmos. Oceans*.
- Schuh, A. E., A. S. Denning, K. D. Corbin, I. T. Baker, M. Uliasz, N. Parazoo, A. E. Andrews, and D. E. J. Worthy, 2010: A regional high-resolution carbon flux inversion of North America for 2004. *Biogeosciences*, **7**, 1625–1644.
- Schultz, D. M., 2001: Reexamining the cold conveyor belt. *Mon. Wea. Rev.*, **129**, 2205–2225.
- Schultz, D. M., 2005: A review of cold fronts with prefrontal troughs and wind shifts. *Mon. Wea. Rev.*, **133**, 2449–2472.
- Sellers, P. J., S. O. Los, C. J. Tucker, C. O. Justice, D. A. Dazlich, G. J. Collatz, and D. A. Randall, 1996b: A revised land surface parameterization (SiB2) for atmospheric GCMs. Part II: Generation of global fields of terrestrial biophysical parameters from satellite data. *J. Climate*, **9**, 706–737.
- Sellers, P. J., Y. Mintz, Y. C. Sud, and et al., 1986: A simple biosphere model (SiB) for use within general circulation models. *J. Atmos. Sci.*, **43**, 505–531.
- Sellers, P. J., D. A. Randall, G. J. Collatz, J. A. Berry, C. B. Field, D. A. Dazlich, C. Zhang, and L. Bounoua, 1996a: A revised land surface parameterization (SiB2) for atmospheric GCMs. Part I: Model formulation. *J. Climate*, **9**, 676–705.
- Simmons, A. J. and D. M. Burridge, 1981: An energy and angular-momentum conserving vertical finite-difference scheme and hybrid vertical coordinates. *Mon. Wea. Rev.*, **109**, 758–766.
- Simmons, A. J. and R. Stru ng, 1983: Numerical forecasts of stratospheric warming events using a model with a hybrid vertical coordinate. *Quart. J. Roy. Meteor. Soc.*, **109**, 81–111.
- Sinclair, V. A., S. L. Gray, and S. E. Belcher, 2008: Boundary-layer ventilation by baroclinic life cycles. *Quart. J. Roy. Meteor. Soc.*, **134**, 1409–1424.
- Smith, R. and P. Gent, 2004: Reference Manual for the Parallel Ocean Program (POP). Ocean Component of the Community Climate System Model (CCSM2.0 and 3.0). Technical report, Los Alamos National Laboratory, Los Alamos, New Mexico. LAUR-02-2484.
- Smith, W. L., C. M. Hayden, D. Q. Wark, and L. M. McMillin, 1979: The TIROS-N Operational Vertical Sounder. *Bull. Amer. Meteor. Soc.*, **60**, 11721187.
- Stephens, B. B., K. R. Gurney, P. P. Tans, C. Sweeney, W. Peters, L. Bruhwiler, P. Ciais, M. Ramonet, P. Bousquet, T. Nakazawa, S. Aoki, T. Machida, G. Inoue, N. Vinnichenko, J. Lloyd, A. Jordan, M. Heimann, O. Shibistova, R. L. Langenfelds, L. P. Steele, R. J. Francey, and A. S. Denning, 2007: Weak northern and strong tropical land carbon uptake from vertical profiles of atmospheric CO₂. *Science*, **316**, 1732–1735.
- Stewart, R. E., K. K. Szeto, R. F. Reinking, S. A. Clough, and S. P. Ballard, 1998: Midlatitude cyclonic cloud systems and their features affecting large scales and climate. *Rev. Geophys.*, **36**, 245–273.
- Stohl, A., 2001: A one-year Lagrangian climatology of airstreams in the northern hemisphere troposphere and lowermost stratosphere. *J. Geophys. Res.*, **106**, 7263–7279.

- Syed, K. H., L. B. Flanagan, P. J. Carlson, A. J. Glenn, and K. E. V. Gaalen, 2006: Environmental control of net ecosystem CO₂ exchange and carbon balance in a treed, moderately rich fen in northern Alberta. *Agr. Forest Meteorol.*, **140**, 97–114.
- Takahashi, T. S., S. C. Sutherland, C. Sweeney, A. Poisson, N. Metzl, B. Tilbrook, N. Bates, R. A. Feely, C. Sabine, J. Olafsson, and Y. Nojiri, 2002: Global Sea-Air CO₂ flux based on climatological surface ocean pCO₂ and seasonal biological and temperature effects. *Deep-Sea Res. Pt. II*, **49**, 1601–1622.
- Tans, P., I. Fung, and T. Takahashi, 1990: Observational Constraints on the Global Atmospheric CO₂ Budget. *Science*, **247**, 1431.
- Tao, W.-K., J. Chern, R. Atlas, D. Randall, X. Lin, M. Khairoutdinov, J.-L. Li, D. E. Waliser, A. Hou, C. Peters-Lidard, W. Lau, and J. Simpson, 2009: Multi-scale modeling system: Development, applications and critical issues. *Bull. Amer. Meteor. Soc.*, **90**, 515–534.
- Tao, W.-K. and J. Simpson, 1993: Goddard Cumulus Ensemble Model. Part I: Model Description. *Terr. Atmos. Ocean. Sci.*, **4**, 35–72.
- Taylor, G. I., 1915: Eddy motion in the atmosphere. *Philos. Trans. R. Soc. Lond. A.*, **115**, 1–26.
- Teillet, P. M., E. Saleous, M. C. Hansen, and et al., 2000: An evaluation of the global 1-km AVHRR land dataset. *Int. J. Remote Sens.*, **21**, 1987–2021.
- Townsend, R. D. and D. R. Johnson, 1985: A diagnostic study of the isentropic zonally averaged mass circulation during the first GARP global experiment. *J. Atmos. Sci.*, **42**, 1565–1579.
- Trenberth, K. E., 1991: Storm tracks in the Southern Hemisphere. *J. Atmos. Sci.*, **48**, 2159–2178.
- Vallis, G. K. and M. E. Maltrud, 1993: Generation of mean flows and jets on a beta plane and over topography. *J. Phys. Oceanogr.*, **23**, 1346–1362.
- Vidale, P. L. and R. Stockli, 2005: Prognostic canopy air space solutions for land surface exchanges. *Theor. Appl. Climatol.*, **80**, 245257.
- Wallace, J. M., G.-H. Lim, and M. Blackmon, 1988: Relationship between cyclone tracks, anticyclone tracks and baroclinic waveguides. *J. Atmos. Sci.*, **45**, 439–462.
- Wang, J. W., A. S. Denning, L. Lu, I. T. Baker, K. D. Corbin, and K. J. Davis, 2007: Observations and simulations of synoptic, regional, and local variations in atmospheric CO₂. *J. Geophys. Res.*, **112**, D04108, doi:10.1029/2006JD007410.
- Wang, K.-Y. and D. E. Shallcross, 2000: A lagrangian study of the three-dimensional transport of boundary-layer tracers in an idealized baroclinic-wave life-cycle. *J. Atmos. Chem.*, **35**, 227–247.
- Worthy, D. E., K. Higuchi, and D. Chan, 2003: North American influence on atmospheric carbon dioxide data collected at Sable Island. *Tellus*, **55B**, 105114.
- Worthy, D. E., I. Levin, N. B. Trivett, A. J. Kuhlmann, J. F. Hopper, and M. K. Ernst, 1998: Seven years of continuous methane observations at a remote boreal site in Ontario, Canada. *J. Geophys. Res.*, **103**, 15995–16007.

- Yang, Z., R. A. Washenfelder, G. Keppel-Aleks, N. Y. Krakauer, J. T. Randerson, P. P. Tans, C. Sweeney, and P. O. Wennberg, 2007: New constraints on northern hemisphere growing season net flux. *Geophys. Res. Lett.*, **34**, L12807, doi:10.1029/2007GL029742.
- Yi, C., K. J. Davis, P. S. Bakwin, A. S. Denning, N. Zhang, A. Desai, J. C. Lin, and C. Gerbig, 2004: Observed covariance between ecosystem carbon exchange and atmospheric boundary Layer dynamics at a site in northern Wisconsin. *J. Geophys. Res.*, **109**, D08302, doi:10.1029/2003JD004164.
- Zhang, G. J. and N. A. McFarlane, 1995: Sensitivity of climate simulations to the parameterization of cumulus convection in the Canadian climate center general-circulation model. *Atmos. Ocean*, **33**, 407–446.
- Zimov, S. A., E. A. G. Schuur, and F. Stuart Chapin III, 2006: Permafrost and the global carbon budget. *Science*, **312**, 1612–1613.
- Zupanski, D., A. S. Denning, M. Uliasz, M. Zupanski, A. E. Schuh, P. J. Rayner, W. Peters, and K. D. Corbin, 2007a: Carbon flux bias estimation employing Maximum Likelihood Ensemble Filter (MLEF). *J. Geophys. Res.*, **112**, D17107, doi:10.1029/2006JD008371.
- Zupanski, D., A. Y. Hou, S. Q. Zhang, M. Zupanski, C. D. Kummerow, and S. H. Cheung, 2007b: Information theory and ensemble data assimilation. *Quart. J. Roy. Meteor. Soc.*, **133**, 1533–1545.
- Zupanski, D. and M. Zupanski, 2006: Model error estimation employing an ensemble data assimilation approach. *Mon. Wea. Rev.*, **134**, 1337–1354.
- Zupanski, M., 2005: Maximum likelihood ensemble filter: theoretical aspects. *Mon. Wea. Rev.*, **133**, 1710–1726.
- Zupanski, M., S. J. Fletcher, I. M. Navon, B. Uzunoglu, R. P. Heikes, D. A. Randall, T. D. Ringler, and D. Daescu, 2006: Initiation of ensemble data assimilation. *Tellus*, **58A**, 159–170.